Implications of the Dense City Centre to Surface-Atmosphere Exchanges

Kotthaus, Simone

Awarding institution:
King's College London

Title: Implications of the Dense City Centre to Surface-Atmosphere Exchanges

Author: Simone Kotthaus

Implications of the Dense City Centre to Surface-Atmosphere Exchanges

PhD Thesis

Simone Kotthaus

Department of Geography

King's College London

University of London

Submitted: July 2013

Defended: Nov 2013

Finalised: Feb 2014

Acknowledgements

I thank Prof Sue Grimmond for the inspiration I found in her work, the guidance she gave me on the path leading to this thesis, and finally the professional and personal support I received from her. I thank Prof Martin Wooster for the motivating discussions, his sound advice and the encouragement I found when exploring new ideas with him.

This thesis was compiled in the Micrometeorological Research Group at the Geography Department at King's College London. It was funded by EUFP7 Grant agreement no. 211345 (BRIDGE) and NERC ClearfLo (NE/H003231/1), supported by NERC ARSF (GB08/19), EPSRC (EP/I00159X/1, EP/I00159X/2) Materials Innovation Hub and additional funding support from KCL.

I thank Dr Andreas Christen (UBC, 2010) for use of his IDL based implementation of the footprint model; Dr Brian Offerle and Dr Fredrik Lindberg for use of their script for morphometric parameter calculations; Dr Arnold Moene at Wageningen University for providing the ECpack software and for all advice regarding its usage; KCL Directorate of Estates & Facilities for giving us the opportunity to operate the various measurement sites.

I would like to thank Dr Catherine Souch and Helen Ward for their comments and proofreading of the manuscript. I thank Neil Crosby for proofreading Chapters II and IV. I appreciate the constructive comments and suggestions of the reviewers, which proved helpful in the development of Chapters III-V.

Explicitly, I would like to thank all past and present members of the micrometeorological research group who contributed to the extensive London Urban Micromet Observatory project, especially those who have experienced the pleasure of the weekly 'micromet-fixing' rota. Namely, I thank Helen Ward, Mariana Lina Gouvea, Lukas Pauscher, Matt Blackett, Thomas Loridan, Tom Smith, Duick Young, Alex Björkegren, Fredrik Lindberg, Leena Järvi, Jinda Sea-Jung, Cris Castillo, John Mustchin, Will Morrison, Jon Durrans, Oscar Finnemore, Grace Healy, Marc Thomas, Veronica Bellucco, Mark de Jong, Pru Robinson, Alessandra Sala, and Lucía López Martínez.

Another special thanks goes to Jiangping He, for supporting the data archive, software development but most of all for calming me down after the big server crash. I would also like to express my gratitude for the technical support I received from Alastair Raynolds, Dr Paul Smith, Dr Bruce Main, and Dr Trevor Blackall.

Further, I specifically thank Dr Tom Smith for introducing me to Fourier Transform InfraRed Spectroscopy and his advice on data collection and processing. I am extremely grateful to Alastair Mac Arthur and Chris MacLallen at the NERC Field Spectroscopy Facility for introducing me to field spectroscopy techniques, and for supporting all my special requests. Similarly, I am grateful to the team at NERC ARSF for their support.

I would like to thank my colleagues in the team A, for the inspiring discussions but most of all for the fun and relaxing moments we have had together. Especially, Helen, Leena, Thomas, Lukas, Mari, Fredrik and Jinda – Kings would not have been the same without you.

From all my heart, I am grateful for the encouragement and support I receive from my friends and family. Thank you so much!

Abstract

In dense urban areas, micro-meteorological processes are closely entangled with human activities. This study of the central business district (CBD) analyses an extended (3.5 years) dataset of surface-atmosphere energy exchanges in London. The focus is on the controls on radiation, anthropogenic heat and the turbulent latent and sensible heat fluxes. The impact of the composition and three-dimensional structure of the urban surface, plus the associated anthropogenic activities, are investigated using remote sensing techniques, *in-situ* observations and modelling at a range of spatial and temporal scales.

Radiative properties of urban surfaces are shown to significantly influence the radiation balance. Spectroscopy measurements of a variety of impervious materials illustrate that spectral features, often used to identify materials, are more distinct in the long-wave compared to the short-wave region. The impact of surface geometry and atmospheric conditions on the radiation balance is investigated based on local-scale measurements of broadband radiation components.

Long-term radiative and turbulent heat flux measurements suggest a significant amount of energy is supplied by the anthropogenic heat flux, which is affirmed by model results. Micro-scale anthropogenic sources of heat, moisture, and carbon dioxide are addressed by a new filtering technique for the processing of local-scale eddy covariance (EC) fluxes.

Surface characteristics and anthropogenic activities influence the energy partitioning of sensible and latent heat: substantial heat storage and additional anthropogenic energy enhance sensible heat exchange, while impervious surfaces restrict moisture availability. Given the limited vegetation in the source area, evaporation is mainly driven by rainwater. The dominant sensible heat and high momentum fluxes favour unstable and neutral atmospheric conditions.

This work demonstrates how, even in the complex setting of a CBD, observations provide useful information about processes governing surface-atmosphere exchange that have to be understood in the context of global urbanisation and climate change adaptation strategies.

Contents

List of Figures

List of Tables

List of Symbols

Symbol	Description	Units
c	speed of light	m s^{-1}
c_p	specific heat at constant pressure	J Kg^{-1} K^{-1}
C_D	surface Drag coefficient	
CO_2	carbon dioxide concentration	mmol m^{-3}
dir	wind direction	°
e	vapour pressure	hPa
E_λ	detected energy spectrum	
F_{CO2}	turbulent flux of carbon dioxide	µmol m^{-2} s^{-1}
G_λ	instrument response (gain)	
h	Planck constant	m^2 kg s^{-1}
H_2O	water vapour concentration	mmol m^{-3}
IQR	inter-quartile range	
k	Boltzmann constant	m^2 kg s^{-2} K^{-1}
krt	kurtosis	
$K_\downarrow$	incoming short-wave radiation	W m^{-2}
$K_\uparrow$	outgoing short-wave radiation	W m^{-2}
l_w	latent heat of vaporisation for water	J kg^{-1}
L	Obukhov length	m
L_λ	Blackbody radiance	W m^{-2} µm^{-1} sr^{-1}
$L_\downarrow$	incoming long-wave radiation	W m^{-2}
$L_\uparrow$	outgoing long-wave radiation	W m^{-2}
MC	med-couple	
med	median	
MED	median	
MIN	minimum	
mr	mid-range	
mrm	absolute deviation from the midrange	
p	barometric pressure	hPa
p_λ	spectral reflectance of a reference panel	
P	total thermal power radiated	W m^{-2}
q	specific humidity	kg kg^{-1}
q	quartile	
Q*	net all-wave radiation	W m^{-2}
$Q_\downarrow$	total incoming radiation	W m^{-2}
Q_E	turbulent flux of latent heat	W m^{-2}
Q_F	anthropogenic heat flux	W m^{-2}
Q_{Fb}	anthropogenic heat flux from buildings	W m^{-2}
Q_{Fm}	anthropogenic heat flux from human metabolism	W m^{-2}
Q_{Ft}	anthropogenic heat flux from traffic	W m^{-2}
Q_H	turbulent flux of sensible heat	W m^{-2}
Q_{RES}	residual of the surface energy balance	W m^{-2}
R_λ	spectral radiance	W m^{-2} µm^{-1} sr^{-1}
$R_{\lambda\downarrow}$	incoming spectral radiance (irradiance)	W m^{-2} µm^{-1} sr^{-1}
$R_{\lambda\uparrow}$	outgoing spectral radiance	W m^{-2} µm^{-1} sr^{-1}
$R_{\lambda d}$	down-welling thermal spectral radiance	W m^{-2} µm^{-1} sr^{-1}
$R_{\lambda p}$	spectral radiance emitted by the atmospheric path	W m^{-2} µm^{-1} sr^{-1}
$R_{\lambda R}$	spectral radiance reflected by a reference panel	W m^{-2} µm^{-1} sr^{-1}
$R_{\lambda T}$	spectral radiance reflected by a target	W m^{-2} µm^{-1} sr^{-1}
R_s	radius of maximum specular reflection	m
std	standard deviation	
sdT_{air}	standard deviation of air temperature	°C
S_λ	spectral radiance emitted inside the spectrometer	W m^{-2} µm^{-1} sr^{-1}
T	temperature temperature	°C or K
T	kinetic temperature	°C or K
T	mean brightness temperature	°C
T_{air}	air temperature	°C
T_{BB}	blackbody temperature	°C or K
T_{gold}	temperature of gold reference panel	°C or K

T_s	sonic temperature	°C
T_{target}	target temperature	°C or K
u*	friction velocity	m s^{-1}
U	horizontal wind speed	m s^{-1}
w	vertical wind velocity	m s^{-1}
w	whiskers for adjusted outlyingness	
x_i	sample i in dataset x	
z'	effective height	m
z_0	roughness length of momentum	*m*
z_{0m}	roughness length of momentum	*m*
z_d	zero-plane displacement height	*m*
z_g	mean ground height	*m*
z_h	mean building height above ground	*m*
z_m	measurement height	*m*
z_r	blending height	m
z_R	height above roof surface	m
α	spectral reflectance	%
α	integrated broadband albedo	
$\overline{\alpha}$	bulk surface albedo	
α_λ	spectral reflectance	%
β	Bowen ratio	
ΔQ_S	net storage heat flux	W m^{-2}
ΔQ_A	advection flux	W m^{-2}
ΔQ_M	latent heat storage flux	W m^{-2}
γ	ratio of molecular masses of water vapour and dry air	
γ_E	IMAS event frequency	%
ε	spectral emissivity	
ε	integrated broadband emissivity	
ε_λ	spectral emissivity	
ε_{max}	maximum emissivity	
ζ	atmospheric stability parameter	
Θ	potential temperature	K
Θ	solar elevation angle	°
λ	wavelengths	nm or µm
λ_{min}	wavelengths minimum	µm
λ_{max}	wavelengths maximum	µm
λ_p	plan area fraction	
λ_f	frontal area index	
ρ	density of moist air	kg m^{-3}
σ	Stefan's constant	W m^{-2} K^{-4}
σ	standard deviation	
σ_v	cross wind standard deviation	m s^{-1}
τ	spectral transmissivity	
τ_λ	spectral transmissivity	

List of Acronyms

ASTER	Advanced Spaceborne Thermal Emission and Reflection Radiometer
BB	BlackBody
BRDF	Bi-directional Reflectance Distribution Function
BT	Brightness Temperature
CAZ	Central Activities Zone
CBD	Central Business District
DN	Digital Number
EC	Eddy Covariance
FOV	Field Of View
FSF	Field Spectroscopy Facility
FTIR	Fourier Transform InfraRed
IBL	internal boundary layers
IMAS	Identification of Micro-scale Anthropogenic Sources
ISL	the inertial sublayer
ISSTES	Iterative Spectrally Smooth Temperature/Emissivity Separation
KCL	King's College London
LAS	Large Aperture Scintillometry
LES	Large Eddy Simulation
LCZ	LCZ (Local Climate Zone,
LUMA	London Urban Micromet data Archive
LWIR	Long-wave InfraRed
MBE	Mean Bias Error
ML	Mixing Layer
MODIS	Moderate Resolution Imaging Spectroradiometer
MWIR	Mid-Wave InfraRed
NERC	National Environmental Research Council
PBL	Planetary Boundary Layer
RMSE	Root Mean Square Error
RS	Remote Sensing
RSL	Roughness SubLayer
SL	Surface Layer
TES	Temperature-Emissivity-Separation
SB	Santa Barbara urban spectral library
SLUM	Spectral Library of impervious Urban Materials
SWIR	Short-wave infrared
UBL	Urban Boundary Layer
UCL	Urban Canopy Layer
UHI	Urban Heat Island
USGS	US Geological Survey
UTC	Universal Time Coordinated
UZE	Urban Zone Energy Partitioning
QAQC	Quality Assurance Quality Control
VIS	VISible wavelength region
WMO	World Meteorological Organisation

I Introduction

This thesis is formed of four publications, each presented as an individual chapter. Conclusions of all studies as summarised subsequently (Chapter VI).

Chapter II

Kotthaus, S, TEL Smith, MJ Wooster, and CSB Grimmond, 2014: Derivation of an urban materials spectral library through emittance and reflectance spectroscopy, *in review*.

Chapter III

Kotthaus, S and CSB Grimmond, 2012: Identification of micro-scale anthropogenic CO_2, heat and moisture sources – Processing eddy covariance fluxes for a dense urban environment, *Atmos. Environ.* 57, 301–316, doi:10.1016/j.atmosenv.2012.04.024

Chapter IV

Kotthaus, S and CSB Grimmond, 2013: Energy exchanges in a dense urban environment Part I: temporal variability of long-term observations in central London, *Urban Climate*. doi:10.1016/j.uclim.2014.10.002

Chapter V

Kotthaus, S and CSB Grimmond, 2013: Energy exchanges in a dense urban environment Part II: impact of spatial heterogeneity of the surface, *Urban Climate*, doi:10.1016/j.uclim.2014.10.001

I.1 Introduction

Urban areas are a major focus of the world's climate agenda (UN-HABITAT 2013) given humanity has entered the *Urban Century* (Clarke Annez et al. 2008). Already, over 50% of the world's population lives in urban agglomerations, with even higher fractions of urban residents in many European countries (e.g. UK 80%, France 85%, Belgium 98% in 2010, UN-HABITAT 2012). Demographic projections indicate most global population growth will take place in urban areas (UN-HABITAT 2010), with global urbanisation reaching 70% by 2050 (UN-HABITAT 2012). This will involve increasing population density in cities and is expected to further urban sprawl.

The functionality and prosperity of urban systems can only be improved, or at least maintained, by design which considers the various processes involved, including climatic effects. In general, urban areas form distinct climates (Oke 1987) with clear implications from human comfort to severe health threats (Barata et al. 2011). Aspects such as large areas of impervious surfaces and reduced green space amplify extreme weather conditions that might occur more frequently in the future due to climate change, such as floods (De Sherbinin et al. 2007) and heat waves (Le Tertre et al. 2006).

Urban climate research has advanced greatly within recent decades (Arnfield 2003), however, many processes are still not fully understood. Challenges arise given the immense heterogeneity and complexity of the urban environment (Grimmond 2006). Most model and measurement techniques, and even some of the underlying theory used to interpret boundary layer processes, have been developed for more homogeneous, less complex settings and advances are needed to accommodate studies of urban forms.

Surface-atmosphere interactions in the heterogeneous urban environment are highly scale dependant. Many aspects impacting human health, such as air quality or thermal comfort, result from a combination of processes at the city scale (e.g. boundary layer growth) down to the micro-scale (e.g. wake-turbulence around buildings). Even global- and meso-scale conditions play an important role (i.e. 'background' climate and weather). Hence, urban micrometeorology needs to understand causalities at various scales, temporal and spatial, and integrate them appropriately for interpretation and applications. This is especially so when observations are used for the development or evaluation of models.

This study focuses on the impact of human activities and complex urban surface characteristics on energy exchanges in the little studied dense urban setting (Section I.2). As context, basics of boundary layer climates and energy exchange processes are summarised briefly (Section I.3) and relevant measurement and modelling techniques are introduced (Section I.4). Finally, the main aims of the research and structure of this study are outlined (Section I.5).

I.2 The dense city centre

Within cities, zones dominated by one specific land use are often clearly identifiable. Traditionally, a *central business district* (CBD) is found in the centre of the city where many businesses are located. Given land and living space are usually expensive in this area, often there are few residents. Thus the daytime population which commutes in can be larger by more than an order of magnitude than the number of people actually living in the area. In dispersed cities, several such zones can be found with slightly different functional foci (e.g. governmental district, financial centre, shopping areas).

Given form follows function, the various urban zones are distinguishable by their appearance (Stewart and Oke 2012). Surface characteristics include the three-dimensional arrangement of urban surface components, such as roads, buildings, vehicles, vegetation and also humans, their density and their materials. These depend on factors such as geographic location, history of the city, economic wealth of the area, and architectural style/era that influence its design. The central parts of many cities are dominated by impervious materials. The latter include natural stones and a variety of materials composed or altered with different processing technologies. Intra-urban differences in form and function result in strong variations in climate conditions.

Generally, comprehensive urban planning strategies require a sound understanding of current urban climates, so that decision-making can prepare the cities for anticipated effects of urbanisation and climate change (Blake et al. 2011). Yamamoto (2005), for example, lists strategies for the mitigation of the urban heat island effect (Howard 1833), which represents the increment of air temperatures found in the urban environment (Oke 1982). These measures include a reduction of anthropogenic heat release, an alteration of artificial surface materials with respect to their radiative properties and water permeability, and an optimised arrangement of surface structures in terms of their radiative behaviour and the ventilation of central urban parts. Rivers, for example, can provide corridors for clean, cool air from outside the city (Ichinose et al. 2009). Increased temperatures in the core of a city do not only affect human health directly (e.g. increased mortality, Kovats and Hajat 2008) but maybe even more severely by affecting atmospheric chemistry and hence air quality (leading to e.g. exacerbated cardio-respiratory morbidity; Pengelly et al. 2007). Beyond these direct effects, changes in air temperature also have an indirect feedback on the climate, given they control cooling and heating demands.

Climate conditions vary spatially even within one city and the impact of the atmosphere on the health of city dwellers is complicated. CBDs present a hotspot for such impact because of the dominance of impervious surfaces and anthropogenic heat release and because population concentrations are particularly high (i.e. many people are exposed to CBD (micro-) climate conditions). To date, urban climate research in CBDs is limited because this environment presents a challenge for both measurement and modelling studies. Methodologies need to be adapted to accommodate the heterogeneous urban structure and more data, from both measurements and modelling work, are required.

Future urbanization is expected to add new levels of complexity and to create even greater need for understanding dense urban environments. Guidelines for sustainable urban planning (UN-HABITAT 2012) suggest urban zones with limited functionality should give way to more integrated approaches. The first principle of the 'new urban model' promoted by the UN (UN-HABITAT 2013), for example, calls for compact, mixed-use urban design to increase/maintain the functionality of a city despite the population pressure. Modern sustainable cities need to integrate economic, domestic and recreational aspects as well as mobility in a limited surface area. Thus climate research on dense urban environments is needed for cities of today and to develop tools that will be applicable to the increasingly complex structure of future cities.

I.3 Surface energy exchanges in the urban environment

The lowest part of the atmosphere is characterised by interactions with the Earth's surface. In this so-called *Planetary Boundary Layer* (PBL, Stull 1988), climate conditions respond to the nature and composition of the underlying surface and their spatio-temporal variations. Boundary layer processes govern energy exchanges between the Sun, the Earth's surface and the atmosphere.

Surface roughness, affected by spatial variations in topography and surface cover types (e.g. open water, plant cover or buildings), is very influential in the formation of the PBL. For homogeneous, flat surfaces, horizontal wind speed basically dissipates close to the ground, at a height defined as the *roughness length* of momentum z_0. Above this it increases, under neutral stratification in a logarithmic wind profile, a characteristic for the so-called *surface layer* (SL). Where the surface is populated with objects, the flow is distorted and the roughness increased (higher z_0). If the surface elements form an approximately closed canopy, such as buildings in a city (*urban canopy layer*, UCL), complex flow patterns are generated between the structures (Hunter et al. 1992; Raupach et al. 1996; Kastner-Klein and Rotach 2004; Karra et al. 2011) and the logarithmic wind profile is initiated above $z_0 + z_d$, with the *zero-plane displacement height* z_d. In this case, the surface layer is split into the *roughness sublayer* (RSL; Raupach et al. 1980) and the *inertial sublayer* (ISL).

The RSL, where the impact of individual roughness elements predominates, extends up to the *blending height* z_r. Above, in the ISL, turbulent fluxes result from a blended mixture of surface components, so that turbulent fluxes are approximately invariant with height (within a range of about 10%). This is where the Monin-Obukhov Similarity theory (Foken 2006) for the formulation of surface layer processes is assumed to apply. The blending height is located well above the canopy and depends on the height of the roughness elements as well as their density. During daytime (i.e. times of surface heating), turbulent energy exchange is efficient and vertical gradients of wind, temperature and humidity largely balance above the SL, where the *mixing layer* (ML) makes up the largest part of the PBL. Its top is marked by a capping inversion.

Where surface cover encounters sharp changes in terms of roughness, surface temperature or humidity, *internal boundary layers* (IBL) are formed which again subdivide the PBL into regions influenced by contrasting atmospheric conditions. Air distinguished by the influence of urban surface cover constitutes a special IBL, the *urban boundary layer* (UBL), usually with atmospheric characteristics far from those observed over other surface types such as vegetation or open water.

This study focuses on energy exchange processes within the SL (Figure I.1) of a dense urban environment. It is concerned with:

A. The role of surface structure and composition, i.e. characteristics of the UCL.
B. The influence of elevated, micro-scale sources of heat, moisture and carbon dioxide on processes in the ISL.
C. The response of energy exchanges measured above the blending height to the surface composition in the local-scale source area (Section I.4.4).
D. Comparison of local-scale fluxes to those observed presumably within the RSL.

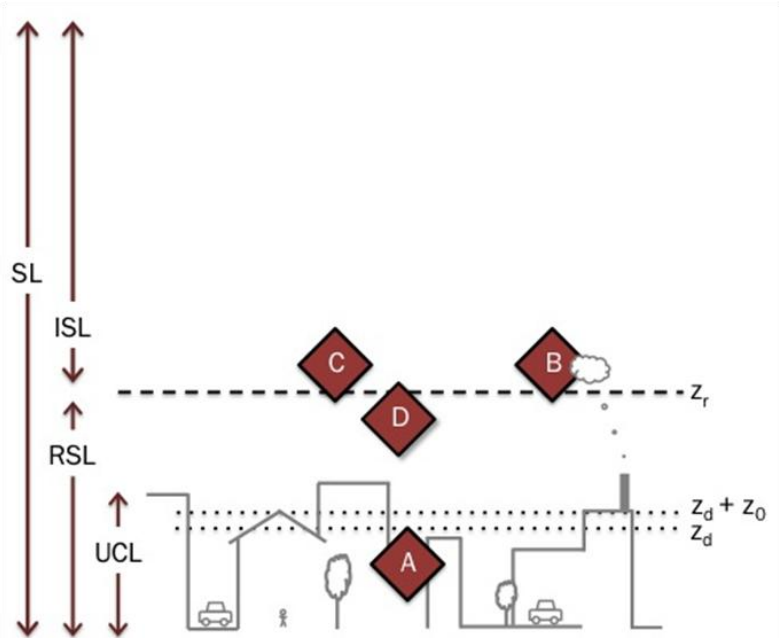

Figure I.1: This study considers a series of energy exchange processes using measurements at different locations within the surface layer (SL); see text for details and symbol definitions.

I.3.1 The urban energy balance

The urban surface energy balance is concerned with the transfer of heat through an infinitesimally thin plane at the top of a volume that comprises all urban constituents such as buildings, roads, vegetation, vehicles and people as well as the air filling the spaces between. Energy exchanges (cf. sketch in Figure I.2) with the atmosphere above the blending height are summarised by the surface energy balance equation:

$$Q^* + Q_F = Q_H + Q_E + \Delta Q_S \qquad \text{I.1}$$

with net all-wave radiation Q*, anthropogenic heat flux Q_F, turbulent sensible heat flux Q_H, turbulent latent heat flux Q_E, and net storage heat flux ΔQ_S. All these energy fluxes can be normalised by a defined surface area and are commonly expressed in W m^{-2}.

Potentially, other components can contribute to the energy balance such as snow-melt or advection (ΔQ_A). However, these are often neglected in local scale measurements of the energy balance terms. Over heterogeneous surfaces, horizontal advection at various scales occurs (Paw U et al. 2000) but it is very difficult to quantify (Finnigan 1999). In this study, potential effects of horizontal advection on the results obtained are discussed where relevant and the residual of the energy balance is analysed with the appropriate caution (i.e. no flux is quantified as the residual of the energy balance). Another term not captured in the basic form of the urban surface energy balance commonly used (eqn. I.1) is the latent heat storage flux (ΔQ_M) associated with melting/freezing of snow. However, given the limited about of snow observed in the rather mild climatological setting of the study area (London, UK), the energy potentially lost due to snow-melt is assumed to be negligible.

While energy fluxes within the canopy are dominated by a small number of sources/sinks (e.g. by the temperature of one building facet), at the blending height z_r they integrate to be from the mixture of various surface components. Above this height (Figure I.1; Figure I.2) they provide measures representative of the *local scale* (100-5000 m, Oke 1987).

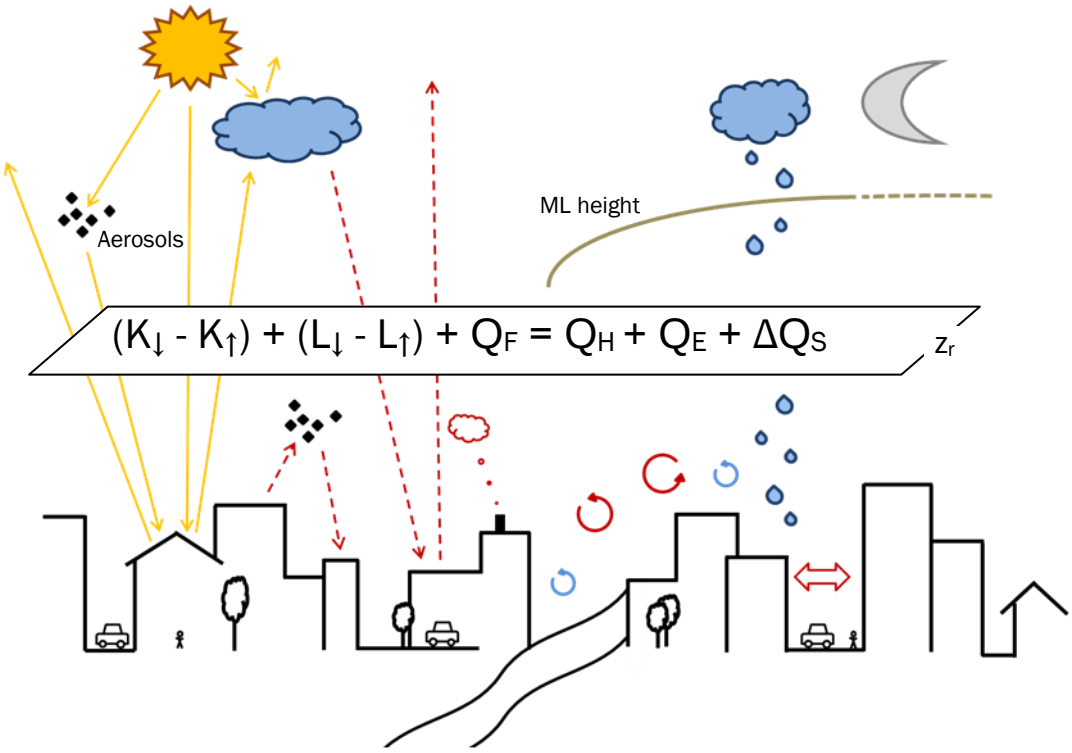

Figure I.2: Schematic diagram of surface energy exchanges of the urban surface volume with atmospheric and extra-terrestrial sources of energy; see text for symbol definitions.

I.3.2 Radiation exchanges

Generally, radiation fluxes provide the most significant amount of energy to the urban surface volume. Net all-wave radiation combines the fluxes of incoming (↓) and outgoing (↑) short- (K) and long-wave (L) radiation:

$$Q^* = (K_{\downarrow} - K_{\uparrow}) + (L_{\downarrow} - L_{\uparrow}). \quad \text{I.2}$$

The ability of a medium to absorb/emit (ε), reflect (α) or transmit (τ) radiation, with $\varepsilon + \alpha + \tau = 1$, depends on the wavelength of the radiation as well as the molecular structure and composition of the material.

The amount of incoming solar radiation that is reflected by the urban surface is described by the bulk surface albedo $\bar{\alpha} = K_{\uparrow}/K_{\downarrow}$. The latter depends on three-dimensional structure and material characteristics. For non-Lambertian surfaces, which do not reflect radiation uniformly in all directions, it is also a function of the sun-surface geometry (Steemers et al. 1998) and the amount of direct and diffuse irradiance, respectively. Passing through the atmosphere, short-wave radiation can be absorbed or scattered (e.g. by aerosols) and play an important role in chemical processes (e.g. ozone formation). Atmospheric transmissivity and scattering (determining the fraction of direct to diffuse solar radiation reaching the surface) are strongly influenced by the total column water content, i.e. presence and types of clouds (Li and Moreau 1996).

According to the Stefan-Boltzmann law, the total thermal power P emitted by an object is a function of its temperature T and emissivity ε:

$$\mathrm{P}(T) = \varepsilon\sigma\mathrm{T}^4 \quad \text{I.3}$$

with Stefan's constant σ. Absorbed incoming solar radiation increases the kinetic temperature of an object and thereby the amount of emitted thermal radiation.

Incoming radiation is affected by the urban environment, however, if air quality is not extremely poor this effect is often smaller than the urban impacts on the outgoing radiative fluxes which are more radically altered in response to the urban surface. Many urban construction materials are efficient absorbers of energy and the three-dimensional surface structure of street canyons diminishes the albedo via radiation trapping. Hence, roofs and roads can heat up considerably during daytime when solar energy is gained by the surface. Decreased albedo, increased emissivity and surface temperature result in larger outgoing long-wave and smaller outgoing short-wave radiation in urban areas compared to their rural surroundings (Christen and Vogt 2004).

Many studies suggest great potential for highly-reflective urban materials applied on roads and roofs for the mitigation of the urban heat island (UHI) phenomenon (e.g. Bretz et al. 1998; Akbari and Rose 2008). It also has been proposed that general brightening of the urban fabric could decrease air temperatures globally (Winton 2006) and is therefore considered a potential

strategy for climate change mitigation which could offset considerable CO_2 emissions (Akbari et al. 2012). However, the impact of high-reflective surface materials at building scale varies between different urban facets. It is crucial to consider if other elements of the urban surface are likely to receive the reflected short-wave radiation. For example, radiation reflected from nearby surfaces has been shown to increase the cooling demand of adjacent buildings (Yaghoobian et al. 2010; Yaghoobian and Kleissl 2012) or actually decrease the thermal comfort of pedestrians (Pearlmutter et al. 2007).

To fully understand the effect of urban materials and radiative properties on urban climates, the short- and long-wave regions of the electromagnetic spectrum need to be considered simultaneously. At the material scale, the ability to absorb or reflect radiation is controlled by the molecular structure, demonstrating how relevant the material composition of the urban canopy is for radiative energy exchanges. Conversely, if these material properties are known at spectral scales, they can provide valuable information about the surface composition (e.g. to quantify urbanization and map urban sprawl, Dewan and Yamaguchi 2009) and condition (e.g. to evaluate road asphalt conditions, Andreou et al. 2011).

Spectrally resolved short-wave reflectance and long-wave emissivity reveal absorption bands and regions according to the molecular structure of materials composing the surface studied (Atkins 2006). Some materials (e.g. siliceous minerals) cause reflection of thermal radiation within the structure due to a change of refractive index. This *reststrahlen* (German for 'residual rays') effect creates local minima in emissivity spectra, associated with the respective absorption bands. Both distinct absorption and reststrahlen bands correspond to the composition of the material. Usually, reflectance or emission spectra are of interest in the short-wave or long-wave region of the spectrum. The two measures are simply the inverse ($\varepsilon = 1 - \alpha$) when transmissivity vanishes ($\tau = 0$), as is the case for most impervious urban surface materials (apart from glass).

Radiation trapping in urban canyons also increases absorption of long-wave energy (Voogt and Oke 1991). Favoured further by the (generally high) heat capacities of urban, anthropogenic materials, the storage heat flux increases with urbanisation (Grimmond and Oke 1999a). Some of the energy that is gained by the surface volume during times of high input (daytime) is released gradually, even after sunset (Offerle et al. 2003), e.g. via the flux of outgoing long-wave radiation. Over longer time scales (the course of a day or an annual cycle), storage heat flux ΔQ_S is balanced, i.e. ultimately no net energy is absorbed. The storage heat flux is often linked to the degree of urbanization (Grimmond and Oke 2002) and can present an important energy source for turbulent fluxes (Oke et al. 1999). As for the short-wave fluxes, thermal radiance can be transmitted, reflected or absorbed by the atmosphere. Again, clouds and aerosols play an important role because they reflect and emit long-wave radiation in the direction of the surface. Overcast conditions reduce radiative cooling of the surface causing repeated reflections below the cloud base.

I.3.3 Anthropogenic heat flux

In cities, the anthropogenic heat flux Q_F (eqn. I.4) is a very important additional source of energy to the urban energy balance (Sailor 2011). As outlined by e.g. Grimmond (1992), it combines emissions from buildings (Q_{Fb}), traffic (Q_{Ft}) and human metabolism (Q_{Fm}):

$$Q_F = Q_{Fb} + Q_{Ft} + Q_{Fm.} \quad \text{I.4}$$

The majority of Q_F usually originates from building emissions (i.e. for heating and cooling demands). This component (Q_{Fb}) changes with season and geographic location (Allen et al. 2011) of a city and can be expressed simply as a function of air temperature and degree of urban development. Anthropogenic heat occurs in the form of both sensible and latent heat, however, the latter is usually distinctly smaller (Iamarino et al. 2012).

By definition, this component of the surface energy balance depends on human activities. It is governed by, amongst other factors, economic activity of the urban population, its density, social habits and response to climate conditions (i.e. the functionality of the various elements of urban infrastructure as well as the urban system as a whole). Efforts aiming to improve sustainability, such as governmental regulations, can therefore directly impact this additive energy input through measures that affect anthropogenic behaviour and the functionality of the city (e.g. optimisation of public transport, minimisation of congestion). For the interpretation and implementation of any estimates of this flux, it should always be kept in mind that it is highly variable on spatial and temporal scales (Lindberg et al. 2013).

Depending on season and geographical location of the site, most energy is supplied to the system of the urban surface volume by net all-wave radiation. However, during cold seasons in higher latitudes or in areas where air conditioning is widely used, Q_F provides additional energy for turbulent transport (Sailor 2011; Iamarino et al. 2012). In winter at some sites the magnitude of the anthropogenic heat flux can be larger than the net all-wave radiation even at its peak round midday (Łódź, Poland; Pawlak et al. 2011).

I.3.4 Turbulent fluxes of sensible and latent heat

In the surface layer, energy made available to the surface volume by the net sum of Q^* and Q_F is partially stored as ΔQ_S and might be released at another time. Also it generates strong vertical gradients of some atmospheric variables (e.g. of temperature and humidity) which drive energy exchange processes via turbulent eddies (Wyngaard et al. 1971). Where temperatures at the surface are increased relative to the overlying air, the turbulent flux of sensible heat Q_H aims to balance these differences. Depending on moisture availability, latent heat may be released at the surface and vertical gradients of specific humidity strengthen the turbulent flux of latent heat Q_E. The turbulent fluxes of latent and sensible heat as well as momentum are key for the vertical growth and decay of the ML, i.e. they determine the diurnal evolution of the boundary layer structure (Stull 1988). When sufficient energy input at the surface maintains unstable atmospheric stratification (Zilitinkevich et al. 1992) so that thermal buoyancy dominates, the ML

height rises. This again enlarges the volume of the urban boundary layer and therefore substantially influences air quality levels (Schäfer et al. 2006).

When driven by radiative input, turbulent fluxes are enhanced during daytime and summer months. As found in the early summertime flux observations in Vancouver (Cleugh and Oke 1986), a large portion of available energy is transported upwards via sensible heat flux. It is largest in the early afternoon when buoyant atmospheric conditions are best developed. With large storage heat fluxes, the upward turbulent transport of sensible heat is supported even after sunset (e.g. in Melbourne, Coutts et al. 2007). In some highly urbanized areas this can maintain unstable atmospheric conditions throughout the night (e.g. Mexico City, Oke et al. 1999; Marseille, Grimmond et al. 2004; Basel, Christen and Vogt 2004). Nocturnal outgoing sensible heat flux at a site in Mexico City (Oke et al. 1999) was reported to range from 20–50 W m^{-2} during a seven-day period in winter, a similar magnitude was found in Marseille during summer time (Grimmond et al. 2004). In Basel (Christen and Vogt 2004), positive nocturnal sensible heat transport was observed over the whole annual course with maximum values reaching ca. 50 W m^{-2}. At that site, a linear correlation between the magnitude of nocturnal upward Q_H and the complete aspect ratio (fraction of complete built-up surface) was found, indicating higher turbulent sensible heat flux where the urban surface volume has a higher heat storage capacity.

These observations using eddy covariance (EC; Section I.4.3) are also supported by results from large aperture scintillometry (LAS). LAS measurements rely on auxiliary observations to determine the sign of the turbulent flux, however, an increasing number of studies (e.g. Salmond et al. 2012) suggests that positive Q_H is observed simultaneously with both methods. Lagouarde et al. (2006) found in Marseille that LAS observations, with a larger source area than EC, had slightly larger nocturnal fluxes. This is also seen in data from systems operated in central London (Pauscher et al. 2012), though there is some dependence on the flux processing methods of scintillometry.

As discussed by Grimmond and Oke (2002), the prevailing unstable atmospheric conditions during the night arising in dense urban environments have significant impact on boundary layer structure and should hence be accounted for in modelling of air quality and surface energy exchange. Studies addressing the structure of the urban boundary layer (Rotach et al. 2005) suggest that the unstable nocturnal residual layer is rather shallow and could be decoupled from the upper part of the boundary layer with increased atmospheric stability (Wood et al. 2010). Again, these findings are supported by LAS observations in central London (Pauscher et al. 2012).

Moisture availability is the main factor controlling the partitioning of the available energy between the two turbulent fluxes. The latter is often quantified by the Bowen ratio ($\beta = Q_H/Q_E$). In cities, evaporative cooling varies with natural and anthropogenic water availability. Often, impervious surfaces dominate, so that rainwater runoff is efficient and the main sources for surface moisture

are green spaces and street trees (i.e. urban vegetation). Many urban agglomerations have evolved near water bodies (e.g. at the coasts of lakes or the sea, at rivers), which can enhance latent heat transport depending on wind direction and atmospheric stratification. Anthropogenic water usage has a large impact on energy partitioning, particularly at times when irrigation of gardens is large (Kalanda et al. 1980). Grimmond and Oke (1995) in a study of North American cities conclude the Bowen ratio is larger in cities which require frequent irrigation ($\beta \approx 1.5$) than those with higher natural water supply ($\beta \approx 1$). Restrictions on domestic water use limited private irrigation in Melbourne (Coutts et al. 2007), resulting in low evaporative fluxes and mean monthly summer Bowen ratios around 2 and daily values larger than 5.

In cities with frequent rainfall, for example Grimmond's (1992) study of suburban Vancouver with its maritime climate, Q_E is of similar magnitude as Q_H or even higher in the wintertime. Studies in Mexico (Oke et al. 1999) and Burkina Faso (Offerle et al. 2005b) emphasise the role of climate conditions and regionally specific landscape characteristics and construction. Natural road and building materials, widely used in West Africa, have a storage heat flux comparable to the rural environment (Offerle et al. 2005b). This, combined with low moisture supply in the dry season, results in large Bowen ratios (e.g. $\beta \approx 8$), also observed in Mexico City (Oke et al. 1999) and a sub-urban desert site close to Cairo (Frey et al. 2011). Evaporation is larger during wet seasons or mid latitude summertime, due to vegetation with greater canopy cover.

I.4 Observations in the urban setting

Many meteorological observations are conducted *in-situ*, i.e. the sensors record environmental variables that describe the immediate surroundings of their locations. *Remote sensing* approaches in contrast, measure atmospheric or surface conditions distant from the sensor location itself often delivering information on larger scales than *in-situ* techniques. Both measurement strategies require thorough consideration regarding the linkage between the observed quantity and the surface area/volume affecting it. This, naturally, creates a great challenge for complex and heterogeneous surfaces, as in the urban case.

I.4.1 Radiation exchanges

Pyranometers and pyrgeometers are commonly used instruments to observe short- and long-wave irradiance at the surface for meteorological applications. As broadband detectors, they provide integrated estimates over a spectral range (of about ~300-2800 nm and ~4500-50000 nm). By reversing their orientation, they can also be used to observe the outgoing counterparts. Net-radiometers monitor all four components of the radiation balance (eqn. I.2).

Net all-wave radiation, representative at the local scale, can be monitored by placing net-radiometers at a height well above the canopy. This is to ensure that, firstly, no obstacles (e.g. taller buildings) obstruct the instrument's field of view (FOV) when recording down-welling radiance and, secondly, the outgoing components observe a large surface area with a range of materials and facets (Schmid et al. 1991). From these measurements, the bulk surface albedo

$\bar{\alpha}$ can be estimated. Assuming the observed urban canopy resembles on average a Lambertian surface, $\bar{\alpha}$ can be interpreted as a surface characteristic, describing the broadband reflectance of short-wave radiation.

Fixed-installed net-radiometers can be used to monitor radiation fluxes continuously, measuring spatially as well as spectrally integrated radiance. From such data, bulk radiative surface characteristics (such as $\bar{\alpha}$) can be derived. Remote sensing techniques again may be limited in terms of temporal coverage but can offer details on the spatial variability of outgoing radiation fluxes and/or spectrally resolved information. Sensors operating on various platforms, from satellites over airborne approaches down to ground based imagery and field spectroscopy, view the surface at different distances and therefore result in dissimilar spatial sampling strategies. While remotely sensed images from satellites and airplanes provide pixel-based spatial information at resolutions from metres to kilometres, ground based imagery ranges from metres to centimetres, and field spectrometers sample individual surfaces at very fine spatial scales, of the order of millimetres to centimetres. Sensors cover different wave-lengths regions from the visible- to short-wave infrared (VIS-SWIR) over mid-wave infrared (MWIR) to long-wave infrared (LWIR), with different spectral and spatial resolutions (Shafri et al. 2012). Hyper-/ multi-spectral remote sensing covering the VIS-SWIR is used to measure reflectance of urban surfaces (Patino and Duque 2012), which can support a wide range of applications (Yang 2011). Remotely sensed, broadband LWIR data are also widely applied in studies concerned with the thermal aspect of the urban environment (Voogt and Oke 2003; Weng 2009). Hyperspectral information in this spectral region is not yet as abundant as for the VIS-SWIR, but will be increasingly available in the future (Kuenzer and Dech 2013). This has great potential to contribute to urban remote sensing studies as many construction materials contain minerals with distinct absorption and reststrahlen features in the LWIR (Christensen et al. 2000).

I.4.2 Anthropogenic heat flux

As a component of the surface energy balance, parts of the anthropogenic heat flux are captured in the measurements of the turbulent fluxes of latent and sensible heat and the outgoing flux of long-wave radiation. If all remaining components of the surface energy balance are measured, it can be estimated as the residual (Offerle et al. 2005a; Pigeon et al. 2007).

To date, no approach has been used to directly observe the flux of anthropogenic heat. Typically two modelling approaches are taken to estimate its three components (Sailor 2011). *Top-down* analysis of energy consumption (Hamilton et al. 2009) is applied at various scales (Iamarino et al. 2012) while *bottom-up* estimates calculated with building energy models (Kikegawa et al. 2003) focus on the building scale. The second usually ignores the contributions from vehicle emission and human metabolism, which make up a smaller fraction of the flux (Allen et al. 2011; Sailor 2011; Iamarino et al. 2012).

I.4.3 Turbulent fluxes of sensible and latent heat

Turbulent energy fluxes can be measured with the established eddy covariance (EC) technique. Based on Reynold's theorems, the equation of state of a scalar can be transformed to its respective transport equation (Stull 1988; Foken 2003). This again simplifies, under the assumptions of negligible fluctuations of air density, horizontal homogeneity of the flow, and a negligible vertical wind velocity. The turbulent flux of a physical quantity (such as temperature or humidity) can be expressed by its covariance with the vertical wind velocity, e.g.

$$Q_H = \rho c_p \overline{w'\theta'} \quad \text{I.5}$$

$$Q_E = \rho l_w \frac{\gamma}{p} \overline{w'e'} \quad \text{I.6}$$

for the fluxes of sensible heat Q_H and latent heat Q_E, with mean density of moist air ρ, specific heat at constant pressure c_p, latent heat of vaporisation for water l_w, the ratio of molecular masses of water vapour and dry air γ, mean air pressure p, vertical wind velocity w, potential temperature Θ and vapour pressure e. The factor γ/p is included for the conversion to specific humidity q, so that both fluxes are in units of W m^{-2}. Close to the surface, potential temperature Θ can be approximated by actual air temperature T.

The EC method determines the respective covariance, by simultaneously measuring high frequency fluctuations, usually at a frequency of 10–20 Hz. A common EC system consists of a sonic anemometer (measuring wind and temperature) and a gas analyser (measuring gas concentrations). Analogous to Q_H and Q_E, fluxes of other gases, such as CO_2, and also the turbulent momentum flux can be observed.

Above the blending height, where fluxes are approximately invariant with height (Haugen et al. 1971), turbulent fluxes observed at a discrete height describe local scale characteristics of a whole layer. EC systems are ideally installed in the inertial sublayer (> about 2 x the mean building height, (Grimmond and Oke 1999b; Roth 2000; Kastner-Klein and Rotach 2004; Grimmond 2006). The sensors need to be located high above the roughess elements to minimise flow distortion caused by the bluff bodies.

Depending on the research question, eddy covariance measurements can also yield useful information when the sensors are deployed within the roughness sublayer, i.e. inside urban canyons (Rotach et al. 2005). However, then they capture atmospheric quantities that are representative at the micro-scale and need to be interpreted accordingly.

Other techniques have been used to quantify turbulent fluxes in the surface layer. Profile and gradient methods rely on the flux gradient relations (Dyer 1974), i.e. the flux is related to measurements of a quantity at different heights. The aerodynamic resistance method (Voogt and Grimmond 2000) can be used to infer the turbulent sensible heat flux from the difference between surface and air temperature. Scintillometry provides another approach to measure

turbulent fluxes directly (Lagouarde et al. 2006), at larger scales than the eddy covariance method.

I.4.4 Source area considerations

Given surface characteristics have a significant impact on surface energy exchanges, analysis of observed energy fluxes needs to consider the probable footprint of the sensor (Schmid 2002). In urban areas, where surface geometry and material composition are heterogeneous, the interpretation of the fluxes with respect to the source area creates a special challenge. Surface characteristics may vary for different flow conditions (e.g. Järvi et al. 2009) or for different fluxes eventually combined in the surface energy balance. While fluxes of outgoing radiance originate mainly from an area right below the radiometer, local scale EC fluxes are typically influenced by a source area upwind of the measurement site (Schmid 1994).

Where the surface is approximately Lambertian, the source area of pyranometer can be described by concentric isopleths around the measurement tower, their radius being a function of the measurement height (Schmid 1997). For non-Lambertian surfaces, this source area model can provide a first approximation of the footprint for the case of diffuse irradiance when reflections from all surrounding surfaces similarly contribute and variations in directional reflectance of the surface have less impact. However, when direct radiation is reflected by a heterogeneous surface, the footprint function needs to incorporate the bi-directional reflectance distribution function (BRDF) of the surface as well as the sun geometry. Hence it varies at both spatial and temporal scales. In an urban setting, the BRDF needs to combine variations due to surface materials and also the three-dimensional form of buildings, vegetation, roads, and canyons. This is unique for every measurement site and sensor height.

The turbulent fluxes of latent and sensible heat change in time and space as a function of sensor position (height), atmospheric conditions (expressed by e.g. wind speed, wind direction, atmospheric stability) and surface characteristics (expressed by e.g. terrain, surface roughness, material composition). Ideally, these aspects should be accounted for in a footprint model to interpret eddy covariance measurements. However, given the complexity, simplified, idealised models are still mostly applied for this purpose (Vesala et al. 2010).

The relatively simple implementation of analytical footprint models provides clear advantages in computing time and ease of use, so they are often applied to gain a first order estimate of probable location and size of flux source areas (Rannik et al. 2012). They are usually chosen for the interpretation of long term datasets. Recent examples of the application of analytical footprint models include the Kormann and Meixner (2001) model to interpret carbon dioxide fluxes (e.g. Vancouver, Christen et al. 2011; Baltimore, Crawford et al. 2011; Beijing, Liu et al. 2012), to improve understanding of turbulent energy transport (e.g. Helsinki, Nordbo et al. 2012; Basel, Salmond et al. 2012) and to match *in-situ* and remote sensing observations (Cairo, Frey and Parlow 2012).

The footprint calculated for individual time periods can be composited by time and space to provide, with an appropriate geographical information database, the sensor field of view or footprint climatology. These have been shown to be beneficial to the interpretation of urban fluxes (e.g. Christen et al. 2011).

I.5 Aims and structure of this study

Globally, urbanisation is expected to generate cities of increased density and complexity, expanding both at vertical and horizontal scales (Section I.2). These changes will affect the climate of each city and will be major drivers, directly and indirectly, of climate change. Hence, decisions made about the development of cities have significant potential for climate change mitigation and adaptation (Section I.3). To support urban planning, surface energy exchanges (eqn. I.1), which are key controls on the formation of boundary layer climates, need to be better understood in this context. New insights can be gained from analysing micrometeorological measurements and remote sensing observations that provide powerful means (Section I.4) to study such exchanges.

In recent decades, great advances have been made in measuring (and modelling) the urban climate, however, processes and effects in this complex environment are still not sufficiently well understood (Arnfield 2003) and there remain many challenges to monitoring efforts (Grimmond 2006). One zone of the city that has been little studied is where the most intense urban development occurs – the central business district. The current study focuses on the CBD of London, with three main aims:

- To quantify fluxes of the surface energy balance in a dense city centre over an extended period (3.5 years)
- To engage with methodological challenges that arise in this complex setting for both measurement and modelling approaches
- To identify characteristic impacts of the complex setting on surface energy exchanges, specifically in terms of addressing the aspects listed herein.

Radiation fluxes:

- What are the spectral radiative characteristics of common impervious urban materials?
- How distinct are the various anthropogenic material composites with respect to their spectral response?
- How variable are spectral radiative properties of impervious materials within one material class and between different types of materials?
- What new insight can be gained if hyperspectral long-wave infrared information is available?
- How are short-wave reflectance and thermal emissivity of impervious urban materials related?
- Under which conditions can the urban surface be considered Lambertian?

- What is the impact of atmospheric scattering and absorption/the presence of clouds on the radiation balance at the surface?

Anthropogenic heat flux:

- How does the anthropogenic heat flux respond to air temperature variations in a central business district where the daytime population is higher than at night?
- Given anthropogenic heat flux is highly scale dependant, can the vertical distribution of sources and sinks in this dense urban setting be quantified by observations?

Sensible and latent heat flux:

- How do local scale fluxes of latent and sensible heat respond to surface controls in the a heavily urbanised zone of a city, specifically in terms of storage heat flux, anthropogenic heat sources, and rainwater input?
- How does surface roughness influence the turbulent flow?
- How do meso-scale conditions influence the urban climate?
- How do the two turbulent fluxes of heat and moisture relate?
- Can the role of impervious surface cover in the process of energy partitioning be quantified?
- How does a major river influence energy exchange processes at the local scale?
- What is the feedback of turbulent energy exchange to the boundary layer and atmospheric stratification?

Storage heat flux:

- Combining the above energy flux components, what conclusions can be drawn about the role of storage heat flux in a dense urban setting?

These questions are addressed using an extensive, long-term set of measurements collected in the CBD of central London, UK. Modelling is incorporated as appropriate, i.e. when additional information could be acquired (e.g. estimation of Q_F) or interpretation supported (e.g. footprint modelling). The study is presented in five chapters, with a series of methodological advances, new data and novel interpretations presented (Figure I.3):

Chapter II: Derivation of an urban materials spectral library through emittance and reflectance spectroscopy

Using two spectroscopy techniques, spectral response of 74 samples of impervious surface materials is measured and compiled into a spectral library of LWIR emissivity and VIS-SWIR reflectance (Appendix B). The performance of the laboratory-based emissivity measurement approach, that in future can also be deployed in the field (e.g. to examine urban materials *in situ*), is evaluated. Spectral characteristics of ten material groups are analysed and the role on radiative exchange of impervious surface materials is discussed.

Chapter III: Identification of Micro-scale Anthropogenic CO_2, Heat and Moisture Sources - Processing Eddy Covariance Fluxes for a Dense Urban Environment

A method is introduced to assess the influence of micro-scale anthropogenic emissions on heat, moisture and carbon dioxide exchange. The new algorithm for the Identification of Micro-scale Anthropogenic Sources (IMAS) is applied with two aims. First, IMAS filters out the influence of micro-scale emissions and allows for the analysis of the turbulent fluxes representative of the local scale source area. Second, it is used to give a first order estimate of anthropogenic heat flux and carbon dioxide flux representative at the building scale.

Chapter IV: Energy exchanges in a dense urban environment Part I: temporal variability of long-term observations in central London

Radiometer and eddy covariance observations at two adjacent sites, at different heights, are presented, for the extended period of 3.5 years. Fluxes are analysed at various temporal scales and with respect to meteorological conditions, such as cloud cover. The role of anthropogenic heat fluxes providing considerable energy input to surface-atmosphere exchanges in this CBD is evaluated and the net heat storage flux is put into context. The influence of rainfall on the energy partitioning between the turbulent fluxes of latent and sensible heat is analysed for this area dominated by impervious surface cover, which keeps moisture availability low and accounts for efficient rainwater runoff.

Chapter V: Energy exchanges in a dense urban environment Part II: impact of spatial heterogeneity of the surface

The impact of site location and heterogeneity of the urban surface on flux observations is investigated for the set of observations introduced in Chapters III and IV. Special effort is made to link the observations to their respective source areas, both for outgoing short-wave radiation and turbulent exchanges. This uses modelled source area estimates, to relate observed fluxes to surface cover characteristics, and analysis of observations from the two nearby measurement sites with differing measurement heights.

Chapter VI: Conclusions

Finally, conclusions from Chapters II-V are combined to show how this study contributes to an improved understanding of the energy exchange processes in a dense urban setting. Recommendations for future work emanating from these findings are presented.

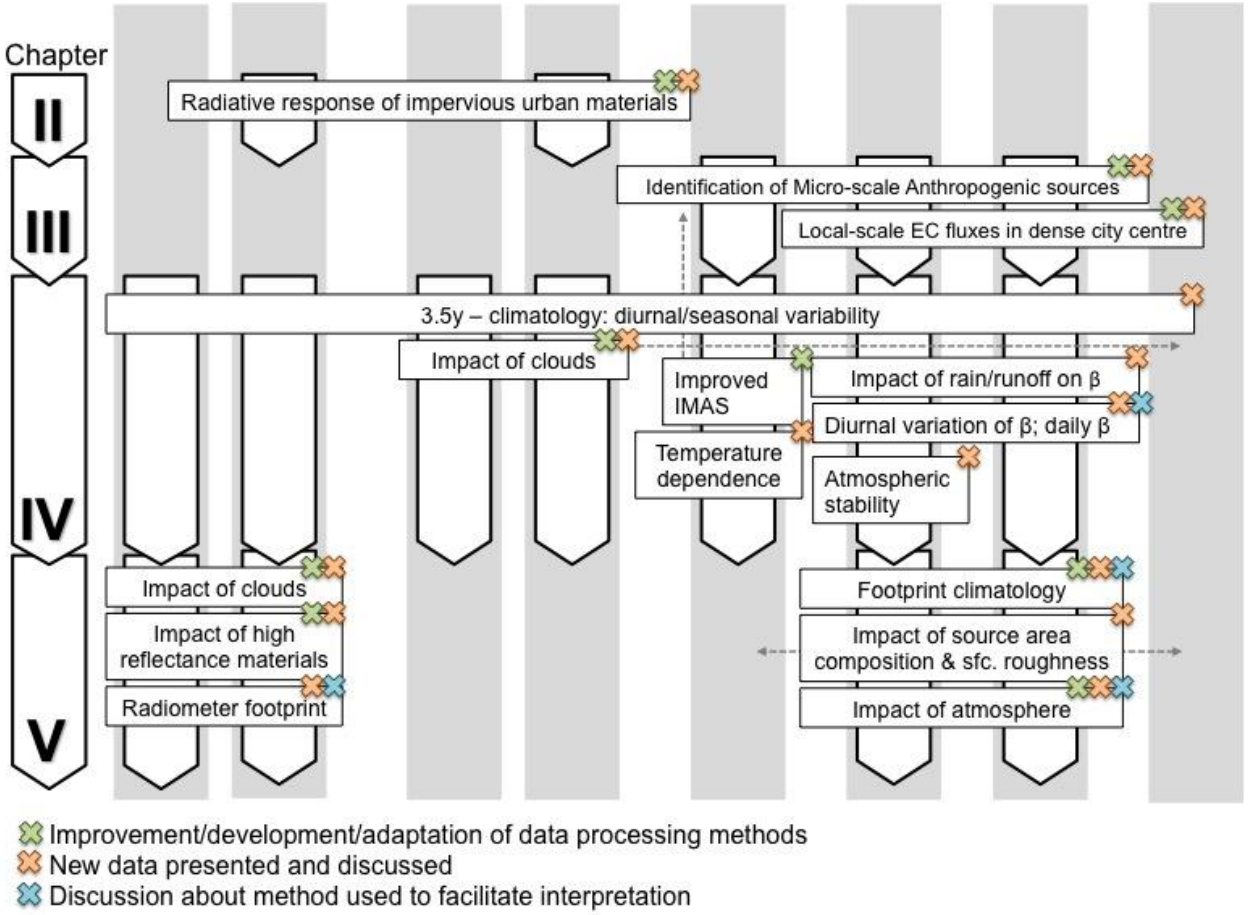

Figure I.3: Structure of the current study showing how the work (arranged in Chapters II-V) contributes to efforts to quantify surface energy exchanges in complex, dense urban settings. This stems from methodological advances, new data and interpretation (as indicated by crosses). Energy fluxes discussed in the current study form the surface energy balance (eqn. I.1). Dashed arrows indicate substantial cross linkages.

II Derivation of an urban materials spectral library through emittance and reflectance spectroscopy

Abstract

Recent advances in thermal infrared remote sensing include increased availability of hyperspectral airborne systems (such as the Hyperspectral Thermal Emission Spectrometer, HyTES), and soon an increased number of separate wavebands in the long-wave infrared (LWIR) region will be measureable from space (by imagers such as HyspIRI). Detailed LWIR emissivity spectra are required to best interpret the observations from such systems. This includes the highly heterogeneous urban environment whose materials are not yet particularly well represented in spectral libraries. Here, we present a new online spectral library of urban construction materials with LWIR emissivity spectra of 74 samples of impervious surfaces derived using measurements made by a portable Fourier Transform InfraRed (FTIR) spectrometer. FTIR emissivity measurements need to be carefully made, else they are prone a series of errors relating to instrumental setup and radiometric calibration, which here relies on external blackbody sources. The performance of the applied laboratory-based emissivity measurement approach, that in future can also be deployed in the field (e.g. to examine urban materials *in situ*), is evaluated. The spectral library further contains matching short-wave (VIS-SWIR) reflectance spectra observed for each urban sample. This allows us to examine which characteristic LWIR and VIS-SWIR spectral signatures may allow for classification of such urban construction materials, often overlapping with respect to their chemical/mineralogical constituents. Hyperspectral or even strongly multi-spectral LWIR information appears especially useful, given that many urban materials are composed of minerals exhibiting notable reststrahlen/absorption effects in this spectral region. The final spectra and interpretations are included in the London Urban Micromet data Archive (LUMA; http://LondonClimate.info/LUMA/SLUM.html).

Kotthaus, S, TEL Smith, MJ Wooster, and CSB Grimmond, 2014: Derivation of an urban materials spectral library through emittance and reflectance spectroscopy, in review.

II.1 Introduction

Recent advances in thermal infrared remote sensing (Kuenzer and Dech 2013) include a new generation of space- and airborne hyperspectral thermal sensors such as HyTES and HyspIRI (Abrams and Hook 2013; Hook et al. 2013), and progress in ground-based techniques (methods and instruments) used both in the field and laboratory (Hecker et al. 2013; Ferrier et al. 2014). Spectrally detailed information across the long-wave infrared (LWIR) atmospheric window offers great potential for two challenges of earth observation: it provides new insights and data for the development and application of algorithms aiming at the separation of surface temperature and surface emissivity effects in remotely sensed LWIR spectral radiance observations and images, and potentially aids the improved characterisation and classification of surface properties and material type.

Current information does not adequately cover the immense diversity of urban materials (Heiden et al. 2007), even though this will be crucial for the interpretation of hyperspectral remote sensing data gathered in such areas in the future. Urban surface properties have important implications for human health, sustainable design and climate change adaptation and hence present fundamental modelling parameters for related studies (Yang 2011). In particular, the radiative response of impervious urban materials determines the radiation balance of incoming and outgoing long- and short-wave fluxes, and thereby urban climate conditions. Its significance recently received global media attention when solar radiation reflected by the façade of a new skyscraper in the City of London created surface temperatures warm enough to melt certain plastic parts of nearby parked cars (Guardian 2013). Spectral information covering the LWIR can help to support surface temperature retrieval algorithms relevant to research concerned with urban climate and air quality. Relations between shortwave albedo and long-wave emissivity/surface temperature (Small 2006) are of particular interest for urban climate studies concerned with human thermal comfort (Matzarakis et al. 2010) and/or building energy demand (Yaghoobian and Kleissl 2012). The kinetic temperature of the surface is often used to study the surface urban heat island phenomenon (Voogt and Oke 2003), to model surface energy exchanges (Voogt and Grimmond 2000), and to evaluate and improve urban canopy models (Kusaka et al. 2001).

This paper aims to support such work by developing a new urban materials spectral library covering both the LWIR and VIS/SWIR atmospheric windows, and by elucidating the methods and uncertainties inherent in the production of such a database using, respectively, FTIR and grating-based spectrometry. Some background information is provided to underline the motivation of this study (Section II.2). Then, the applied spectroscopy methods are introduced (Section II.3), providing details on radiometric calibration, background correction and the separation of emissivity and temperature. Investigations of the thermal properties of reference radiation sources (that provide the basis for the radiometric calibration) permit uncertainties arising from the methodology to be quantified. A framework for laboratory-based FTIR emissivity observations

is developed (similarly applicable outdoors) and spectra of the different material-classes are analysed (Section II.4). Finally, uncertainties of the FTIR spectroscopy observations are summarised and implications of the results for remote sensing of impervious urban materials are considered (Section II.5).

II.2 Motivation

Current spectral libraries provide information on a variety of materials (e.g. MODIS spectral library, Moderate Resolution Imaging Spectroradiometer, Wan et al. 1994; US Geological Survey, USGS, Clark et al. 2007; ASTER, Advanced Spaceborne Thermal Emission and Reflection Radiometer, Baldridge et al. 2009), however, the coverage of impervious urban materials remains limited, especially in the LWIR region (e.g. see Table II.1).

Urban spectral libraries have been developed from airborne and/or ground truth observations for example in: Tel-Aviv, Israel (Ben-Dor et al. 2001 using library spectra of Price 1995), Potsdam and Dresden, Germany (Heiden et al. 2001; Roessner et al. 2001; Heiden et al. 2007), Bonn, Germany (Franke et al. 2009) and Santa Barbara, USA (Herold et al. 2004; Herold 2007), with increasing interest in the LWIR spectral response of anthropogenic materials. Only a few studies include *in-situ* measurements of the same surfaces covering short and long wavelengths (e.g. Kerekes et al. 2008).

Table II.1: Spectral libraries of anthropogenic materials (by year of publication). (*) data are freely available on the web. Specifications given (i.e. spectral range, instrumentation and data acquisition) relevant to the spectral information used in this study. More spectra might be available in respective libraries that cover different wavelengths and/or are measured with other devices.

Reference	Study area	Materials	Spectral range [nm]	Instrumentation	Data acquisition
Wan et al. (2001) *MODIS UCSB emissivity library	Various locations, USA	Building, roofing, pavement, road	3300–14500	MIDAC FTIR M2510-C	Laboratory
Ben-Dor et al. (2001)	Tel-Aviv, Israel	Building, roofing, pavement, road, sports infrastructure	430–940	CASI & ASD FieldSpec3	Airborne & in-situ
Heiden et al. (2001, 2007)	Dresden & Potsdam, Germany	Building, roofing, pavement, road, partially impervious	400–2500	HyMAP & ASD Fieldspec3	Airborne & in-situ
Herold et al. (2004) *Santa Barbara (SB) spectral library	Santa Barbara, CA, USA	Building, roofing, pavement, road, sports infrastructure	350–2400	ASD FieldSpec3	In-situ
Baldridge et al. (2009) *ASTER spectral library	Various locations, USA	Building, roofing, pavement, road, paint	400–15400	Perkin-Elmer Lambda 900 UV/VIS/NIR, Perknic & Nicolet 520FT-IR	Laboratory
Clark et al. (2007) *USGS spectral library	Various locations, USA	Building, roofing, pavement, road, plastic	400–3000	Beckman 5270 & ASD FieldSpec3	Laboratory
Nasarudin and Shafri (2011)	University campus, Malaysia	Roofing, road	350–2500	ASD FieldSpec3	In-situ

Cities are very complex spatially, given their three-dimensional structure and immense heterogeneity. But also temporarily, conditions are changing at fast rates compared to many more 'natural' environments, due to human movements, re-construction (new developments replacing old structures) or technological advances in manufacturing techniques (making new construction materials available). The latter may be used to reduce costs or to yield novel architectural benefits (e.g. flexibility of PVC), but increasingly the environmental aspects of materials and surfaces are being considered in the context of climate change mitigation. Highly reflecting materials are deployed to reduce absorption of solar energy at the surface, which can help to cool urban areas (Akbari et al. 2009). Furthermore, with the need to reduce life-cycle carbon emissions (e.g. DCLG 2013) there is demand to replace materials (e.g. demand for carbon-neutral cement, Damtoft et al. 2008). Knowledge about chemical compositions and radiative properties of both novel and older construction materials are required to ensure that their dynamic impacts are incorporated into our understanding of the ever-changing urban environment. Applications in a research context, range from the characterisation of sites where atmospheric quantities are measured and modelled *in situ* to improved interpretation of airborne or satellite remote sensing data.

As many materials have distinct spectral absorption features in the visible to short wave infrared (VIS-SWIR) region of the electromagnetic spectrum, multi- or hyper-spectral information across the these wavelengths is applicable to a variety of environmental research questions (e.g. Clark 1999). Amongst others, they provide a basis for the land cover classification of natural materials, such as soil types (Rossel et al. 2006), vegetation (Adam et al. 2010), and also anthropogenic materials (Townshend et al. 1991). This requires some *a priori* knowledge of features of the materials' spectral characteristics (Heiden et al. 2001), usually obtained from "ground truth" field spectroscopy, often carried out simultaneously with air-/space-borne data acquisition, and/or from spectral libraries. Urban applications of such classifications (Weng 2012) cover a wide range of purposes; such as mapping of urbanization (Deng et al. 2009), identification of impervious surface cover for the quantification of flood risk (Schueler 1994), assessment of concrete quality (Brook and Ben-Dor 2011), and evaluation of road network conditions (Herold et al. 2003; Pascucci et al. 2008).

Some materials however, pose a challenge to land cover classification algorithms based on VIS-SWIR information because they lack distinct spectral features in this spectral region. Roberts et al. (2012) suggest that urban land cover classification (e.g. differentiation between bare soil and asphalt) could be significantly improved by including hyperspectral LWIR data, emphasising the great potential of a comprehensive LWIR spectral library. This is because many materials are featureless at shorter wavelengths (e.g. mineral composites, Cloutis et al. 2008), but reveal clear absorption and reststrahlen bands in the LWIR region. The *reststrahlen* (German, 'residual rays') effect describes reflection of radiation in a certain absorption band due to changes of the refractive index within the medium. In combination with absorption features, the related

wavebands ('reststrahlen bands') allow conclusions to be drawn about the material's molecular structure.

In addition to the benefits to land cover classification, spectral LWIR emissivity is of further interest because it relates outgoing radiance, or a body's 'brightness temperature', to its actual surface kinetic temperature (Gillespie et al. 1998). All LWIR remote sensing approaches require a method to partition the measured radiance into its contributions from the kinetic temperature of the surface and its emissivity. Several temperature-emissivity-separation (TES) algorithms (e.g. Gillespie et al. 1998) have been developed (Dash et al. 2002) depending on sensor specifications (e.g. number of channels available). The very limited work on urban-specific materials (Sobrino et al. 2012) suggests that such methods can provide appropriate emissivity estimates in cities (e.g. Xu et al. 2008; Sobrino et al. 2012). However, emissivity of some complex anthropogenic materials (e.g. metals) is difficult to characterise (Sobrino et al. 2012). A comprehensive library of urban building materials covering both the VIS-SWIR and LWIR regions could provide the foundation for these developing methodologies to be more applicable in city environments.

Fourier-Transform InfraRed (FTIR) field spectroscopy offers a technique to measure spectral thermal radiance with portable instrumentation (Griffiths 1983; Korb et al. 1996). Widely applied to observe absorption spectra from gases (e.g. Wooster et al., 2011), this technique is also used to quantify surface emissivity (absorbance) of solid surfaces (Breen et al. 2008), commonly by direct measurements of the sample's thermal emitted radiance (e.g. Ruff et al. 1997; Christensen et al. 2000; Kerekes et al. 2008). The latter needs to exceed the incoming radiance from the background (e.g. the sky outdoors or ceiling/walls of the laboratory) to improve the signal to noise ratio (Horton et al. 1998). Radiometric calibration of the observed energy spectrum commonly relies on further supplementary measurements of radiation sources of known emissivity and temperature, the latter introducing further measurement uncertainty (Lindermeir et al. 1992).

The objectives of this study relate to both the methodology and the observed results. Two spectroscopy methods were used to derive short-wave (VIS-SWIR) reflectance and long-wave (LWIR) emissivity measures for samples of impervious materials found across a major city, London, UK. Given that portable FTIR spectrometers now enable emissivity observations to be performed in standard laboratories or even in the field (rather than being confined to highly specialised laboratories), this methodology was evaluated first. Measurement uncertainties were quantified specifically for a setting with moderate temperatures (40–70°C) as chosen for the collection of emissivity spectra in this study. Secondly, the observed VIS-SWIR reflectance and LWIR emissivity spectra are interpreted to assess the variability of the spectral characteristics of building materials studied. The data are compiled into a spectral library of impervious urban materials (SLUM), available from the London Urban Micromet data Archive (LUMA; *http://Londonclimate.info/LUMA/SLUM.html*).

II.3 Methods

As with most spectral libraries (e.g. USGS and ASTER), the measurements made here were conducted under controlled laboratory conditions. However it is the case that certain types of samples require a spectrometer to be used in the field, even though no information can be obtained in the spectral regions where atmospheric water vapour absorption is high (Joseph 2005). The spectroscopy methods and equipment used here could, however, also be made outdoors if required (see Appendix B; Appendix II.A).

The wavelength (λ) dependence of infrared radiation L_λ emitted by an ideal emitter (a perfect blackbody, BB) at temperature T follows Planck's radiation law (Planck 1901):

$$L_\lambda(T)_{BB} = \frac{2h}{\lambda c^2} \frac{1}{e^{\frac{h}{\lambda k T}} - 1} \quad \text{II.1}$$

with the Planck constant h, speed of light c and Boltzmann constant k. Spectral emissivity represents the fraction of the spectral radiance R_λ emitted by an object of kinetic temperature T relative to that emitted by a perfect blackbody L_λ at the same kinetic temperature:

$$\varepsilon_\lambda = \frac{R_\lambda(T)}{L_\lambda(T)_{BB}} \quad \text{II.2}$$

Hence, measurements of the sample's thermal emitted radiance spectra can be used to derive spectral emissivity information (e.g. Ruff et al. 1997; Christensen et al. 2000; Kerekes et al. 2008). Short-wave reflectance spectra α_λ were derived as the fraction of incoming radiance reflected by the target in the VIS-SWIR spectral region.

Here, LWIR target spectral radiance data are gathered using an FTIR spectrometer that records an energy spectrum in raw digital numbers (DNs). The radiometric calibration of the latter into units of radiance requires auxiliary information, here obtained via two blackbody sources at different temperatures that are sampled along with the targets. The target-leaving radiance observed with the spectrometer is composed of an emitted fraction (related to the target's kinetic temperature and emissivity) and the reflected incoming radiance originating from the background (i.e. laboratory's walls and ceiling; or the sky if outdoors). This component is measured by observing the radiance spectra from a reference target of low emissivity and thus high reflectivity (a gold reference panel). To improve the signal to noise ratio, the radiance emitted by the target was kept high relative to the incoming reflected thermal radiance, essentially by heating the samples well above room temperature.

II.3.1 Measurement setup

II.3.1.1 Short-wave reflectance spectroscopy

Laboratory observations of VIS-SWIR reflectance spectra of various materials were conducted with an HR-1024 field spectroradiometer (SVC, *Spectra Vista Corporation*, Poughkeepsie, NY,

USA). The instrument has three diffraction grating spectrometers: one silicon (512 discrete detectors) and two indium gallium arsenide (InGaAs; 256 discrete detectors each) diode arrays. The 1024 spectral bands cover the measurement range of 3500–2500 nm, with resolutions of ≤ 3.5 nm (350–1000 nm), ≤ 9.5 nm (1000–1850 nm), and ≤ 6.5 nm (1850–2500 nm). Calibration into spectral radiance units is performed by the SVC HR-1024 PC data acquisition software. Radiance from the target and the reference panel, respectively, were stored along with the relative reflectance derived. As fore-optics a 4° field of view (FOV) lens was applied resulting in an instantaneous FOV of ~ 25 mm at a 350 mm distance between lens and target.

To ensure strong, uniform illumination two 300 W Videolight 6 (*Kaiser Fototechnik*, Buchen, Germany) lamps were used. The SVC HR-1024 sensor detects a cone of upwelling radiation, so that the setup was between bi-conical and hemispherical-conical. Irradiance was measured by sampling a surface of known high reflectivity that approximates a completely Lambertian surface. Here, a "white" Spectralon reflectance panel with a VIS-SWIR broadband albedo of 0.98 (serial number 4240A, calibrated by NERC FSF, National Environmental Research Council Field Spectroscopy Facility, on 21/03/2010) was used. Its reflectance spectra were collected at the same nadir viewing geometry (i.e. 0° zenith angle) as the target.

Absolute spectral reflectance α_λ was calculated by dividing the target radiance $R_{\lambda T}$ by the reference panel radiance $R_{\lambda R}$, incorporating the non-unity spectral reflectance of the reference panel p_λ (NERC FSF calibration): $\alpha_\lambda = (R_{\lambda T} / R_{\lambda R}) \times p_\lambda$. All targets were sampled ten times in total, observing two different areas of the target's surface (5 samples each) to get a first order estimate of potential spatial inhomogeneity of the material. The reference panel was measured once preceding the target measurements.

II.3.1.2 Long-wave emission spectroscopy

Long-wave target radiance was measured with a M2000 Fourier Transform InfraRed spectrometer (FTIR, *MIDAC*, Westfield, MA, USA), across a spectral range of 650–5000 cm^{-1} (2.0–15.4 µm) at a spectral resolution of 2 cm^{-1}. Data analysis focused on the 8.0–14.0 µm LWIR region, as the signal-to-noise performance of the FTIR significantly declines at shorter wavelengths when observing objects at temperatures < ~ 100°C as is the case here. Since the thermal emittance signal of Earth surface materials at ambient temperatures peak in the LWIR region, this is the spectral region most important for surface emissivity investigations related to kinetic temperature determination. Further, it bears crucial information about the long-wave response of impervious construction materials given the presence of the many reststrahlen bands of abundant minerals (Clark 1999).

Each spectral measurement consisted of 16 consecutively sampled spectra, and each target was measured ten times after single measurements of two IR-2100 Blackbody Systems (*Infrared Systems Development*, Winter Park, FL, USA) and the InfraGold reference panel (*Labsphere*, North Sutton, NH, USA), respectively. This strategy was chosen because the combination of ten

samples improves the signal-to-noise ratio while allowing a set of measurements to be collected in a relatively short time period (~2 min). This is important as incoming radiance and instrument response are assumed stable throughout this time. The latter assumption is tested (Section II.4.1.3).

The flat plate blackbody sources have an aperture of 63.5 mm x 63.5 mm and a spectrally flat surface emissivity of 0.96. The gold standard has a mean spectral emissivity of 0.05 across the LWIR region, and the manufacturer specified spectral emissivity curve (50 cm^{-1} spectral resolution) was re-sampled to match the 2 cm^{-1} spectral resolution of the FTIR observations. The blackbodies, gold reference panel and targets were swapped manually and placed vertically in front of the spectrometer at a distance of about 100 mm, at which point the spectrometer's FOV subtends a diameter of about 30 mm (Chris MacLellan, NERC FSF, personal communication). In order to improve stability of the thermal conditions, the FTIR was switched on an hour prior to the measurement commencement, allowing it to reach its operation temperature. Given that the measurements were performed in the laboratory, the samples were heated to moderate temperatures of 50–60°C. The two adjustable blackbodies were set to temperatures of 40–45°C and 70°C respectively, in order to bracket the target temperature.

Auxiliary information on the performance of the blackbody sources were collected with a TESTO 875-1 thermal imaging camera (*TESTO*, Alton, Hampshire, UK) with a resolution of 160 x 120 and a spectral range of 8–14 µm. The IR camera was calibrated against a radiation standard, a cavity IR-563/301 Blackbody System (*Infrared Systems Development*) with a small aperture (~ 20 mm) and an emissivity of > 0.99, over a temperature range of 50–100°C. An independent, extended area (304 x 304 mm) blackbody source, an IR-140/301 Blackbody System (*Infrared Systems Development*) with an emissivity of 0.96, was also used in this assessment.

II.3.2 Data processing

Data processing used R (version 15.2, R developmet core team 2005) scripts, developed based on NERC FSF guidelines and the FSF post processing MATLAB toolbox (Robinson and Mac Arthur 2012). The HR-1024 measurement software stores VIS-SWIR radiance spectra observed from the reference panel and target, respectively, and the derived relative reflectance with the meta information in text files (*.sig; SVC). The FTIR data collection software (AutoQuant Pro, *MIDAC*) creates a binary file format (*.sb) that was converted to text files (*.csv) using an IDL (version 8.2.1, EXELIS Visual Information Solutions) script. Wavelengths in the VIS-SWIR (LWIR) are given in units of nm (µm).

Albedo, the broadband estimate of reflectance covering the region 300–2500 nm, is weighted by a standard terrestrial solar spectrum (*ASTM G173-03* global solar spectrum, NREL 2000) and integrated spectrally. Broadband emissivity is integrated over the wavelength region of 8–14 µm and normalised by the Planck radiance spectrum (eqn. II.1) calculated at 290 K, a typical value for urban surface temperatures in mid-latitudes.

II.3.2.1 Short-wave reflectance

The measurement ranges of the silicon detector array and the first InGaAs detector array overlap slightly in the transition region of 960–1005 nm. Although the SVC software allows removal of the overlap to store a continuous spectrum, the complete measurements were stored to avoid uncontrolled loss of information (NERC FSF personal communication). During post processing, overlapping data were interpolated by fitting a cubic spline through data from the long-wave end of the first and the short-wave end of the second detector array. This created a combined spectrum using the wavelengths of the latter to 980 nm. Removing this overlapping region reduced the number of available bands from 1024 to 988. Following calculation of the absolute reflectance (α_λ), smoothing via the Savitzky-Golay filter (Savitzky and Golay 1964) was used with a frame size of 31 (Robinson and Mac Arthur 2012). The final short-wave reflectance spectra for each target were obtained by averaging the respective samples.

II.3.2.2 Long-wave emissivity

II.3.2.2.1 Radiometric calibration

As internal parts of the infrared spectrometer (e.g. mirrors, lenses) interact with the incoming radiation, they also alter the recorded DNs. These effects can be described by an instrument specific calibration. Radiation entering the instrument R_λ is retrieved from the detected energy spectrum E_λ (raw digital numbers, DN) by accounting for the instrument response of the spectrometer G_λ, hereafter referred to as *gain*, and the instrument's self-emission S_λ, i.e. the spectral radiance originating from inside the spectrometer:

$$R_\lambda = S_\lambda + G_\lambda \cdot E_\lambda \qquad \text{II.3}$$

For many techniques, the gain is quite stable and can be calculated theoretically or measured under specialised laboratory conditions. When observing thermal radiance, however, instrument-internal conditions themselves vary with the observed quantity so that calibration needs to be performed near simultaneously with the measurement itself. To account for the complex effects of the instrument components several instantaneous calibration techniques have been developed for thermal remote sensing applications (e.g. Revercomb et al. 1988; Lindermeir et al. 1992; Hook and Kahle 1996; Ruff et al. 1997). These usually involve reference observations of one or multiple blackbody systems (i.e. sources of 'known' radiance) simultaneously or in turn with the sampling of the target.

A commonly used approach is the 2-BB (blackbody) method (e.g. Hook and Kahle 1996; Korb et al. 1996), where two blackbodies of known temperature (T_{BB1}, T_{BB2}) are measured along with the target. Given their emitted radiance R_λ can be described by Planck's law, when incorporating their non-unitary emissivity, coefficients for radiometric calibration can be obtained from their radiance:

$$\begin{aligned} R_\lambda(T_{BB1}) &= S_\lambda + G_\lambda \cdot E_\lambda(T_{BB1}) \\ R_\lambda(T_{BB2}) &= S_\lambda + G_\lambda \cdot E_\lambda(T_{BB2}) \end{aligned} \qquad \text{II.4}$$

Under the assumption of a linear radiometric response with incoming spectral radiance, these equations can be combined to calculate instrument self-emission and gain:

$$S_\lambda = \frac{R_\lambda(T_{BB1})E_\lambda(T_{BB2}) - R_\lambda(T_{BB2})E_\lambda(T_{BB1})}{E_\lambda(T_{BB2}) - E_\lambda(T_{BB1})} \quad \text{II.5a}$$

$$G_\lambda = \frac{R_\lambda(T_{BB2}) - R_\lambda(T_{BB1})}{E_\lambda(T_{BB2}) - E_\lambda(T_{BB1})} \quad \text{II.5b}$$

Based on these spectrally varying coefficients, the detected energy spectrum from observing the target $E_\lambda(T_{target})$ can be calibrated to the target's radiance (eqn. II.3). Measurements of the blackbodies should be performed directly before/after sampling the target to minimize potential effects of instrument drift (Salvaggio and Miller 2001) and changes in background conditions. The accuracy to which we know the kinetic temperatures of the reference blackbody systems (T_{BB1}, T_{BB2}) adds uncertainty to the calibrated target radiance, thus emphasizing the need for high quality equipment and careful operation (e.g. enough time for the BB systems to stabilise at the set temperature). Even though there are approaches to circumvent this limitation (e.g. using three BB to gain additional information, Lindermeir et al. 1992), they are not yet well established and the 2-BB method remains the most commonly used calibration method (e.g. Hook and Kahle 1996; Bassani et al. 2007).

II.3.2.2.2 'Background' correction

The 'background' correction addresses the impact of down-welling radiation from the surroundings (e.g. cool outside 'sky', or warmer lab walls and ceilings) and the atmospheric paths through which the radiation travels. Radiance leaving a target of temperature T_{target} is composed of radiance emitted by a blackbody at the same temperature $L_\lambda(T_{target})_{BB}$, which is expressed by the Planck function (eqn. II.1), multiplied by the target's emissivity ε_λ, the path thermal radiance of the air between the target and the sensor $R_\lambda(T_{air})_p$ and the down-welling radiance emitted from the background $R_{\lambda d}$, the latter reflected by the target (assuming it has a non-unitary emissivity).

Taking into account the transmissivity of the atmosphere between the emitter and the measurement device, τ_λ, the relation can be expressed (Ottle and Stoll 1993):

$$R_\lambda(T_{target}) = \tau_\lambda \left| \varepsilon_\lambda L_\lambda(T_{target})_{BB} + (1-\varepsilon_\lambda)R_{\lambda d} \right| + R_\lambda(T_{air})_p \quad \text{II.6}$$

Given the very short distance between the target and the sensor for the spectroscopic observations in this study, which are made in the 8–14 µm atmospheric window, atmospheric emission along the path is neglected ($R_\lambda(T_{air})_p = 0$) and perfect atmospheric transmissivity ($\tau_\lambda = 1$) is assumed. Eqn. II.6 then simplifies to:

$$R_\lambda(T_{target}) = \left| \varepsilon_\lambda L_\lambda(T_{target})_{BB} + (1-\varepsilon_\lambda)R_{\lambda d} \right| \quad \text{II.7}$$

i.e. the radiance leaving the target is composed of the radiance emitted by the latter, plus the fraction (1- ε_λ) of down-welling radiance reflected. Measuring a target with known spectral emissivity, here the gold reference panel with spectral emissivity $(\varepsilon_\lambda)_{gold}$, allows this equation to

provide an estimate of the down-welling spectral radiance $R_{\lambda d}$. The latter is the difference between the calibrated radiance observed from the gold reference $R_{\lambda}(T_{gold})$ and the Planck radiance (eqn. II.1) of a BB at the temperature of the reference panel $L_{\lambda}(T_{gold})_{BB}$, taking into account the spectral emissivity of the gold plate:

$$R_{\lambda d} = \frac{R_{\lambda}(T_{gold}) - (\varepsilon_{\lambda})_{gold} L_{\lambda}(T_{target})_{BB}}{1 - (\varepsilon_{\lambda})_{gold}} \quad \text{II.8}$$

Assuming background conditions remain constant throughout the measurement, this down-welling radiance is then used within a re-arrangement of eqn. II.7 to calculate the target's absolute emissivity spectrum:

$$\varepsilon_{\lambda} = \frac{R_{\lambda}(T_{target}) - R_{\lambda d}}{L_{\lambda}(T_{target})_{BB} - R_{\lambda d}} \quad \text{II.9}$$

II.3.2.2.3 Separation of emissivity and temperature

The target temperature T_{target} is required (eqn. II.9) to calculate the respective Planck radiance $L_{\lambda}(T_{target})_{BB}$. Given the difficultly in accurately measuring target surface temperature with contact probes (as conduction and convection effects can be significant), several methods have been developed to quantify T_{target} based on the spectrometric measurements themselves (Cheng et al. 2007). For outdoor measurements, the Iterative Spectrally Smooth Temperature/Emissivity Separation (ISSTES, Borel 1998) based on atmospheric absorption lines is an apparently well performing approach (Horton et al. 1998; Cheng et al. 2007). For the current laboratory-based study the *blackbody fit* method (BB-fit; Kahle and Alley 1992) was used. This assigns an emissivity value (local maximum) in a certain wavelength range, and by varying the assumed temperature in the emissivity retrieval process, the surface temperature that results in the best fit to this pre-defined emissivity value is determined. Expected values (Table II.2) were derived based on:

- Spectra of similar materials from other libraries.
- Emissivity spectra had to remain below unity within the region 9–14 µm.
- For most samples additional outdoor LWIR spectral radiance observations were available (Appendix B). Processed using the ISSTES method, these data provided information about the location and magnitude of the local spectral maxima.

Complex material classes such as cement/concrete or metal were characterised by multiple reference points.

Table II.2: Emissivity maxima ε_{max} and their locations defined by wavelength range [λ_{min} – λ_{max}] for the selection of impervious urban materials studied, used as input in the blackbody fit method.

Material	ε_{max}	λ_{min} [µm]	λ_{max} [µm]
Asphalt	0.975	12.0	12.5
Tarmac	0.970	11.5	12.0
Cement brick	0.975	12.0	12.5
Clay brick	0.975	7.5	8.5
Clay brick with beige paint	0.950	9.0	10.0
Clay brick with white paint	0.975	12.0	12.5
Clay brick with cement	0.975	12.0	12.5
Cement	0.960	9.5	10.5
Cement	0.960	10.5	11.5
Cement	0.950	11.0	11.5
Concrete	0.975	12.0	12.5
Granite	0.975	12.0	12.5
Roofing shingle	0.960	12.0	12.5
Ceramic roofing tile	0.950/0.975	12.0	12.5
Cement roofing tile	0.975	12.0	12.5
Limestone	0.940	9.5	10.5
Sandstone	0.975	12.0	12.5
PVC roofing sheet	0.960	11.0	12.0
Aluminium plus zinc	0.850	10.0	11.0
Stuccoed aluminium	0.050	8.5	9.5
Metal with paint	0.970	10.5	11.5
Lead	0.940	8.0	9.0
Black iron	0.970	9.0	10.0
Quartzite conglomerate	0.97/0.95	12.0	12.5
Silica sand	0.975	12.0	12.5

II.3.3 Impervious construction materials

Construction materials used for roads, pavements, building walls and roofs in London were studied using the measurement techniques described herein. Given *in-situ* measurements cannot fully cover the immense variety of urban surface materials[1], the samples analysed are grouped into classes (Table II.3). While most classes relate to fabricated materials, some natural impervious materials (e.g. granite or sandstone) are also included as they represent common constituents of composite construction materials, such as asphalt and concrete. Other natural materials such (e.g. vegetation, soils) play an important role in urban areas, however, they are usually well represented in existing spectral libraries and hence not studied here. Each sample

[1] Comment on Kotthaus et al. (2014): materials were selected to approximately cover the most commonly used construction materials used across London, however, this limited number of samples does not represent the immense diversity of materials used in this city. Here, special emphasize was given to roofing tiles, which are particularly under-represented in existing spectral libraries (Table II.1). Further the aim was to include a variety of samples within one material class to enable evaluation of the variability within and between material types.

analysed was coded with a material class ID (Table II.3) plus sample ID (numerical). The initial classification based on usage and composition consists of ten classes with some refined into sub-classes (Appendix II.B). Composition was determined from labels, visual inspection and spectral response.

Table II.3: Classes of impervious urban materials analysed from London.

Material class	Class ID	Sub-class	Number of samples
Quartzite	X	Quartzite conglomerate	3
Stone	S	Sandstone	3
		Limestone	2
Granite	G	Granite	5
Asphalt	A	Road asphalt	9
		Asphalt roofing paper	1
Concrete/cement	C	Concrete	4
		Cement	3
Brick	B	Clay brick	7
		Cement brick	7
Roofing shingle	L	Roofing shingle	4
Roofing tiles	R	Ceramic roofing tile	7
		Concrete roofing tile	5
Metal	Z	Metal	5
		Metal, painted	3
PVC	V	PVC	6

II.4 Results and discussion

First the sources of uncertainty in the laboratory-based spectral emissivity measurements are presented (Section II.4.1), including tests of both the measurement system performance and the methodology. Then the derived emissivity spectra are presented and discussed (Section II.4.2) along with VIS-SWIR reflectance spectra of the same samples.

II.4.1 Methodology evaluation of long-wave infrared spectroscopy

Radiometric calibration describes conversion of the recorded energy spectrum in raw DN to spectral radiance units (Section II.3.2.2.1). The accuracy of the 2BB-method depends on the thermal uniformity and accuracy of the calibration sources, the linearity between recorded energy spectrum and observed radiance, and the temporal stability of the instrument response (gain) and self-emission. These are investigated in turn below and compared to the uncertainty of the estimation of the target temperature using the BB-fit approach (Section I.4.3).

II.4.1.1 Thermal properties of the calibration blackbody system

Thermal properties of the flat plate blackbodies used to calibrate the FTIR data were evaluated using a handheld thermal imaging camera. To ensure the accuracy of this information,

measurements made by the imager were first compared to a high quality cavity radiation standard with a small aperture and high spectral emissivity (ε > 0.99 across the LWIR wavelength range). The measured thermal imagery brightness temperatures were very close to the 'true' kinetic temperature of the cavity emitter (Figure II.1a), and the slight difference derived from the linear best fit was applied to all the subsequent thermal imager data.

The thermal imager was then used to collect data of the flat plate BB sources at a series of nine different temperatures, ranging from 40 °C to 100 °C and representing approximately equal spectral radiance intervals (Figure II.1b). The thermal image brightness temperatures were compared to the controller temperature to assess how closely the latter resembles the actual surface emission temperature (Figure II.1b). Applying the calibration relation derived for the thermal imager (Figure II.1a) and converting brightness into kinetic temperature estimates by accounting for the emissivity of the BB system, a good agreement was established (Figure II.1b). The derived relation was applied to all observations of the BB systems used in this study. During the analysis the two BB sources (Section I.3.3) were found to have very similar thermal responses, so that only results from the first source (BB1) are shown here.

In this study, the FTIR FOV approximately covered the central 30 mm x 30 mm of the flat plate BB radiation sources so that an assessment of their thermal, spatial homogeneity was warranted. With the radiation sources set to a fixed temperature (e.g. 76 °C shown in Figure II.2; similar behaviour at other temperatures) the edges of the blackbody aperture showed strong temperature gradients over a distance of about 5 mm (Figure II.2a). The blackbody source was a little cooler towards the edges, and thermal gradients differed slightly between the vertical and horizontal direction (solid lines, Figure II.2a). This could be attributed to spatial variations of the

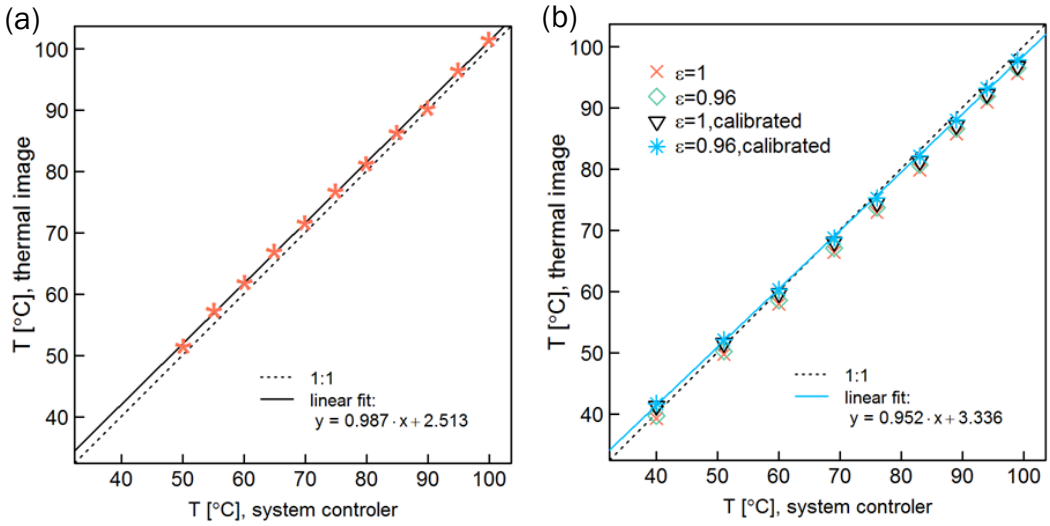

Figure II.1: Measured radiometric temperature from the thermal imager as a function of blackbody (BB) body temperature, as displayed by the BB system controller for (a) a high emissivity (ε > 0.99) cavity radiation standard and (b) a 'flat plate' BB radiation source (ε = 0.96) later used for FTIR calibration. Both are observed with the same LWIR (8–14 µm) thermal imaging camera. In (b) four settings illustrate the impact of adjusting the LWIR brightness temperature measurement of the thermal imaging camera for the non-unitary emissivity of the target, and of taking into account the adjustment to the thermal imager calibration shown in (a).

heating of the BB area, however, some impact might also arise from directional viewing effects and reflected down-welling radiance. The latter adds small contributions to the observed temperature because the radiation source is not quite a perfect blackbody but rather has an emissivity of 0.96 (Section I.3.3). Either way, the spatial distribution of surface brightness temperatures observed using the thermal imager represents the thermal characteristics generally 'viewed' by the FTIR in the current setup.

If positioned accurately, the FOV of the spectrometer covers the central area of the BB radiation source (B, Figure II.2b; circular FOV approximated here by rectangular subset). If the FTIR is placed closer to the BB, the observed area is smaller (subset A) with marginally lower spatial temperature variability. Given the slightly cooler temperatures at the right edge of the source, a small decrease (increase) of the average temperature $\overline{T}$ (the standard deviation σ) across the area occurs when the distance between the BB source and the FTIR is increased (larger FOV, subsets C-D, Figure II.2b). If the viewing direction slightly differs from NADIR, the FOV shifts to the side (subset E or F). These statistics reveal that average brightness temperature varies by less than 0.15 °C if an area of the blackbody within the central 16 cm^2 is viewed and thermal variability across the tested areas is small (σ < 0.02 °C). Being almost one order of magnitude lower than the temperature resolution of the BB temperature control unit (0.1 °C) these spatial variations introduce negligible errors. At 8–14 µm and the moderate temperatures considered here a temperature difference of 0.15 °C equates to a difference in Planck radiance (eqn. II.1) of only ~ 0.02 W m^{-2} μm^{-1} sr^{-1}, and the homogeneity of the BB radiation sources is therefore assumed sufficient within the central area. A comparison (not shown) of raw DN observed by the

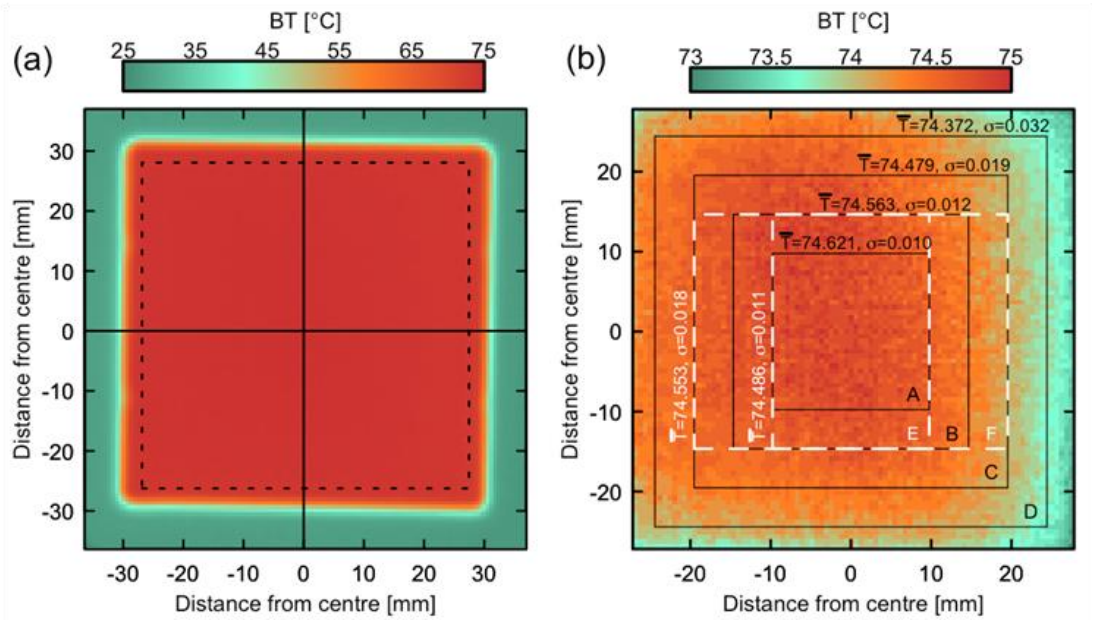

Figure II.2: Brightness temperature (BT) imagery of flat plate blackbody (BB1) at a system controller temperature of 76 °C recorded using the LWIR (8–14 µm) thermal imager described in Figure II.1. (a) Whole aperture; solid lines: selected cross sections; dotted line: subset without strong edge effects (cf. b); (b) central area of flat plate BB; solid/dashed lines: subsets of varying size/location. Given the high spatial resolution of the image (mean pixel size = 0.6 mm × 0.6 mm), no adjustment is applied to account for small variations in pixel size across the image when calculating areal statistics of mean brightness temperature ($\overline{T}$) and standard deviation (σ).

FTIR of the BB source at a central viewing direction and displaced to the left and to the right (similar to subsets E and F, Figure II.2b) confirms that the response is similar within the central 16 cm^2, but changes when parts of the BB are sampled that are more than 20 mm away from its centre.

II.4.1.2 Linearity of instrument response

Assuming the response of the spectrometer to incoming radiance is linear (Section II.3.2.2.1), the gain (slope) and instrument self-emission (intercept; eqn. II.5a) can be obtained from the recorded energy spectrum in raw DN and the incoming radiance calculated from the flat plate blackbodies, both changing as a function of wavelength.

To evaluate this presumably linear relation, raw DN recorded by the FTIR system during observation of the blackbodies at 40–100°C (solid lines in Figure II.3) were analysed in relation to the theoretically expected Planck radiance (eqn. II.1) at these temperatures (dashed lines), taking into account the BB emissivity of 0.96. While the theoretically expected radiance decreases with increasing wavelength across the 8–14 µm region, the recorded raw DN curves have a concave shape with a maximum between 10–11 µm (Figure II.3). This illustrates the instrument's changing relation between raw DN and incoming radiance across the LWIR wavelength range.

The same data (as Figure II.3) illustrate that, at a given wavelength (e.g. 9 µm), BB radiance can

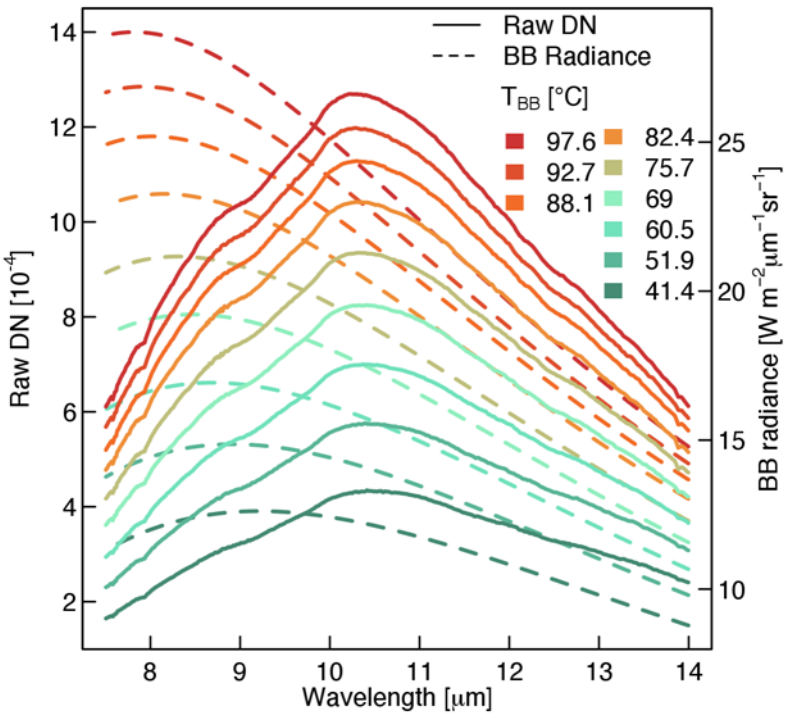

Figure II.3: Raw digital numbers (DN) recorded by the MIDAC FTIR system when observing the flat plate blackbody (BB1) of Figure II.2 from a distance of 10 cm (BB2 is similar but not shown). Observations at a series of different temperatures TBB (as displayed by the BB controller unit) are shown along with the respective spectral radiance curves deduced using the Planck function (eqn. II.1) and the BB emissivity of 0.96.

be expressed as a function of the measured raw DN signal across the observed temperature range (Figure II.4). Using observations at all nine temperatures, instrument self-emission (intercept) and gain (slope) are estimated (dashed lines, Figure II.4). The small root mean square errors (RMSE: 0.26–0.07 W m^{-2} μm^{-1} sr^{-1} for 8–14 µm) confirm that the relation between raw DN and incoming spectral radiance appears to be well approximated by a linear function. To test the accuracy of this relation, a third (independent) BB radiation source (ε = 0.96) was observed at eight different temperatures, along with the flat plate calibration blackbodies. With the target BB heated to about 50–60°C, the flat plate BB sources for radiometric calibration were set to 40–45°C and 70°C respectively. The detected energy spectrum from the target BB source was calibrated from raw DN to radiance units using the linear regression equation obtained from all nine measurements of the flat plate BB sources (as in Figure II.4); and by choosing 20 combinations of two different temperatures selected from the set of nine temperatures (T_{BB1} = 40–76°C; T_{BB2} = 82–98°C).

Generally, this radiometric calibration yields radiance values very close to the theoretically expected Planck radiance for the independent target (Figure II.5, solid lines). The spectral RMSE describing the linear fit at each wavelength is shown as the shaded area, providing an indicator of the uncertainty. Especially well represented is the radiance at temperatures in the range important to the current study (50–60°C), while radiance at higher temperatures (65.8, 72.1, 78.9°C) appears overestimated between 8–10 µm or underestimated (84.5, 89.1°C)

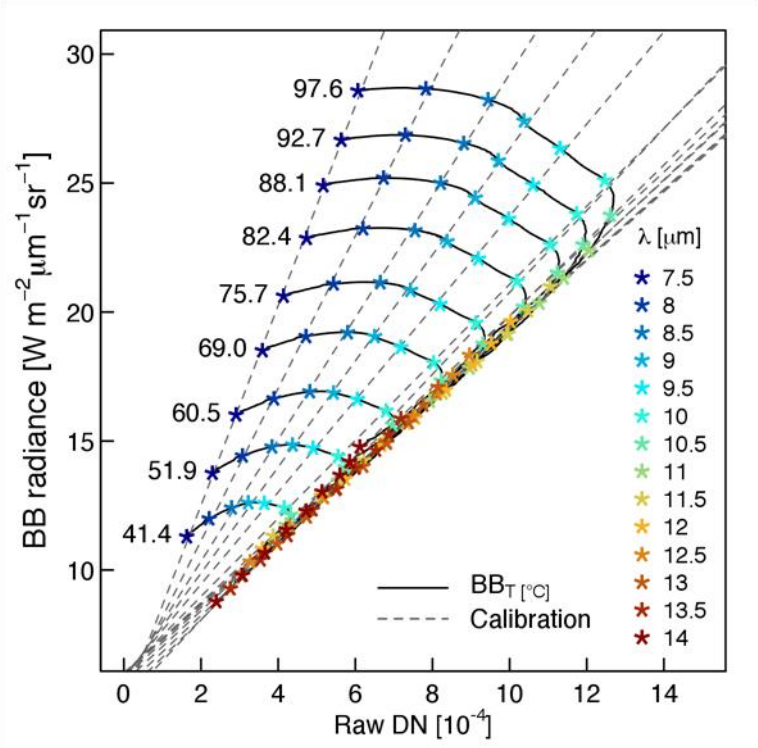

Figure II.4: Spectral radiance as calculated for the flat plate blackbody system (BB1; BB2 similar, not shown) with ε = 0.96 (whose data are shown in Figure II.1 –Figure II.3) at different temperatures T (labelled [°C]), displayed against Raw DN (digital numbers) recorded by the MIDAC FTIR system when observing the same BB source. Linear relations, that define the radiometric calibration between raw DN and spectral radiance, are shown for a series of selected wavelengths (dashed lines).

above 10 µm. Below wavelengths of 8 µm, the calculated radiance starts to deviate distinctly from the expected values suggesting that the linearity of the relation between raw DN and incoming spectral radiance becomes invalid. Fortunately, measurements at these wavelengths are not used in the current analysis, in part because they are outside the 8–14 µm atmospheric window.

When calibration is based on BB observations at only two temperatures (20 combinations tested here, dashed lines, Figure II.5), the calculated radiance generally agrees with the expected function in terms of shape and magnitude, however, some uncertainty is evident. The radiance retrieved for the lower temperature target (e.g. 38.5 °C) has a particularly larger spread. Presumably, coefficients derived from two higher temperatures do not represent an accurate calibration function for a colder target. This again supports the assumption that the 2-BB method works best if the BB sources are set to temperatures closely bracketing the temperature of the target. With this setting, the errors introduced by the calibration remain small (mean bias error between 8–14 µm: 0.06 W m^{-2} μm^{-1} sr^{-1}), hence it is used for all subsequent observations in this study.

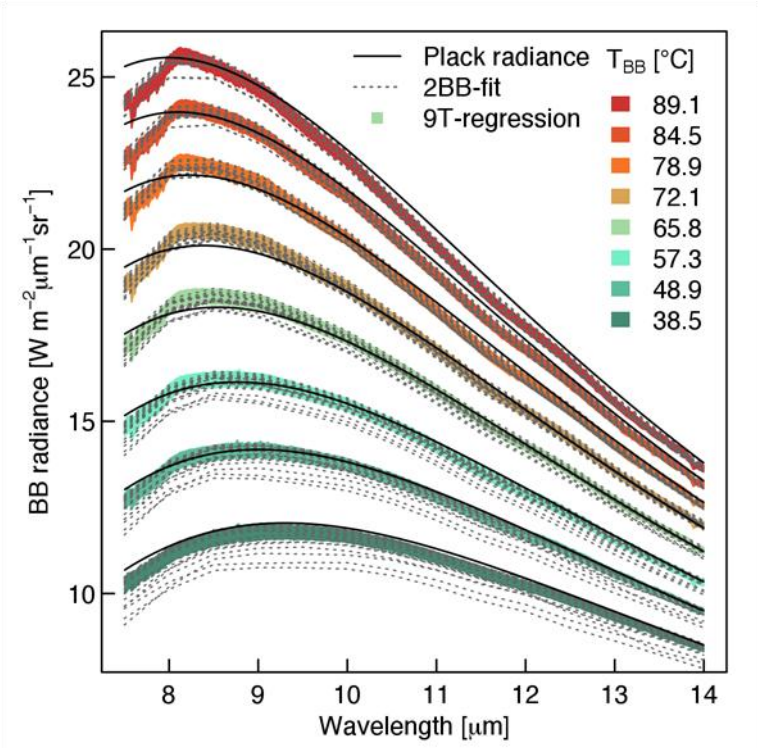

Figure II.5: Blackbody spectral radiance of an independent radiation source at different temperatures (T_{BB}), calibrated using the observations of the flat plate black bodies at nine temperatures (9T) (see Figure II.1): shaded area: spectral radiance calculated via the application of the linear calibration relations derived through all nine BB observations ± spectral root mean square error, dashed lines: spectral radiance calculated from linear calibration relations derived through observations at 20 combinations of two selected BB temperatures. For reference (solid line), expected values according to the Planck Function (ε = 0.96). Statistics (see text) calculated for thermal infrared region 8-14 µm.

II.4.1.3 Stability over time

Sampling the target spectral radiance multiple times improves the signal-to-noise ratio, but the measurement situation must remain static during this period. To balance these priorities, ten samples were chosen to allow a reasonably quick measurement period (~2 min). To estimate how stable the whole measurement environment remains during one set of observations, the calibration sources, an independent BB source (at 55 °C) and the gold reference panel were sampled ten times, resembling the sampling strategy used for the target measurements (Section I.3.3). The raw DN were converted using one set of calibration measurements with BB temperatures of 40 and 70 °C. To account for self-emission from the InfraGold, the gold radiance was converted to down-welling radiance (eqn. II.8).

Firstly, temporal variability of both instrument self-emission and gain (eqn. II.5) are evaluated (Figure II.6), both clearly varying as a function of wavelength. As standard deviations of both estimates reveal, calibration is most stable for the 9–11 µm spectral region, and increases below 8.5 µm and above 11 µm. This is associated with the convex-shaped spectral pattern of the detected energy spectrum itself (raw DN in Figure II.6), presumably indicating a better signal-to-

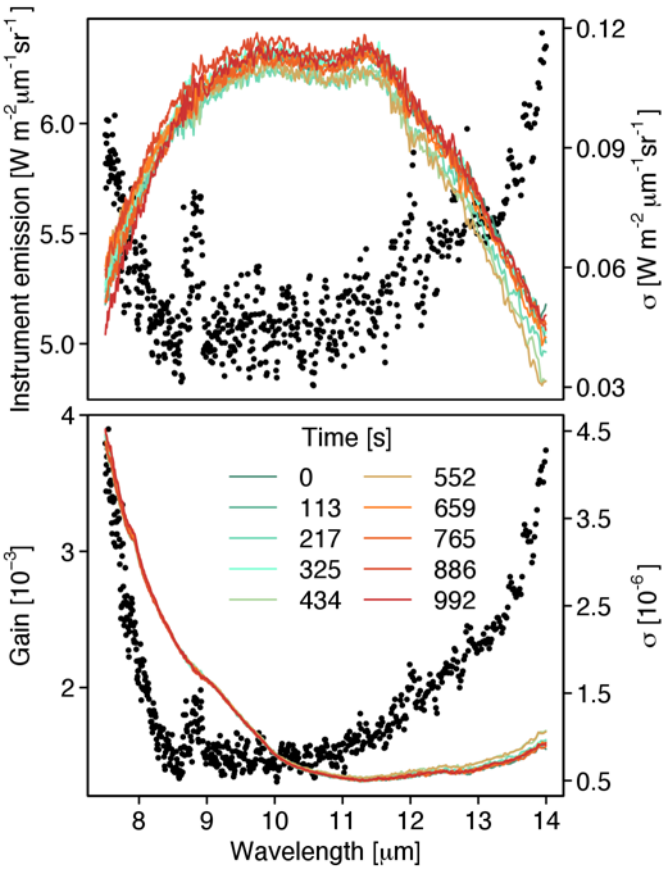

Figure II.6: Radiometric calibration coefficients for the MIDAC FTIR spectrometer system, describing the linear relation between the measured energy spectrum in raw DN and the spectral radiation (eqn. II.5): (top) instrument self-emission (S_λ); and (bottom) gain (G_λ). Coefficients derived from ten subsequent measurements of two flat plate BB sources at 40 °C (BB1) and 70 °C (BB2), respectively, using the method described (Section II.3.2.2.1); (dots) respective standard deviations across the ten samples. Legend lists time-difference since first measurement.

noise in the centre of the LWIR region for the temperatures used here. Particularly increased noise is identified between 8.6–9.0 µm.

At a timescale of about two minutes (i.e. time to collect 10 samples) both the radiance reflected by the reference panel and that emitted by the independent BB varied only slightly (Figure II.8), by approximately 0.3% and 0.6%, respectively. Temporal variability of the calibrated radiance (spectral standard deviation of 10 measurements) is clearly related to the calibration coefficients (cf. Figure II.6), with a more stable region between 9–11 µm. The error propagation is less pronounced above 11 µm, where the increase in standard deviation of instrument emission and gain is less evident in the standard deviations of the final calibrated radiance values of both blackbody target and down-welling radiance (Figure II.8). The overall uncertainty (RMSE between 8–14 µm: 0.02 W m^{-2} μm^{-1} sr^{-1}) introduced by these temporal variations is lower than that linked to the assumption of calibration relation linearity (Section II.4.1.2). However, as the two sources of measurement error are related they cannot be quantified completely independently via the means available here.

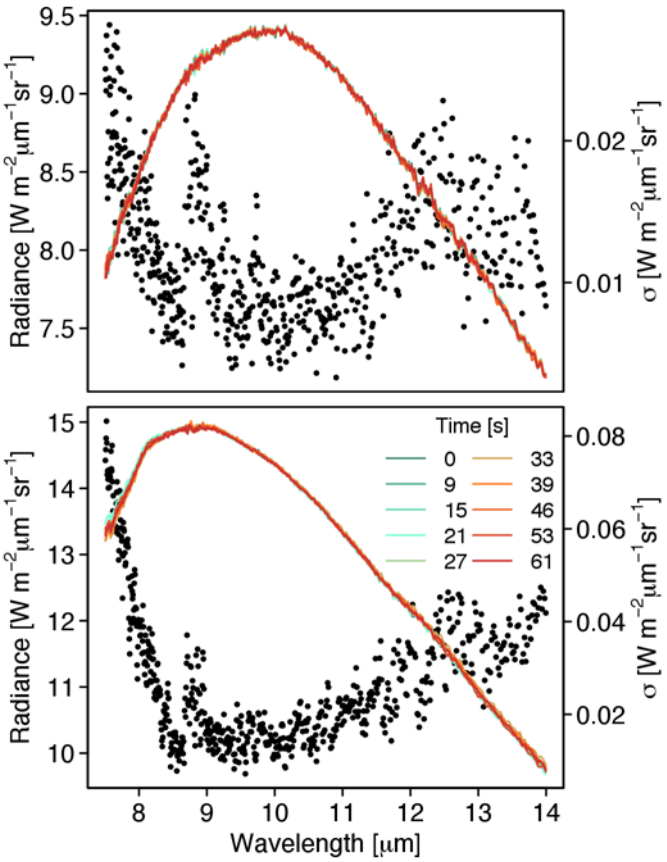

Figure II.7: Temporal variability in the calibrated spectral radiance over the course of ten contiguous measurements (solid lines), displayed as normalised standard deviation (dots) of (top) down-welling spectral radiance as characterised by observations of the gold reference panel, and (bottom) calibrated spectral radiance emitted by an independent blackbody target (ε = 0.96). Observations are calibrated into spectral radiance using a single set of calibration blackbody measurements made just before the first measurements. Legend lists time-difference since first measurement.

II.4.1.4 Evaluation of the emissivity retrieval method

The experimental setup plus retrieval method for the measurement of long-wave emissivity spectra was assessed using a sample of known composition (Figure II.8). A quartz sample (Ottawa silica sand) was chosen as a reference given its clear and well pronounced reststrahlen features (Salisbury and D'Aria 1992).

To separate the emissivity information contained within the spectral radiance measurements from the kinetic temperature, the blackbody fit method (Section I.4.3) was applied. This introduces uncertainty as *a priori* knowledge about the target's spectra is required (Table II.2). While the wavelength location of the local emissivity maximum can be specified as an approximate band, its actual magnitude (e.g. 0.985 between 12.0-12.5 µm for the Ottawa silica sand sample) needs to be rather accurately known as this can directly impact the results. An error of ± 0.01 in this emissivity value causes a temperature error of ~ 0.5 °C and hence introduces uncertainty to the specified Planck radiance (shading around dashed line in Figure II.8, top).

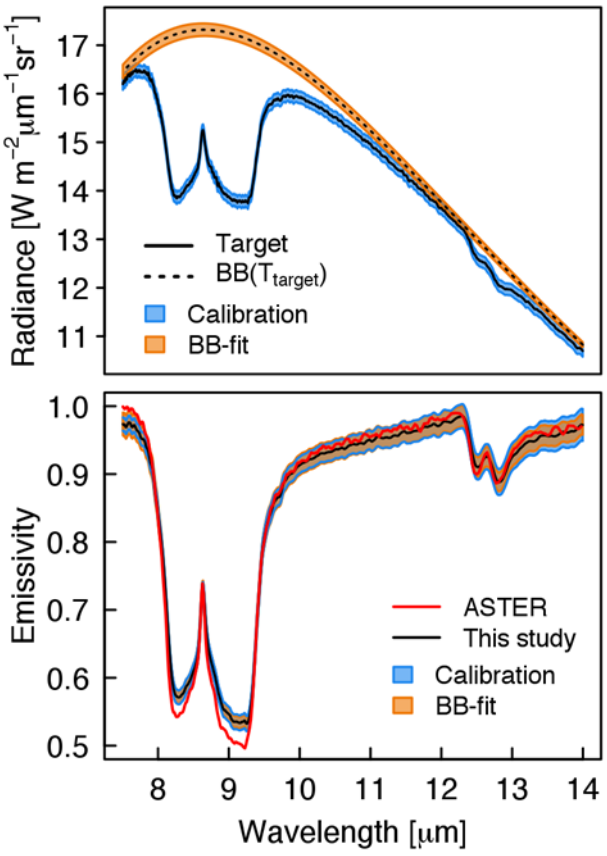

Figure II.8: Observations of silica sand (Ottawa) taken with the MIDAC FTIR system (described in this study) deployed in the laboratory: (top) calibrated spectral target radiance and theoretical Planck radiance of a blackbody at the same temperature (T_{target}), (bottom) spectral emissivity derived from these measurements (cf. top) along with reference spectrum from the ASTER spectral library (Baldridge et al. 2009). Shading indicates uncertainty linked to radiometric calibration and BB-fit method, respectively.

The discussed measurement errors linked to the radiometric calibration (Sections II.4.1.2, II.4.1.3) could accumulate to a spectral measurement uncertainty of around 0.08 W m^{-2} μm^{-1} sr^{-1} in the final calibrated target radiance (denoted by the shading around the solid line in Figure II.8, top). Conversion to spectral emissivity illustrates (Figure II.8, bottom) that the total uncertainty expected from radiometric calibration and system performance have an impact comparable to an uncertainty of ± 0.01 in the maximum specified emissivity.

The retrieved spectrum of the silica sand compares well to that from the ASTER spectral library (Ottawa silica sand, Baldridge et al. 2009; Figure II.8, bottom). The ASTER library data are mostly within the range of uncertainty specified for the sample measured here. Only around the emissivity minima does the ASTER spectrum differ (being slightly lower). Furthermore, the two spectra have the same integrated broadband emissivity of 0.85 (difference = 0.003). This proves that under controlled laboratory conditions the tested portable FTIR system and radiometric calibration setup can be used to collect high quality emissivity spectra.

II.4.2 Spectral response of impervious urban materials

The results of this study are available as an online spectral library of impervious urban materials (SLUM) within the London Urban Micromet data Archive (LUMA, *http://Londonclimate.info/LUMA/SLUM.html*). VIS-SWIR reflectance spectra and LWIR emissivity spectra of 74 material samples obtained from construction sites across London are included. The materials studied are grouped into ten classes according to appearance and usage (Appendix II.B) and derived broadband albedo and emissivity are provided (Appendix II.C, Table II.C.1). Here, the spectra most representative of the material classes studied are presented graphically, while others are put into context (Section II.4.2.1). Given the similarity of spectral signatures of certain materials across classes, these are then grouped according to their LWIR radiative response (Section II.4.2.2). A combination of both classification approaches appears most appropriate to characterise the complex urban surface composition.

II.4.2.1 Characteristics of the impervious urban materials studied

II.4.2.1.1 Quartzite conglomerate

As feldspar and quartz do not create specific absorption features in the short-wave region, the reflectance spectrum of the quartzite conglomerate sample (X001; Figure II.9a) reveals a somewhat unexpected pattern. The locations of the strongest features (i.e. 1700 and 2300 nm) suggest contributions of hydrocarbons (C-H combinations; King and Clark 1989) such as found in industrial solvents (e.g. benzene, toluene, and trichlorethylene; van der Meer and Jong 2002). Hence, it is speculated these absorption bands maybe attributed to the influence of the binder applied to fix the quartzite grains. Spectral emissivity of the quartzite conglomerate (Figure II.9b) appears to be less affected by that binder, as its shape is clearly dominated by the characteristics quartz doublet (Figure II.8). Still, it could impact the overall magnitude of the LWIR emissivity.

LUMA samples of quartzite conglomerates vary in grain size and colour. Their short-wave reflectance spectra reveal the same absorption bands; however, one sample has a higher reflectance overall. In terms of spectral emissivity, the additional samples (X002; X003) differ from the one presented (X001) being dominated by a constantly high emissivity leaving no evidence of any reststrahlen effects. The binder materials in the conglomerate may again explain this. Further information on the composition would be required to understand why the binder does not dominate the LWIR spectrum of the X001 sample. The measurements have been repeated, both in the lab and in the field (see Appendix II.A for methodology), in order to eliminate measurement errors as the cause of this difference.

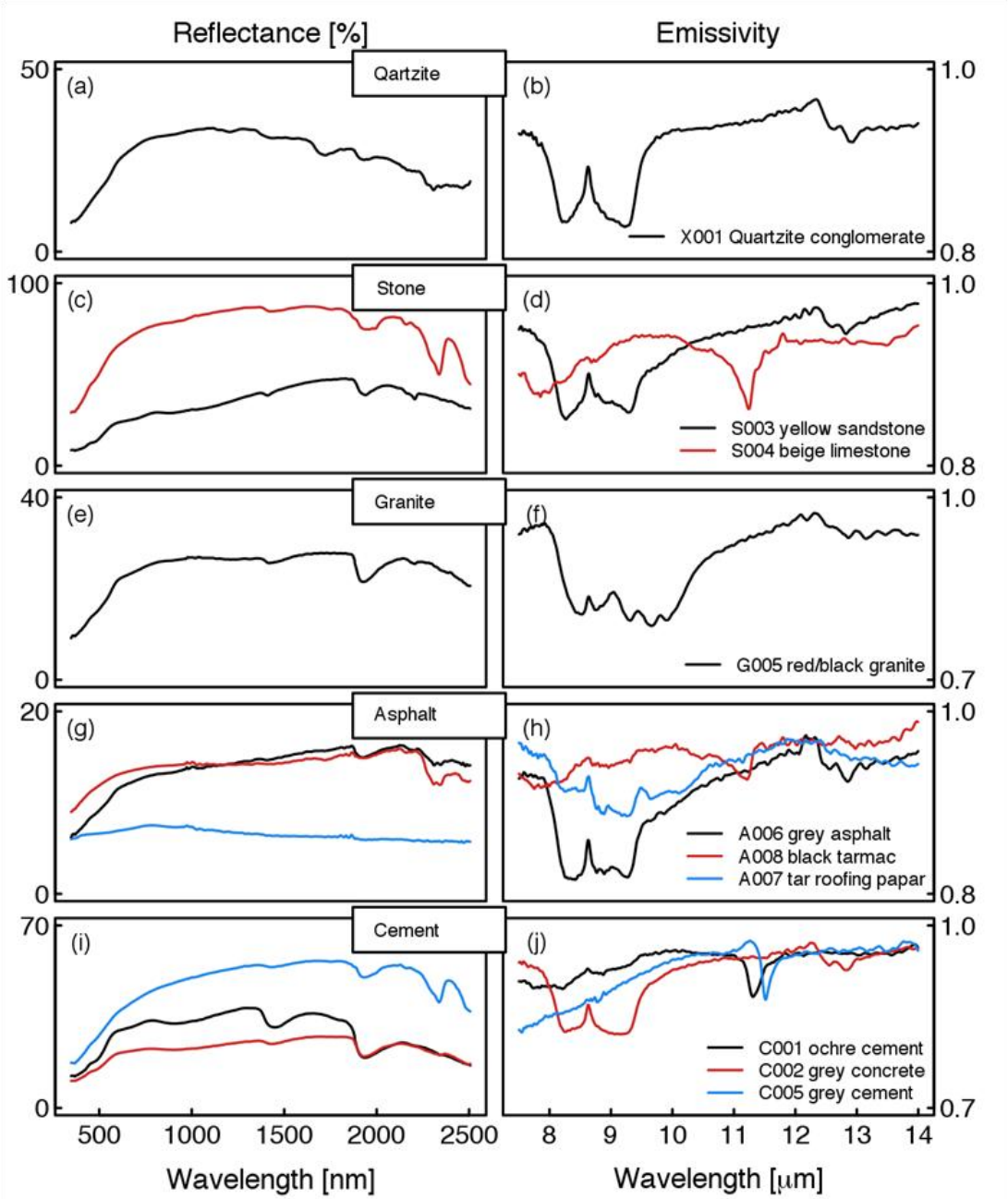

Figure II.9: Examples of (left) absolute VIS-SWIR reflectance spectra and (right) absolute LWIR emissivity spectra for five classes of impervious urban materials (Section II.3.3). Spectra determined using the SVC HR2014 (VIS-SWIR) and the MIDAC FTIR system (LWIR) (described Section II.3.1) deployed in the laboratory.

II.4.2.1.2 Stone

In the VIS-SWIR, the beige limestone (S004; Figure II.9c) has a very high overall reflectance and shows strong absorption at the characteristic 1900 and 2350 nm (and presumably 2550 nm) wavelengths. The sandstone sample (S003; Figure II.9c) reveals contributions of both iron oxides as well as clay minerals, with the pronounced H_2O absorption at 1900 nm suggesting a smectite mineral (potentially montmorillonite). Clearly more distinct are the characteristics of the two stones in the LWIR region (Figure II.9d). While limestone can be identified based on its characteristic reststrahlen band at around 11.3 µm, the spectral emissivity of sandstone is close to the quartzite signature (Figure II.9b).

The LUMA spectral library includes other samples in the stone material class (not shown; Appendix II.C, Table II.C.1). The grey carboniferous limestone (S002) shows only weak absorption features and has a much lower overall reflectance than the beige limestone (S004). Spectral emissivity is more similar, but again, the carboniferous limestone has a weaker reststrahlen signature. The two additional sandstone samples (S001; S005) have a very similar response as the presented samples (S003) across both the short- and long-wave regions.

II.4.2.1.3 Granite

VIS-SWIR reflectance spectra of the granite samples do not show particular characteristics, apart from a broad H_2O absorption feature at 1900 nm. The sample presented (G005; Figure II.9e) is the one with the lowest albedo. The LWIR response of the various granite samples differs slightly, however, as for the sample shown (G005; Figure II.9f), all resemble some combination of quartz and feldspar spectra. Superimposed over the quartz reststrahlen bands (forming the doublets between 8.0–10.0 µm and 12.3–13.0 µm) are the absorption peaks of feldspar at 9.0, 9.5, and 9.8 µm (Christensen et al. 2000).

II.4.2.1.4 Asphalt

The VIS-SWIR spectra of the weathered road asphalt and tarmac samples (A006 and A008; Figure II.9g) are typical of dark hydrocarbon materials, i.e. reflectance is quite low overall (note varying y-axis scale in Figure II.9) and slightly increases with wavelength. The tar roofing paper (A007; Figure II.9g) is coated with slate chippings that cause low reflectivity (cf. L001d; Figure II.10c). Due to the strong hydrocarbon absorption, long-wave emissivity of asphalt and tarmac is generally high (A006 and A008; Figure II.9h). Materials with high aggregate fractions at the surface (e.g. asphalt sample A006) show the associated absorption features (of e.g. granite or quartz) in their spectra, while hydrocarbon absorption dominates the response of those with smaller aggregate contributions (e.g. tarmac sample A008). The feature at around 11.3 µm of the black tarmac sample (A008) indicates contributions from carbonate minerals that would explain the increased absorption at 2350 nm found in its VIS-SWIR reflectance spectrum (Figure II.9g). In agreement with its VIS-SWIR radiative response, LWIR emissivity of the asphalt roofing paper (A007; Figure II.9h) has slate characteristic features (cf. L001d; Figure II.10d). A range of

additional asphalt and tarmac material samples are included in LUMA SLUM (Appendix II.C, Table II.C.1). Their broadband response in both regions differs with the amount of aggregate. As all samples were exposed (weathered, dirty, dusty) to London's atmosphere, this probably also affects their spectral characteristics.

II.4.2.1.5 Concrete and cement

Cement and concrete are both composed of variations of silica and carbonates, possibly with other minerals and rocks contributing to concrete materials. Here, materials dominated by quartz signatures in their long-wave radiative response are classified as concrete, whereas the remainder are assigned to the cement category. However, it should be noted that the two materials are very similar (given cement is the main constituent of concrete) with the relative relation of siliceous and calcareous minerals governing their spectral radiative response.

All VIS-SWIR spectra of the cement/concrete class exhibit a reflectance increase up to about 600–700 nm, and strong absorption around 1940–1970 nm (Figure II.9i). The latter indicates H_2O related absorption of the gypsum component. As seen in the spectrum of the ochre cement sample (C001) some cement and concrete materials have signatures of iron oxides or absorption at other H_2O related bands (e.g. around 1410 nm). The grey cement (C003) spectrum again shows a deep reflectance minimum around 2310–2350 nm, which could represent C-H features characteristic of bitumen/asphaltic materials (Figure II.9g) or carbonate features known from limestone.

The absorption/reststrahlen features of cement and concrete differ distinctly across the LWIR. Given their congruence in mineral-composition, LWIR spectral emissivity of cement (carbonate dominated) and concrete (quartz dominated; Figure II.9j) is generally similar to that of limestone and sandstone (cf. Figure II.9c; note varying y-axis scale in Figure II.9), respectively. While the emissivity of the grey cement sample (C003) closely resembles that of pure limestone, with a pronounced minimum at 11.3 µm, the quartz-doublet reststrahlen feature dominates the spectra of the concrete samples (C002). The emissivity spectrum of the ochre cement sample again (C001) is formed of a superposition of absorption features of these two minerals. The clear carbonate reststrahlen signature of the grey cement sample (C003) indicates that the short-wave absorption band around 2310 nm (Figure II.9i) is also attributed to this mineral.

II.4.2.1.6 Brick

Bricks made of clay or cement both hold some hydroxyl and water related absorption in the VIS-SWIR (Figure II.10a). Clean clay brick samples show very strong absorption up to 520 nm, with further signatures at 670 and 870 nm, as is characteristic for iron oxides (B004; B008; B013). However, the yellow cement brick sample (B001) also shows signatures that could be linked to iron oxide absorption (Figure II.10a), suggesting that these features cannot be used to reliably distinguish between ceramic and cement materials. The depth of the iron oxide features varies between the samples, possibly due to weathering effects. The black cement brick (B006) has a

constantly low reflectance. Generally, the clay brick samples in this study have a higher overall reflectance than those made of cement.

Differentiation between cement and ceramic-based bricks is more obvious from their thermal response. The red clay brick sample (B004; Figure II.10b) has a near classic clay signature of diminished emissivity between about 8.0–12.0 µm (minimum at ~ 9.2 µm) while the black cement brick (C008) is dominated by silica features only. The spectrum of the light red clay brick (B008) also shows the response of clay minerals, however, emissivity is a little higher overall and the minimum is shifted to ~ 8.8 µm. The spectrum of the yellow cement brick sample (B001) indicates contributions from quartz as well as carbonate mineral reststrahlen effects, similar to the ochre cement sample (C001; Figure II.9j). The clay signature of the extremely weathered red

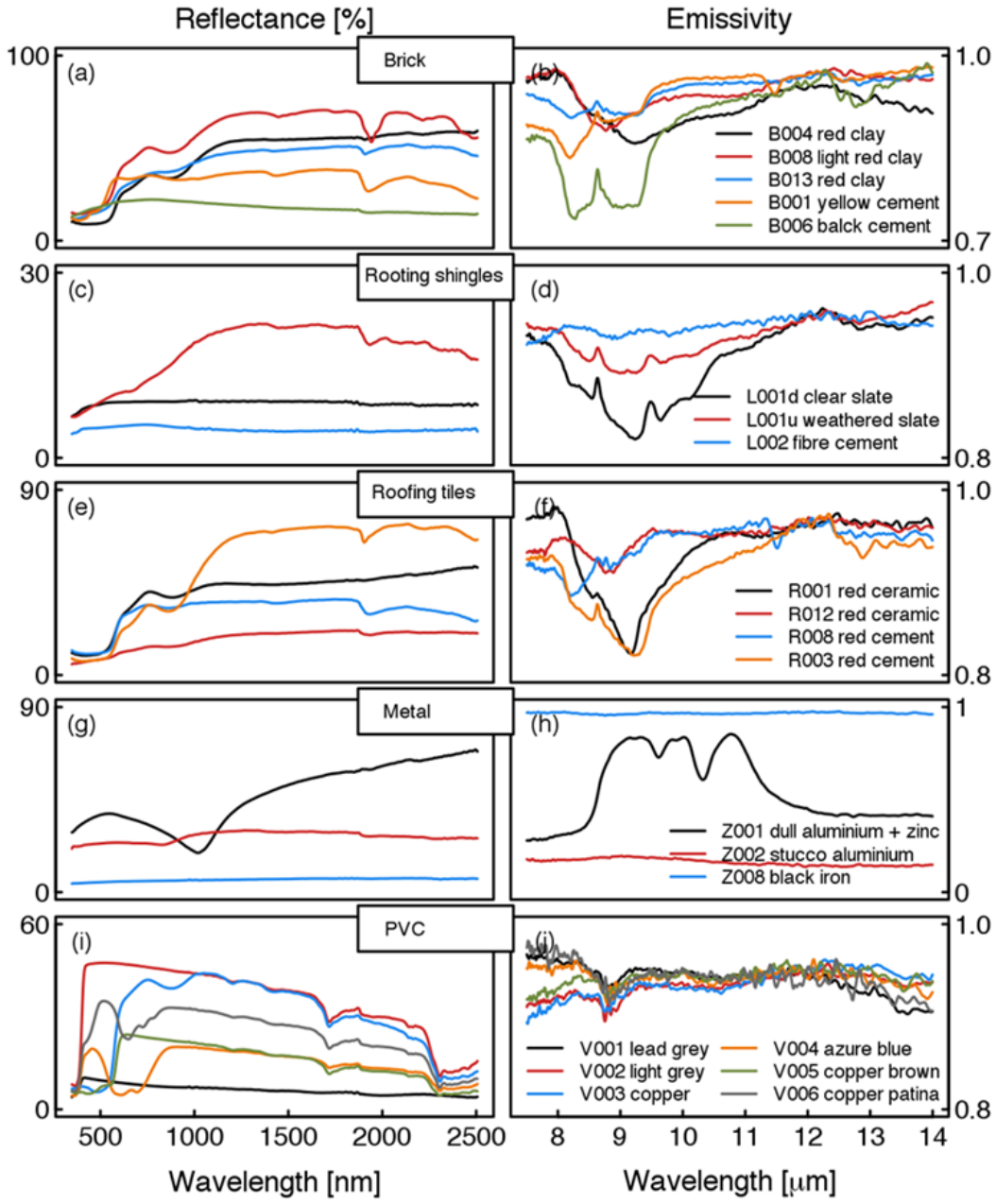

Figure II.10: As for Figure II.9 for additional material classes.

clay brick (B013) is obscured because some cement mortar remains on its surface clearly affect its LWIR emissivity spectrum, introducing the quartz reststrahlen doublet.

II.4.2.1.7 Roofing shingles

The clean slate roofing shingle (L001d) has a constant, low reflectance in the VIS-SWIR (Figure II.10c) with no evident absorption features. This signature is similar to that of the asphalt roofing shingle (Figure II.9g) coated with slate chippings. The fibre cement sample (L002; Figure II.10c) also has a very low, featureless reflectance, despite being weathered. The effect of weathering on the slate shingle is vast. Mostly due to moss, its reflectance is increased considerably (even doubled for some wavelengths) and some O-H absorption is introduced (L001u; Figure II.10c). Spectral emissivity of slate is formed by the spectral response of clay minerals and siliceous minerals. Superimposed over the quartz reststrahlen bands are the absorption characteristics of muscovite at 8.6, 9.4, 9.8, and 10.7 µm (Rodriguez et al. 1999). These features are evident in both slate samples (L001d and L001u; Figure II.10d), albeit with variations in the depths of the absorption troughs. Presumably, the moss on the weathered slate shingle (L001u) increases the emissivity. As in the SWIR region, the black fibre cement shingle is an efficient absorber in the LWIR, with no apparent absorption or reststrahlen bands in their emissivity spectra (L002).

II.4.2.1.8 Roofing tiles

The roofing tile short-wave spectra (Figure II.10e) confirm iron oxide features are often present in the spectral reflectance of both ceramic and cement tiles, supporting the conclusion drawn (Section II.4.2.1.6) that the detection of these chromophores alone is not sufficient to distinguish ceramic materials. The overall reflectance of both materials varies greatly for the different samples of various colours. Generally, weathering appears to increase absorption in the VIS-SWIR for ceramic tiles, e.g. the weathered red ceramic tile (R012) compare to the new red ceramic tile sample (R001; Figure II.10e). The cement roofing tiles observed in the current study are all new materials (e.g. R008; R003), so the effect of weathering in this material class cannot be examined.

The roofing tiles exhibit a similar diversity as bricks (Figure II.10b) in the spectra of LWIR emissivity (Figure II.10f). Again, clay minerals shape the response of ceramics such as the new red ceramic tile (R001) while a combination of silica and carbonate minerals dominates the cement tiles (e.g. R003; R008). The reststrahlen effect of the clay minerals is diminished for the weathered red ceramic tile (R012) so that its overall emissivity is higher than that of the new red ceramic tile (R001) and the emissivity minimum is slightly shifted to shorter wavelengths. Generally, given all roofing tiles are manufactured, composite materials, they tend to have reststrahlen features of various minerals superimposed. For example, the quartz doublet of the red cement shingle (R008) is weakened by carbonate absorption so that the spectrum closely resembles that of the yellow cement brick (B001; Figure II.10b). Even in the emissivity spectrum of the red ceramic tile (R001) a weak silica abruption signature at 8.6 µm can be identified. These combinations of absorbing minerals in the materials' compositions can make it difficult to

find clear criteria for the classification of such materials given spectra within one sub-class can vary as much as between sub-classes. For example, the emissivity spectra of the two red cement tiles (R003; R008) more closely resemble the shape of the new red ceramic tile (R001) and the weathered red ceramic tile (R012), respectively, than one another.

II.4.2.1.9 Metal

Metal samples in the LUMA SLUM include new, weathered and painted samples. Spectra of SWIR reflectance of aluminium usually tend to increase with wavelength after a broad absorption dip at the respective characteristic locations. Of the three examples presented, only the grey/dull aluminium plus zinc sample (Z001) exhibits this characteristic shape (Figure II.10g) while the shiny/stucco aluminium (Z002) is rather featureless in the VIS-SWIR. Similarly, the black iron manhole cover (Z008) has a consistently low reflectance. The diversity of spectral signatures within the metal category is even greater in the LWIR, given materials with both extremely high and low emissivity are included (Figure II.10h). As in the VIS-SWIR, the black iron sample (Z008) does not show any spectral variations. Presumably, the dull aluminium/zinc sample includes some further constituents that generate its particular emissivity signature (Z001). As in the short-wave region, the latter clearly differs from that of the shiny, stucco aluminium (Z002).

II.4.2.1.10 PVC

The SWIR reflectance of PVC samples (Figure II.10i) shows that the dominant hydrocarbon absorption features are manifestly the same for all samples, apart from the slate-grey PVC (V001), which is again characterised by a particularly low reflectance throughout the whole VIS-SWIR region. The different colours of the PVC samples cause great variability in terms of reflectance for visible wavelengths. No LWIR emissivity spectra of PVC materials are available from the reference online libraries listed (:). The spectral emissivity of the PVC roofing materials (Figure II.10j) is somewhat comparable to the signature of a weathered, red ceramic roofing tile (R012; Figure II.10f), with a local absorption minimum at ~8.8 µm. Depending on colour, PVC sheets exhibit an increase or decrease of emissivity at wavelengths shorter than 8.5 µm.

II.4.2.2 Classification of urban materials

The spectral observations provide additional information beyond optical appearance and usage of construction materials (Section II.4.2.1). This allows for the impervious urban materials to be grouped by the constituents dominating the radiative response. Distinct absorption/reststrahlen features were identified in many LWIR spectra observed which allows most impervious materials studied to be grouped by their dominant chemical composition (Figure II.11). Metals, PVC and 'contaminated' materials (e.g. painted) are omitted from this classification due to their diversity and complexity.

In addition to the abundant quartz and feldspar, carbonate minerals are important given that limestone (consisting of calcium carbonate) is an essential ingredient of composite materials such as cement. Also other silicates (phyllosilicates) are frequently found in impervious urban

construction materials (clay minerals: e.g. brick or roofing tiles; mica: e.g. slate roofing tiles). The dominance of these minerals on the radiative response becomes apparent in the comparison of the LWIR spectra (Figure II.11). Emissivity of the material samples analysed can be attributed to the controls of carbonates, phyllosilicates, quartz, or a combination of quartz plus feldspars or quartz plus carbonates. Only a few materials with featureless spectra are presumably governed by hydrocarbons.

In the SWIR reflectance spectra show some similarities within these mineral groups, however,

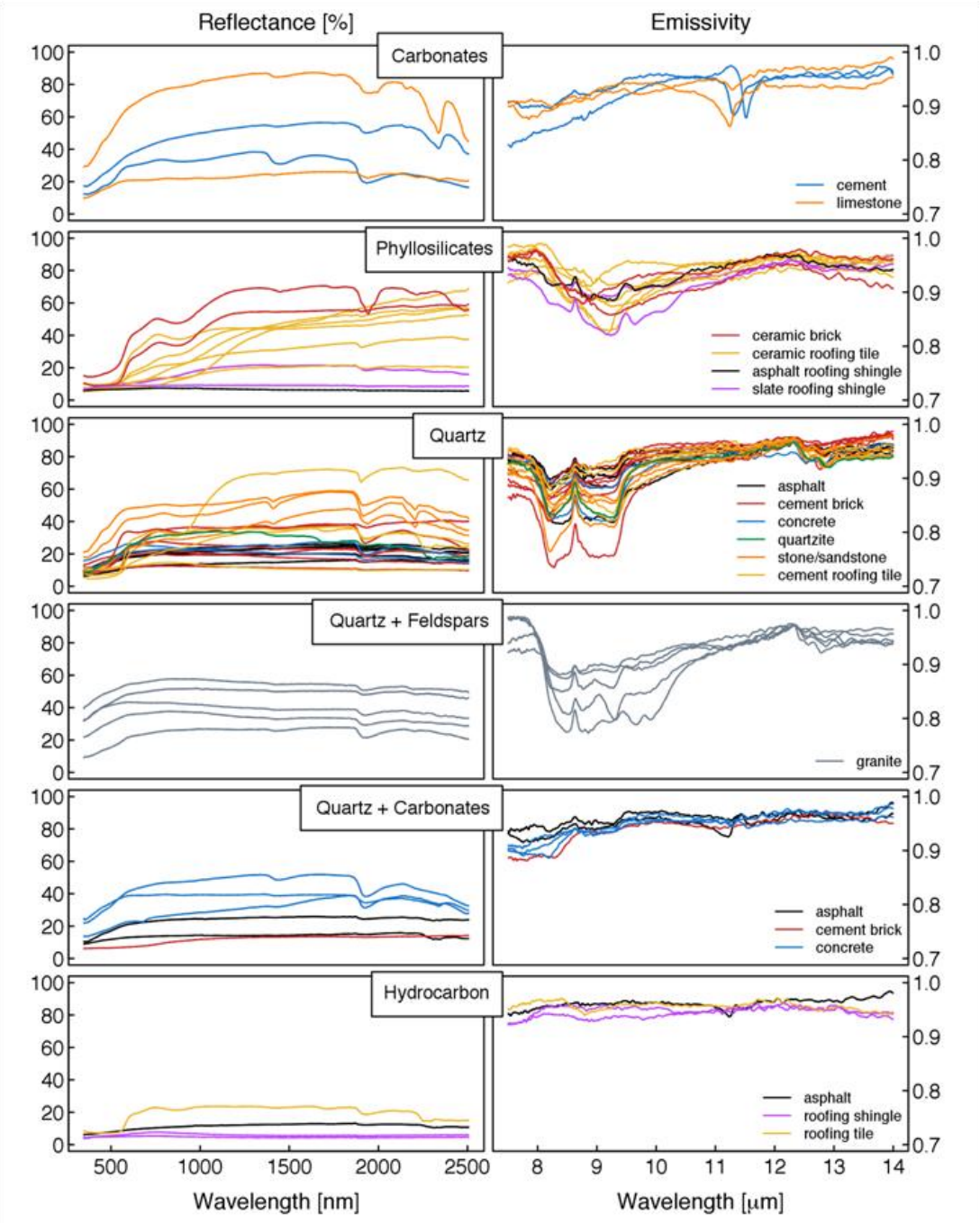

Figure II.11: As for Figure II.9 for impervious urban materials whose long-wave radiative response is dominated by carbonates, clay minerals (phyllosilicates), quartz minerals, quartz plus feldspar, quartz plus carbonate or hydrocarbons.

distinct features are rare (e.g. carbonate) and not always unique to one group (e.g. iron oxide features). This demonstrates clearly the potential of hyperspectral LWIR data for characterising impervious urban surface materials.

II.5 Conclusions

This study presents one of the first spectral libraries of impervious urban materials covering both the VIS-SWIR and the LWIR spectral regions. Data of 74 samples were collected using field-portable spectrometers in controlled laboratory conditions with methodologies mostly applicable also to an outdoor setup. All spectra are combined in the online spectral library of the London Urban Micromet data Archive (LUMA; http://LondonClimate.info/LUMA/SLUM.html).

A detailed framework for the spectral emissivity measurements using a field-portable FTIR spectrometer was developed. It was demonstrated how uncertainties linked to the instrumental setup and radiometric calibration can be assessed using a thermal imaging device and auxiliary observations from independent radiation sources. In order to ensure a suitable signal-to-noise ratio, targets observed under laboratory conditions need to be heated substantially above room temperature immediately prior to the spectral sampling (not necessary outdoors). The methodology and setup were evaluated by measuring a sample of known composition (Ottawa silica sand), revealing that errors from radiometric calibration and system performance have a comparable impact as that which arises from the approach taken to separate the temperature and emissivity signature of the target.

The short-wave response of composite construction materials varies greatly, while long-wave response is more consistent within a single material class. Given that many materials consist of minerals, which often have very distinct reststrahlen and absorption features in the LWIR, hyper-spectral information in this spectral region has great potential for the characterisation of these constituents. The group of metals, found to have the most diverse radiative response in both the short- and long-wave region, is still under-represented in spectral libraries and requires special attention. Due to the development of new materials and coatings the characterisation of the urban surface according to its spectral radiative response can expected to be an on going and dynamic process.

Impervious urban materials are complex because of their diverse compositions. Although a large number of samples have been analysed in the current study, more research is needed to understand the spectral response of the wide range of materials that comprise the urban surface. A comprehensive library covering the VIS-SWIR and the LWIR region for urban building materials could be the foundation for the development of a temperature- emissivity-separation (TES) algorithm applicable for the whole urban surface, including materials (e.g. metals) which pose problems for current TES methods (e.g. the ASTER TES algorithm; Sobrino et al. 2012). This

would significantly advance urban remote sensing, and enhance the usability of thermal airborne or satellite imagery in these vitally important human environments.

Acknowledgements

This study was funded by EUFP7 Grant agreement no. 211345 (BRIDGE) and NERC ClearfLo (NE/H003231/1), EPSRC (EP/I00159X/1, EP/I00159X/2) Materials Innovation Hub and KCL. Supported by NERC FSF (Natural and Environmental Research Council Field Spectroscopy Facility) we thank Alasdair MacArthur and Chris MacLellan for their technical advice on the operation of both the SVC HR-1024 and the MIDAC FTIR. Some of the material samples were kindly provided by Paul Baldwin at ARUP. We thank Jeremy Bourdon and Margot Myers for their help in gathering material samples and Dr Bruce Main, Dr Trevor Blackall, Grace Healy, Oscar Finnemore, John Mustchin and Will Morrison for their assistance when performing the measurements. We thank Simon Hook at NASA JPL for providing the Ottawa sand sample.

Appendix II.A Outdoor short-wave reflectance observations

In addition to the laboratory measurements, short-wave reflectance measurements were performed under outdoor conditions, too. These data are also included in the LUMA spectral library hence the methodology is outlined briefly.

The instrumental setup used for the outdoor measurements is the same as in the laboratory (Section I.3.2), except that, the sun was the source of irradiance instead of artificial light sources. Under clear sky conditions, diffuse radiation supplements the direct beam of sunlight so that irradiance conditions were in-between hemispherical (uniform irradiance from all directions over a hemisphere) and conical (irradiance restricted to a cone). As the incoming radiance travels through the atmosphere before interacting with the target and then the spectrometer, effects of that path need to be considered. Field observations are thus generally restricted to clear sky conditions, when atmospheric effects (absorption or scattering of radiation by water vapour, gases and aerosols) are small. However, even under good weather conditions no useful surface spectral reflectance information can be easily obtained around the water vapour absorption lines (Peixoto and Oort 1992), and thus spectra between 1350–1460 nm and 1790–1960 nm were removed from spectra collected in the field.

As in the lab, targets were sampled ten times. However, a different, random area of the target was moved into the FOV for every sample to better capture the heterogeneity of the materials. The panel was sampled after every fifth measurement to account for the potentially rapid variations in atmospheric conditions and their impact on the down-welling radiance. Other than for the laboratory measurements, the SVC software was set to automatically merge the spectra at the overlap region of the silicon detector array and the first InGaAs detector.

Appendix II.B Classes of impervious urban materials studied

Spectral response of materials grouped into ten classes is discussed in the current study (Section II.4.2.1). Material characteristics and typical absorption/reststrahlen features are outlines here to provide the necessary context.

II.B.1 Quartzite conglomerate

Quartzite conglomerate coatings increase surface traction, and are applied to road surfaces in areas where traffic slow down is intended, such as pedestrian crossings (Paul Baldwin, ARUP personal communication, June 2013). Geologically, quartzite originates from sandstone by heating or compression. The metamorphic rock is usually grey or white in colour, but depending on the minerals (e.g. iron oxide) in the composition it can also be yellow, red or pink. Quartzite is mainly composed of quartz and some feldspar. Both minerals show hardly any absorption features in the visible and near-infrared. However, they exhibit broad reflectance peaks between 8–10 µm (Lyon 1964) caused by Si-O stretching vibrations. For quartz, an absorption peak

divides these reststrahlen bands at 8.6 µm (Salisbury and D'Aria 1992), thus forming a characteristic shape in the emissivity spectrum - the asymmetric quartz doublet. Maximum emissivity is reached at 7.4 and 12.2 µm, again caused by Si-O stretching vibration (Salisbury and D'Aria 1992). Adjacent to the main doublet, a secondary, weaker one is formed between 12.3–13.0 µm.

II.B.2 Stone

Within the stone category are sedimentary rocks - sandstone and limestone. Both are used in crushed form as an ingredient for anthropogenic materials such as concrete, but are also often deployed for the construction of buildings or pavements directly. Limestone, composed mainly of calcium carbonate ($CaCO_3$), shows an absorption peak around 2350 nm caused by carbonate overtone vibrations (Hunt and Salisbury 1971). Carbonate minerals (e.g. dolomite or calcite) exhibit further vibrational absorption bands at 1900 and 2550 nm (Gaffey 1985). In the long-wave region, a reststrahlen band is located at around 11.3 µm (Christensen et al. 2000). As in quartzite, the primary constituents of sandstone are quartz and feldspar. Hence, it is the combination of minerals in the sandstone which give it its colour and are responsible for its spectral response in the SWIR (Bowen et al. 2007).

Iron oxides absorb in the region between 750–1300 nm (Bowen et al. 2007), with hematite giving a clear signature at 870 nm and goethite a broader absorption band around 930 nm (Deaton and Balsam 1991). Clay minerals are usually connected to water absorption features at around 1400 and 1900 nm (Clark 1999). For smectite minerals, the H_2O absorption at 1900 nm is generally stronger than for the kaolin or illite groups. Further, hydroxyl combinations are responsible for absorption at 2200 nm, as a doublet in the case of kaolinite. Illite shows one feature at that band and further causes absorption at 2350 and 2450 nm (Bowen et al. 2007). Clay minerals are phyllosilicates (Deer et al. 1992) and so silica reststrahlen bands dominate the LWIR absorption of sandstone comprising those minerals.

II.B.3 Granite

Granite, one of the most abundant igneous rocks on the Earth's surface, is particularly hard, strong and quite resistant to weathering. Hence it is widely deployed as a construction material. It is used in buildings, roads and pavements, and is often favoured as street curbing material because it outperforms concrete in terms of resilience (Paul Baldwin, ARUP personal communication June 2013). Mainly composed of quartz and feldspar, it is characterised by large grain sizes resulting in a colourful appearance, often as a combination of grey to white and red to pink shadings. In the short-wave region, granite can show H_2O vibration combinations at 1900 nm (Rivard et al. 1992).

II.B.4 Asphalt

Asphalt is the dominant material used for road surfaces in many European cities and worldwide,

and is composed of a binder and some rocky aggregates of variable type and grain size. However, the minerals selected as aggregates vary with geological region and road type. Natural asphalt refers to the variety of natural bitumen (solid or semi-solid mixtures of hydrocarbons) that usually serves as binder in road construction materials (Meyer and de Witt 1990). Although clearly dominated by a complex mixture of hydrogen and carbon constituents, most natural bitumen also contains nitrogen, oxygen, sulphur, and trace metals such as iron, nickel and vanadium (Meyer and de Witt 1990).

Asphalt is a dark coloured material, typically black or grey. Broad absorption of hydrocarbon compounds are responsible for the overall low reflectance in the visible part of the spectrum, with no distinct absorption features due to the complex chemical structure of asphalt (Testa 1995). A decrease in absorption with longer wavelengths is characteristic for hydrocarbons, such as in spectra of coals or oils (Cloutis 1989). In the SWIR region where absorption is generally lower than in the VIS, two absorption features can often be identified: a C-H stretch first overtone band at 1730 nm and a C-H stretch combination band at 2310 nm (Cloutis 1989).

The spectral reflectance of asphalt usually changes with age. It darkens due to tire abrasion and road cracking (Herold 2007), while increased reflectance is observed after contamination with dust and abrasion of the asphaltic binder, the latter excavating larger fractions of the aggregate. Thus, older road surfaces may have mineral absorption features with weakened hydrocarbon signatures or the latter may be intensified from sealed cracks as bitumen patches are usually darker than asphalt itself because of the lack of aggregate.

Tarmac (short for tar-macadam) is a road surface material very close to asphalt. Macadam is the procedure used to combine aggregates with the tar binder, a hydrocarbon processed form of pitch. Other than the natural bitumen and asphalt, however, tar is made from wood or roots and is less close to crude oil. Still, the spectral radiative response of tarmac is similarly dominated by broad C-H absorption and hence included in the asphalt material class here.

II.B.5 Concrete and cement

Concrete, a ductile construction material of high strength, is deployed in a great variety of applications: construction of bridges and buildings (walls, roofs), roads and pavements (often as tiles). Concrete consists of cement with various aggregate materials of different grain sizes added. As aggregate usually makes up a large fraction of the concrete's volume it significantly determines the physical characteristics of the construction material, such as density and porosity. The most basic cement type combines ground clinker (calcium silicates) with a small percentage of gypsum (Mineral Product Association Cement, (MPA Cement 2012)). Additional compounds such as fly ash (containing SiO_2 and CaO), limestone, or blast furnace slag (a combination of CaO, SiO_2, Al_2O_3, and MgO) may be added. The basic clinker is produced from natural minerals: calcium carbonate ($CaCO_3$) is decarbonized into calcium oxide (CaO) which then reacts with silica (SiO_2). Portland cement, one of the most common types, is composed of

dicalcium silicate (Belite, Ca_2SiO_4) and tricalcium silicate (Alite, Ca_3SiO_5), which are responsible for the cements' strengths. Natural resources for calcium carbonate are in limestone, chalk and often other minerals (e.g. from clay and shale).

Brick

Bricks are commonly used in the construction of buildings (especially residential) and pavement in London and elsewhere. The *brick* category includes cuboids of rectangular plan and cross section made of original brick clay, but also those made of cement of various colours. Thus, the spectral features of cement block bricks are similar to the *concrete/cement* category.

Clay minerals evolve from silicate minerals by weathering. Hence, they can show characteristic absorption bands for water and hydroxyl ions. Other constituents of clay minerals include alumina, iron oxides, and carbonates. Absorption features of iron oxide at 520, 670, and 870 nm are clearly evident in VIS-SWIR spectra of new, red clay brick (Hunt 1977; Ben-Dor et al. 2001; Herold et al. 2004). Brick clay is burned during the production process of *ceramic* materials, so that water and hydroxyl absorption features (typically found in spectra of fresh clay) are often diminished in the radiative response or might even be absent (Heiden et al. 2001). In the LWIR, clay minerals exhibit a broad absorption trough between about 8.5–10.5 µm. Absorption bands of common clay minerals include 9.8, 10.7, 12.6, and 14.5 µm (kaolinite), 9.6 µm (montmorillonite), and 9.7 µm (illite), and the wavelength of minimum absorption further varies with clay type (Hunt et al. 1950). Masonry has mortar as a binding material between the bricks/blocks composed of cement and sand, sometimes with lime or plasticizer added.

II.B.6 Roofing shingles and tiles

Shingles and tiles are both common roofing materials. They are distinguished here based on shape, with the shingles generally being "flat" rather than fabricated with a distinct shape (e.g. curved) to enhance prevention of rain entry into the building roof space. Roofing shingles sampled here are either natural slate or artificial fibre cement. Slate is a foliated metamorphic rock originated from shale, mainly composed of quartz and muscovite or illite. Even though slate naturally occurs in different colours, ranging from beige through purple to grey, dark grey or black shingles are installed most commonly. Slate is also applied as flooring (e.g. patios) or wall coverings. Fibre cement shingles are mainly used for roofing, but in some regions also for the cladding of walls. The material is composed of sand, cement and fibre (often cellulose).

Roofing tiles, commonly used for residential buildings in London, either consist of clay-based ceramics (and hence have similar features as clay bricks), or cement/concrete of different colours. As seen for clay bricks, the LWIR response of ceramic materials is characterised by a broad reststrahlen region with an absorption minimum around 9.3 µm, which, however, can shift significantly to longer or shorter wavelengths depending on the particular clay minerals involved. This signature is used here to subdivide the roofing tile category into ceramic tiles, and other roofing tiles – mostly made of cement/concrete.

II.B.7 Metals and PVC

Metals are quite often used as roofing materials (e.g. copper, aluminium), but also have other applications, especially in modern architecture. For example, the outer surfaces of modern skyscrapers are often largely composed of glass and metal. Commonly metals found in urban areas include steel, copper, aluminium and zinc (ZINC 2003), often painted. Paint critically impacts the radiative response signatures, as these are generally determined by the upper 50 µm thick layer of the target (Ben-Dor et al. 2001). Thus, these coatings (Wray and Akbari 2008) significantly alter the reflectance values. A similar effect is seen for the particular finishing (e.g. shiny or dull) used for the metal surfaces. Pure aluminium shows a broad and deep absorption band at 840 nm, while zinc has a similar feature at 1020 nm (Heiden et al. 2007). Absorption features of aluminium minerals (e.g. muscovite) can change their shape and position, depending on the aluminium in the crystal structure (Clark 1999).

New roofing materials include sheets made of polyvinyl chloride (PVC). They can be manufactured in various colours and often are designed to resemble traditional roofing materials (e.g. copper or slate) in their optical appearance. Features dominated by hydrocarbon signatures include deep absorption at 1200, 1700 (caused by C-H stretch vibrations), 2170, and 2300 nm (Heiden et al. 2007; Cloutis 1989). Pure colour pigments also have their effect.

Appendix II.C Integrated broadband albedo and emissivity

The spectral response in the two regions of the electromagnetic spectrum can be integrated to broadband estimates. The latter are used in many modelling applications that commonly do not resolve the details of spectral variations, such as many land surface models. Given these integrated values are often applied in conjunction with broadband radiation estimates, the reflectance and emissivity spectra are weighted by appropriate reference spectra (Section II.3.2) before performing the wavelengths aggregation. It should be noted that the VIS-SWIR reflectance spectra do not represent hemispherical reflectance. Even though two light sources were used to illuminate the sample, which gives a more homogeneous field of irradiance than a single source, the conically observed reflected radiation was measured at a single fixed angle. Given most of the observed materials cannot be assumed to be Lambertian, directional reflectance variations can be expected which are not captured by the data collected here. To completely characterise the BRDF (bi-directional reflectance distribution function) a significantly more complex measurement setup would be required. The absorption signatures discussed (the main focus of this work) are less influenced by these directional variations because their locations correspond to the material's molecular structure. Their depth, however, may be slightly altered when viewed from different angles. Many remotely sensed short-wave reflectance estimates have these directional limitations, so integrated values from such approaches should be used with care. Still, useful information about the overall albedo of the various materials can be gained from bi-directional spectra.

Broadband estimates of short-wave albedo and long-wave emissivity were derived from the laboratory-based observations for all materials sampled (Table II.C.1). Overall, broadband values have less variability in the LWIR ($0.89 > \varepsilon > 0.97$; only some metals with $0.16 < \varepsilon < 0.89$) than in the VIS-SWIR ($0.05 < \alpha < 0.68$). Materials dominated by hydrocarbons or quartz plus carbonates tend to have a higher emissivity compared to the other mineral classes. Quartz and ceramic materials constitute the most diverse groups with respect to their long-wave response. However, such trends are less evident for the short-wave albedo.

Table II.C.1: Meta data for the London impervious urban materials samples, with their measured broadband albedo (300–2500 nm) and emissivity (8–14 μm).

ID	Class/Sub-class	Material	Colour	Status	Dimensions [mm]	Albedo	Emissivity
X001	Quartzite conglomerate	Quartzite	Beige/brown/black/red	New	360x4x220	0.26	0.92
X002	Quartzite conglomerate	Quartzite	Beige/brown/black/red	New	360x4x220	0.32	0.96
X003	Quartzite conglomerate	Quartzite	Brown	New	148x27x97	0.25	0.97
S001	Stone	Sandstone	Beige	Used	215x35x105	0.40	0.90
S002	Stone	Carboniferous coral limestone	Grey	Used	120x19x90	0.20	0.94
S003	Stone	Sandstone	Yellow	Used	120x80x27	0.26	0.93
S004	Stone	Limestone	Beige	Used	70x55x25	0.68	0.93
S005	Stone	Sandstone	Light grey	Dusty, smooth	28x75x180	0.46	0.92
G001	Granite	Granite	White/black	New, rough	142x56x52	0.48	0.92
G002	Granite	Granite with cement	White/red	Weathered	101x95x88	0.34	0.93
G003	Granite	Granite with cement	White/black	Weathered	215x57x105	0.41	0.89
G004	Granite	Granite	White/red/black	Weathered	233x60x78	0.54	0.93
G005	Granite	Granite	Red/black	Smooth	125x50x111	0.22	0.89
A001	Road asphalt	Asphalt with stone aggregate	Black/grey	Weathered	190x83x68	0.21	0.96
A002	Road asphalt	Asphalt with stone aggregate	Black/grey	Weathered	60x100x200	0.18	0.94
A003	Road asphalt	Asphalt with stone aggregate	Black/grey	Weathered	60x90x150	0.21	0.94
A004	Road asphalt	Asphalt with stone aggregate	Black/grey	Weathered	50x120x170	0.18	0.94
A005	Road asphalt	Asphalt with stone aggregate	Black/grey	Weathered	55x75x130	0.19	0.93
A006	Road asphalt	Asphalt with stone aggregate	Black/grey	Weathered	30x145x180	0.12	0.91
A007	Asphalt roofing shingle	Tarmac roofing paper	Grey	New	3x165x170	0.07	0.93
A008	Road asphalt	Tarmac	Black	Weathered	140x25x140	0.13	0.95
A009	Road asphalt	Tarmac	Black	Weathered	21x60x85	0.08	0.95
A010	Road asphalt	Tarmac	Black	Weathered	21x65x80	0.10	0.96
C001	Cement	Cement	Grey/ochre	Weathered	397x60x140	0.29	0.94

C002	Concrete	Concrete	Grey/white	New	198x53x100	0.21	0.92
C003	Cement	Cement	Grey	Weathered	268x44x148	0.23	0.95
C004	Concrete	Concrete	Grey	Weathered	110x72x85	0.37	0.95
C005	Cement	Cement	Grey	Weathered	45x80x115	0.41	0.91
C006	Concrete	Concrete	White	Weathered	90x150x250	0.42	0.95
C008	Concrete	Concrete	Grey	Weathered, rough	20x120x108	0.25	0.95
B001	Cement brick	Cement brick	Yellow	New	200x60x100	0.30	0.94
B002	Cement brick	Cement brick, with sand	Black/light grey	New	200x58x98	0.11	0.94
B003	Cement brick	Cement brick	Black	New	195x52x98	0.09	0.95
B004	Ceramic brick	Brick clay, with cement	Red	Weathered	62x35x52	0.31	0.91
B005	Cement brick	Cement brick	Red	Weathered	138x60x100	0.17	0.94
B006	Cement brick	Cement brick, with sand	Black	Weathered	200x60x100	0.20	0.89
B007	Cement brick	Cement brick	Light red	New	200x60x100	0.22	0.94
B008	Ceramic brick	Brick clay	Light red	New	63x100x212	0.43	0.94
B009	Cement brick	Cement	Red	Weathered, curvy	63x105x110	0.27	0.95
B010	Ceramic brick	Brick clay, painted	Red with beige and grey	Weathered	80x110x100	0.53	0.93
B011	Ceramic brick	Brick clay, with cement	Red/grey	Weathered	63x110x230	0.35	0.95
B012	Ceramic brick	Brick clay, painted	Red with white	Weathered, rough	70x112x107	0.56	0.95
B013	Ceramic brick	Brick clay	Red	Weathered	46x60x100	0.32	0.95
B014	Ceramic brick	Brick clay	Yellow/grey	Weathered, dusty	68x90x130	0.43	0.96
L001u	Roofing shingle	Slate	Black	Weathered	255x3x210	0.09	0.90
L001d	Roofing shingle	Slate	Black	Clear	255x3x210	0.14	0.93
L002	Roofing shingle	Fibre cement	Black	Weathered	232x3x241	0.05	0.94
L003	Roofing shingle	Fibre cement	Black	Weathered	230x207x3	0.06	0.95
R001	Ceramic roofing tile	Ceramic	Red	New	150x11x150	0.31	0.93
R002	Ceramic roofing tile	Ceramic	Brown	New	300x10X200	0.20	0.93

R003	Cement roofing tile	Cement	Rustic red	New	270x12X170	0.32	0.91
R004	Ceramic roofing tile	Ceramic	Burnt red	New	300x13X200	0.24	0.92
R005	Cement roofing tile	Cement	Rustic red with dark shading	New, shiny	260x12x165	0.17	0.96
R006	Cement roofing tile	Cement	Slate grey	New	265x11x165	0.12	0.94
R007	Ceramic roofing tile	Ceramic	Black	New	410x15x320	0.16	0.92
R008	Cement roofing tile	Cement	Rustic red	New, dull	260x12x165	0.26	0.95
R009	Cement roofing tile	Cement	Autumn red	New, rough	260x12x165	0.19	0.92
R010	Ceramic roofing tile	Ceramic	Red	Weathered	10x130x165	0.19	0.95
R012	Ceramic roofing tile	Ceramic	Red	Weathered	12x90x195	0.13	0.95
R013	Ceramic roofing tile	Ceramic	Red	Weathered	12x115x130	0.12	0.95
Z001	Metal	Aluminium plus zinc	Grey, dull	New	390x1x295	0.36	0.58
Z002	Metal	Aluminium, stucco	Grey, shiny	New	380x1x295	0.25	0.16
Z003	Metal painted	Metal with paint	Green	New	1x102x150	0.11	0.93
Z004	Metal painted	Metal with paint	Copper patina	New	1x150x192	0.45	0.94
Z005	Metal painted	Metal with paint	Slate grey	New	1x152x205	0.12	0.94
Z006	Metal	Aluminium	Grey	Weathered	1x220x230	0.26	0.81
Z007	Metal	Lead	Grey	Weathered	254x2x200	0.21	0.86
Z008	Metal	Iron	Black	Weathered	428x5x110	0.05	0.97
V001	PVC	PVC roofing material	Lead grey	New	1x146x204	0.08	0.94
V002	PVC	PVC roofing material	Light grey	New	1x146x204	0.43	0.93
V003	PVC	PVC roofing material	Copper brown	New, structured	1x146x204	0.29	0.94
V004	PVC	PVC roofing material	Azure blue	New	1x146x204	0.14	0.94
V005	PVC	PVC roofing material	Copper brown	New	1x146x204	0.17	0.94
V006	PVC	PVC roofing material	Copper patina	New	1x146x204	0.28	0.94

III Identification of micro-scale anthropogenic CO_2, heat and moisture sources – processing eddy covariance fluxes for a dense urban environment

Abstract

Anthropogenic emissions of heat and exhaust gases play an important role in the atmospheric boundary layer, altering air quality, greenhouse gas concentrations and the transport of heat and moisture at various scales. This is particularly evident in urban areas where emission sources are integrated in the highly heterogeneous urban canopy layer and directly linked to human activities which exhibit significant temporal variability. It is common practice to use eddy covariance observations to estimate turbulent surface fluxes of latent heat, sensible heat and carbon dioxide, which can be attributed to a local scale source area. This study provides a method to assess the influence of micro-scale anthropogenic emissions on heat, moisture and carbon dioxide exchange[2] in a highly urbanized environment for two sites in central London, UK. A new algorithm for the Identification of Micro-scale Anthropogenic Sources (IMAS) is presented, with two aims. Firstly, IMAS filters out the influence of micro-scale emissions and allows for the analysis of the turbulent fluxes representative of the local scale source area. Secondly, it is used to give a first order estimate of anthropogenic heat flux and carbon dioxide flux representative of the building scale. The algorithm is evaluated using directional and temporal analysis. The algorithm is then used at a second site which was not incorporated in its development. The spatial and temporal local scale patterns, as well as micro-scale fluxes, appear physically reasonable and can be incorporated in the analysis of long-term eddy covariance measurements at the sites in central London. In addition to the new IMAS technique, further steps in quality control and quality assurance used for the flux processing are presented. The methods and results have implications for urban flux measurements in dense urbanised settings with significant sources of heat and greenhouse gases.

Kotthaus, S, and CSB Grimmond, 2012: Identification of Micro-scale Anthropogenic CO_2, heat and moisture sources – Processing eddy covariance fluxes for a dense urban environment. Atmos. Environ., 57, 301–316, doi:10.1016/j.atmosenv.2012.04.024.

[2] Amendment of Kotthaus and Grimmond (2012): exchanges between the surface and the atmosphere

III.1 Introduction

In cities emissions of heat, moisture, gases and particulate matter impact atmospheric processes at various scales resulting in distinct urban climates with direct implications for human well-being. The emission of anthropogenic heat, a distinct urban addition to the surface energy balance, increases the energy available for turbulent fluxes. It is highly variable and scale dependent with micro- or local scale emissions far exceeding average values for larger areas as a consequence of urban patterns of land use, traffic and population density. For example, Iamarino et al. (2012) documented the annual mean anthropogenic heat flux (for the years 2005–2008) to be 10.9 W m^{-2} for the Greater London area (1596 km^2), while peak annual mean values in the city centre (estimated on a 200 m x 200 m grid) reach up to 210 W m^{-2}. This spatial variability and scale dependence is also evident for CO_2 fluxes (Mills 2007; Velasco and Roth 2010).

Micrometeorological observations improve our understanding of the links between human activities and the environment but are constrained by site-specific challenges particularly in urban areas (e.g. permissions to install towers and equipment, access to measurement sites, health and safety concerns etc.) to not disturb the functioning of the area yet observe the typical activity. This has implications for the representativeness of the data collected, like the necessity of homogeneous flow conditions. The latter makes it even more complex to find a site suitable for eddy covariance (EC) observations given the highly heterogeneous nature of the urban environment. EC instruments when mounted at the top of a tower of sufficient height to be above the blending height, can yield fluxes that can be interpreted according to their local scale source areas. However, restrictions on construction and planning permissions in dense city centres may not allow for unrestricted extension of the sensor height far enough above the building height. Thus under some conditions anthropogenic emissions may reach the instruments before sufficient turbulent mixing can occur and hence measured turbulent fluxes are affected by short, intense signals in temperature and gas concentrations which are attributed to the micro-scale (see for example the work of Sparks and Toumi (2010), their ‘power plant’ impact, in South Kensington, London). The objective of this paper is to address this issue.

Following detailed data analysis of flux data in central London, we present the IMAS-technique (Identification of Micro-scale Anthropogenic Sources) to identify the effect of micro-scale emissions and sources and to separate them from local scale processes. This allows for the interpretation of the fluxes in terms of both the source area of the flux tower and the impact of micro-scale anthropogenic sources at the building scale. Hence, two audiences could benefit from the analysis: first those concerned with EC analysis as a new approach to deal with the special challenge of strong point sources for EC measurements is discussed; and, secondly, those concerned with the analysis of the impact of anthropogenic emissions on surface heat, water and carbon dioxide exchange.

This study uses long term micrometeorological observations collected in the very dense central London area (Figure III.1a). To date there are only a relatively small number of studies with

annual eddy covariance measurements in urban areas (e.g. Soegaard and Moller-Jensen 2003; Christen and Vogt 2004; Moriwaki and Kanda 2004; Offerle et al. 2006; Coutts et al. 2007; Järvi et al. 2009; Crawford et al. 2011) and very few in dense city centres. While other measurements have been made of carbon dioxide fluxes in London, these have been in a partly residential area south of Hyde Park (Sparks and Toumi 2010) and on top of BT-tower (Helfter et al. 2011) (Figure III.1a). The latter measurements are taken at 190 m a. g. l. which results in a large source area and periods when the surface fluxes and the measurement level are effectively decoupled.

III.2 Methods

III.2.1 Measurement site

The study area is located in the Central Activity Zone of London, UK (Figure III.1a). Observations are carried out on two towers mounted on rooftops at the Strand Campus of King's College London (KCL, 51°30' N, 0°7' W) in the central business district (a High Density UZE, urban zone energy partitioning, Loridan and Grimmond 2012, calculated by Loridan et al. 2013); or based on images, compact midrise LCZ (Local Climate Zone, Stewart and Oke 2012). The area is dominated by impervious surfaces with little vegetation (grass and trees) present (Figure III.1a, close up shown in Figure III.15). In all wind directions, the KCL Strand campus is surrounded by dense urban land cover with large daytime population and large traffic volumes. The only exception is the River Thames to the south. Two measurement sites, located within approximately 60 m of each other, are referred to as *KSS* and *KSK* respectively (Figure III.1b). At both, the instruments are mounted on the top of an extendable tower installed on top of a building; for KSK a single tube mast (Clark Masts CSQ T97/HP) and for KSS a triangular tower (Aluma T45-H). Using the footprint model of Kormann and Meixner (2001), source area climatologies are calculated for both sites and the whole period of analysis (not shown). Based on these areas, mean ground heights of the stations' source areas are 9.5 m (KSK) and 11 m (KSS).Thus measurement heights above ground height are 38.6 m (1.9 x mean building height z_h) and 48.6 m (2.2 x z_h), respectively.

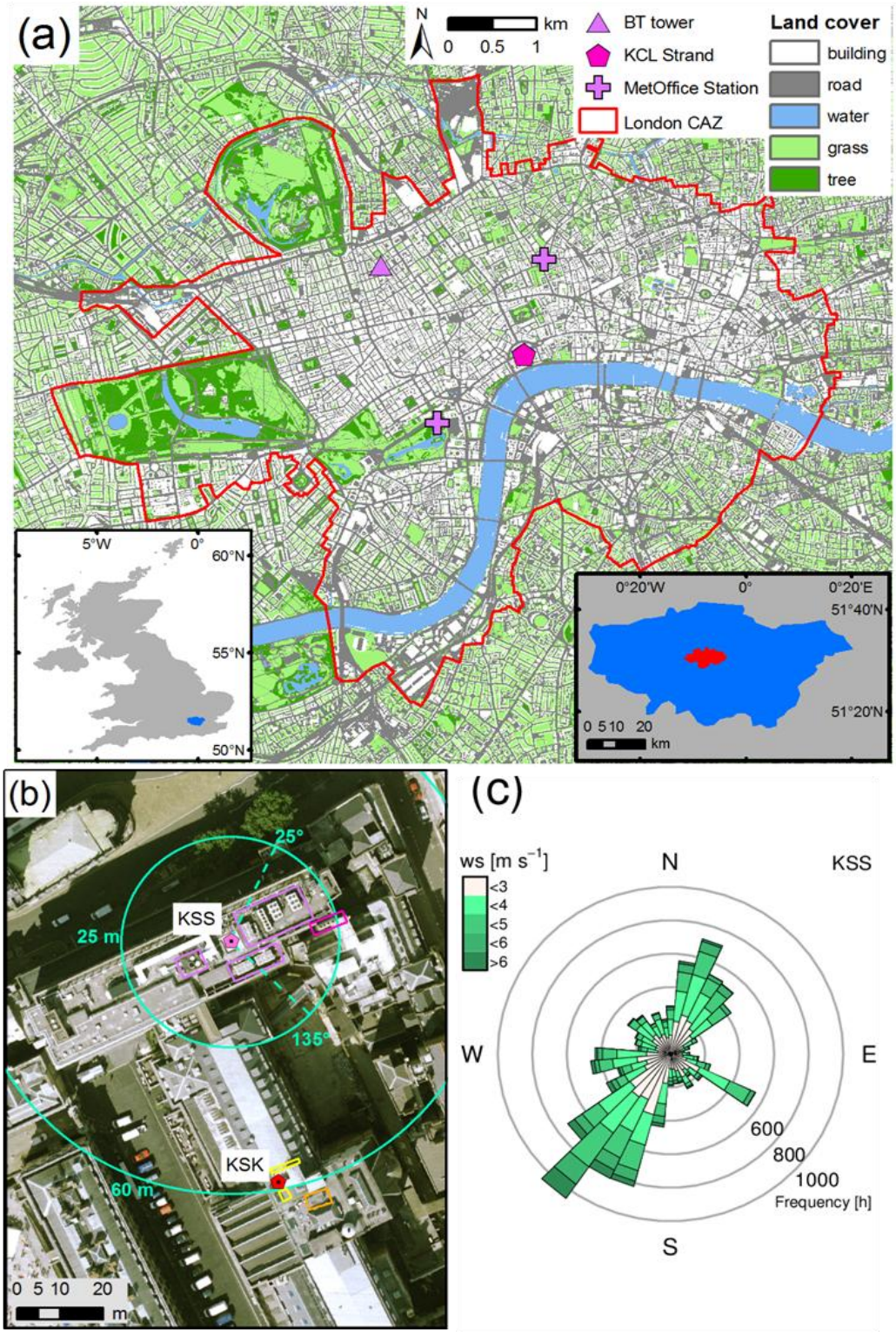

Figure III.1: (a) Land cover map (based on OS MasterMap) of the Central Activity Zone (CAZ) and vicinity of Central London with locations of KCL Strand, Met Office measurement stations and BT Tower. In this study observations from St. James' Park[3] are also used. The location of CAZ within the Greater London area is shown in right inset and this within Great Britain in the left inset. (b) Aerial photo (NERC ARSF 2008) showing locations of KSS and KSK towers. Anthropogenic sources at KSS: smaller ventilation systems and chimney with largest emissions; and KSK: small ventilation systems and ventilation ductwork.
(c) Frequency distribution of wind speed measured at KSS by wind direction, separated into 10° sectors.

[3] Comment on Kotthaus and Grimmond (2012): St. James' Park station: Met Office site west of KCL Strand.

The EC system at KSS is assumed to operate above the blending height; i.e. it should measure atmospheric conditions that can be attributed to surface sources and characteristics aggregated over the local scale source area upwind of the site (Figure III.2). This assumption holds true for many observation periods; however, there are some sources for heat, moisture and CO_2 located in close vicinity of the tower (Figure III.1b) which include several ventilation systems and a larger chimney, most of which are to the east. The amount of gas and heat released from there depends on human activities within the building. These can be expected to be most significant during daytime, the building is mostly empty at night. Depending on their operating time, in combination with wind speed and direction, emissions from these sources can reach the instruments before turbulent mixing can establish sufficient blending with the surrounding air. Given that the emissions are often distinctly different to the background conditions (e.g. very dry and hot) their influence is obvious in the data. Thus in order to be able to interpret the local scale surface fluxes these data need to be filtered out (Section III.2.3.2). At KSK, a few smaller systems are operational (Figure III.1b).

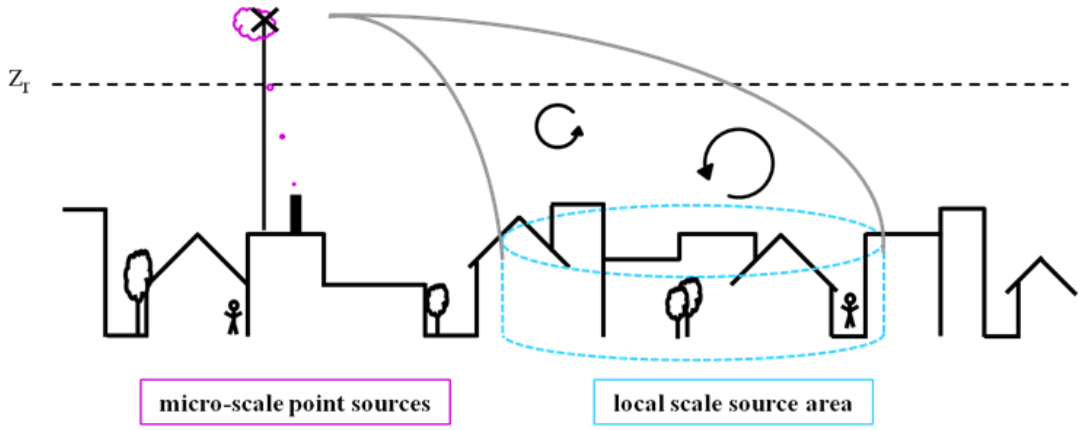

Figure III.2: Schematic of urban canopy indicating local scale source area and micro-scale point source influencing eddy covariance measurements above blending height z_r.

III.2.2 Instrumentation and data collection

In order to study surface turbulent exchange, the EC method is used to measure turbulent fluxes of sensible heat Q_H, latent heat Q_E and carbon dioxide F_{CO2}. The EC-system at both sites consists of a CSAT3 sonic anemometer (Campbell Scientific) and a Li7500 open path infrared gas analyzer (LiCOR Biosciences), both sampling at a frequency of 10 Hz. Sonic anemometers are installed facing towards the predominant wind direction (southwest) relative to the mast in order to minimize flow distortion. Basic meteorological observations, namely air temperature, station (or ambient) pressure, horizontal wind speed and direction as well as relative humidity are obtained by a WXT510 automatic weather station (Vaisala). This instrument is also used to monitor precipitation simultaneously with a tipping bucket rain gauge (ARG100, Campbell Scientific). All instruments except from the WXT510 are connected to a datalogger (Campbell Scientific, both CR3000 and CR5000 models were in use). The KSK flux tower was installed in 2008 and KSS in 2009 (Table III.1). Additional instrumentation on KSS tower includes a vertical

Table III.1: Instrumentation at the two sites (KSK and KSS), by instrument (rows) and operational time period within the years 2008-2011 (specified as day of year). Overall period of operation refers to the total of all available days for each site.

	Instrument	Model	Manufacturer	2008	2009	2010	2011
KSK	Sonic anemometer	CSAT3[4]	Campbell Scientific	274-366	001-280	022-365	001-181
	Infrared gas analyser	Li7500	LiCOR Biosciences	274-366	001-280		
	Weather station	WXT510	Vaisala	274-366	001-365	001-365	001-069
		WXT520	Vaisala				096-181
	Radiometer	CNR1	Kipp&Zonen	274-366	001-280		
		CNR4	Kipp&Zonen			264-365	001-181
KSS	Sonic anemometer	CSAT3	Campbell Scientific		305-365	001-365	001-181
	Infrared gas analyser	Li7500	LiCOR Biosciences		305-365	001-365	001-181
	Weather station	WXT510	Vaisala		286-356	001-365	001-181
	Radiometer	CNR1	Kipp&Zonen		289-356	001-365	001-181

profile with eight levels of fine wire thermocouples (Omega) to measure air temperature and tubing through which air is sucked down to a Li840 closed path gas analyser (LiCOR Biosciences).

Flux calculations are performed based on 30 min block averages. An Ogive test (Moncrieff et al. 2004) was used to determine the appropriate averaging interval for the sites to ensure no significant energy is lost at the low frequency end of the spectrum. Meteorological observations are sampled and recorded with a temporal resolution of 5 s and averaged to 30 min intervals in order to match the temporal resolution of the flux data. All recording and data analysis is done in UTC (Universal Time Coordinated) which corresponds to local time in winter and an hour earlier in summer.

III.2.3 Data processing

For EC processing the software package *ECpack* (van Dijk et al. 2004) is used in conjunction with several pre- and post processing steps performed using scripts written in R (R Development Core Team, 2005). Commonly used corrections (Section III.2.3.3) are applied to the data in order to ensure reliability of the resulting fluxes. The IMAS procedure (Section III.2.3.2) is used to filter out micro-scale effects.

The corrections that require water vapour density [kg m^{-3}] and station pressure [Pa] use WXT510 data. These data are subject to simple quality control (i.e. restricted to a physically reasonable range) and gap filling. Gaps of up to two hours are filled by linear interpolation; larger data gaps are replaced by readings from the alternative site (i.e. KSS filled by KSK and vice versa). In order

[4] Amendment of Kotthaus and Grimmond (2012): Two rows with details on CSAT3 at KSK combined.

to account for siting differences, linear regression relations, based on the day before and after the gap, are applied to the replacement data. Remaining gaps of up to two days are filled via a cubic smoothing spline through the data of the two surrounding days. This preserves the diurnal pattern of the meteorological variables. Rain gauge data are gap filled using the alternative site, or when both sites have no data, the nearest WMO station is used (St. James's Park, 3770, approx. 1.3 km NW of KCL, Figure III.1a).

III.2.3.1 Pre-processing

The pre-processing addresses the possible time lag between the time series of the infra-red gas analyser and sonic anemometer readings. According to Mauder et al. (2007) temporal incongruity can account for CO_2 flux differences of up to 10%. To eliminate this, time series are shifted to ensure maximal cross correlation between H_2O concentration and sonic temperature.

Subsequent quality control detects erroneous values in the recorded raw data. Gas concentrations are excluded from all processing if the Li7500 gas analyzer reports path obstruction of 75% or greater, indicated by the diagnostics value. Similarly, observations from all variables are classified as erroneous if the CSAT3 diagnostic value indicates problems. The observed data are restricted to physically reasonable values defined by the measurement range of the instruments. In some cases extremely high variability of H_2O concentrations within a 30 min window are observed, mostly when conditions are close to saturation. Data points are only used if the standard deviation of H_2O concentration within one 30 min interval does not exceed 20 mmol m^{-3}.

In addition to these general restrictions, single values and short term periods which differ distinctly from the pattern observed during the respective 30 min period are identified. Those 'spikes' are commonly found in EC raw data (e.g. due to irregularities in power supply) but need to be removed because of their high impact on (co-) variance calculations. The de-spiking procedure applied in this study is slightly different from commonly used approaches (e.g. Schmid et al. 2003) which often use statistics to detect suspicious data points. The applied procedure restricts measured quantities within a short time period to a physically reasonable range and is therefore variable specific (Table III.2). For example, if the difference between the maximum sonic temperature and the third highest reading within the same 1 min window is larger than 2°C, the two highest data points are flagged as outliers. The minutes are treated as consecutive blocks of data, as tests with moving windows did not reveal an improved detection procedure. Each minute is filtered several times. During development of this despiking procedure, based on subsets of data of various conditions, the empirical thresholds (Table III.2) were determined with three iterations being found to be sufficient. If rain is recorded in a 30 minute interval, that period as well as the subsequent period are not used.

Table III.2: Spike removal procedure: within a 1 min period the highest (lowest) values are defined as spikes if the absolute difference between the specified ranked value and the maximum (minimum) exceeds the respective threshold. Specifications based on data analysis.

Variable	Ranked value	Difference threshold
T_{sonic}	3rd	2 °C
u-wind and v-wind	3rd	2 m s^{-1}
CO_2	3rd	0.5 mmol m^{-3}
H_2O	5rd	4.0 mmol m^{-3}

III.2.3.2 Identification of Micro-scale Anthropogenic Sources (IMAS)

Here we describe a new technique to identify micro-scale anthropogenic sources (IMAS) in eddy covariance observations from emissions that can be traced back to sources in the vicinity of the flux tower. These are separated from those observations which are believed to be influenced by the blended mixture of sources within the local scale source area. Micro-scale events stand out due to their large magnitude. Given such signals are unlikely to remain after sufficient turbulent mixing, they are described as micro-scale events in this study. Following detailed manual analysis of the high frequency raw-data, four types of events are identified with clear signals in sonic temperature and/or concentrations of CO_2 and H_2O (Table III.3). These are also observed in vertical profile measurements of temperature and gas concentrations up the tower at KSS (Section III.3.3). Type I, characterised by short, large increases in CO_2 and H_2O concentrations, are only occasionally connected to warm anomalies (Figure III.4); whereas the remaining three types are associated with an increase in temperature at all times (Figure III.3). Additionally, Type III and IV are associated with short dry spells and an increase in CO_2 concentration. Type IV differs from the first three as it is more persistent.

While these features are obvious when data are inspected manually, they cannot be flagged easily automatically by common filtering procedures. As they vary in intensity, duration and frequency neither simple threshold criteria can be applied to the whole 30 min period, nor can spectral analysis mark suspicious data points reliably. The IMAS procedure tries to address the diversity of the patterns and is therefore based on a combination of various statistics applied to different time periods. Traditional standard deviation (*std*), median (*med*), and kurtosis (*krt*) are used. Formal skewness statistics were initially included in the procedure but do not provide additional information. Instead a less common measure of skewness is used, the absolute deviation of the midrange (the mean of minimum and maximum) from the median:

$$mrm(x) = \left| med(x) - \left[\frac{\min(x) + \max(x)}{2} \right] \right| \qquad \text{III.1}$$

for dataset x. These four statistical values (*std*, *med*, *krt*, and *mrm*) are calculated on time periods of 1 min length. Additionally, the 30 min median (MED_{30}) is computed from the 1 min medians. All five metrics were calculated for sonic temperature, CO_2 concentration and H_2O concentration.

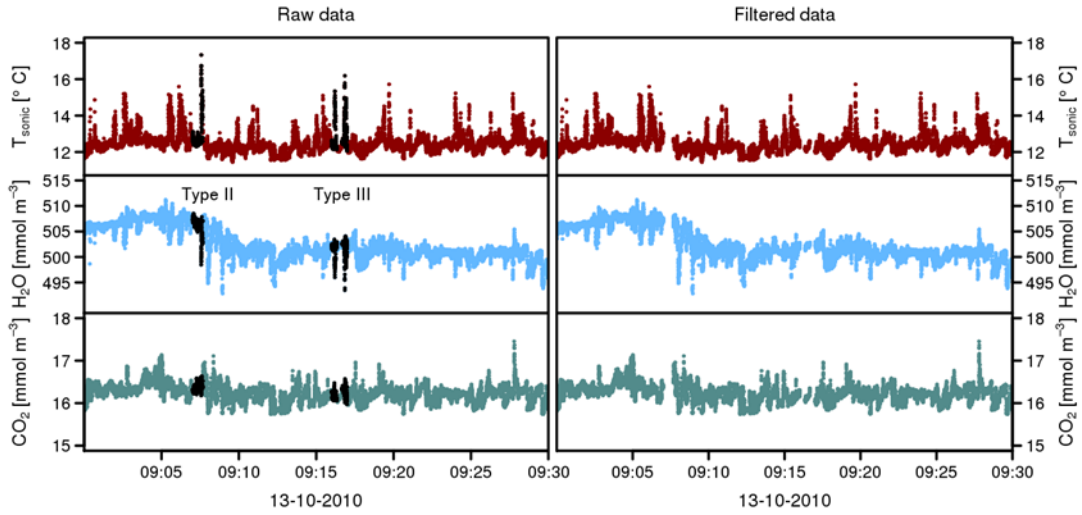

Figure III.3: Example of IMAS Type II and Type III events for a 30 min period on 13th Oct 2010 at KSS recorded in sonic temperature and H_2O and CO_2 concentration. (Left) raw data, (right) data after IMAS filtering.

During the development of IMAS, thresholds were found which allow for the tagging of the different types of events. By process of elimination, the descriptive criteria could be reduced to a smaller list (Table III.3). The duration of IMAS events within a half hour period is one measure for the impact of micro-scale sources on the observations. In order to facilitate analysis and discussion we define the variable γ_E as the '*event frequency*' – namely the percentage of samples flagged by IMAS within each 30 min period. If $\gamma_E > 40\%$, the data are excluded from the analysis of local scale fluxes[5].

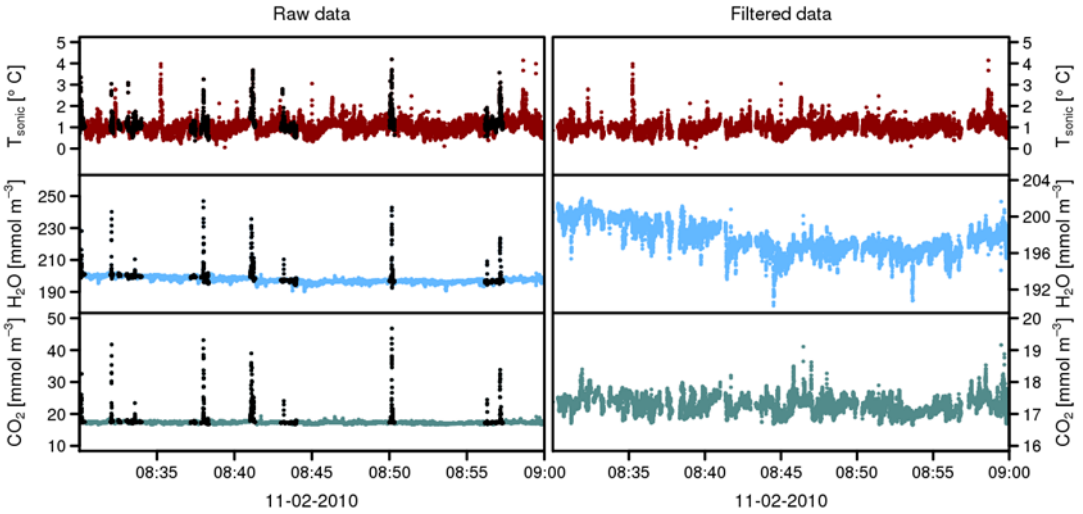

Figure III.4: Example of IMAS Type I event for a 30 min period on 11th Feb 2010 at KSS recorded in sonic temperature and H_2O and CO_2 concentration. (Left) raw data, (right) data after IMAS filtering.

[5] Comment on Kotthaus and Grimmond (2012): The threshold ($\gamma_E > 40\%$) was chosen as a compromise between data availability and quality assurance with the constrained that more than half of the data should represent the local scale flow rather than being effected by micro-scale emissions. This is based on the assumption that intervals within each measurement period are affected randomly and that the turbulent flux described by the remaining > 60% of the 10 Hz data is representative of the whole 30 min interval.

It should be noted that some features in the time series of wind, temperature, moisture and carbon dioxide concentration, here assumed to originate from micro-scale anthropogenic sources in close vicinity of the KSS tower, do have similar characteristics as bursts and sweeps from street canyons (Salmond et al. 2005). In EC measurement time series, these events of pronounced turbulent exchange appear as coherent structures, which can be detected e.g. using wavelet analysis (Christen et al. 2007). The signature of anthropogenic heat, moisture and carbon dioxide emissions from micro-scale sources in EC observations might resemble those typically detected as ejections from street canyons, e.g. a sharp increase of CO_2 concentration in connection with an increase in temperature. However, most events detected by IMAS consist of very high peaks in the respective 10 Hz time series (Figure III.4) which are unlikely to have their origin in turbulent transport from the street canyons. The latter are usually of smaller magnitude (e.g. see night time example in Salmond et al. 2005). Therefore it is assumed that only rarely does the IMAS falsely single out events which are not connected to the nearby building emissions, even though this cannot be ruled out completely.

Table III.3: The general behaviour and definition of the four IMAS types based on sonic temperature and concentration of H_2O and CO_2. Arrows indicate the tendency of related variables. Statistics applied to 1 min intervals are median (*med*), standard deviation (*std*), kurtosis (*krt*) and absolute deviation of mid-range from median (*mrm*). The median of the 1 min medians is computed for a 30 min window (MED_{30}). To be defined as an IMAS event of a specific type all criteria must be met.

IMAS	T_S [°C]	H_2O [mmol m^{-3}]	CO_2 [mmol m^{-3}]
(a)	Classification		
Type I	(↑)	↑	↑
Type II	↑	–	–
Type III	↑	↓	↑
Type IV	↑	↓	↑
(b)	Definition		
Type I	–	–	*mrm* > 0.7 & *krt* > 0.3
Type II	(*mrm* > 1 & *krt* > 3) or (*std* > 1 & *krt* > 7)	–	–
Type III	*krt* > 1	*mrm* < - 0.5	–
Type IV	(*std* > 0.9 & *krt* > 1) or $MED_{30(med)}$ > 1	*mrm* < - 0.1	*mrm* > 5

III.2.3.3 Flux processing with ECpack

The ECpack software includes planar fit coordinate transformation (Wilczak et al. 2001; Lee et al. 2004). Here a 24 h window is used, followed by an additional yaw rotation (Kaimal and Finnigan 1994). This supplementary rotation does not affect the calculation of turbulent fluxes but presents wind speed results aligned to the mean wind field. The sonic temperature is corrected for humidity effects (Schotanus et al. 1983). Gas concentrations are corrected for density fluctuations (Webb et al. 1980). Spectral corrections are based on Moore (1986).

III.2.3.4 Post-processing

The In the post-processing, a combination of daily statistics and Li7500 diagnostics are used to exclude erroneous turbulent fluxes and friction velocity (u_*). Gaseous fluxes of CO_2 or H_2O are regarded as unrealistic if the discrepancy between the 30 min value and the daily average is larger than three times the daily standard deviation and path obstruction is reported by the gas analyser for at least 1% of the 30 min period. Less rigorous criteria are chosen for values calculated solely from sonic observations. Sensible heat fluxes and friction velocities with large deviation from the daily average are only discarded for times with a path obstruction for at least 90% of the period.

In the final quality control stage, the outliers are removed from the time series of the fluxes of sensible heat, latent heat and carbon dioxide. The Hubert and Van der Veeken (2008) method based on the principle of 'adjusted outlyingness' (Hubert and Vandervieren 2008) is used. It enables robust outlier detection in skewed data of unknown distribution. The detection method applies adjusted boxplot statistics, where whiskers (w_1 and w_2) are defined as the most extreme values which fall in the range between $q_{25} - 1.5 \cdot e^{-4MC} \cdot IQR$ and $q_{75} + 1.5 \cdot e^{3MC} \cdot IQR$ (Hubert and Vandervieren 2008), with the first and third quartile q_{25} and q_{75}, respectively, the inter-quartile range IQR, and the med-couple MC (Brys et al. 2004). The latter is a robust skewness measure which relates data to the sample median med. 'Adjusted outlyingness' is calculated as $(x_i - med)/(w_2 - med)$ for all samples $x_i > med$ and $(x_i - med)/(w_1 - med)$ for all samples $x_i < med$. It provides an estimate of how far each sample deviates from the median, taking into account the skewness of the distribution. All samples which exceed the cutoff value defined as $q_{75} + 1.5 \cdot e^{3MC} \cdot IQR$, calculated for the adjusted outlyingness, are classified as outliers and are not used for data analysis. As strong seasonal variations occur in all three turbulent fluxes, outlier detection is performed separately by month of year (i.e. data are grouped by month to calculate statistics – with all data measured in a month (e.g. January, regardless of the year) form the basis of one run of outlier detection). This time period was chosen as a compromise between climatologically consistent conditions and sufficient variability of values (obviously synoptic conditions may differ for the same month in different years or even within an individual month). Based on this, cutoff values were determined which are not too conservative (this could potentially eliminate abnormal but appropriate observations) but still manage to automatically restrict the results to a physically reasonable range.

III.2.4 Data availability

Data analysis and interpretation requires knowledge about data quality and quantity (Goulden et al. 1996; Foken et al. 2004). For the current study, the percentage of reliable observations for the respective operational periods (895 days for KSK and 607 days for KSS, Table III.1) ranges from 81.8% for Q_E at KSS to 90.2% for u* at KSK (Figure III.5); i.e. it is generally quite high. Maintenance and quality control of EC observations often lead to much larger data gaps of typically 20–60% of the observation period (Moffat et al. 2007). For the operational periods

(Table III.1), the overall capture rates are 97.4% and 98.7% for KSK and KSS, respectively. Time periods which fail one or more of the steps of the QAQC procedure (Section III.2.3.3) reduce the database available for final analysis and interpretation. These are six different types of QAQC conditions, namely

a) Diagnostics: instrument diagnostics reporting errors
b) Precipitation: precipitation during or just before measurement period
c) Limits: physically reasonable thresholds applied to raw data, including restriction for standard deviation
d) IMAS: percentage of IMAS larger than 40%
e) Statistics: criteria combining diagnostics and daily statistics
f) Outliers: detection based on adjusted outlyingness

In general, criteria based on precipitation and instrument diagnostics result in the largest fraction of excluded data. The highest percentage of poor quality data are found for the latent heat flux, especially at KSS. This is mainly due to the restriction on standard deviation of H_2O concentrations (Section III.2.3.1). High IMAS frequency occurs more often at the KSS site (1.7% for Q_H) compared to KSK (0.07% for Q_H). The new filtering technique preserves high data availability for final analysis which could not be maintained otherwise.

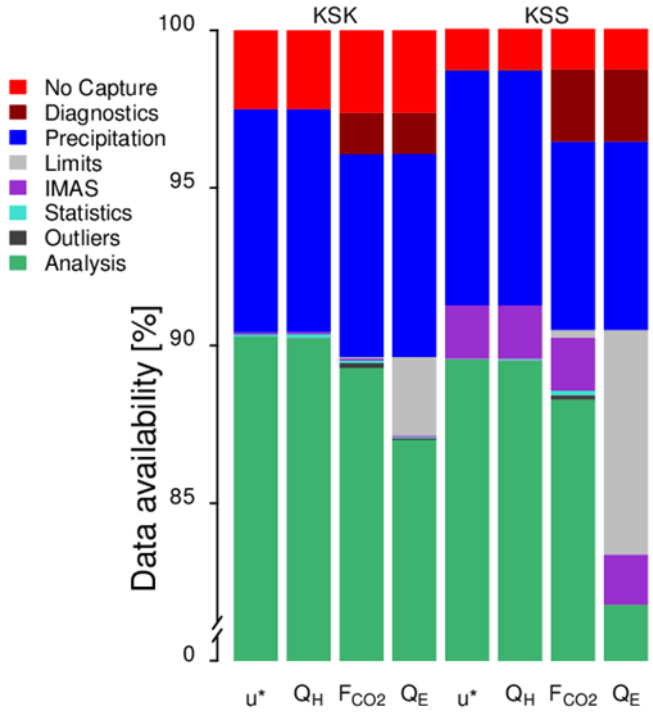

Figure III.5: Overall data availability by variable for KSK and KSS (see Table III.1 for respective period of operation) with impact of six steps in quality control (see text).

III.3 Results

III.3.1 Impact of IMAS filter on turbulent surface fluxes and friction velocity

Turbulent fluxes for KSK and KSS are calculated for all available periods using the processing approach outlined in Section III.2.3. The IMAS filtered data are defined as level 2 (L2) data. In order to investigate the impact of micro-scale anthropogenic emissions on the heat fluxes and the flux of carbon dioxide at the two sites, the calculations are also performed without applying the IMAS filter (termed L1). The variables are impacted differently by the IMAS filter (Figure III.6). While latent heat flux and friction velocity only have a very slight decrease, the fluxes of sensible heat and carbon dioxide are reduced considerably. The L2 sensible heat fluxes are systematically smaller than L1 with no apparent sub-sets in the scatter. This can be explained by the fact that positive temperature anomalies are related to at least three of the four IMAS types (Table III.3). Wind components on the other hand are altered in a complex manner during IMAS events and are not included in the definition of the different types. They are filtered based on the IMAS

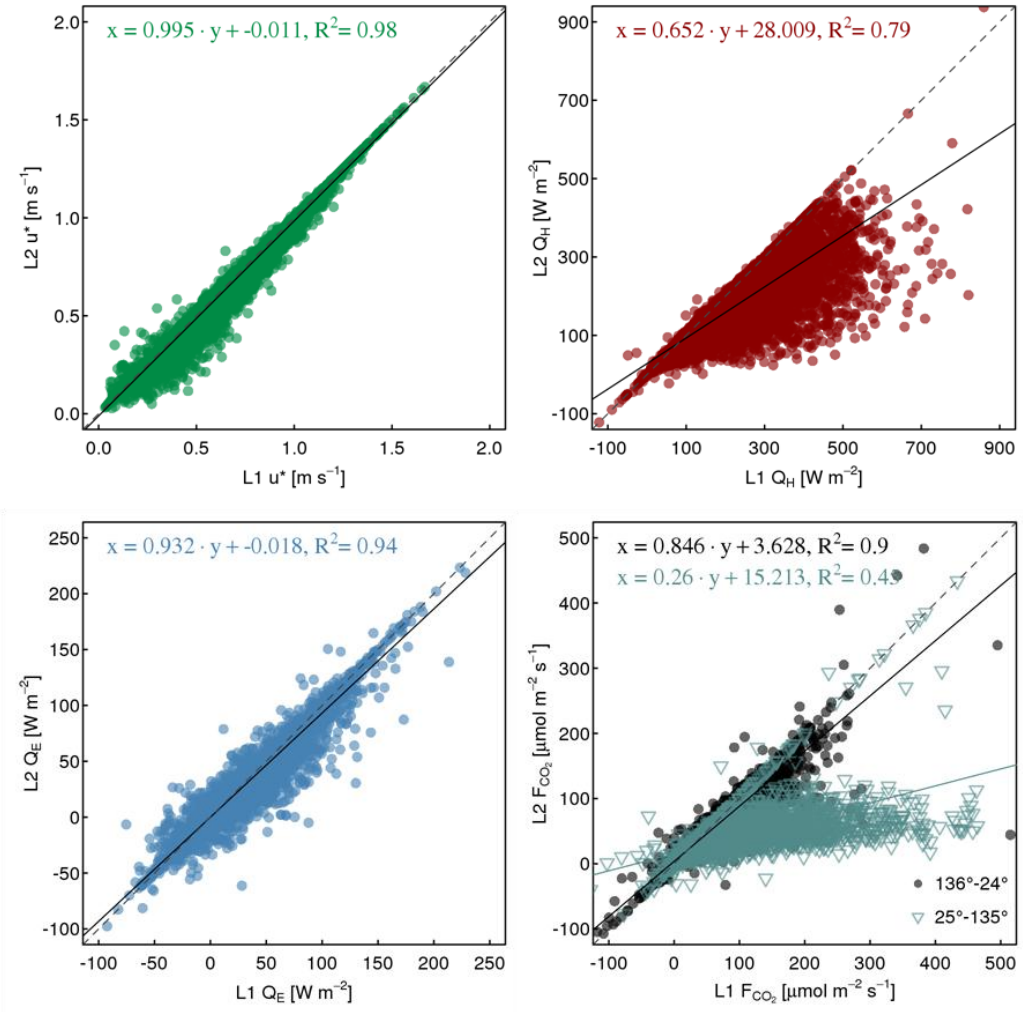

Figure III.6: Comparison of L1 and L2 results for friction velocity, sensible heat flux, latent heat flux, and CO_2 flux at KSS (01/09/2009–30/06/2011). The CO_2 flux is divided into two sub-sets defined by wind direction. Dashed 1:1 line, solid line is the linear regression between two variables given by the equations.

criteria in order to remove any micro-scale effects. As a result, L2 friction velocity is smaller when compared to L1 values in most cases, but IMAS can also lead to a slight increase for some periods. Similarly, IMAS can be connected to an increase or decrease in the latent heat flux, which is again linked to the observed micro-scale emissions. Water vapour concentration has the largest difference between the micro-scale anthropogenic source types, i.e. increase for IMAS Type I, no indication for Type II, and decrease in Type III and Type IV. Hence, the impact can be in both directions. Comparing L1 and L2, F_{CO2} values are more complex; some values are slightly increased but most have a large decrease driven by the role of CO_2 concentration in the definition of IMAS types (Table III.3). It appears that two sub groups could be identified in the F_{CO2} comparison. This is further discussed based on directional analysis (Section III.3.2).

Given the large amount of data (current analysis for KSS is for 607 days), frequency distributions of L1 and L2 results are compared to illustrate the impact of the IMAS filter (Figure III.7). While the general shape of the distributions are retained, IMAS reduces median (Med) and inter-

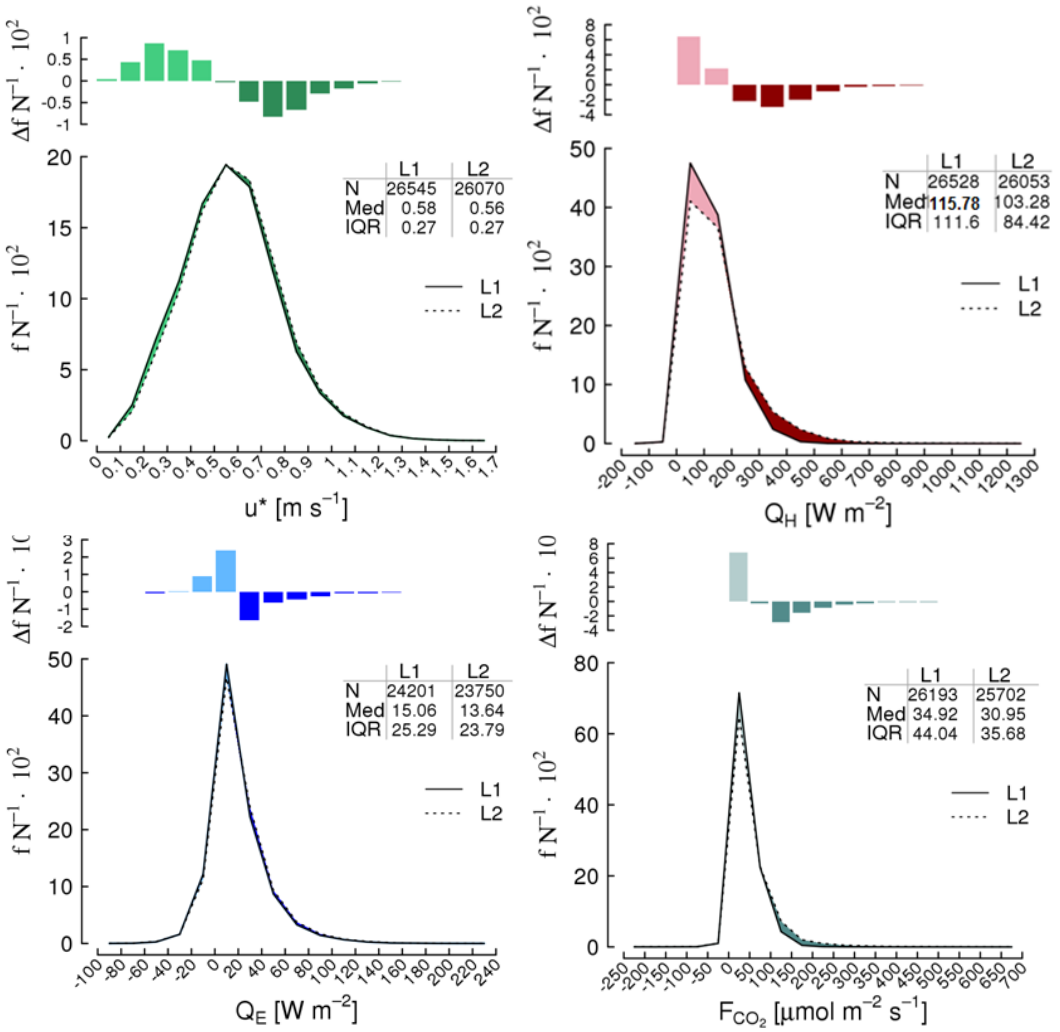

Figure III.7: Frequency distribution (frequency f for each interval relative to total number of samples N, multiplied by 10^2) of friction velocity u*, sensible heat flux Q_H, latent heat flux Q_E and carbon dioxide flux F_{CO2} at KSS (01/11/2009–30/06/2011). L1 (dotted line, common processing) and L2 (solid line, incl. IMAS filter). The L1-L2 differences are shown as (upper) bars and (lower) shading. Tables: number of 30 min periods available (N), median (Med) and inter-quartile range (IQR) for the two distributions.

quartile range (IQR) of the turbulent fluxes. Most pronounced is the diminished variability for sensible heat flux; with the IQR of the L2 data only 76.6%[6] of the L1 value. For the carbon dioxide flux there is 20.1%[6] reduction in IQR, whereas for the latent heat flux and friction velocity variability is less affected. The L2 overall data ranges for sensible heat and carbon dioxide flux are markedly reduced from the L1 estimates. However, the distributions are shown with the same bins to allow for a direct comparison. The difference between the two distributions (barplots in Figure III.7) shows the decrease in the number of very high values in favour of smaller ones for all variables. However, the distributions of friction velocity and latent heat flux have a very small shift with a decrease in median of 2.5%[6] and 9.9%[6], respectively. The F_{CO2} difference is not particularly evident in the absolute frequency distributions because of the large range of L1 carbon dioxide flux data (907.0 µmol m^{-2} s^{-1}). The barplot showing the difference between the two F_{CO2} frequency distributions though reveals that about 7.8% more 30 min periods fall into the interval 0–50 µmol m^{-2} s^{-1} for L2 data, while the intervals with higher turbulent fluxes occur less frequently. Frequency differences for F_{CO2} are of the same order of magnitude as those for the turbulent flux of sensible heat.

III.3.2 Directional analysis

The relative location of the sources which influence the observations at KSS at the micro-scale (Figure III.1b) suggests that the impact of these emissions should be highest under easterly flow conditions. Several small sources as well as a larger chimney are located on that side of the measurement tower. In the western and especially northern direction of the tower, the micro-scale influence should be less discernible. Directional analysis of extreme values of CO_2 fluxes (L1, no IMAS filter applied) confirms this (Figure III.8a). Three percentiles (99th, 95th and 90th) based on wind direction bins of 10° are used to illustrate the variability. It is evident that the higher end of the distribution is formed mainly by periods with an approach flow from the sector between 25° and 115°. These extreme F_{CO2} values most likely originate from the micro-scale sources which are located within the sector between 25° and 135° where most of the sources for building emissions at KSS are found (Figure III.1b).

Congruence with the described directional pattern is found in the event frequency, which quantifies the relative duration of the micro-scale influence. To highlight the IMAS impact, only time periods with an event frequency of ≥2% are used to estimate the frequency distribution of γ_E by wind direction (Figure III.8b). The frequency distribution is normalized by wind direction frequency in 10° intervals for event frequencies ≥2%. This shows clearly that the sector between 15–125° is strongly affected. When the flow comes from these directions, more than 60% of the data have considerable event frequencies. Further, it is evident that larger event frequencies (shaded areas in Figure III.8b are less frequent if the wind comes from north-westerly directions where the least impact of micro-scale anthropogenic sources is expected because of the fewer sources in the vicinity of the KSS EC tower (Figure III.1b).

[6] Percentages stated in Kotthaus and Grimmond (2012) are slightly incorrect. Corrections:
$IQR(Q_H)$ L2 ≈ 75.6% L1; $IQR(F_{CO2})$ L1-L2 ≈ 18.9%; $med(u^*)$ L1-L2 ≈ 3.4%; $med(Q_E)$ L1-L2 ≈ 9.4%

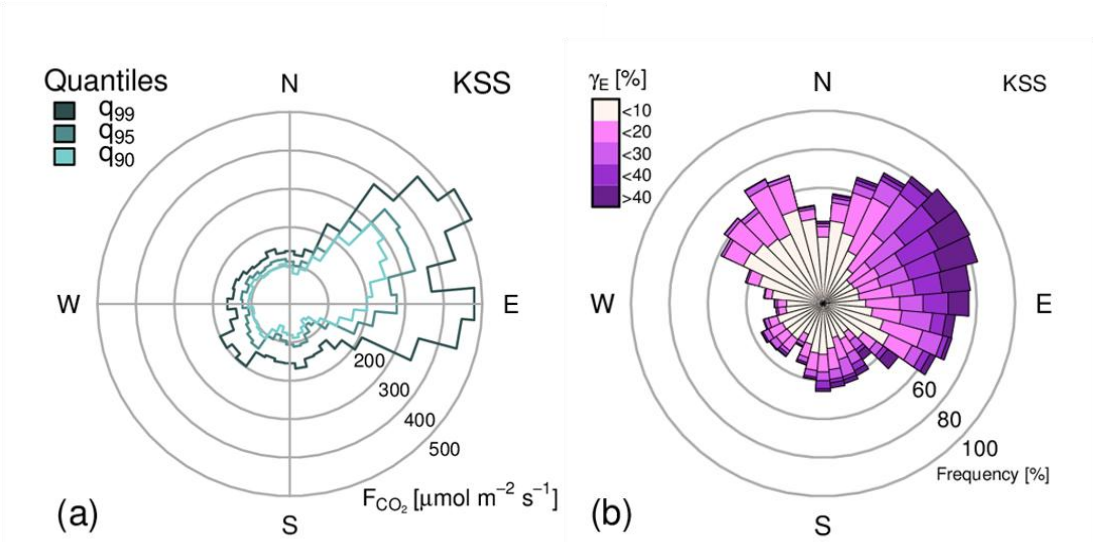

Figure III.8: Statistics by wind direction (10° intervals) at KSS (01/11/2009 - 30/06/2011): (a) quantiles of carbon dioxide flux and (b) frequency distribution of IMAS event frequency $\gamma_E \geq 2$, normalized by frequency distribution of wind direction.

The high probability of micro-scale influence from easterly wind directions further demonstrates the need for this new filtering technique as the micro-scale anthropogenic impact is swamping the local scale flux and is disproportionate to the local scale footprint. Without the IMAS filter, all the affected periods would need to be excluded from the analysis, e.g. for Q_H at KSS 53% of the L2 data have an event frequency between 1% and 40% and therefore should not be used for local scale interpretations without the IMAS filter. Even though the predominant wind direction does not coincide with the predominant IMAS sector, this would introduce gaps into the long-term database so that observations from the highly urbanised surrounding would be lost.

III.3.3 Further evidence for the Applicability of IMAS

Stationarity of atmospheric conditions is a necessary requirement for the application of the EC technique, hence quality control usually involves some form of steady state testing (Foken et al. 2004). In the current study, requirements for stationarity of turbulence are not included. However, the impact is found to be negligible because only a very small percentage (u*: 0.11%, Q_H: 0.01%, Q_E: 0.63%, F_{CO2}: 0.18%) of the L2 data from KSS do not fulfil the steady state criteria of Foken and Wichura (1996). Even L1 data are similarly low (u*: 0.11%, Q_H: 0.02%, Q_E: 0.64%, F_{CO2}: 0.17%). Hardly any of the periods with an IMAS event frequency $\gamma_E > 40\%$ are flagged by steady state criteria. This comparison reveals that the commonly applied steady state test is not an appropriate method to deal with the impact of strong micro-scale anthropogenic sources at KSS.

The development of the IMAS procedure (Section III.2.3.2) is solely based on observations at KSS. In order to investigate the effect of the processing approach on independent data, it was used likewise to calculate turbulent surface fluxes at KSK. At this site, fewer sources for anthropogenic building emissions exist (Figure III.1b). They consist of a small ventilation unit immediately south of the tower, one to the north and a larger exhaust ventilation ductwork to the southeast. The latter was installed on the roof of the building in September 2009 (i.e. after the aerial photo in Figure III.1b was taken). IMAS detects events from micro-scale anthropogenic sources based on observations of temperature, humidity and carbon dioxide concentrations so that the event frequency determined solely using sonic data is usually smaller compared to calculations which incorporate observations from the infrared gas analyser. Given the different operational periods of the Li7500 at the two sites (Table III.1), a comparison of event frequency between KSS and KSK between January 2010 and June 2011 is biased. However, subsequent to the analysis period a Li7500A (LiCOR Biosciences) was installed on top of KSK tower so that data for two month within the heating period (Nov and Dec 2011) are available to demonstrate the effect of IMAS at an independent site. Cumulative frequency distributions of the event frequency γ_E (defined in Section III.2.3.2) estimated in intervals of 2% are compared for KSK and KSS (Figure III.9a). Both sites show a comparable occurrence of smaller events and an overall similar shape of the cumulative frequency distribution. Larger events, however, are slightly more likely at KSS where 6% of the data show an even fraction of at least 20%, compared to 1% at KSK. This could be explained by site-specific differences of anthropogenic emissions. At KSS, there are more and larger sources (Figure III.1b). As found for the KSS directional analysis (Section III.3.2), the distribution of KSK IMAS event frequency (Figure III.9b) coincides with the locations of the nearby building emission sources (Figure III.1b). For KSK, micro-scale emissions are found to be associated with a broad south easterly wind sector (105–185°) and a more narrow north-west

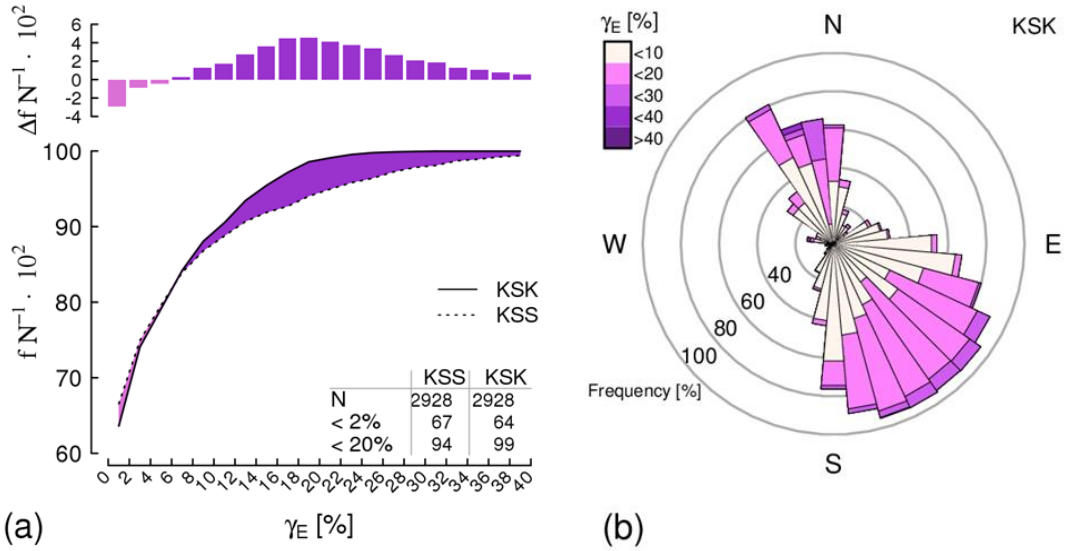

Figure III.9: (a) Cumulative frequency distribution (frequency f for each interval relative to total number of samples N, multiplied by 10^2) of IMAS event frequency (γ_E) at KSK and KSS (01/11/1011 – 31/12/2011). (upper) Differences between the two distributions KSK - KSS. Table inset in (a): number of 30 min periods available (N) by site and amount of data [%] with event frequency lower than 2% and 20%. Distributions shown for periods when event frequency is less than 40% (others are excluded from L2 data for all analyses). (b) Statistics by wind direction (10° intervals) at KSK (22/08/2011 – 31/12/2011): Frequency distribution of IMAS event frequency $\gamma_E \geq 2$, normalized by frequency distribution of wind direction.

sector (325–5°). This agreement shows that the IMAS filter, developed using observations from KSS can be used at an independent site to detect micro-scale emissions in close vicinity of the sensors.

Further evidence for the presence of micro-scale anthropogenic sources and the ability of IMAS to identify their emissions is found in measurements of CO_2 concentration and air temperature in a vertical profile along the flux tower at KSS. These observations taken at different heights between the roof top and the top of the tower reflect a response in accordance with the L1 fluxes from the EC system at KSS. The mean and standard deviation (sdT_{air}) of the air temperature is measured by fine wire thermocouples, recorded at 10 min intervals. As the latter provides a measure of air temperature variability, they reflect the increased range of conditions induced by the emissions of warm air in close vicinity of the profile. Based on an example day (13/10/2010), it is demonstrated how distinctly micro-scale scale heat emissions show up in the vertical temperature profile (Figure III.10). Data from one of the eight measurement heights are not available for this case study day. On the Wednesday 13th October 2010, a rapid increase in sensible heat flux [L1] of 601.6 W m^{-2} is observed at KSS (Figure III.10c) within only one hour (11:30 to 12:30 UTC) while wind direction changes from 30.2° to 37.8°. This peak is followed by a decrease of flux intensity. A comparable pattern is evident in the air temperature measured at all heights along the profile, apart from the lowest one (Figure III.10d) and the corresponding standard deviations of air temperature (Figure III.10e). Especially the standard deviations, but also the mean temperature at some heights, suggest prolonged micro-scale emissions throughout the day until 21:10 UTC. Air temperature values at heights in the middle of the tower seem to be most affected (means at 38.8, 40.6, 41.4 m and standard deviation at 38.8, 41.4, 43.9 m). As can be seen from the time series of IMAS event frequency γ_E (Figure III.10a), the automatic identification procedure picks up micro-scale events especially during those times with increased temperature variability (Figure III.10e). Consequently, these patterns coincide with a period of pronounced difference between L1 and L2 sensible heat flux estimates at KSS (Figure III.10b, c) which supports the applicability of IMAS.

III.3.4 Quantification of micro-scale anthropogenic impact

Anthropogenic heat flux has been determined by top-down, bottom-up and energy balance closure techniques (Sailor 2011). Top-down analysis of energy consumption (Hamilton et al. 2009) has been used at various scales (Iamarino et al. 2011) by accounting for stationary sources Q_{Fb} (mainly buildings), vehicles Q_{Fv} and metabolism Q_{Fm} (Grimmond 1992): $Q_F = Q_{Fb} + Q_{Fv} + Q_{Fm}$. Building energy balance models (Kikegawa et al. 2003) allow a bottom up estimate from the scale of the building but ignores traffic and metabolism contributions which are typically much smaller (Allen et al. 2011; Iamarino et al. 2012; Sailor 2011). The third approach uses micrometeorological observations of surface energy balance fluxes to allocate the residual to the anthropogenic heat flux (Offerle et al. 2005a; Pigeon et al. 2007). This provides local scale

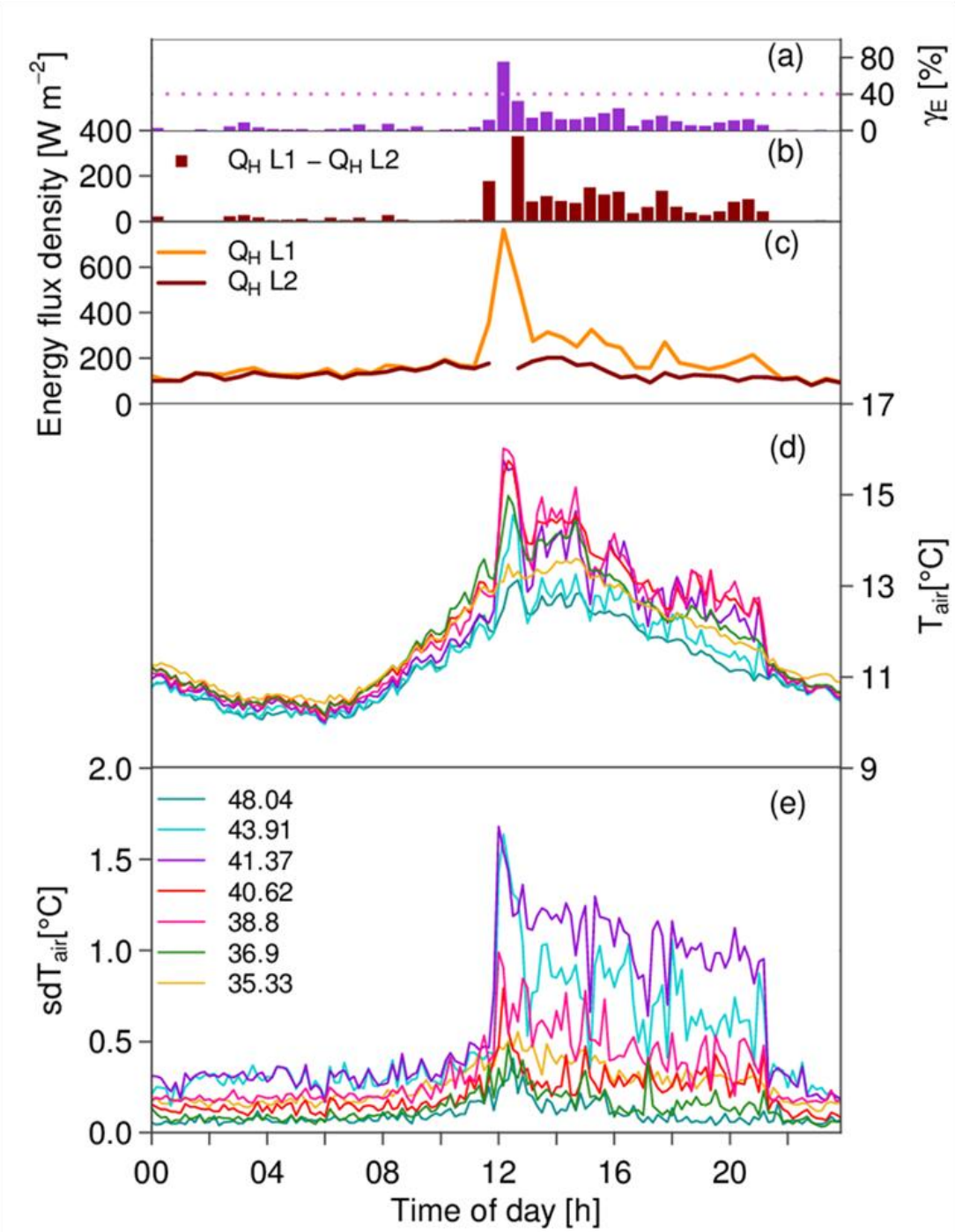

Figure III.10: Example of IMAS impact at KSS (13/10/2010): (a) event frequency γ_E [%], periods which exceed the threshold of 40% are excluded from L2 data; (b) difference between L1 and L2 estimates of turbulent sensible heat flux; (c) L1 and L2 data turbulent sensible heat flux; (d) air temperature and (e) standard deviation of air temperature (10 min) observed by vertical temperature profile up the tower at seven heights [m a. g. l.].

information linked to measurement source areas but does not distinguish between the three categories of anthropogenic emissions.

Here, a fourth approach is proposed to quantify anthropogenic fluxes of sensible heat, latent heat and carbon dioxide at the building scale (Q_{Fb}) based on the IMAS procedure for processing of

eddy covariance fluxes. In order to obtain a first order estimate of the impact of the micro-scale emissions on the flux results, the following assumptions are made:

a) The IMAS procedure can be used to reliably distinguish between extreme micro-scale events and the background local scale turbulence.
b) Duration, frequency and amplitude of the micro-scale events, as observed by the EC-system in a 30 min period, describe the anthropogenic heat flux on the building scale.
c) Even though the IMAS filter introduces gaps into the local scale database (L2), no significant information is lost.

As the IMAS filter mainly identifies extreme events with flow conditions aligned with source locations at both sites (Sections III.3.2 and III.3.3), we accept assumption (a). Micro-scale events at KSS are linked to activities in a big office building (e.g. water use or heating) and their timing and intensity is highly variable. Moreover, they are only recognised by the EC-system if wind direction and speed allow these emissions to reach the instruments on the tower. Taking all these considerations into account, it is obvious that duration, frequency and amplitude of the observed micro-scale events can vary even within a half hour period. Some periods are only affected for a short time and fluxes initiated by the micro-scale sources are only captured partially. However, this can lead to an over- or under-estimation of the micro-scale events and hence it can be assumed that on average IMAS flagged observations can be interpreted as the flux induced by the closely located micro-scale emissions; i.e. it is feasible to accept (b). Inherent in (b) is another assumption – the impact of micro-scale anthropogenic sources is attributed to turbulent surface fluxes disregarding the possibility that vertical convection or mechanically introduced acceleration could be the initiating cause of transport rather than turbulent mixing. Free or forced convection from the chillers and chimney could induce an updraft which could violate the assumption of a negligible mean vertical velocity, inherent in EC theory. This would most likely be the case in low wind speed conditions which would allow emissions to rise mainly due to the convection induced by the sources themselves. However, a certain horizontal velocity is required to transport the emissions from the sources over to the tower. Considerable IMAS events are mostly observed when the horizontal wind velocity is strong enough to diminish the convection solely forced by the sources themselves.

Considering the timing of human activities within the building and the variability of flow characteristics (Section III.3.2), the effect on local scale observations is unlikely to be systematic therefore masking specific frequencies. Given the large dataset available for analysis it is therefore reasonable to assume that no significant local scale information is concealed by the strong micro-scale events. Assumptions (a) – (c) enable the quantification of the impact seen from the micro-scale events which, in the case of Q_H and Q_E, can further be interpreted as the micro-scale anthropogenic heat flux representing a part of Q_{Fb}.

The difference between L2 and L1 values could provide an estimate of the amount of energy and carbon dioxide that could be attributed to anthropogenic activities at the micro-scale. The

average IMAS impact is calculated simply as the difference between L1 and L2 results. Obviously micro-scale anthropogenic heat and carbon dioxide fluxes are blended into the local scale but the near-field micro-scale influences are effectively eliminated by computing the difference between L1 and L2 results. The overall L1 flux represents local scale as well as micro-scale sources, which can, similar to a top-down approach, be separated into contributions of both scales using the IMAS filter. While the resulting L2 flux is believed to represent the fluxes originating from the local scale source area, the difference L1-L2 only captures the micro-scale flux under certain atmospheric conditions.

The IMAS impact shows distinct patterns when distributed by wind direction and time of day (Figure III.11). Most influence is found during daytime. The sensible heat flux experiences a peak of micro-scale influences between 0800 UTC and 1600 UTC. During this period average L1 values for Q_H are found to exceed L2 values by more than 80 W m^{-2} on occasions. Absolute differences are naturally much lower for the flux of latent heat (range < 8 W m^{-2}) but again for this variable a clear maximum is found during the daytime. These estimates fit in the range of anthropogenic heat fluxes in London found by energy consumption modelling approaches, which show that Q_F can reach up to 150 W m^{-2} (when fluxes from buildings are analysed on a 1 km^2 grid, Hamilton et al. 2009) or even 210 W m^{-2} (when calculating average Q_F on a 0.4 km^2 grid; Iamarino et al. 2012). For the 200 x 200 m grid cell which coincides with the location of KSS, the model of Iamarino et al. (2012) estimates an average anthropogenic heat flux from buildings Q_{Fb} of 99 W m^{-2} (2005–2008) with hourly values ranging from 27 W m^{-2} (minimum night time value) to 270 W m^{-2} (daytime maximum). The maximum difference in F_{CO2} is 519.6 µmol m^{-2} s^{-1}, observed at a wind direction of 106.6°. Compared to the other fluxes, the impact on the flux of carbon dioxide is more concentrated in terms of wind direction. However, the heat fluxes also have a clear directional dependence in terms of IMAS impact, which coincides with the location of the anthropogenic sources[7] (Figure III.1b).

A more detailed view of the temporal and directional variability in IMAS results is evident when separating the IMAS event frequency by time of day, month and wind sector (Figure III.12). As already discussed, the event frequency is highest for the easterly wind sectors and during the daytime. Furthermore, it is confirmed that the filter identifies more data during November to April (the heating period). The detailed illustration reveals that micro-scale events during the period from May to October are more frequent in morning hours, while their influence is spread over the whole day and for some sectors even into the night for winter and spring. This can be related to seasonal differences in building and water heating demands. As heat and carbon dioxide are emitted by a university building, less activity is expected in July and August when fewer students and staff are present.

[7] Comment on Kotthaus and Grimmond (2012): The directional patterns of the IMAS determined flux (L1-L2, Figure III.11) differ for the three turbulent fluxes observed (Q_H, Q_E and F_{CO2}) because different types of emission sources are located in the vicinity of the site (Figure III.1b). The main source (chimney), emitting heat moisture and CO_2 is found in the northeast while additional ventilation shafts are contribute mainly to sensible (and some latent) heat emissions in the southeast.

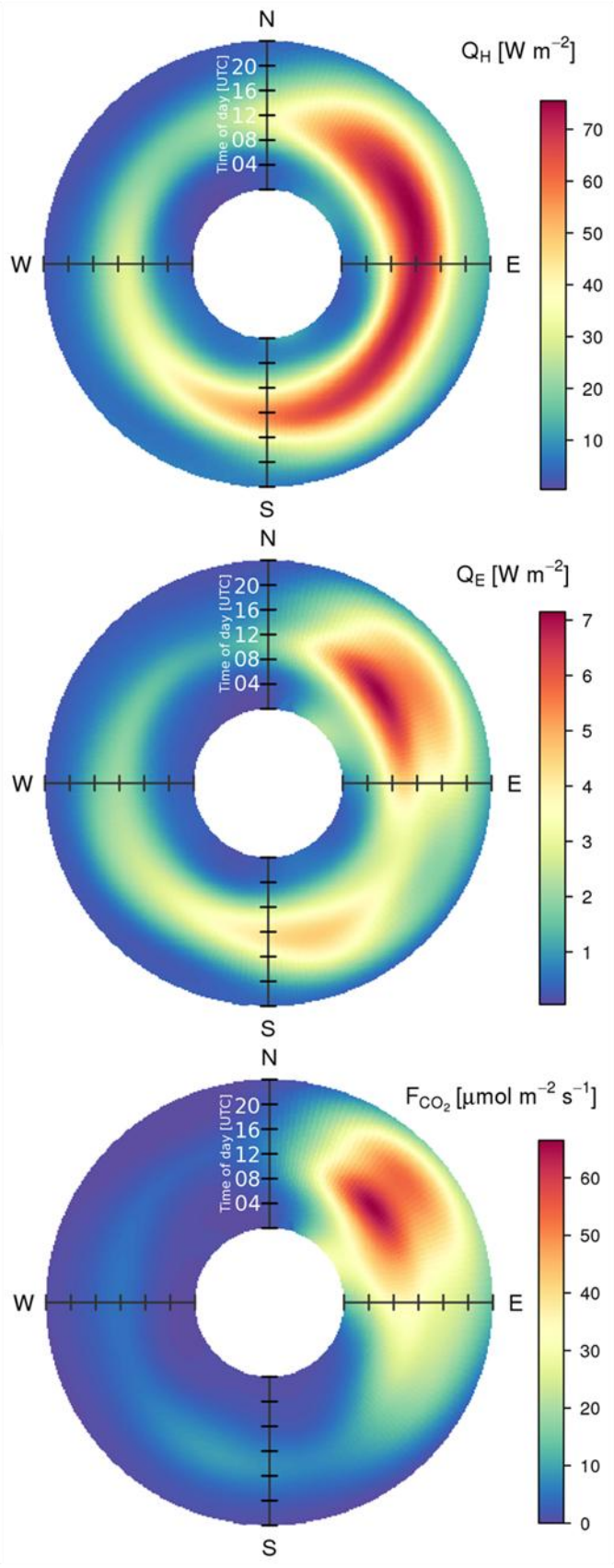

Figure III.11: Average size of IMAS determined flux (L1-L2) at KSS (01/11/2009–30/06/2011): turbulent sensible heat flux Q_H, latent heat flux Q_E and flux of carbon dioxide F_{CO2} by wind direction and time of day.

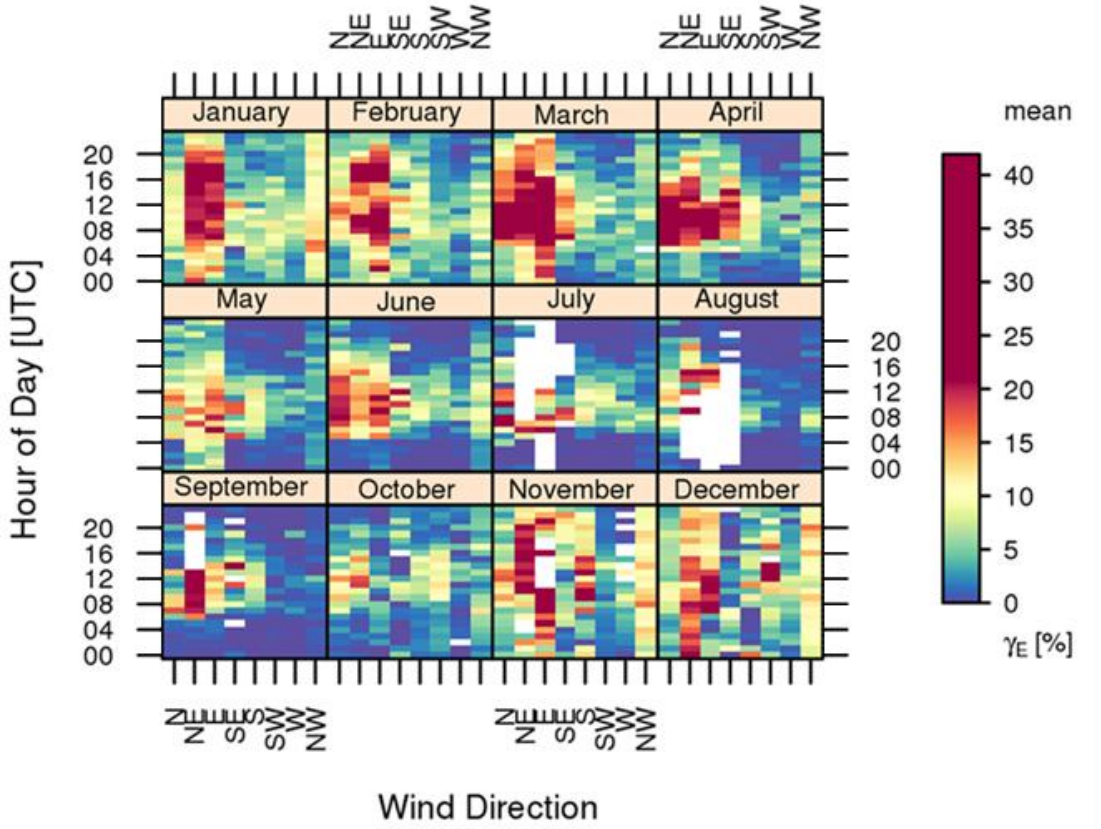

Figure III.12: Average event frequency at KSS by hour of day, month and wind direction sector (01/11/2009–30/06/2011), (number of periods in each cell can differ). White cells represent times when no data are available for the specific wind sector and time.

III.3.5 Case studies

In order to show the response of turbulent fluxes on micro-scale anthropogenic sources at the KSS site, two case study periods are presented (Figure III.13, Figure III.14). Eleven days in summer/autumn (27/08/2010–06/09/2010) give an example of the impact on sensible heat flux while a week in winter time (12/02/2011–18/02/2011) reveals the influence on the flux of carbon dioxide.

Two measures of IMAS impact at KSS, namely the event frequency (Figure III.13a) and the difference between sensible heat flux L1 and L2 values (Figure III.13b) are shown along with the actual observations of turbulent sensible heat flux (Figure III.13c). The Q_H time series of both L1 and L2 data are presented for KSS and KSK together with the flux of net all-wave radiation flux Q*. The sensible heat flux at both sites and both levels is mostly positive representing an upwards transport of heat from the urban canopy into the atmosphere. As the sites are located in a high density urban area, it is reasonable to assume that strong storage heat flux maintains the energy release during times of negative net all-wave radiation.

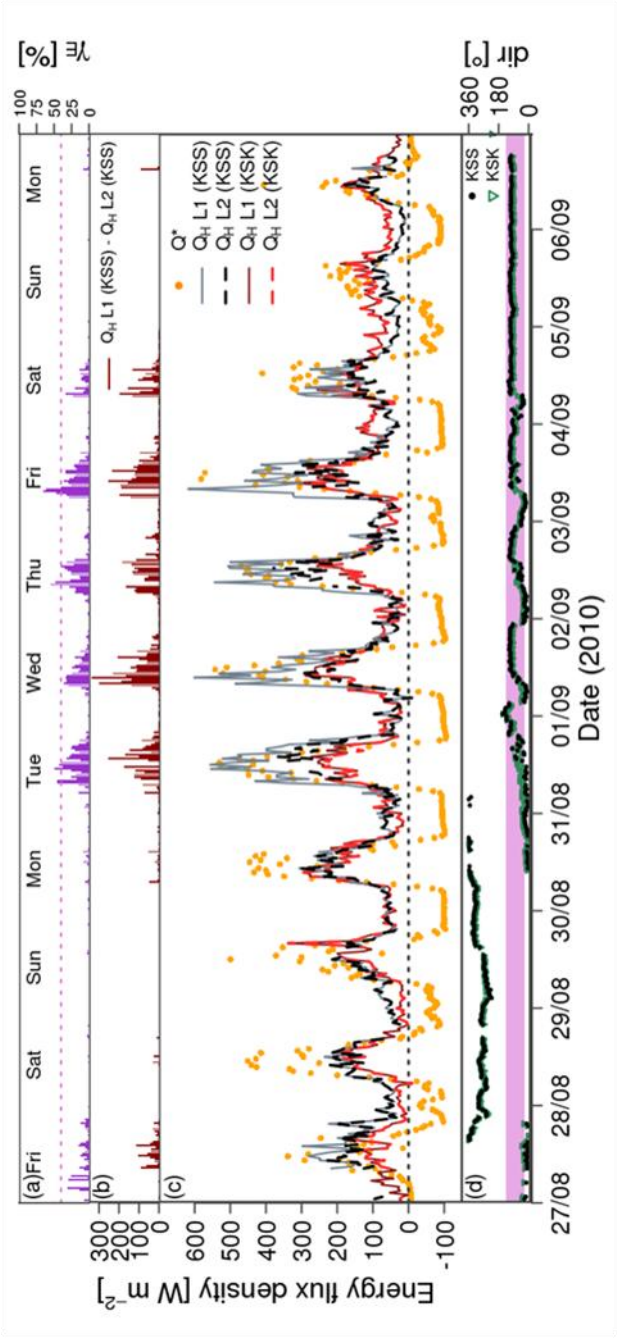

Figure III.13: Case study of IMAS impact for a summer/autumn period (27/08/2010–06/09/2010): a) event frequency γ_E [%] at KSS, periods which exceed the threshold of 40% are excluded from L2 data; b) difference between L1 and L2 estimates of turbulent sensible heat flux at KSS; c) L1 and L2 data turbulent sensible heat flux at KSS and KSK and net-all wave radiation at KSS; d) wind direction at KSS and KSK, the shading marks the easterly wind sector where most micro-scale anthropogenic sources are located (25–135 °).

While the turbulent sensible flux for both processing levels at KSK is quite similar during the whole period, L1 fluxes at KSS have distinctly higher values than those of L2 in the morning of the 27th August and during daytime from 31st August until 4th September. During these periods KSS L2 sensible heat flux is closer to the fluxes observed at KSK than to L1 KSS values – the latter being in the same order of magnitude as net all-wave radiation. On some occasions Q_H [L1] at KSS exceeds the radiative flux; especially during morning hours it seems likely that intense anthropogenic heat emissions supply energy to the turbulent flux of sensible heat at KSS. From 31/08/2010–04/09/2010 a strong increase around 07:00UTC (08:00 British Summer time) of Q_H [L1] at KSS is evident, that is too large to be associated solely with radiation. A comparison of

average values for morning hours (07:00–08:30UTC) quantifies this different behaviour. While Q* is slightly higher than Q_H [L1] at KSS for 28th–30th August and 5th – 6th September, the morning average Q_H [L1] at KSS exceeds the net radiative flux by up to 236% (on 03/09/2011 average morning Q_H = 434.3 W m^{-2} and Q* = 129.1 W m^{-2}). The energy required for such strong turbulent sensible heat fluxes in the morning is likely associated with human activities. However, the very high magnitudes of the turbulent heat fluxes are too extreme to be well-blended local scale anthropogenic heat fluxes.

As discussed (Section III.3.2), most micro-scale anthropogenic sources at KSS are located in the sector east of the tower (Figure III.1b). The time series of wind direction measured at KSS and KSK (Figure III.13d) reveals that the flow comes roughly from this wind sector (25–135°, indicated by shading in Figure III.13d) during all periods with high IMAS event frequency (Figure III.13a). This gives additional evidence that anthropogenic heat sources analysed in the current case study are likely to be supplied by micro-scale emissions in close vicinity to the observation site rather than sources in the local scale footprint area. In order to substantiate this reasoning, the cumulative source area for the case study period is sub-divided by wind direction, i.e. wind directions within the affected sector (25–135°) vs. remaining (Figure III.15a). In both cases roads make up the highest surface fractions in the local scale source area, followed by buildings. However, it is indicative that with 37% road and 35% building both percentages are lower for the easterly wind sector than for the remaining times (50% road, 45% building). As both buildings and roads are major sources for sensible heat in urban areas, it would suggest that these surface fractions would explain the sensible heat flux should be higher for the remaining flow conditions (Figure III.15a). As their footprint includes busy roads and intersections with high traffic volumes, it can be concluded that the high sensible heat flux estimates under easterly flow conditions cannot be associated with surface characteristics of the local scale source area.

Both measures of IMAS impact (Figure III.13a, b) pick up micro-scale events leading to high sensible heat flux values of L1 KSS data. Their diurnal variation during the affected days confirms particularly strong events in the morning, both in terms of duration (Figure III.13a, high event frequency in morning on 31/08, 02/09, and 03/09) and intensity (Figure III.13b, high L1-L2 difference on 01/09). As L2 variables are only used up to an event frequency of 40%, the persistent events on the 31st of August and 2nd and 3rd of September cause missing values in the Q_H difference between L1 and L2. These days which suggest remarkable influence of micro-scale anthropogenic heat sources are weekdays, apart from Saturday 4th September which shows lower L1-L2 differences (Figure III.13b) and shorter events (Figure III.13a) compared to Tuesday – Friday of the same week. The probability that the EC system at KSS detects IMAS events depends on wind direction of the approach flow and on human activities in the building, which determine timing and strengths of anthropogenic emissions. This is in accordance with the IMAS interpretation outlined so far.

Similar conclusions with regards to the impact of micro-scale anthropogenic sources on the turbulent fluxes at KSS can be drawn from the analysis of the winter case study (Figure III.14). For the winter case, the sensible heat and carbon dioxide fluxes for both levels (L1 and L2) are shown with net all-wave radiation (Figure III.14c). During winter, local scale anthropogenic heat flux can be assumed to contribute significantly to the urban energy balance – typically heat emissions increase due to heating requirements and simultaneously incoming solar energy is reduced. This explains why daytime Q_H [L2] (which represents the local scale flux) can be of the order of magnitude of net all-wave radiation, or even higher.

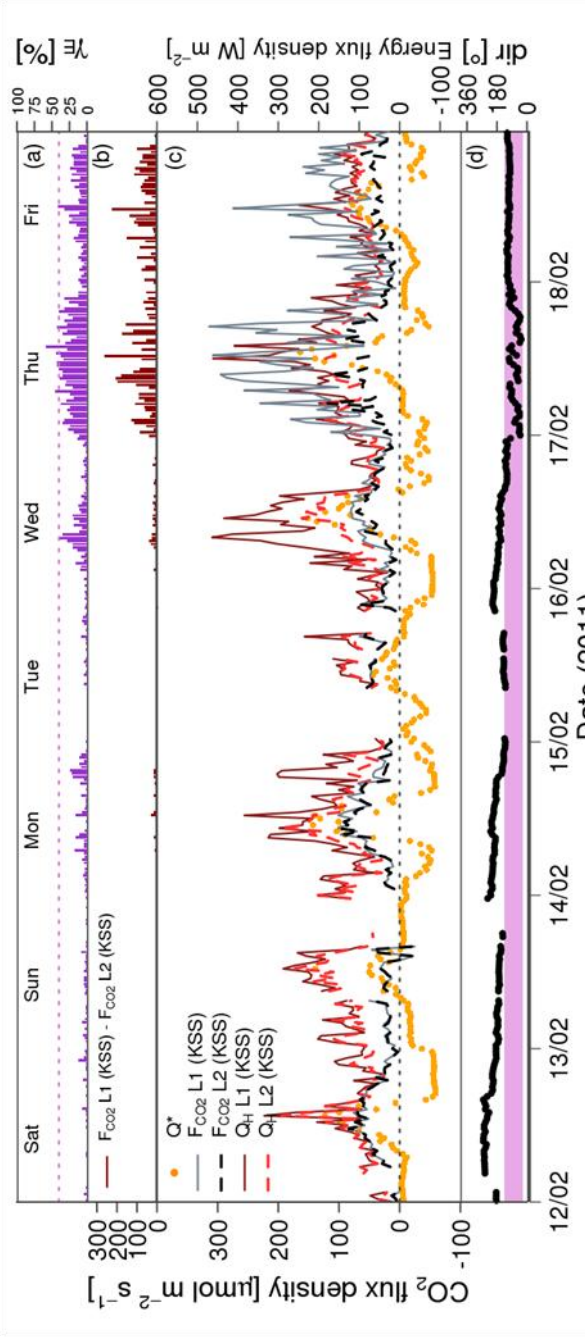

Figure III.14: Case study of IMAS impact for a winter period (12/02/2011–18/02/2011): a) event frequency γ_E [%] at KSS, periods which exceed the threshold of 40% are excluded from L2 data; b) difference between L1 and L2 estimates of turbulent flux of carbon dioxide at KSS; c) L1 and L2 turbulent sensible heat flux and turbulent flux of carbon dioxide at KSS and net-all wave radiation at KSS; d) wind direction at KSS, the shading marks the easterly wind sector where most micro-scale anthropogenic sources are located (25–135°).

As for the summer/autumn case (Figure III.13), Q_H [L1] at KSS is larger than L2 values predominantly during weekdays (when human activities in the University building are expected to be higher) with flow from easterly wind directions (shading in Figure III.14d). For example, similar

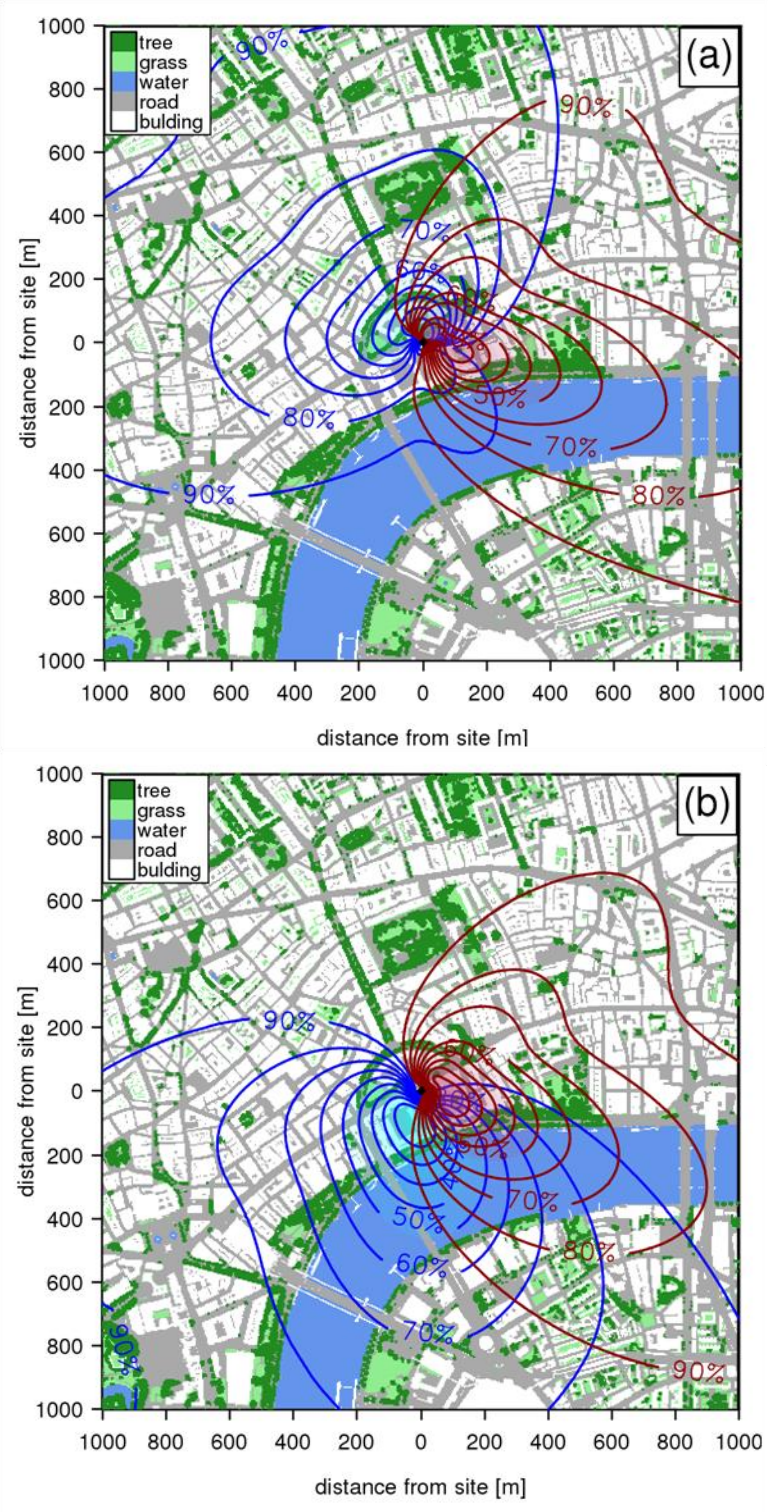

Figure III.15: Local scale source area for turbulent fluxes as measured at KSS, accumulated for the case study periods in (a) summer (27/08/2010–06/09/2010, Figure III.13) and (b) winter (12–18/02/2011, Figure III.14). Accumulated source area weights for wind directions in the sector 25–135° (black, red in online version) are separated from remaining directions (grey, blue in online version). Area contributing up to 50% of the source area is shaded. Underlying map of land cover types, 4 m resolution (based on OS MasterMap and vegetation data from Lindberg and Grimmond 2011). The map is centred on the KSS tower.

Q_H [L1] values are observed at KSS on Sunday 13th February and Wednesday 16th February with average wind directions of 172° and 154°, respectively. However, increased activity in the university building on Wednesday can presumably explain the strong IMAS impact expressed in the large L1-L2 difference of Q_H at KSS compared to Sunday in this case study week.
Wind direction dependence of turbulent flux of carbon dioxide at KSS is even more distinct than for the turbulent sensible heat flux (Section III.3.2). The winter case study gives a good example of this relation. L1 and L2 F_{CO2} observations at KSS (Figure III.14c) are similar for 12th–16th February when the flow is mainly coming from south–southwest. On Thursday (17/02/2011) and Friday (18/02/2011), when the flow comes from the easterly wind sector (shading in Figure III.14d) the two measures of turbulent carbon dioxide flux (L1 and L2) diverge (Figure III.14c). Again, no evidence is found in the local-scale source area characteristics (Figure III.15b) which would explain this sudden change. Both cumulative footprint areas have a road percentage of 36%, only the build percentage is slightly higher for easterly conditions (35% compared to 28% for the remaining). However, there is a clear response in IMAS intensity (L1-L2 F_{CO2}, Figure III.14b) and duration (event frequency, Figure III.14a). This suggests that due to micro-scale anthropogenic CO_2 emissions, the daily average L1 carbon dioxide flux at KSS is 3.0 (2.9) times higher than the local scale L2 flux on 17th February (18th February). The maximum difference between the two F_{CO2} estimates is 264.9 µmol m^{-2} s^{-1} (Figure III.14b). It is evident from the event frequency (Figure III.14a), the flux difference (Figure III.14b) and the time series of the L2 flux itself (Figure III.14c) that micro-scale emissions impact the flux even during the night, if the flow falls into the easterly wind sector.

III.4 Conclusions

Eddy covariance (EC) measurements carried out in dense urban environment are analysed with particular attention to human activities and their impact on near-surface atmospheric conditions. Given such observations generate special challenges in terms of instrument setting, data acquisition and data processing, the current study provides a new approach to identify micro-scale anthropogenic sources in raw EC data. This procedure, termed here IMAS, filters out extreme events in sonic temperature, water vapour and carbon dioxide concentrations. It is incorporated into the processing of turbulent fluxes to enable separation of micro-scale events from those attributed to the local scale source area. Using a long term dataset gathered in a very dense urban environment at the KSS site in central London, the applicability of this new filtering technique is tested. First it is verified that extreme signals in the observations can be attributed to anthropogenic sources which are located near the instruments. At KSS where significant emissions sources are present, the time periods affected are identified. When tested on data collected at the proximal KSK site, the IMAS filter shows comparable functionality as for KSS.

From qualitative analysis, the results calculated with the new processing procedure show physically reasonable diurnal patterns. The impact of the filter on friction velocity, sensible heat flux, latent heat flux and flux of carbon dioxide can be explained physically and shows consistent behaviour both in a direct comparison of L1 (no filter) and L2 (with IMAS filter) results and in a

summary given by frequency distributions. Altogether, the filter has a diminishing effect on the surface fluxes. Analysis by wind direction reveals that extreme fluxes are enhanced when the flow is coming from the direction of the sources. Further it is shown that the percentage of flagged data points (the event frequency γ_E) coincides with this directional behaviour.

An attempt is made to quantify the impact of IMAS on the turbulent surface fluxes. For the turbulent fluxes of sensible and latent heat, this estimate essentially is linked to the component of anthropogenic heat flux originating from building emissions. If certain assumptions are fulfilled, the procedure presented here enables the direct measurement of contributions to Q_{Fb} at the building scale. When analysing long-term average effects, the magnitudes of observed micro-scale anthropogenic heat flux are comparable to modelling studies which are commonly used to estimate Q_F (Sailor 2011). The quantitative analysis suggests that sensible heat flux and the flux of carbon dioxide are strongly influenced. For all results, the magnitude of micro-scale induced fluxes can be explained by temporal variability of human activities and variations in approaching flow direction.

The new approach can be used to extract micro-scale influence from EC measurements. It allows for calculation of fluxes originating from local scale characteristics and hence enables the analysis and interpretation of a dataset gathered in a highly complex environment. Additionally, the IMAS filter can be seen as a basic principle for observing anthropogenic heat flux on the building scale.

Acknowledgements

Support was provided by the EU FP7 BRIDGE Grant agreement no.: 211345, NERC grant ClearfLo and NERC ARSF (GB08/19). We thank Dr Arnold Moene at Wageningen University for providing the ECpack software and for advice regarding its usage; Dr Fredrik Lindberg for land cover data analysis; Dr Andreas Christen (UBC, 2010) for his IDL based implementation of the footprint model; all those at KCL who contributed to the data collection; KCL Directorate of Estates & Facilities for giving us the opportunity to operate the various measurement sites; and funding support from KCL. Further we thank an anonymous reviewer for their constructive comments and suggestions. Figure III.11 and Figure III.12 are created using the Openair R package (Carslaw and Ropkins 2011).

Appendix III.A Further evidence for the applicability of IMAS

Auxiliary data from a temperature profile along the measurement tower were incorporated in the analysis to show that the effect of the micro-scale anthropogenic sources can also be identified in completely independent observations (Section III.3.3). As seen in the directional analysis of IMAS induced fluxes (Figure III.11), the micro-scale impact is detected in a wider range of wind directions compared to F_{CO2}. Severe additional sensible heat fluxes are observed (Figure III.A.1) even for wind directions slightly north of the main affected sector (20--135°) when the building is occupied, i.e. during daytime.

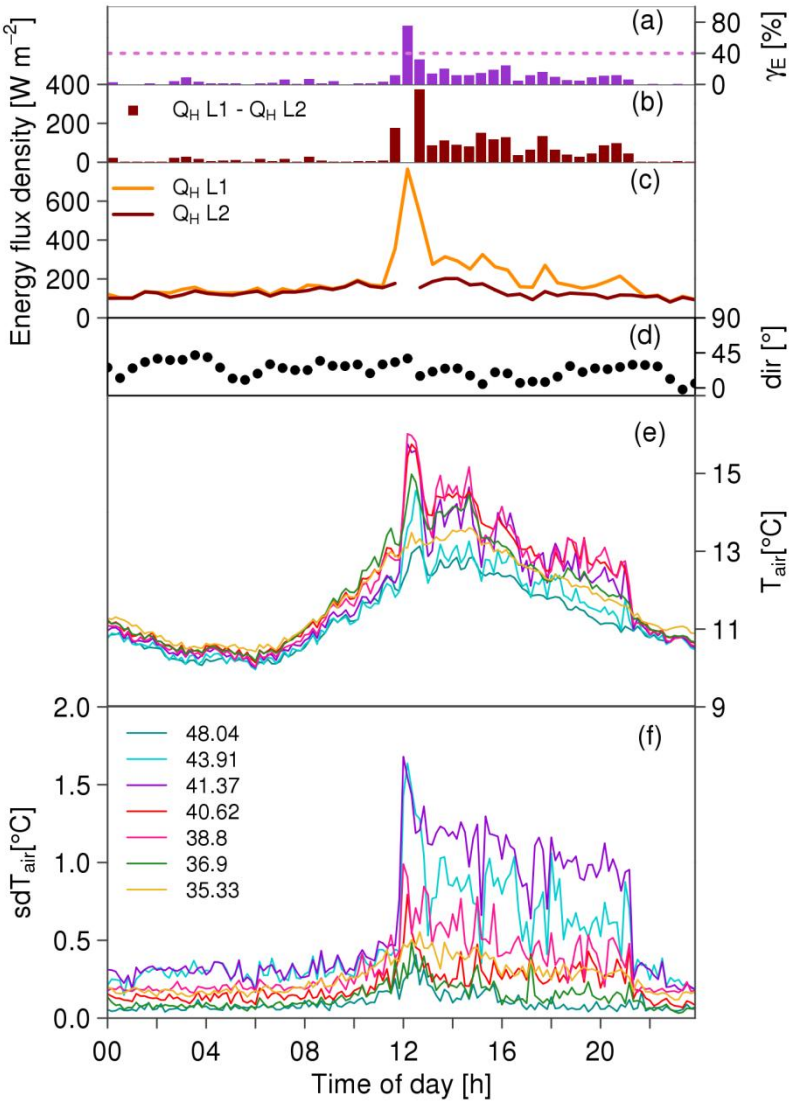

Figure III.A.1: Example of IMAS impact at KSS (13/10/2010): (a) event frequency γ_E [%], periods which exceed the threshold of 40% are excluded from L2 data; (b) difference between L1 and L2 estimates of turbulent sensible heat flux; (c) L1 and L2 data turbulent sensible heat flux; (d) wind direction; (e) air temperature and (f) standard deviation of air temperature (10 min) observed by vertical temperature profile up the tower at seven heights [m a. g. l.].

IV Energy exchange in a dense urban environment – Part I: temporal variability of long-term observations in central London

Abstract

Though anthropogenic impacts on boundary layer climates are expected to be large in dense urban areas, to date very few studies of energy flux observations are available. We report on 3.5 years of measurements gathered in central London, UK. Radiometer and eddy covariance observations at two adjacent sites, at different heights, were analysed at various temporal scales and with respect to meteorological conditions, such as cloud cover. Although the evaporative flux is generally small due to low moisture availability and a predominately impervious surface, the enhancement following rainfall usually lasts for 12–18 h. As both the latent and sensible heat fluxes are larger in the afternoon, they maintain a relatively consistent Bowen ratio throughout the middle of the day. Strong storage and anthropogenic heat fluxes sustain high and persistently positive sensible heat fluxes. At the monthly time scale, the urban surface often loses more energy by this turbulent heat flux than is gained from net all-wave radiation. Auxiliary anthropogenic heat flux information suggest human activities in the study area are sufficient to provide this energy.

Kotthaus, S, and CSB Grimmond, 2013: Energy exchange in a dense urban environment – Part I: temporal variability of long-term observations in central London. Urban Climate, doi:10.1016/j.uclim.2014.10.002.

IV.1 Introduction

Urban areas present a special challenge for understanding near-surface climate conditions in the atmospheric boundary layer. Human activities, which vary with time, combined with the highly complex and heterogeneous surface structure across cities impact exchanges of energy and pollutants. Observations offer a crucial means to improve the understanding and interpretation of atmospheric processes, and provide the basis for model development and evaluation. In order to take into account this diversity, micrometeorological research needs to address a variety of different urban land uses (Arnfield 2003).

Grimmond (2006) and the WMO (Grimmond et al. 2010) identify the need for more urban energy flux observations that cover long time periods and a greater variety of locations in order to study the full spectrum of urban influences and also seasonal variations of the urban energy balance influenced by distinct weather/climate conditions and surface properties. Although more flux sites have been installed in the last decade (Grimmond 2006), the coverage still does not yet address the diversity or range of urban areas globally. As Goldbach and Kuttler (2012) list, recent turbulent flux observations include European cities; *viz*, Basel, Switzerland (Christen and Vogt 2004), Marseille, France (Grimmond et al. 2004), Toulouse, France (Masson et al. 2008), Łódź, Poland (Offerle et al. 2006a,b; Pawlak et al. 2011; Fortuniak et al. 2012b), Helsinki, Finland (Vesala et al. 2008a), Essen, Germany (Weber and Kordowski 2010) and Oberhausen, Germany (Goldbach and Kuttler 2012), while earlier research focused largely on cities in North America (e.g. Grimmond and Oke 1995, 2002). New insights are also being gained from turbulent surface exchange studies located in different climates and synoptic conditions (e.g. Tokyo, Japan, Moriwaki and Kanda 2004; Ouagadougou, Burkina Faso, Offerle et al. 2005a, Melbourne, Australia, Coutts et al. 2007; Helsinki, Finland, Järvi et al. 2009; Cairo, Egypt, Frey et al. 2011). Data sets for longer time periods are allowing seasonal and annual variability to be examined (e.g. Christen and Vogt 2004; Offerle et al. 2006a; Coutts et al. 2007; Järvi et al. 2009). Most study sites though are still located in suburban, residential or industrial areas. Thus our knowledge of surface exchange processes in dense city centres remains limited (e.g. Basel, Christen and Vogt 2004; Helsinki, Nordbo et al. 2012). Further, we might expect that locations where large and dense urban populations work and live are areas of some of the most extreme urban influences.

The focus of the current study is London, UK, one of the European Union's most densely populated cities with a population of over 8.2 million (Greater London, mid-2011 census, Office for National Statistics 2012). The history of urban climate studies in London reaches back to the historical contributions of Luke Howard starting in the early 1800s (Howard 1818, 1833). Since then, the UK capital has undergone extensive growth. Recent urban climate observations in London have been concerned with dispersion of pollutants (DAPPLE, Arnold et al. 2004; Robins 2008; REPARTEE, Harrison et al. 2012) and the applicability of similarity theory in the urban environment (Wood et al. 2010). Wood et al. (2010) report observations undertaken at 190 m

above ground (BT tower) which, in addition to heat and momentum flux measurements, also include observations of atmospheric chemistry (Langford et al. 2010; Helfter et al. 2011). In contrast to the observations on the BT tower, the measurements presented in this study are in the very centre of the city, at a lower measurement height. Thus the source area is more homogeneous and reflects London's central business district, designated the 'Central Activities Zone' (CAZ, a) by the Greater London Authority (GLA 2011). The measurements are conducted right next to Somerset House, which in the nineteenth century housed the Royal Society. This is where Luke Howard's 'urban' sensor was located (Mills 2008) that enabled him to identify the urban warming effect.

The objective of this paper is to describe the temporal characteristics of observations undertaken in the dense urban city centre of London. The impact of the spatial heterogeneity of the urban surface on the flux observations is addressed in Chapter V, based on footprint analysis and a comparison of two adjacent sites. Here, data collection and processing methods, including the auxiliary data of an anthropogenic heat flux model, are presented (Section IV.2). The results are analysed (Section IV.3) in terms of the seasonal and monthly behaviour of the energy balance components. The role of precipitation and the temporal evolution of energy partitioning over the course of a day are also studied. Our key findings (Section IV.4) contribute to current understanding of the microclimate of highly urbanised environments.

IV.2 Methods

Investigating surface energy exchange in urban areas requires a combination of different methodologies in order to estimate the components of the surface volume energy balance (Oke 1987):

$$Q^* + Q_F = Q_H + Q_E + \Delta Q_S + \Delta Q_A.$$

In addition to radiative energy input given by the net all-wave radiation Q^*, the anthropogenic heat flux Q_F plays a significant role in many urban areas. Available energy is partitioned into the turbulent fluxes of sensible heat Q_H and latent heat Q_E. The storage heat flux ΔQ_S is related to the net heating and cooling of the urban canopy volume. Finally, ΔQ_A describes net energy exchanges via vertical or horizontal advection.

In the present study, net all-wave radiation as well as sensible and latent heat fluxes were derived from *in-situ* observations. Anthropogenic heat flux was incorporated in the analysis using estimates from a top-down approach based on energy consumption (*GreaterQf* model, Iamarino et al. 2012). The storage heat flux is very difficult to measure directly (Grimmond 1992), requiring extensive observations that cover the diversity of buildings, canyons and other elements of the urban canopy volume. Hence it is often calculated as the residual Q_{RES} of the energy balance equation assuming a negligible advective flux ΔQ_A. Cautious analysis of this Q_{RES} is required as it incorporates uncertainties of all other fluxes and implies energy balance closure (Grimmond and Oke 1999a; Foken et al. 2006). The interpretation of the various fluxes as a 'balance' assumes that the radiation, anthropogenic heat and turbulent fluxes have spatially consistent source areas

or that the surface characteristics within the source areas of each are spatially representative (Roberts 2010).

IV.2.1 Measurement site

The study area is located in the 'Central Activities Zone' (CAZ) of London, UK, the destination of many commuters in (and to) the capital. While about 275 000 people live in this area (GLA 2011), the daytime population is several times higher. The CAZ covers parts of the three busiest London boroughs with daytime populations of 520 000 (Camden), 603 000 (City of London), and 987 000 (Westminster), respectively (GLA 2012).

London has a temperate marine climate that experiences mid-latitude low pressure systems, inducing precipitation, clouds and increased wind speeds (Met Office 2012a). Typically these frontal systems have a somewhat diminished intensity when they reach the South-East of England on their passage from the west. As this part of the British Isles is closest to the European mainland, continental weather conditions occasionally influence the area. Due to this proximity and the sheltering effect by the UK landmass from mid-latitude cyclones, the South-East receives less precipitation than the rest of the country (Met Office 2012a). It does, however, experience added convective activity and the large area of Greater London (1,570 km^2) might account for some increase in cloud cover and convective precipitation (Atkinson 1969). On average[8], the annual rainfall in central London is 570 mm and mean daily (24 h) temperature ranges from about 5 °C in January to 19 °C in July. The area is on occasion exposed to sea breezes (Bohnenstengel et al. 2011; Chemel and Sokhi 2012).

Two measurement towers, referred to as *KSS* and *KSK,* are located at the Strand Campus of King's College London (KCL, 51°30' N, 0°7' W), approximately 60 m apart (Figure IV.1). Loridan et al. (2013) classify the surrounding area as a "High Density" UZE (Urban Zone for Energy partitioning, Loridan and Grimmond 2012). From the image-based classification approach of Stewart and Oke (2012) it is "compact midrise" LCZ (Local Climate Zone).

At both sites, sensors are mounted on the top of extendable towers (KSK: single tube mast, Clark Masts CSQ T97/HP; KSS: triangular tower, Aluma T45-H), which are installed on top of buildings. The measurement height above ground level (agl) is 49 m at KSS and 39 m at KSK, which equates to a ratio of 2.2 and 1.9, respectively, compared to mean building height z_h. Detailed information on surface cover, building heights, their variations around the sites, and the implications for surface roughness are discussed in Chapter V. There potential impacts from the River Thames in close vicinity of the sites to the south (Figure IV.1) are also analysed.

[8] observed at St. James's Park WMO station, based on the 26 years with complete data availability in the archive of the British Atmospheric Data Centre (BADC), i.e. 1981–1991 and 1997–2011

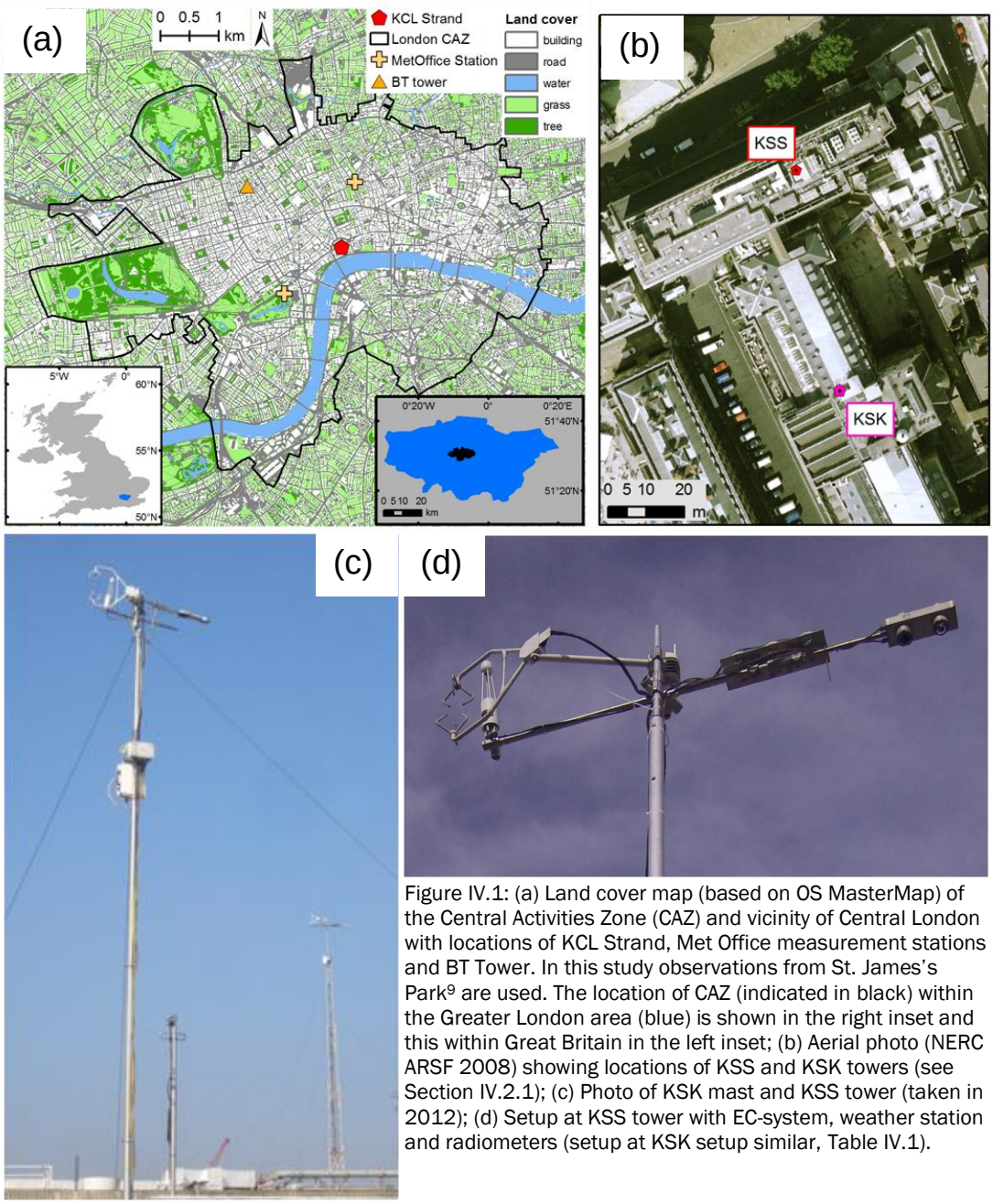

Figure IV.1: (a) Land cover map (based on OS MasterMap) of the Central Activities Zone (CAZ) and vicinity of Central London with locations of KCL Strand, Met Office measurement stations and BT Tower. In this study observations from St. James's Park[9] are used. The location of CAZ (indicated in black) within the Greater London area (blue) is shown in the right inset and this within Great Britain in the left inset; (b) Aerial photo (NERC ARSF 2008) showing locations of KSS and KSK towers (see Section IV.2.1); (c) Photo of KSK mast and KSS tower (taken in 2012); (d) Setup at KSS tower with EC-system, weather station and radiometers (setup at KSK setup similar, Table IV.1).

IV.2.2 Data collection and processing

Three components of the surface energy balance are measured directly: net all-wave radiation and the turbulent fluxes of sensible and latent heat. The KSK site has been operational since 2008, and KSS since 2009 (Table IV.1). Radiometers (CNR1 & CNR4, Kipp & Zonen) provide the four constituents of Q*, i.e. long-wave and short-wave incoming and outgoing/reflected radiation ($L_{\downarrow}$, $L_{\uparrow}$, $K_{\downarrow}$, $K_{\uparrow}$), 15 min averages are recorded. Radiation data are restricted to physically reasonable thresholds and short-wave radiation is forced to zero during night-time to correct for the instrument related night-time offset error (Michel et al. 2008).

[9] Comment on Kotthaus and Grimmond (2013a): St. James' Park station: Met Office site west of KCL Strand.

Table IV.1: Instrumentation at the two sites (KSK, KSS) and the periods within the years 2008-2012 analysed in this study, specified as day of year.

	Instrument	Model	Manufacturer	2008	2009	2010	2011	2012
KSK	Sonic anemometer	CSAT3	*Campbell Scientific*	274-366	001-280	022-365	001-365	001-091
	Infrared gas analyser	Li7500	*LiCOR Biosciences*	274-366	001-280			
		Li7500A	*LiCOR Biosciences*				231-365	001-091
	Weather station	WXT510	*Vaisala*	274-366	001-365	001-365	001-069	
		WXT520	*Vaisala*				096-365	001-091
	Radiometer	CNR1	*Kipp & Zonen*	274-366	001-280			
		CNR4	*Kipp & Zonen*			264-365	001-365	001-091
	Rain gauge	ARG100	*Campbell Scientific*	274-366	001-365	001-365	001-365	001-091
	Ceilometer	CL31	*Vaisala*	274-366	001-112			
KSS	Sonic anemometer	CSAT3	*Campbell Scientific*		305-365	001-365	001-365	001-084
	Infrared gas analyser	Li7500	*LiCOR Biosciences*		305-365	001-365	001-365	001-084
	Weather station	WXT510	*Vaisala*		286-356	001-365	001-365	001-084
	Radiometer	CNR1	*Kipp & Zonen*		289-356	001-365	001-365	001-084
	Rain gauge	ARG100	*Campbell Scientific*		351-365	001-365	001-365	001-091
	Ceilometer	CL31	*Vaisala*		112-365	001-365	001-365	001-091

Cloud cover was retrieved from atmospheric backscatter observed with a ceilometer (CL31, Vaisala) located near KSK (until April 2009) and then KSS (April 2009 to present). Based on the vertical atmospheric backscatter profile observed, the cloud height derived by the instrument software was used in the post-processing to determine cloud cover as a percentage. As the ceilometer raw data (8192 Hz mean pulse repetition rate, Münkel et al. 2006; 15 s reporting interval) give an instantaneous profile above the sensor, the field of view is increased by using a 30 min moving window to determine the percentage of time when clouds at any height are detected (centred at each 15 s interval). The 15 s values were again averaged to 15 min intervals to coincide with the time periods of the radiation measurements.

The turbulent exchanges of latent and sensible heat are observed using the eddy covariance (EC) method. Systems at both sites consist of a CSAT3 sonic anemometer (Campbell Scientific) and a Li7500 (Li7500A) open path infrared gas analyser (LiCOR Biosciences), sampled at 10 Hz. Automatic weather stations (WXT510 and WXT520, Vaisala) provide air temperature, station pressure, horizontal wind speed and direction, as well as relative humidity, sampled at 0.2 Hz. The latter is converted to vapour pressure deficit (VPD). Tipping bucket rain gauges (ARG100, Campbell Scientific) are used to monitor precipitation; accumulated rain is recorded based on 15 min intervals. The sonic anemometer, gas analyser, rain gauge and net radiometer are connected to dataloggers (CR3000 and CR5000, Campbell Scientific). Flux calculations are performed based on 30 min block averages. All recording and data analysis is done in UTC (Universal Time

Coordinated) which is local time in the winter and an hour earlier during summer (daylight savings period).

Meteorological observations from the weather stations and the rain gauges are cleaned and gap-filled (Chapter III). Eddy covariance fluxes are calculated by ECpack (van Dijk et al. 2004) with a series of pre- and post-processing steps which are implemented in order to improve the quality of the results and to maximise data availability. A detailed description of the data processing procedure is presented in Chapter III. Tests comprise a new despiking approach and an automatic Identification of Micro-scale Anthropogenic Sources (IMAS, Chapter III). The latter is used to filter effects of micro-scale emissions so that the calculated fluxes are representative for the local scale source area. The algorithm (Chapter III) used here is improved in order to capture periods of extremely high temperatures (i.e. IMAS Type V is similar to Type II but more persistent). The updated IMAS algorithm (summarised in Table IV.2; see Chapter III for details) is applied to all data presented in the current study. Only small emission sources are present at KSK so that IMAS generally has less impact than at KSS. However, even at the KSS site, IMAS is mainly detected under easterly wind directions so it hardly concerns fluxes from the main wind directions (in the southwest and northeast, Chapter V). After quality control, 751.2 days at KSS (1056.4 days at KSK) of sensible heat flux data are available for analysis (Table IV.1). More data fail quality control criteria for latent heat flux, leaving 685.2 at KSS (490.3 at KSK) days for interpretation (note that at KSK, the sonic anemometer has a much longer measurement period than the gas analyser).

Table IV.2: Five IMAS types: (a) classification, (b) definition, and (c) detection are based on observations of sonic temperature T_{sonic} and concentrations of H_2O and CO_2. The classification considers if there is an increase (↑) or decrease (↓) of the variable during an IMAS event. Statistics used in the definition and detection are calculated based on 10 s intervals: mid-range (mr_{10s} = mean of minimum and maximum) and standard deviation (std_{10s}); 1 min intervals: mid-range (mr), standard deviation (std), median (med), kurtosis (krt), and absolute deviation of mid-range the from the median (mrm); 30 min intervals: median (med_{30}), standard deviation (std_{30}). Also, the minimum (MIN_1) and inter-quartile range (IQR_1) of mid-range mr_{10s} and the median (MED_{30}) of med are calculated over 1 min and 30 min intervals, respectively. IMAS Types I-IV are presented in Chapter III. Type V is included in the improved IMAS algorithm used for the current study.

IMAS	T_{sonic} [°C]	H_2O [mmol m^{-3}]	CO_2 [mmol m^{-3}]
(a)	Classification		
Type I	(↑)	↑	↑
Type II	↑	–	–
Type III	↑	↓	↑
Type IV	↑	↓	↑
Type V	↑	–	–
(b)	Definition		
Type I	–	–	$mrm > 0.7$ & $krt > 0.3$
Type II	($mrm > 1$ & $krt > 3$) or ($std > 1$ & $krt > 7$)	–	–
Type III	$krt > 1$	$mrm < -0.5$	–
Type IV	($std > 0.9$ & $krt > 1$) or (med - $MED_{30}(med)$) > 1	$mrm < -0.1$	$mrm > 5$
Type V	($mr - med_{30}$) > 0.9 or $mrm > 2.5\ std_{30}$	–	–
(c)	Detection		
Type I	–	$mr_{10s} > MIN_1(mr_{10s}) + IQR_1(mr_{10s})$	
Type II	$mr_{10s} > MIN_1(mr_{10s}) + IQR_1(mr_{10s})$	–	–
Type III	$std_{10s} > 0.5$		
Type IV	Whole 30 min period detected as IMAS		
Type V	$mr_{10s} > MIN_1(mr_{10s}) + IQR_1(mr_{10s})$ or $std_{10s} > 0.5$	–	–

Daily-accumulated energy fluxes of net all-wave radiation, sensible heat flux and latent heat flux are estimated based on median monthly diurnal patterns. Frequency distributions of the observed fluxes by time of day (not shown) reveal a slightly systematic under representation of specific hours when more observations are affected by micro-scale anthropogenic emissions. However, the overall data availability is still high, i.e. for more than 94% (82%) of the time at least twenty observations contribute to each monthly median of 30 min Q_H (Q_E) values and the number of samples never drops below 12 (10). Hence the median diurnal pattern is assumed to describe the monthly statistics sufficiently accurately such that they provide the basis for the calculation of monthly mean daily totals, rather than gap-filling individual time periods. Using the mean instead of the median leads to very similar results for Q_H (ca. 2% difference); indicating a sufficiently normal distribution. This difference is somewhat larger for Q_E (ca. 17%), however this represents about 5 W m^{-2} and hence is probably within the range that can be expected for the uncertainty of this flux.

Anthropogenic heat fluxes Q_F are estimated using the GreaterQf model (Iamarino et al. 2012). This quantifies building emissions (Q_{Fb}), road traffic (Q_{Ft}) and metabolism (Q_{Fm}), with:

$$Q_F = Q_{Fb} + Q_{Ft} + Q_{Fm},$$

on a regular grid with 200 m resolution. These values represent total fluxes of sensible and latent heat flux contributions. The Q_F grids are chosen based on the modelled source area (Chapter V), i.e. variable in time and space, to try to ensure the Q_F values are representative of the surface volume observed by the EC method. Depending on wind direction, between two to four grid values are combined.

As anthropogenic heat fluxes from building emissions vary with air temperature (Sailor and Lu 2004), the temperature variations observed (Oct 2008—Mar 2012, Table IV.1; Section IV.3.1, Figure IV.3) were accounted for using relations determined from Iamarino et al.'s (2012) data (Figure IV.2). Daily mean building anthropogenic heat flux from the GreaterQf model for the four-year period 2005-2008, was compared to air temperature at a site in central London (St. James's Park WMO station, Figure IV.1a). Above a threshold temperature (≈ 17.5 °C) Q_{Fb} remains effectively constant, whereas below this, approximately linear functions describe the relation (Figure IV.2). Because of the strong impact of human activities, the coefficients differ between weekdays (Figure IV.2a) and weekends (Figure IV.2b). This modelled Q_F indicates the order of magnitude that can be expected as direct anthropogenic energy input into the urban surface volume.

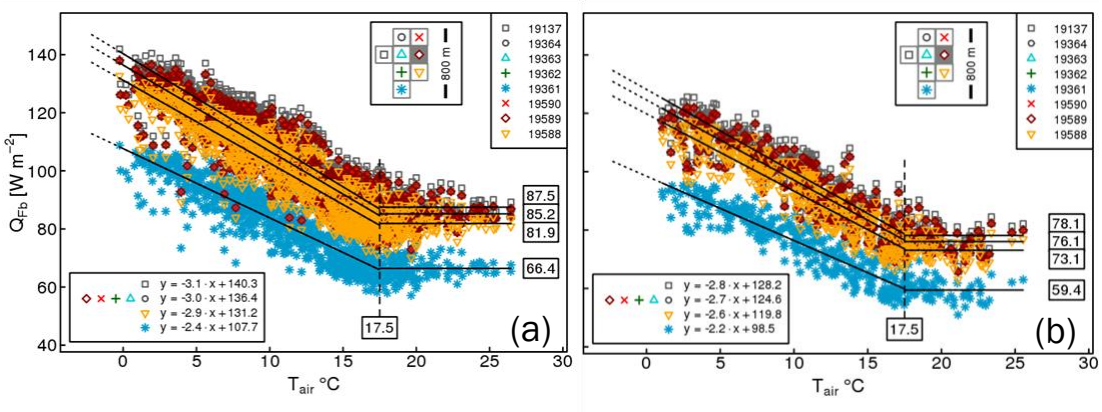

Figure IV.2: Mean daily (24 h) anthropogenic heat flux from building emissions modelled with the GreaterQf model (Iamarino et al. 2012) as a function of mean daily temperature observed at St. James's Park Met Office (WMO) station (Figure IV.1) for 2005–2008 for (a) weekdays and (b) weekends. Eight 200 m x 200 m model grids (legend = grid ID) are selected to represent the source area of the turbulent fluxes (see Chapter V). (Top inset) grid locations relative to measurement sites which are both situated in the shaded grid square; (bottom inset and boxed labels) equations and coefficients to describe functions fitted to the data (solid lines); (dotted lines) indicate course for lower temperatures (as in observation period); see Section IV.2.2.

Storage heat flux ΔQ_S was not directly observed or modelled in the current study. However, in this dense urban environment it is expected to be a significant energy balance flux when calculated as the residual of the incoming and outgoing energy terms:

$$Q_{RES} = Q^* + Q_F - (Q_H + Q_E).$$

Energy balance closure, which this assumes, is complicated by spatial as well as temporal variations of each of the fluxes (Offerle et al. 2005a), thus adding uncertainty. However, this residual provides some useful insight into the storage heat flux. For the energy balance discussion (Section IV.3.6), it is assumed that the footprint of the radiation fluxes is representative of the local scale source area of the turbulent fluxes. According to the analysis in Chapter V both types of observations are mostly influenced by impervious surfaces, suggesting this approach is feasible. However, this spatial analysis suggests that horizontal advection induced by channelling along the River Thames, may impact the observations at KSS, reducing the sensible heat flux for certain wind directions. This potential energy loss would result in an overestimation of Q_{RES}.

IV.3 Results

IV.3.1 Meteorological conditions

The meteorological conditions observed in central London at KCL (Figure IV.3, Table IV.1[10]) over a period of 3.5 years provide the context for the analysis of surface energy exchange. With respect to the whole observation period, maximum (minimum) air temperature ranged from 16.9 °C (-5.4 °C) during winter (DJF) to 30.9 °C (7.4 °C) during summer (JJA). Annual rainfall was highest in 2010 (581.4 mm) compared to 2009 (525.7 mm) and 2011 (546.0 mm), respectively. The beginning of 2012 (JFM) was dry with only 80.9 mm, whereas 150.0 mm rainfall fell in the last

[10] Comment on Kotthaus and Grimmond (2013a): Table IV.1 provides details on measurement periods.

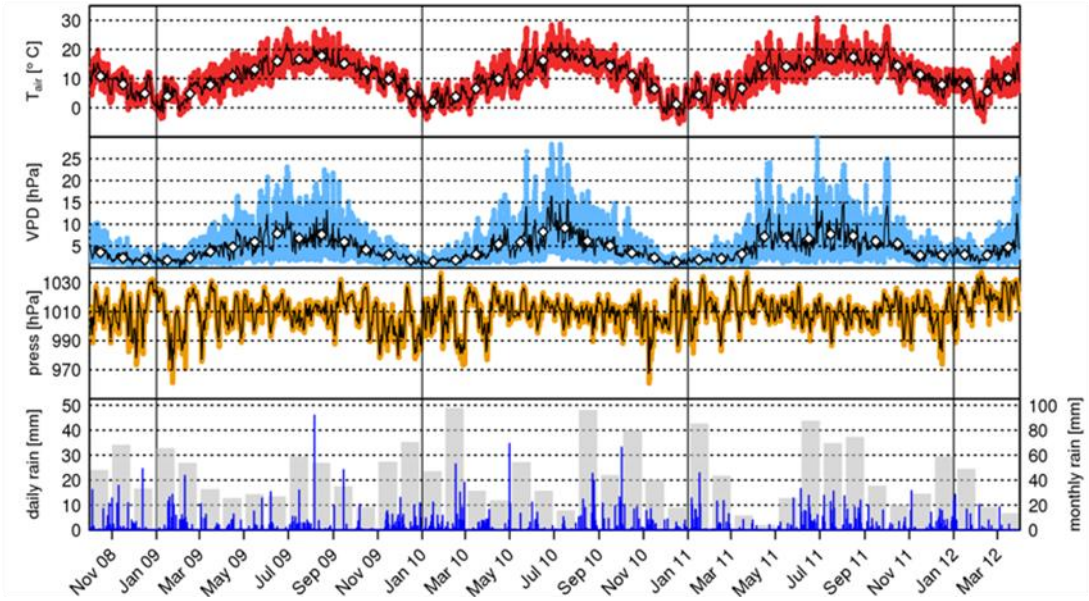

Figure IV.3: Meteorological observations (after quality control) for 10/2008–03/2012, measured with a WXT510 (WXT520) weather station and ARG100 rain gauge at KSK, gap filled with KSS: air temperature, vapour pressure deficit, and station pressure as 15 min (dots), daily (solid line) and monthly averages (diamonds); daily (lines) and monthly (bars) accumulated precipitation.

three months of 2008. At the monthly time scale: most rain was recorded in February and August 2010 (98.0 mm; 96.2 mm) and the least in March and April 2011 (11.6 mm; 4.0 mm). The coldest (and driest) months were January and December 2010 (2.0, 1.2 °C) while November 2011 to January 2012 was anomalously warm (11.4, 7.9, 7.7 °C, NDJ). The dry April 2011 was warmer (13.7 °C) compared to April 2009 (10.9 °C) and 2010 (9.9 °C), respectively. The wind speed usually ranges from 0.2 to 6.0 m s^{-1}, occasionally reaching higher values (not shown). The overall mean wind velocity at KSS (KSK) is 3.4 m s^{-1} (2.7 m s^{-1}).

At the synoptic scale of several days to weeks, both air temperature and humidity respond to mid-latitude high- and low-pressure systems. Passages of the latter show up clearly in the observed station pressure (Figure IV.3). Persistent high pressure is usually associated with clear sky conditions enabling long-wave radiative cooling at night and short-wave radiative heating during the day. Due to low solar elevation angles, the effect of heat loss dominates in winter so that air temperature decreases considerably when high pressure persists for several days (e.g. 26/12/2008–10/01/2009). Naturally, little precipitation is recorded during these times, which contributes to the relatively lower levels of humidity (e.g. 01/03–18/03/2010).

IV.3.2 Radiation component

Radiative energy is generally the most important source in the surface energy balance. All four components of the net-all wave radiation are observed at KCL Strand (Figure IV.1b): a combined time series of measurements at the two sites (KSK: 10/2008–09/2009; KSS: 11/2009–03/2012; CNR1, Figure IV.1b) illustrates their variability (Figure IV.4).

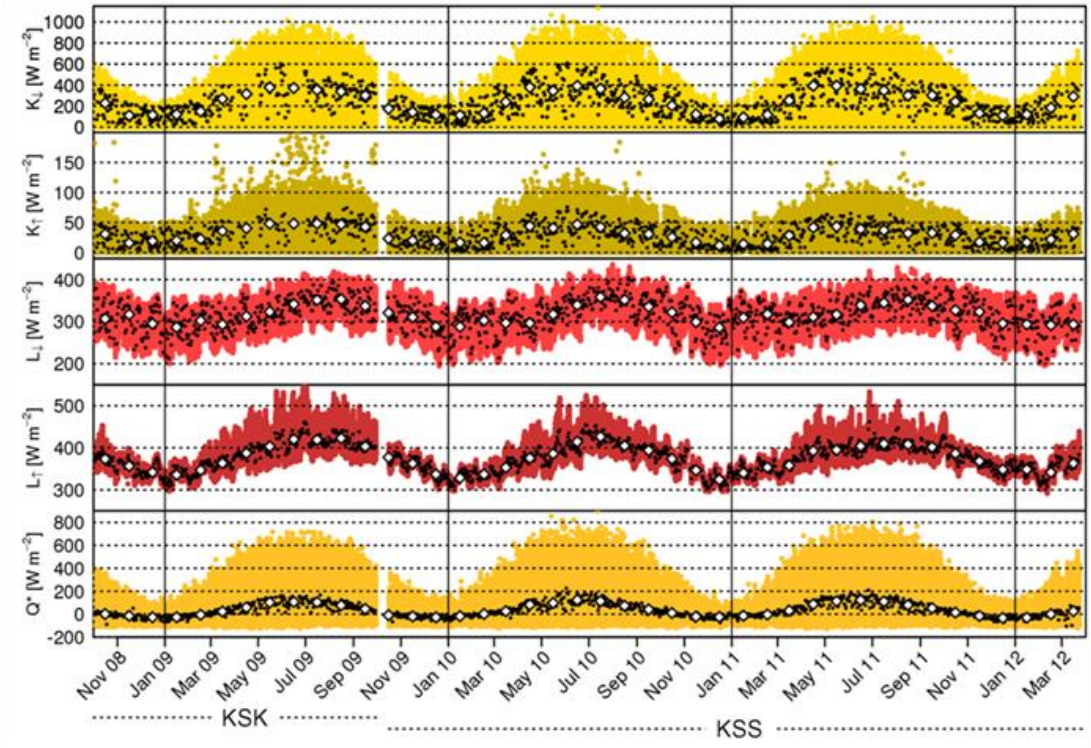

Figure IV.4: Observations of the CNR1 net radiometer (after quality control) at KSK (10/2008–09/2009) and KSS (10/2009–03/2012): net all-wave radiation Q* is the sum of incoming (↓) and outgoing (↑) long- (L) and short-wave (K) radiation, averages: 15 min (coloured dots), daily (K: daytime, L & Q*: 24h, black dots) and monthly (white diamonds). Data gap in October 2009 due to maintenance.

IV.3.2.1 Short-wave radiation

At the central London sites, daytime maxima of incoming short-wave radiation ($K_{\downarrow}$) range from about 200 W m^{-2} in winter to 1000 W m^{-2} in summer. As expected there is little inter-annual variation. Surface influence is evident in observations of reflected short-wave radiation ($K_{\uparrow}$). While daily maxima usually range between 50 W m^{-2} (winter) and 120 W m^{-2} (summer), some extreme values are observed at both sites (Figure IV.4). They occur more frequently at KSK (2008 & 2009) where many of them exceed 150 W m^{-2}. Fewer extremes are seen at KSS (mainly in May and September 2010 & 2011). These 'outliers' are caused by specular reflections at surfaces of high reflectivity in the radiometer's source area (Chapter V). In Chapter V the impact of surface heterogeneity and cloud cover on observations of surface albedo is investigated. There it is concluded that the lower bulk surface albedo of 0.11 at KSS (compared to 0.14 at KSK) is more representative of the local-scale.

IV.3.2.2 Long-wave radiation

Variations of incoming long-wave radiation ($L_{\downarrow}$) can be expressed as a function of near surface atmospheric conditions (temperature and humidity) and presence of (low) clouds (Flerchinger et al. 2009). The annual cycle of the observed down-welling thermal radiance (Figure IV.4) is characterised by larger energy fluxes during warm and dry times of the year (Figure IV.3). At the two central London sites, daily maxima of $L_{\downarrow}$ range from about 350 W m^{-2} in winter to 430 W m^{-2}

in summer. Diurnal patterns under clear sky conditions are mostly governed by diurnal temperature variations, while long-wave radiation increases during overcast conditions. In the winter, lower air temperatures often coincide with clear sky conditions. Relatively warm autumn (or winter) periods (e.g. Nov 2011) are associated with overcast conditions that reduce radiative cooling during the night. Accordingly, the lowest monthly mean $L_{\downarrow}$ was observed in December 2010 (285.9 W m^{-2}), the coldest month in the observation period (Section IV.3.1) and the coldest month on record for the whole UK (national records since 1910, MetOffice 2013).

While incoming long-wave radiation exhibits fairly strong variability throughout the year as a response to the water content of the atmosphere, its outgoing counterpart is characterised by differing behaviour between warm and cold months (Figure IV.4). Outgoing long-wave radiation ($L_{\uparrow}$) is directly related to the skin temperature of the urban surface, hence depends on the amount of total incoming radiative energy $Q_{\downarrow} = K_{\downarrow} + L_{\downarrow}$ (in addition to convection or conduction processes) and the three-dimensional structure of the urban surface. The latter enables multiple reflections of incoming radiation (both, short- and long-wave) which increases energy absorption by the urban canopy. However, it also is responsible for the formation of complex shadow patterns, reducing the fraction of the complete three-dimensional surface that receives direct solar insolation, and hence diminishing the surface temperature in certain areas of the canopy. This explains the variations of the diurnal range of $L_{\uparrow}$ over the course of the year, with larger scatter seen from April to September (Figure IV.4). During winter the urban fabric does not warm up as much, rather it stays close to the near surface air temperature whose pattern can then be recognised in the time series of outgoing long-wave radiation (compare T_{air} in Figure IV.3 and $L_{\uparrow}$ in Figure IV.4, e.g. Feb 2012).

The dependence of long-wave radiation fluxes on cloud cover was examined separately for day and night-time (Figure IV.5). In order to account for variations of day-length, medians by cloud cover percentage are presented as a function of solar elevation angle during daytime (Figure IV.5e) and as a function of standardised night-time, i.e. night-time normalised by night-length (Figure IV.5a-c). Ceilometer cloud cover percentages were binned into 12 classes. Their frequencies (presented as total duration in days) reveals that clear-sky (cloud cover = 0%) and overcast conditions (cloud cover = 100%) depict the most common classes. The high frequencies at both ends of the distribution, compared to adjacent classes (e.g. compare = 100% to 90% < cloud cover ≤ 100%), were confirmed by comparison to cloud cover derived from diffuse radiation measurements (not shown). The distribution is probably explained by persistence of meteorological conditions that favour overcast and clear-sky conditions for longer periods (up to several days), while partly cloudy skies are associated with more variable atmospheric conditions.

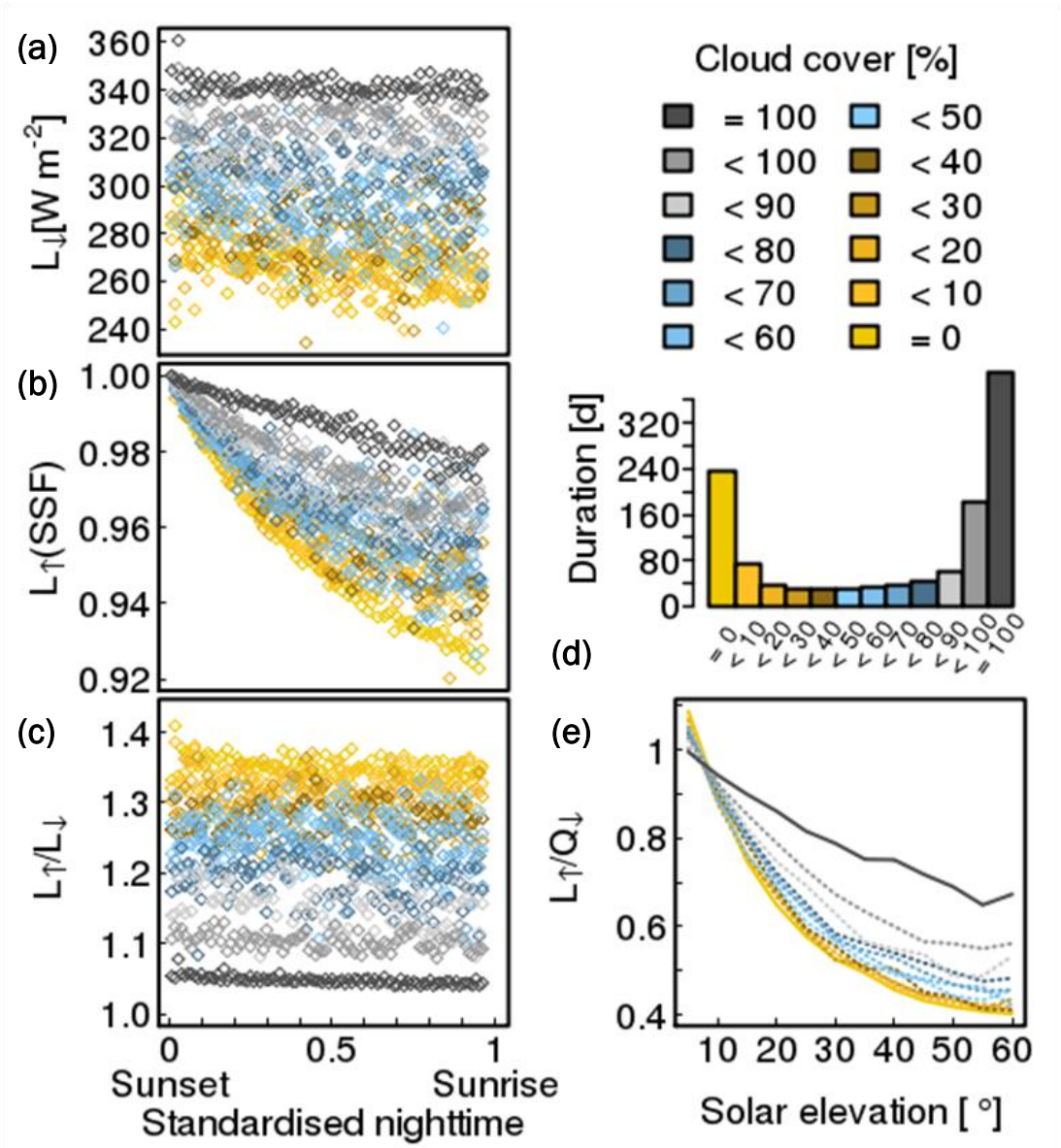

Figure IV.5: Long-wave radiation fluxes stratified by cloud cover [%] separately for (a-c) night (by standardised night-time) and (e) day (by solar elevation angle); (d) Accumulated duration of detected cloud cover in days [d] in 10% bins (interval definition: lower limit ≤ cloud cover < upper limit; except for clear sky (totally overcast) conditions with cloud cover = 0% (= 100%)). Only those periods are included when measurements of all relevant radiation components are available. (a) Incoming long-wave radiation, (b) outgoing long-wave radiation normalised by the value observed at sunset: sunset fraction SSF, (c) ratio of outgoing and incoming long-wave radiation, and (e) outgoing long-wave radiation normalised by total incoming radiation $Q_{\downarrow}$. Observations (CNR1) are from KSK (Oct 2008–Oct 2009) and KSS (Nov 2009–Mar 2012).

Clouds enhance incoming long-wave radiation, which is particularly important during the night when this is the only incoming radiative flux (Figure IV.5a). When night-time values of incoming long-wave radiation were normalized by the sunset value (termed here 'sunset fraction', SSF), a slight increase (decrease) is evident over the course of the night for overcast (clear sky) conditions (not shown). This is probably explained by the different cooling rates of the atmospheric column and the associated changes in vapour pressure. In terms of absolute values, no apparent impact of cloud cover can be identified in night-time outgoing long-wave radiation. However, the SSF of $L_{\uparrow}$ clearly illustrate that cooling rates of the urban surface decrease with

increasing cloud cover (Figure IV.5b), i.e. over the course of a night with 100% (0%) cloud cover $L_{\uparrow}$ decreases by an average of 2% (7%). This is probably explained by the fact that clear sky nights often follow a day with low cloud cover so that more energy was stored in the canopy and surface temperatures tend to be higher. However, a small fraction of the outgoing long-wave radiation is attributed to reflected and re-emitted $L_{\downarrow}$, introducing a secondary dependence to cloud cover. The amount of reflected $L_{\downarrow}$ is particularly important where materials with low emissivity are present. The night-time radiation balance (Figure IV.5c) reaveals that up to 35% more energy is observed to leave the surface via radiative processes than is received ($L_{\uparrow} \approx 1.35\ L_{\downarrow}$ for clear skies) whereas the long-wave fluxes are close to equilibrium for overcast sky conditions.

During daytime, when short-wave radiative input significantly increases the total incoming radiation flux, the median ratio of outgoing long-wave radiation to all-wave radiative input ($L_{\uparrow}/Q_{\downarrow}$) is lower than unity (Figure IV.5d). $K_{\downarrow}$ accounts for the pronounced variation with solar elevation angle during daytime with minimal values of the median $L_{\uparrow}/Q_{\downarrow}$ fraction at maximum irradiance (for maximum sun elevation and clear sky conditions) of about 0.4. Hence, for a certain solar elevation angle during daytime, the normalised outgoing long-wave radiation $L_{\uparrow}/Q_{\downarrow}$ increases with higher cloud cover.

Net all-wave radiation Q* (Figure IV.4) combines all four components of the radiation balance and hence incorporates all their dependencies on sun elevation, cloud cover and surface characteristics. Daily maximum values range from about 150 W m^{-2} in winter to about 700 W m^{-2} in summer. The overall slightly lower values of the radiation budget before November 2009 are explained by KSK's higher surface albedo (Chapter V). During winter months, radiative cooling exceeds the gain from solar input so that monthly median Q* becomes negative.

IV.3.3 Temporal variations of surface energy exchange

Net all-wave radiation Q*, sensible heat flux Q_H and latent heat flux Q_E all exhibit a pronounced diurnal cycle throughout the year (Figure IV.6). In addition to their monthly median diurnal patterns (lines, Figure IV.6), accumulated energy fluxes (also for day- and night-time) are presented (bars, Figure IV.6). Diurnal and seasonal patterns seen in the net all-wave radiation are formed by a combination of the processes affecting its components (Section IV.3.2). Nocturnal radiative cooling (negative Q*) is generally stronger from March till October when more heat is stored within the urban canopy and surface temperatures are higher (compare Figure IV.3 and Figure IV.6). However, due to reduced daylight periods in winter, more energy is lost by the surface volume during the night than gained during the few hours of incoming solar radiation. The monthly 24 h - radiation budget is negative from November to January. During these months, total upward energy flux during the night (1.2–3.2 MJ d^{-1} m^{-2}) exceeds the energy gained during the short days (0.2–1 MJ d^{-1} m^{-2}). Particularly large total night-time radiation flux (> 3 MJ d^{-1} m^{-2}) also occurred in spring and autumn (Apr & Sep 2011, Mar 2012). However, these months had large energy daytime gains associated with predominantly clear sky conditions, high air temperatures, low humidity and small precipitation amounts (Figure IV.3). Positive monthly

median net-all wave radiation from March to September provides energy for turbulent fluxes and conduction into the surface. The largest gain of radiative energy by the surface is between April and July, ranging between 3.3–11.2 MJ d^{-1} m^{-2}. February and November mark the transition periods with very small total fluxes in either direction.

Sensible heat flux Q_H is largest from April to September (Figure IV.6) when its monthly median diurnal maxima often exceed 200 W m^{-2} and accumulated daytime upward energy transport (about 6.7–9.8 MJ d^{-1} m^{-2}) accounts for most of the 24 h - total flux (about 9.0–12.2 MJ d^{-1} m^{-2}). During colder months when net all-wave radiation provides less energy into the system, daytime sensible heat fluxes are considerably lower. However, even at these times sensible heat flux continues to provide significant energy transport away from the surface into the urban boundary layer, with median diurnal maxima of at least 100 W m^{-2} (December and January). This suggests that strong anthropogenic energy sources are located in the study area. A combination of anthropogenic heat flux and a large heat storage capacity of the urban canopy could further explain the constant night-time upward transport of sensible heat at the central London site (Figure IV.6). As found for other dense urban environments (e.g. Mexico City, Velasco et al. 2005), Q_H remains positive throughout the night and is observed to almost exclusively be responsible for energy transport away from the surface (only 0.5% of all nocturnal Q_H estimates are negative).

Monthly median nocturnal Q_H fluxes have lower magnitudes during winter (around 50 W m^{-2}) than summer (around 100 W m^{-2}), but these still are larger flux values than found in comparable studies such as for Marseille (Grimmond et al. 2004) or Basel (Christen and Vogt 2004). Due to the short day-length in the cold season, day- and night-time totals are comparable in November and February. In December and January, nocturnal sensible heat flux even exceeds daytime totals. Thus, the monthly 24 h - sensible heat flux never falls below 5.3 MJ d^{-1} m^{-2} (Nov 2011).

A comparison between the monthly median incoming radiative energy and the turbulent sensible heat transport indicates a large anthropogenic component in the surface energy balance. In general, total monthly turbulent sensible heat flux exceeds radiative input (by up to 8.5 MJ d^{-1} m^{-2}, Jan 2012) and only for one month in the observation period (Jun 2010) is it less than the 24 h - radiation budget (by 0.8 MJ d^{-1} m^{-2}). Some of this discrepancy might be explained by the differing source areas of the two energy flux estimates. However, especially during winter, when both fluxes characterise net energy loss by the urban surface volume, considerable energy would need to originate from alternative sources. Under the assumption of a balanced storage heat flux (over the course of 24 hours) and negligible horizontal advection, this is most likely associated with anthropogenic activities (Section IV.3.6).

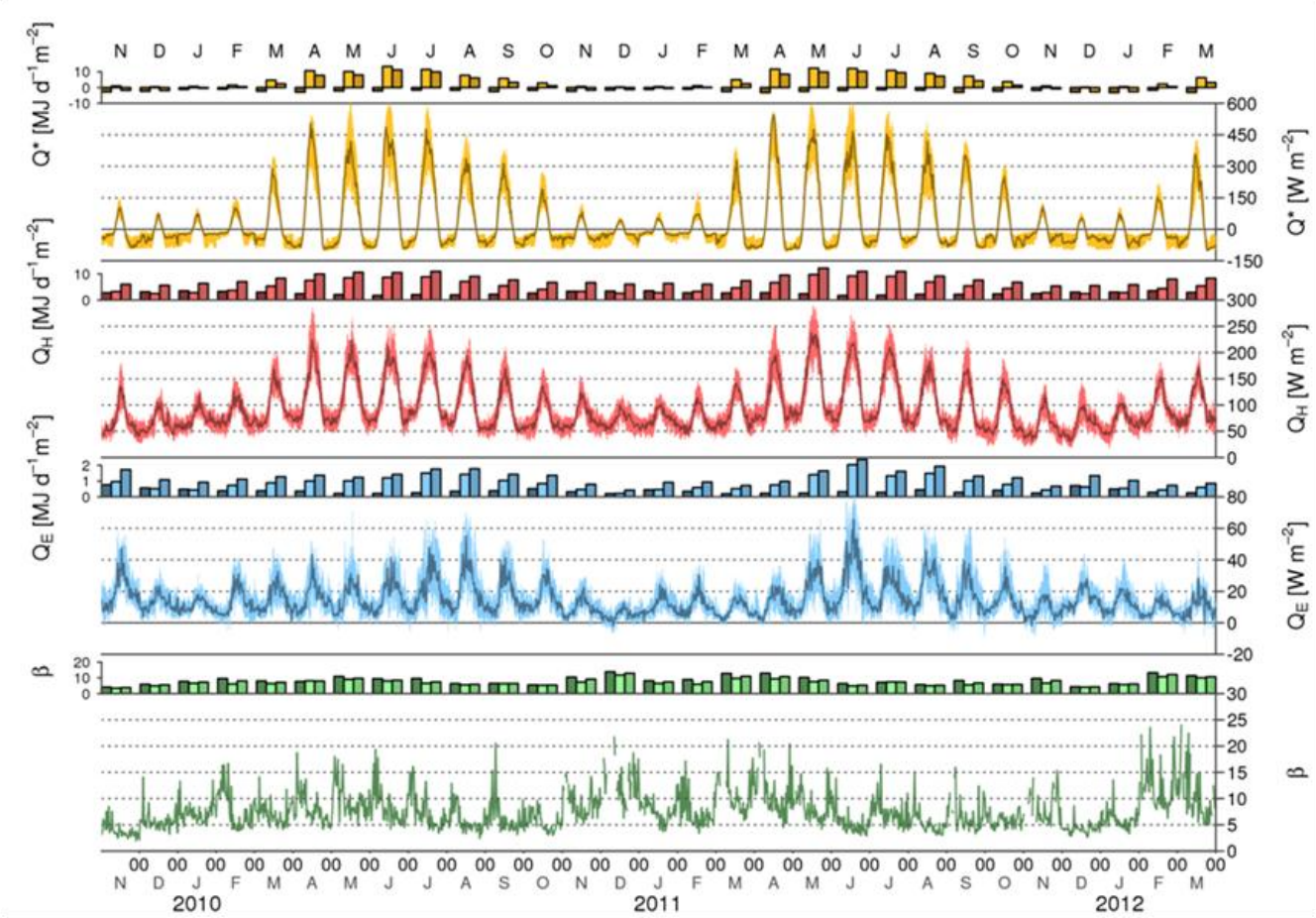

Figure IV.6: Monthly energy fluxes at KSS (11/2009–03/2012): (vertical bars) accumulated energy flux for (left) night, (middle) day, and (right) total 24 h; (solid line) median diurnal patterns with inter-quartile range (shading) of net all-wave radiation Q*, sensible heat flux Q_H, and latent heat flux Q_E. Lowest panel (solid line) is the Bowen ratio (β - ratio of the monthly median diurnal Q_H/Q_E fluxes); (vertical bars) mean β separated into (left) night-time, (middle) daytime, and (right) total 24 h. β only calculated for times with considerable latent heat flux, i.e. $|Q_E| > 3$ W m^{-2}.

Note, there is evidence that the KSS fluxes might be affected by advective fluxes under some flow conditions (Chapter V) which adds uncertainty to the residual term. However, those situations are associated with a decrease in sensible heat flux and hence a reduction in the discrepancy between radiation and turbulent fluxes.

The turbulent latent heat flux Q_E observed at KSS (Figure IV.6) exhibits a diurnal pattern that is presumably driven by the course of available energy as the moisture availability in central London can be assumed to not vary systematically over a 24 h period. The surface cover is dominated by impervious surfaces with little vegetation (Chapter V). Hence, seasonal phenological variations (which might be strong enough to contribute slightly to enhanced evaporation from late spring to early autumn) would be difficult to detect in the local scale measurements. The River Thames to the south and southwest of the site was not identified as a significant source for evaporation and the spatial morphology may impede the measurement of large local-scale EC evaporation fluxes from this source (Chapter V). Monthly total latent heat flux ranges between approximately 0.4–2.4 MJ d^{-1} m^{-2}. As for the sensible heat flux, nocturnal fluxes are larger during warmer months, but with generally small magnitudes (< 20 W m^{-2}). Occasionally, the monthly median latent heat flux is very close to zero or even negative. This could correspond to downward moisture transport. However, given the uncertainty of these measurements, values of such small magnitude should be interpreted with caution.

Precipitation seems to be the most likely driving factor for temporal variations in the evaporative flux. Months with high amounts of accumulated rainfall (Section IV.3.1, Figure IV.3) tend to have increased Q_E and a corresponding lower Bowen ratio β (here calculated as monthly median diurnal Q_H over Q_E). The Bowen ratio (Figure IV.6) is persistently dominated by the sensible heat flux. Monthly median hourly values mostly range between five and ten (solid line in lower panel of Figure IV.6). In comparison to previous urban surface flux observations, these Bowen ratio values are at the higher end. Most flux sites in European cities have more vegetation in the measurement footprint. At these sites, Bowen ratio values are below 2 during summer and up to about 5 when vegetation effects are limited during winter (Goldbach and Kuttler 2012, their Table 1) or the vegetation fraction in the source area of the flux site is extremely small (Marseille, France; Grimmond et al. 2004). An example for observations at a vegetation-free site is presented by Christen and Vogt (2004) who measure a Bowen ratio of 6 at the top of a canyon in Basel in the summer. On a monthly basis, the mean Bowen ratio is slightly larger during the night. However, generally it is quite independent of the averaging period (compare 24 h, nocturnal and daytime bars in lower panel of Figure IV.6).

IV.3.4 Atmospheric stability

The persistently strong net upward motion of warm air can be expected to have an influence on the atmospheric boundary layer in central London with important implications for air quality and larger scale meteorological processes. The observed positive nocturnal sensible heat fluxes impact the atmospheric stability, which is represented by the stability parameter $\zeta = z'/L$, where L

is the Obukhov length and z' the effective height ($z' = z_m - z_d$, the difference between measurement height z_m and zero-plane displacement height z_d). The relative frequency of stability conditions by time of day (Figure IV.7), divided into four stability classes (extremely unstable: $\zeta < -0.5$, unstable: $-0.5 \leq \zeta < -0.1$, neutral: $-0.1 \leq \zeta < 0.1$, and stable: $0.1 \leq \zeta$) and for warmer periods with higher sensible heat flux (Apr–Sep) and colder periods with lower sensible heat flux (Oct–Mar), shows that, overall, only 0.5% of all observations are classified as stable. This could be explained by the predominantly high turbulent sensible heat fluxes (no minimum threshold has been applied for Q_H during the calculations of ζ). In addition to the strong upward motion maintained by the dense urban environment, the high roughness of the urban canopy (Chapter V) is reflected in the stability parameter. While it is probably the significant buoyancy that inhibits stable stratification, the magnitude of the friction velocity u* (not shown) seems to determine which of the remaining three stability classes is applicable.

At KSK (Figure IV.7a), local stability is neutral more than half the time in both parts of the year and about 15% of the time very unstable. The diurnal pattern of unstable conditions varies little with season but daytime frequencies increase in Apr-Sep at the expense of neutral conditions which become more likely at night. At KSS, the variations with season appear a bit more complex (Figure IV.7b). In the colder months (Oct–Mar) the probability of neutral and unstable conditions is similar with both around 40–50% over the course of the day. Diurnal variations favouring neutral conditions during the night compared to the day are hardly detectable. However, during the warmer months (Apr–Sep) neutral conditions make up less than 40% until late afternoon (1600 UTC) and become more likely (even exceeding 50%) in the evening hours. Very unstable conditions are more frequently observed in the early morning hours and unstable conditions during daytime. Overall, about a third of the observations at KSS are classified as neutral.

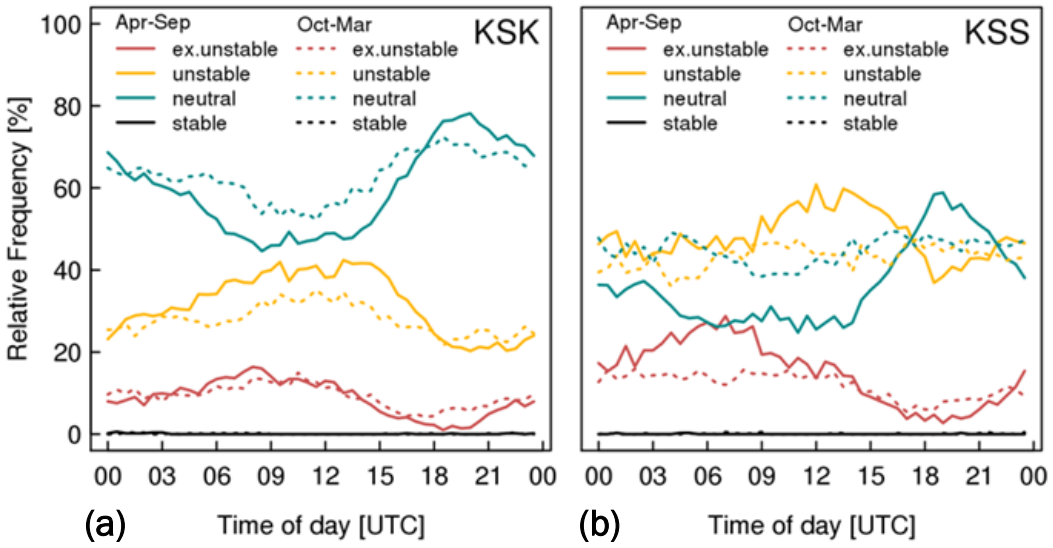

Figure IV.7: Relative frequency of stability conditions by seasons or strength of sensible heat flux: spring/summer (Apr-Sep, stronger) and autumn/winter (Oct-Mar, weaker) for (a) KSK and (b) KSS. See text for stability definitions.

Presumably, observations at the lower KSK site are more influenced by the immediate surroundings than those at KSS (Chapter V). A combination of variations in radiative energy input and increased roughness effects explains the increased probability of neutral local stability at this lower site. The observations at KSS (Figure IV.7b) are a result of surface atmosphere exchanges over a larger, local scale area where storage heat flux and anthropogenic heat flux play a major role in the surface energy balance (Section IV.3.6). These maintain buoyant heat fluxes and hence make neutral stratification less likely.

At both sites during Apr–Sep neutral conditions show their peak frequency around 2000 UTC. The evening peak of neutral conditions is more pronounced at KSS, where this reaches 60% at 1800 UTC but drops back to 40% at midnight. These diurnal variations appear to be associated with the diurnal patterns of Q_H and u* relative to each other (not shown). Especially during summer months, friction velocity remains high in the evening hours and decreases to night-time magnitudes later than the turbulent heat flux, causing peak ζ-values during that time of day. The diurnal pattern of the friction velocity is less pronounced during winter. These flow patterns may be influenced by horizontal advection induced by the River Thames (Chapter V).

IV.3.5 Energy partitioning

The timing of turbulent energy transport with respect to solar noon is evaluated by normalizing the median conditions (based on all data) by their respective maxima (Figure IV.8). This climatological analysis confirms that both turbulent fluxes start rising in the early morning hours and reach their maxima later than the radiative fluxes because of the uptake of energy by the storage heat flux. In addition to this well-known time lag between radiative input and turbulent surface energy exchange, a shift between the sensible heat flux and the latent heat flux is observed. The normalised estimates show that evaporation is relatively higher in the afternoon compared to the morning hours, which is probably explained by the rising water vapour pressure deficit. The relatively stronger evaporation after solar noon results in a pattern of decreasing Bowen ratio (diamonds in Figure IV.8) from ~7.4 to ~5.5. The slightly decreasing relative importance of sensible heat leads to a robust estimate of daytime Bowen ratio of 6.4 for the central London site (6.5 for hours when $K_{\downarrow} > 0$ W m^{-2}; 6.4 for hours when $Q^* > 0$ W m^{-2} and a period of 2 or 4 h around solar noon). The independence of the chosen time interval suggests that, due to the diurnal variation of energy partitioning, no uncertainty should arise from differing definitions of the time period of interest when comparing the average Bowen ratio estimate to those found in other studies (Goldbach and Kuttler 2012), which often do not have consistent daytime periods applied for the calculation of β.

On a monthly time scale, times with high accumulated precipitation seem to slightly favour the evaporation flux, leading to smaller Bowen ratio values (compare Figure IV.3 and Figure IV.6). However, due to the overall very weak evaporation fluxes, the potential link between rainfall and energy partitioning is not always clearly evident in the magnitude of Q_E. Rather, available energy appears to be the dominant driving factor. At shorter time intervals again, it can be illustrated

that more energy is used for evaporation directly after rain (see the frequency distribution of the Bowen ratio relative to the time since rainfall was recorded; Figure IV.9; KSS). Due to quality control restrictions (Chapter III) no observations are available during rainfall and the subsequent 30 min period. In the periods 1–6 h after rain, the Bowen ratio is most frequently between 1–2.5 and for some periods within the first 2–3 h Q_E is larger than Q_H ($\beta < 1$). With increasing time after rainfall, small Bowen ratio values become less likely and slightly higher values (around 3) have the highest probability until about 12 h post-event. About 8–9 h after rainfall, Bowen ratio values of greater than 10 are more probable. While evaporation is important immediately following precipitation, the sensible heat flux quickly regains its dominance. As the locally weighted regression (Lowess) and the median curve show (Figure IV.9), the energy used by Q_E decreases rapidly in the first 12 h and then the energy partitioning behaves more similarly. In some cases, such as when the overall fluxes (especially the solar input) are low, water might remain on the surface for longer. However, analysis shows that after ~12–18 h most precipitation events no longer exert control over the energy partitioning between the turbulent fluxes of latent and sensible heat. Since the site is located in a dense urban setting where impervious surfaces dominate the land cover (Chapter V), efficient surface runoff is likely responsible for this comparatively short time interval; at other sites with more bare soil or vegetation fractions, rain events can influence the energy balance over several days (e.g. Ward et al. 2013).

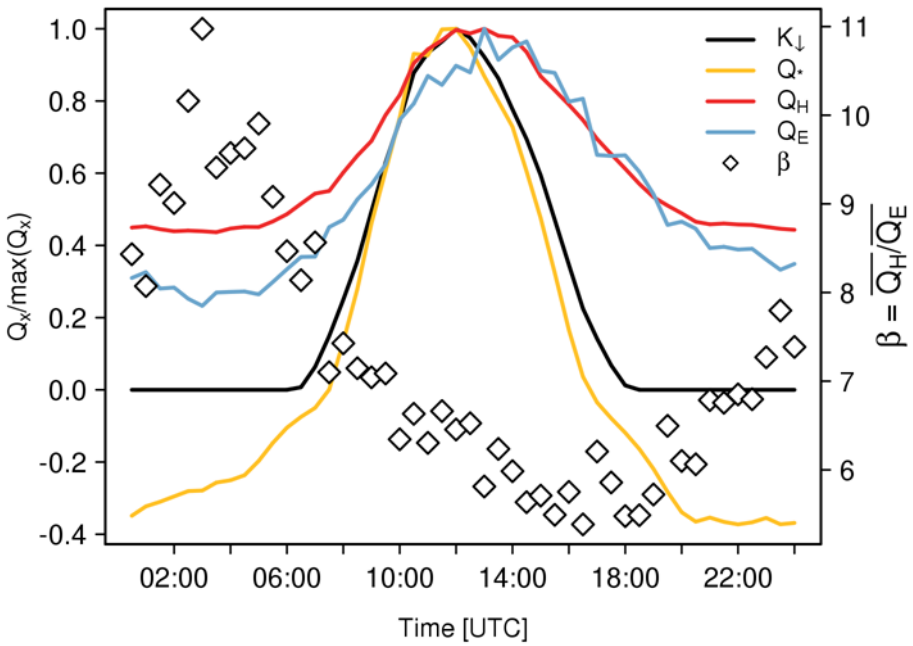

Figure IV.8: Median diurnal pattern of energy fluxes Q_X at KSS, normalised by respective maximum max(Q_X): net all-wave radiation Q*, shortwave incoming radiation $K_\downarrow$, and turbulent fluxes of sensible heat Q_H and latent heat Q_E. Bowen ratio β (diamonds) calculated from the median diurnal patterns of sensible and latent heat flux (restricted to $|Q_E| > 3$ W m^{-2}).

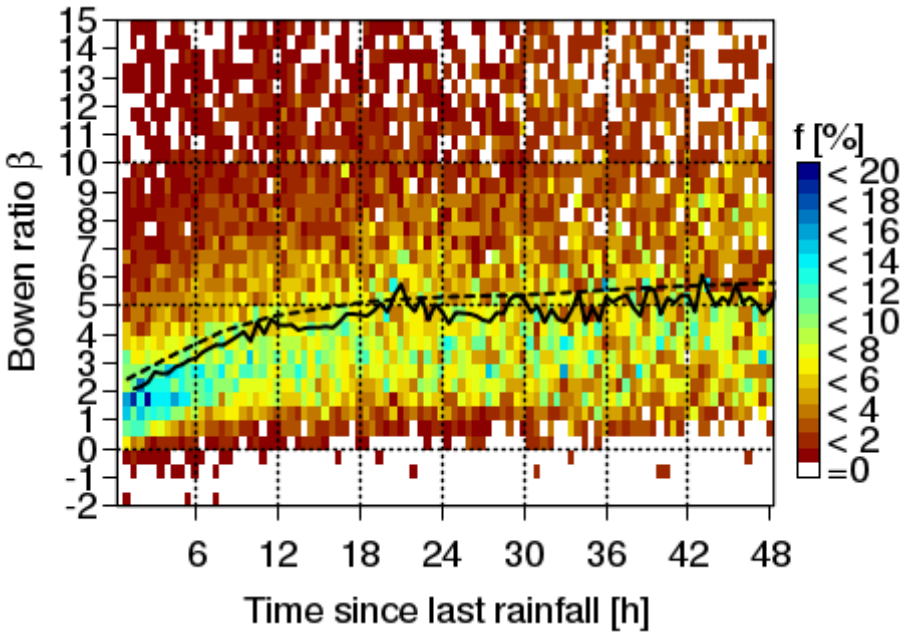

Figure IV.9: Frequency distribution (frequency f [%]) of Bowen ratio β (calculated for times with considerable latent heat flux, i.e. $|Q_E| > 3$ W m^{-2}) by time since last rainfall. Statistics (excluding β > 25, i.e. 2% of all available Bowen ratio values): locally weighted polynomial regression using Lowess filter with a smoother span of 1/5 (dashed line) and median Bowen ratio by time since rainfall (solid line). Only Bowen ratios β < 15 and times of up to 48 h after rainfall are shown.

IV.3.6 Monthly surface energy balance

To analyse inter-monthly variations, total fluxes measured (methodology described in Section IV.2.2) for the 3.5-year period are considered (Figure IV.10). The energy gain and loss by the urban surface volume (positive and negative bars in Figure IV.10) are shown with the anthropogenic heat flux (Q_F) derived using the GreaterQf model (Iamarino et al. 2012; Section IV.2.2). As suggested in the discussion of sensible heat flux estimates (Section IV.3.3), anthropogenic heat flux plays a major role in the surface energy balance of the study area. Monthly total model estimates selected to represent the footprint of the turbulent fluxes (Section IV.2.2; Chapter V) range between 8.6 MJ d^{-1} m^{-2} (Aug 2009) and 12.4 MJ d^{-1} m^{-2} (Dec 2010), with building emissions contributing the majority of energy. During winter, energy input appears to be governed by anthropogenic impacts while net radiative input reaches similar magnitudes as Q_F during summer. Only in June and July (and May 2011) does the energy gained by net radiation become more important than that from anthropogenic emissions. Although these data do not permit a detailed analysis of the relation between Q* and Q_F, the combination of the two fluxes provides qualitatively reasonable patterns. While maximum radiative input occurs around June, anthropogenic impact becomes minimal from June to October due to its dependence on air temperatures (Figure IV.2; Iamarino et al. 2012). Anthropogenic heat flux reaches a maximum in December and January, when radiation has a negative effect on the surface energy budget.

As discussed, both turbulent fluxes generally transport energy away from the surface (Section IV.3.3). Whereas Q_H has a very pronounced seasonal variability, Q_E responds strongly to moisture availability from precipitation (Section IV.3.5). In Chapter V the effects of source area characteristics on both radiative and turbulent energy fluxes at the two nearby sites are investigated, which explains that turbulent fluxes observed at KSK (Oct 2008 - Oct 2009 selected for Figure IV.10) are smaller (on average by 40%) than at KSS (Nov 2009–Mar 2012) because of differences in the flow conditions observed at the two heights. At both, the overall monthly energy loss (negative bars in Figure IV.10) corresponds well to the pattern of available energy (positive bars in Figure IV.10). As the sum of radiative and anthropogenic input is highest in late spring/early summer strongest turbulent fluxes are observed at this time of the year. In general, similar monthly patterns are found for negative and positive monthly totals in all years. Quantitatively, the comparison suggests that high sensible heat flux observations, including the explicit night-time contributions discussed (Section IV.3.3), are physically reasonable for this dense urban environment. Still, both much larger and smaller Q_H could occur. From GreaterQf model results, anthropogenic heat emissions could be larger than the sensible heat fluxes observed with the EC systems. Horizontal advection may cause reduced fluxes for certain wind direction conditions (Chapter V). Thus the temporal variability is critical and long-term quantification may be misleading in the context of the overall energy balance analysis (Figure IV.10).

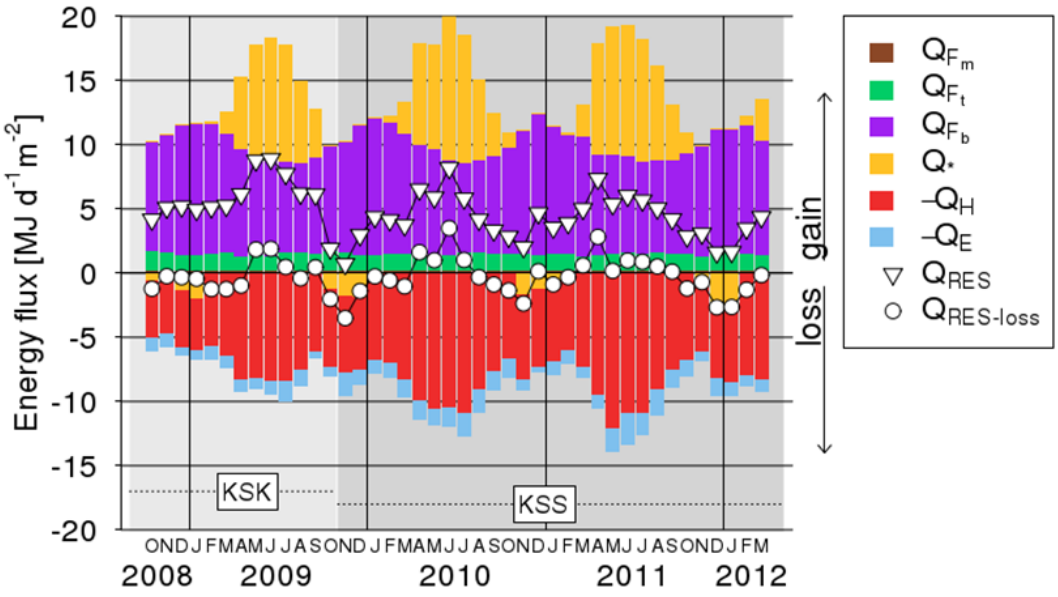

Figure IV.10: Mean daily energy fluxes by month: modelled anthropogenic heat flux (metabolism Q_{Fm}, road traffic Q_{Ft}, and building emissions Q_{Fb}), and observed net all-wave radiation (Q*), sensible heat flux (Q_H), and latent heat flux (Q_E) at KSK (10/2008-10/2009; only 5 days of observations available for 10/2009) and KSS (11/2009–03/2012). Residual (Q_{RES}) assumes energy balance closure (EBC) by month, and $Q_{RES\text{-}loss}$ with EBC assuming an underestimation of the turbulent fluxes by 20% at KSS (48% at KSK accordingly) and overestimation of the anthropogenic heat flux by 26%. Positive (negative) fluxes indicate energy gain (loss) by the surface volume.

The daily average (24 h mean) anthropogenic heat flux around the sites ranges from ~73 W m^{-2} (river dominated model grid in Jul 2010) to 159 W m^{-2} (impervious dominated model grid in Dec 2010). These values are high compared to those estimated for other central city areas (around 20 W m^{-2} in Basel, Christen and Vogt 2004; up to 75 W m^{-2} in Marseille during summer, Grimmond et al. 2004; about 85 W m^{-2} in Singapore, Quah and Roth 2011). Daily average anthropogenic heat fluxes from building emissions (GreaterQf model) are from 64 to 131 W m^{-2} whereas the building scale heat flux observations (Chapter III) at the KSS site were ~70 W m^{-2} for sensible heat flux and 7 W m^{-2} for the latent heat. This suggests that the derived building emissions (Figure IV.2) may be too high. Anthropogenic heat flux estimates are extremely scale-dependent (e.g. Chapter III; Lindberg et al. 2013) so spatial (mis)alignment of the modelled fluxes to the source area of the turbulent fluxes (Section IV.2.2, Figure IV.2) will introduce uncertainties. Despite these uncertainties, the large observed Q_H can only be maintained by anthropogenic heat sources which exceed the radiation balance in terms of providing energy to the surface nearly all year round.

Assuming energy balance closure, the residual flux Q_{RES} (Section IV.2.2) includes the storage heat and all the uncertainties of the measured and modelled energy balance components. A first estimate suggests the residual Q_{RES} could exceed 8 MJ d^{-1} m^{-2} in some months (triangles, Figure IV.10), with highest values when energy gain is largest (mean for Apr-Aug: $Q_H + Q_E$ is 9.3 MJ d^{-1} m^{-2} [KSK 2009] or 12.0 MJ d^{-1} m^{-2} [KSS 2010-2011] and $Q^* + Q_F$ is 16.8 MJ d^{-1} m^{-2} [KSK] or 18.0 MJ d^{-1} m^{-2} [KSS]) and the minima in winter months with some large outgoing fluxes (Q_{RES} is 0.7 MJ d^{-1} m^{-2} in Nov 2009 due to high Q_E and 1.6 MJ d^{-1} m^{-2} in both Dec 2011 and Jan 2012). Although Q_{RES} remains positive suggesting a net warming, the seasonal pattern seems appropriate. However, these results include any errors (e.g. spatial mismatch of source areas, contributions of horizontal advection, and differences arising from combining observed and estimated data) so further examination of Q_{RES} is warranted.

The results suggest that some outgoing energy is not accounted for, energy input may be over-estimated and/or energy may be double counted. In terms of energy input, the net all wave-radiation may be slightly underestimated if the source areas of the radiometers are biased towards roof surfaces (especially at KSK; Chapter V). As noted above, the modelled anthropogenic heat flux may be over-estimated due to potential spatio-temporal mismatch with the observations and/or due to the fact that some of it being already accounted for in the long-wave radiation balance and the turbulent fluxes observed. Obviously, some error is attributed to the modelled Q_f data from the GreaterQf model (Iamarino et al. 2012) itself. The latter however is still very difficult to quantify. EC fluxes do not always capture the full turbulent energy transported (e.g. Culf et al. 2004), as widely discussed in the context of the energy balance closure (Foken 2008). Further, single tower flux sites are not suitable to quantify the complex issue of horizontal advection (Spronken-Smith et al. 2006). As suggested in Chapter V horizontal advection induced by the River Thames may cause reduced sensible heat fluxes observed at KSS under some conditions. A second estimate assuming a 20% underestimation of the EC fluxes (e.g. Hollinger

and Richardson 2005; Dragoni et al. 2007) at KSS (~50% at KSK accordingly, on average Q_H at KSK is ~60% of that at KSS, Chapter V), and an over-estimation of Q_F by 26%[11] (dots, Figure IV.10) causes the mean annual residual to be zero.

The storage heat flux ΔQ_S, which is part of Q_{RES}, is expected to be close to zero at time scales of a day or a year but to have small monthly gains in summer and losses in winter as the urban fabric heats up and cools down. The residual flux does have the expected seasonal cycle. Anthropogenic sources are likely to affect the size of the actual storage term (Grimmond et al. 1991). It is closely related to radiative energy which is absorbed by the surface fabric of the canyon walls and changes with solar elevation angle and surface geometry (Moriwaki and Kanda 2004).

IV.4 Conclusions

The dataset of observed energy exchanges in the CBD of London for a 3.5 year period discussed in this paper provides new information both with respect to urban zone (dense city centre) and seasonality (multi-year observations) for two sets of instruments in proximity. From analysis of these data the following conclusions are drawn.

At night, up to 35% more energy leaves the urban surface than is received via long-wave radiation under clear sky conditions. With increasing cloud cover this percentage decreases, so that for an overcast sky $L_\uparrow$ and $L_\downarrow$ are nearly equal. Cloud cover diminishes nocturnal cooling rates of the urban surface, so that outgoing long-wave radiation decreases by only 2% over the course of a night for overcast conditions compared to 7% for clear nights. During daytime, outgoing long-wave radiation drops to 40% of the total incoming radiative energy under clear sky conditions, remaining higher for overcast periods (about 70%). Although clouds play a similar role in all environments, knowledge of the impact to long-wave radiation is important because of the significant trapping of the latter in cities, which directly impacts the storage heat and sensible heat fluxes.

Sensible heat fluxes are positive all year round, even at night, sustained by a combination of storage and anthropogenic heat fluxes. Monthly median nocturnal fluxes (50–100 W m^{-2}) are amongst the highest observed in cities to date but are not unexpected given the building densities and activities in this central city area. The strong positive Q_H inhibits stable atmospheric stratification, which rarely occurs. However, the resulting stability classification is determined predominantly by the diurnal pattern of friction velocity over the rough urban surface. Neutral stratification (about a third of time at KSS) has peak frequencies in the early evening associated with the diurnal cycles of momentum and sensible heat fluxes.

[11] Comment on Kotthaus and Grimmond (2013a): the value of 26% Q_F over-estimation is determined based on the annual cycle observed (Figure IV.10) as the best fit to reduce Q_{RES} to accumulate to zero over the course of a year.

Turbulent latent heat fluxes are very small, with variations in phenology not detectable due to the small surface vegetation fraction. Rather, variations are controlled (beyond the available energy) by rainfall. The Bowen ratio immediately following rainfall is depressed. Values of between 1–2.5 dominate for a period 1–6 h after the event. Thereafter the ratio increases as impervious surfaces remove surface water efficiently. The effect of most precipitation events is limited to a period between 12–18 h after the rain has stopped. The Bowen ratio is mostly larger than one (mean β = 6.4 at KSS) and decreases throughout the day.

Turbulent sensible heat flux systematically exceeds the input from net all-wave radiation. Analysis at the monthly time scale demonstrates these high Q_H fluxes are likely maintained by anthropogenic heat fluxes which may also exceed the net all-wave radiation nearly all year round. Modelled building anthropogenic heat fluxes remain similar once the mean daily air temperature exceeds a threshold of about 17.5°C. A monthly time scale analysis of energy balance closure, initially gives a constantly positive residual (0.7-8.9 MJ d^{-1} m^{-2}); whereas accounting for a measurement underestimation of the EC fluxes (20%) and an over-estimation of Q_F (26%) the mean annual residual is effectively zero.

To improve understanding of the role of the storage heat flux in such dense urban settings, more work is needed better characterise the scale dependence of all fluxes and to quantify the uncertainty of EC observations over complex surfaces. Also, consideration of various source areas and closer to real-time estimates of the anthropogenic heat flux is required. In Chapter V detailed footprint analysis and the role of surface controls are discussed.

Acknowledgements

This study was funded by EUFP7 Grant agreement no. 211345 (BRIDGE) and NERC ClearfLo (NE/H003231/1), supported by NERC ARSF (GB08/19), EPSRC (EP/I00159X/1, EP/I00159X/2) Materials Innovation Hub and KCL. We thank Dr Arnold Moene at Wageningen University for providing the ECpack software and for all advice regarding its usage; Dr Jiangping He for support of our data archive; Dr Catherine Souch and Dr Helen Ward for their comments; all the many people/students at KCL who contributed to the data collection; KCL Directorate of Estates & Facilities for giving us the opportunity to operate the various measurement sites. We appreciate the constructive comments and suggestions of both reviewers, which proved very helpful in the development of this work.

Appendix IV.A Discussion of uncertainty

IV.A.1 Anthropogenic heat flux

In this study (Section IV.2.2), anthropogenic heat flux estimates are based on information combined in the GreaterQf model (Iamarino et al. 2012). This model combines an extensive list of relevant data such as energy consumption, traffic counts and population density. All data are thoroughly evaluated and adequately combined in the GreaterQf model, still, the various uncertainties within the underlying data propagate to the final model results. The latter are further affected by a series of assumptions being made in the construction of the model (e.g. allocation of energy consumed based on population profiles). Given total anthropogenic heat flux is very difficult to measure from physical processes a direct evaluation of the model results cannot be performed with the means available to date. However, Iamarino et al. (2012) demonstrate the anthropogenic heat flux estimates to have physically reasonable temporal and spatial patterns and successfully put them into context to a series of other relevant studies (e.g. Hamilton et al. (2009).

The anthropogenic heat flux data applied here further take into account the thermal regime in the observation period (Section IV.2.2; Figure IV.2). Given building anthropogenic heat flux highly depends on outdoor climates, the measured air temperature was considered when calculating appropriate estimates for the study area based on the modelled data (Iamarino et al. 2012). The scatter in Figure IV.2 indicates that some uncertainty is introduced when applying the generalised functions describing the temperature dependence of Q_f. However, standard errors of this fit are small (< 3 %) and the correlations (weekday: $R^2 \approx 0.80$; weekend: $R^2 \approx 0.83$) are significant.

In order to optimise the spatio-temporal alignment of the anthropogenic heat flux estimates with the turbulent flux measurements, Q_f estimates were aggregated from a selection of model grids (200 m x 200 m) depending on the modelled turbulent flux source area (Chapter V). This effort is being made in order to account for the spatial variations in anthropogenic heat emissions that can be large in the vicinity of the site (Chapter III). Some error in the final Q_f estimate will be explained by inadequate source area assignment, however, the model data used (both for anthropogenic heat flux and turbulent flux source area) are the best estimates available. Even though both are prone to a number of uncertainties, especially in this complex urban setting (Chapter V) no methods have yet been found to quantify such uncertainties explicitly.

IV.A.2 Analysis of energy partitioning

During the discussion on energy partitioning overall monthly diurnal patterns are analysed, normalised by their respective maxima (Section IV.3.5; Figure IV.8). The associated variability over the course of the measurement period is illustrated by the inter-quartile range statistics (Figure IV.A.1).

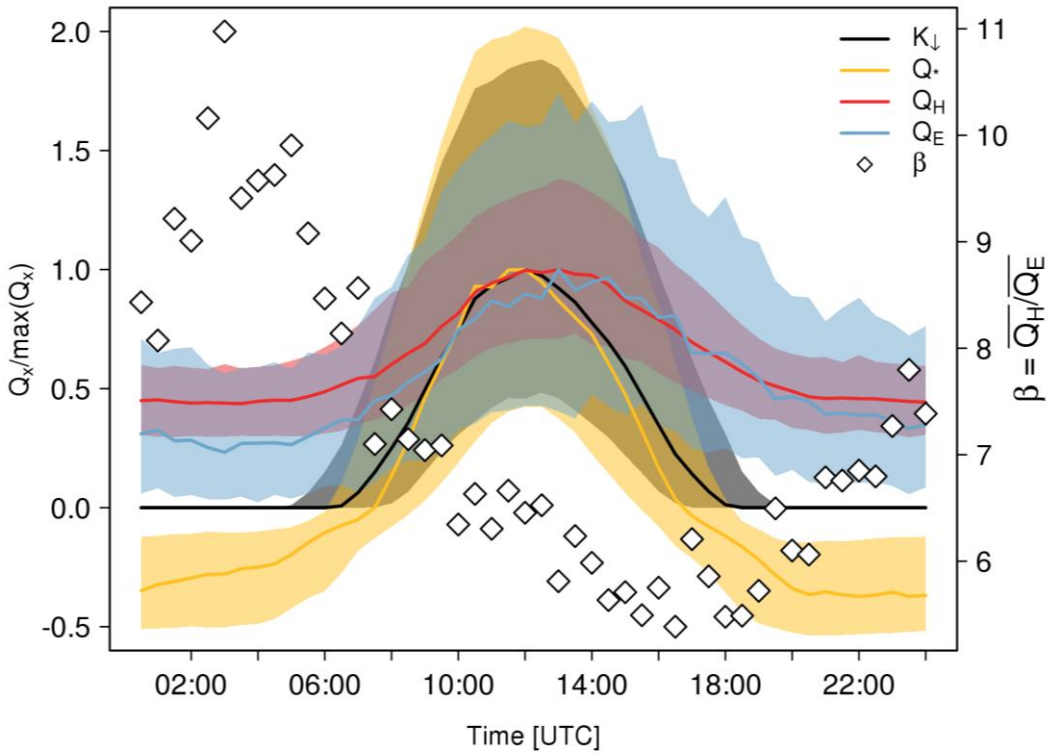

Figure IV.A.1: As for Figure IV.8 (Section IV.3.5) with inter-quartile range (shading).

The analysis (Section IV.3.5) revealed rainfall to be the main source of moisture driving evaporation. The Bowen ratio is clearly decreased in time periods succeeding a rain event (Figure IV.9). Given this finding could be influenced by the type and timing of rain events (e.g. intermittent showers keeping the surface wet), a sensitivity test is performed by further restricting time periods analysed. The general pattern of decreased Bowen ratio in the first 6-12 h succeeding a rain event is persistent for various criteria: when only events are considered with

a) no rain recorded within the succeeding 3 h or 6 h (Figure IV.A.2)
b) a duration of > 1 h or ≤ 1 h (Figure IV.A.3) or
c) a total accumulated rainfall of ≥ 0.1 mm or < 0.1 mm (Figure IV.A.4).

These test suggest that the impact of rainfall on the evaporation observed is a robust signature at this central urban site.

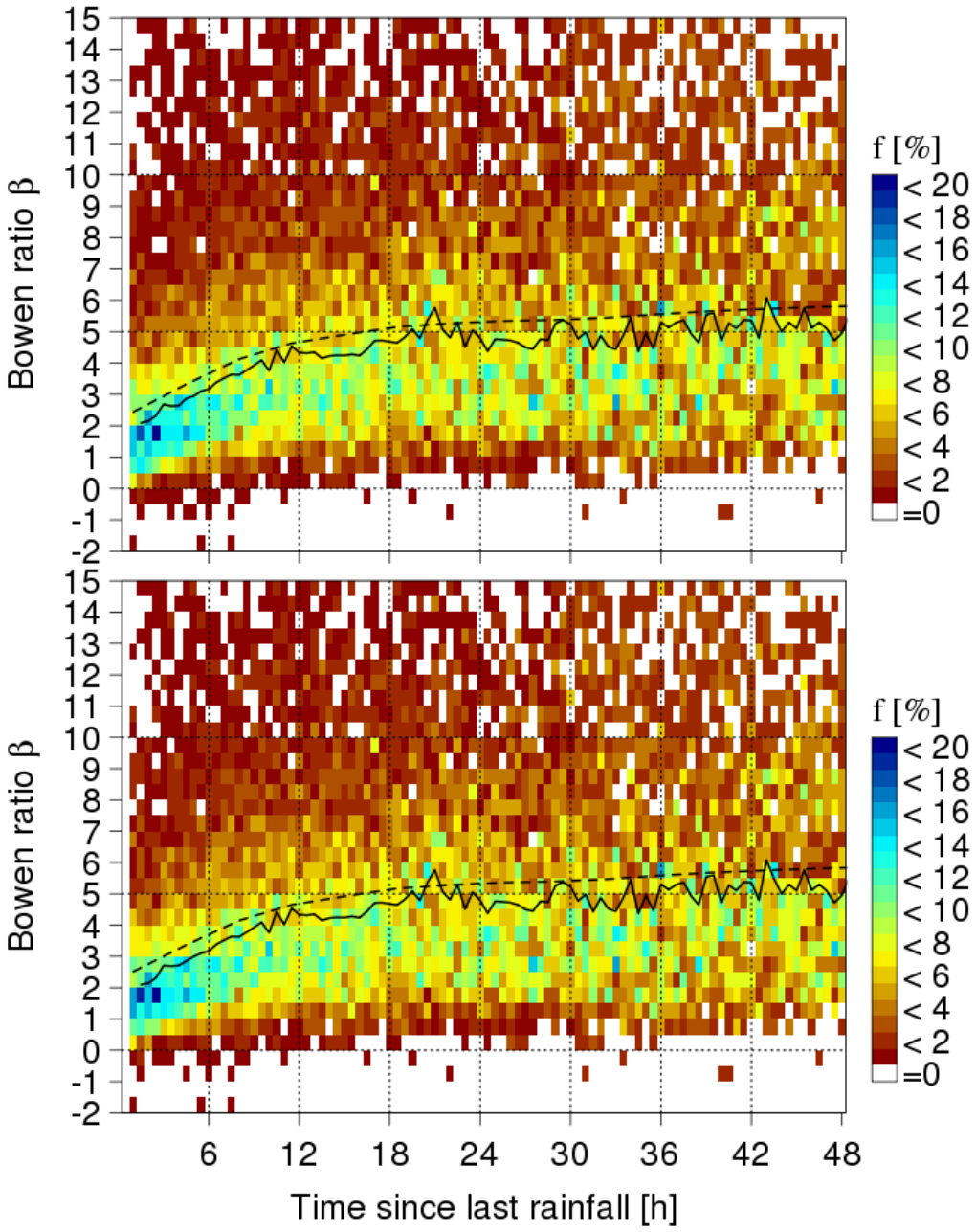

Figure IV.A.2: As for Figure IV.9 but restricted to rain events with no rainfall within the (top) 3 h and (bottom) 6 h succeeding the rain event.

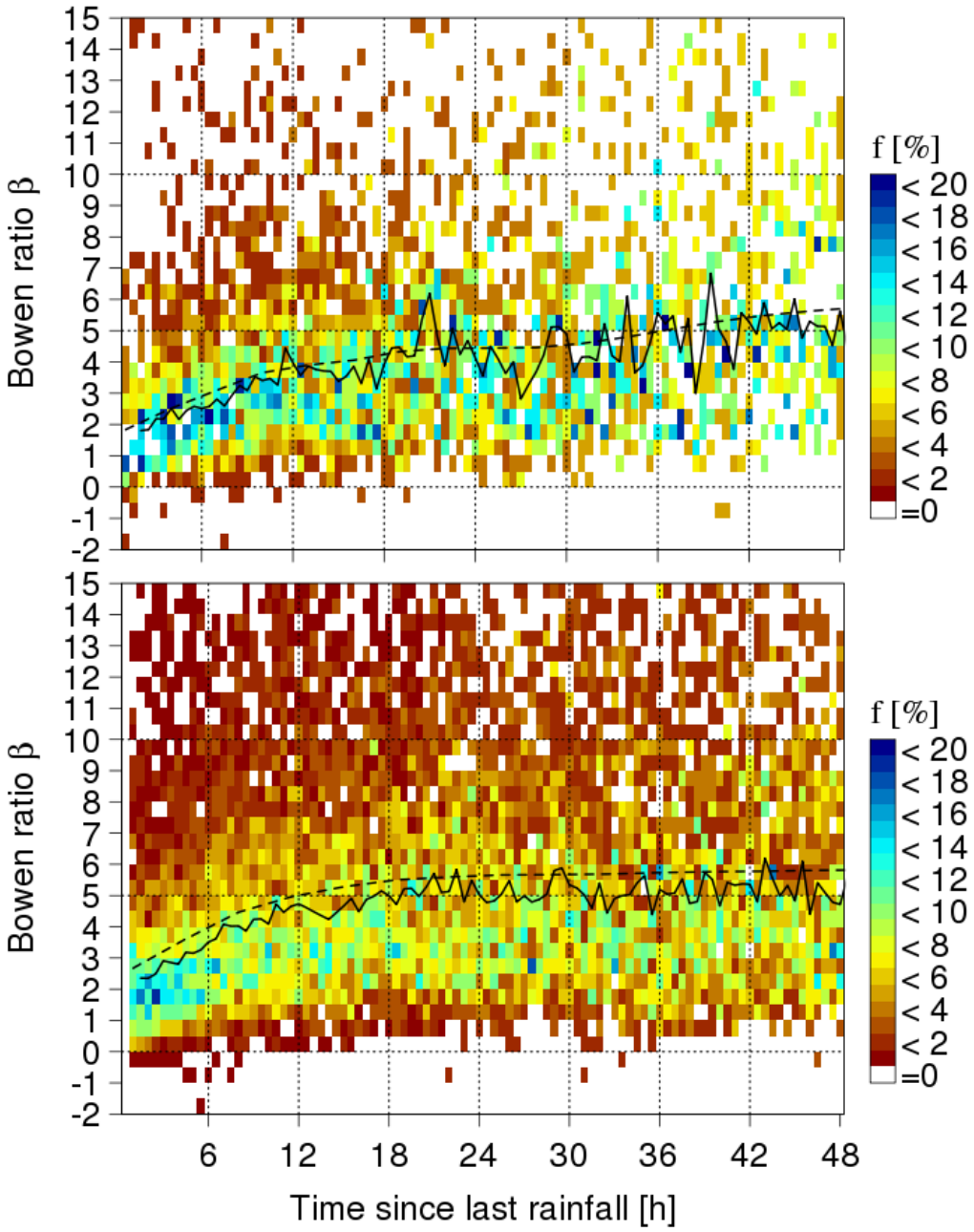

Figure IV.A.3: As for Figure IV.9 but restricted to rain events with a duration of (top) > 1 h and (bottom) ≤ 1 h.

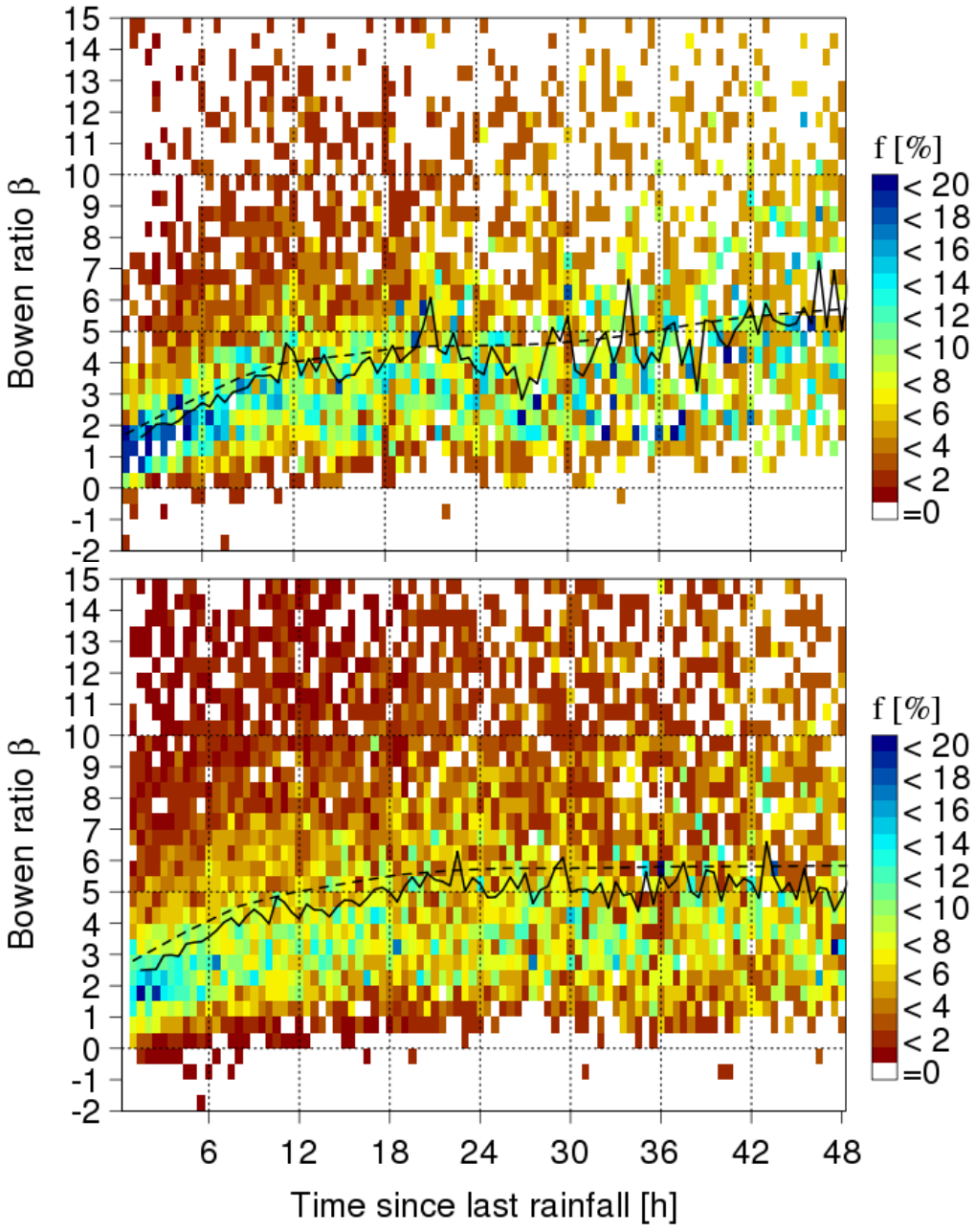

Figure IV.A.4: As for Figure IV.9 but restricted to rain events with a total of (top) ≥ 0.1 mm and (bottom) < 0.1 mm per event.

V Energy exchange in a dense urban environment – Part II: impact of spatial heterogeneity of the surface

Abstract

The centre of cities, characterised by spatial and temporal complexity, are challenging environments for micrometeorological research. This paper considers the impact of sensor location and heterogeneity of the urban surface on flux observations in the dense city centre of London, UK. Data gathered at two sites in close vicinity, but with different measurement heights, were analysed to investigate the influence of source area characteristics on long-term radiation and turbulent heat fluxes. Combining consideration of diffuse radiation and effects of specular reflections, the non-Lambertian urban surface is found to impact the measurements of surface albedo. Comparisons of observations from the two sites reveal that turbulent heat fluxes are similar under some flow conditions. However, they mostly observe processes at different scales due to their differing measurement heights, highlighting the critical impact of siting sensors in urban areas. A detailed source area analysis is presented to investigate the surface controls influencing the energy exchanges at the different scales.

Kotthaus, S, and CSB Grimmond, 2013: Energy exchange in a dense urban environment – Part II: impact of spatial heterogeneity of the surface. Urban Climate, doi:10.1016/j.uclim.2014.10.001.

V.1 Introduction

Surface characteristics, such as the arrangement of roughness elements, the locations of heat and moisture sources, or the texture of materials, all play a role in the formation of climate conditions in the lowest part of the atmosphere. Urban areas often have a particularly complex mix of surface materials, with buildings and roads (made of e.g. concrete or asphalt), right next to vegetation (e.g. street trees, gardens or parks) or water bodies (e.g. rivers or lakes). This combination of surface materials and their spatial arrangement are instrumental in generating distinct urban climates. The manipulation of these so called 'blue/green/grey' surfaces is core to many sustainable urban planning strategies aimed at mitigating negative urban climatic effects. The diversity of surface characteristics creates challenges for boundary layer and urban meteorology research and applications. This spatial variability has implications for all studies of the urban climate, independent of measurement technique or modelling approach. Scale and representativeness become central issues to consider when results obtained with different techniques are combined (Schmid 1997).

To date, the spatial variability of urban eddy covariance energy flux measurements have been addressed in three ways. First, intra-urban variations have been evaluated through simultaneous observations at multiple sites within a city (e.g. Basel, Christen and Vogt 2004; Łódź, Offerle et al. 2006; Melbourne, Coutts et al. 2007; Essen, Weber and Kordowski 2010; Helsinki, Nordbo et al. 2012), in some cases with a rural reference site. Second, variations of turbulent sensible heat fluxes within one land use unit have been observed for short periods (e.g. multiple sites in a suburban area of Vancouver at the local-scale, Schmid et al. 1991; in a densely built up residential area of Tokyo within the roughness sublayer, Kanda et al. 2006). Third, vertical flux variations have been investigated (e.g. Rotach 1995; Grimmond et al. 2004), allowing consideration of where the blending height or top of the roughness sublayer may be located.

Given the patchiness of the urban surface and its complex roughness characteristics it is often challenging to undertake EC observations in urban areas that are representative of a local-scale land use (e.g. Schmid et al. 1991; Vesala et al. 2008a; Feigenwinter et al. 2012). However, the need to better understand energy exchange processes in these environments is leading to an increase in the number of EC sites being operated – even in dense city centres such as in this study. The objective of this study is to investigate how flux observations can be used to study energy exchanges in a dense urban city centre. Here two nearby sites with different measurement heights in London (UK) are analysed with respect to the impact of site location and heterogeneity of the urban surface on flux observations. Evaluation is made as to whether simple source area modelling can aid interpretation of the results and the aspects most crucial to improve understanding. Details of the measurements (e.g. data collection, processing methods) and their temporal variability are presented in Chapter IV. First the methodology for footprint calculations is presented (Section V.2). Second, the surface influence on short-wave radiative fluxes is analysed (Section V.3). Third, the spatial variations of the observed turbulent fluxes are

interpreted with respect to their source areas and a comparison between two nearby sites is presented (Section V.4). Implications of these findings for turbulent flux source area modelling in urban areas and the critical aspect of siting are discussed (Section V.5). Conclusions of this study (Section V.6) outline both the challenges of energy flux observations in dense urban settings and the new interpretations obtained.

V.2 Methods

Net all-wave radiation Q* and the turbulent fluxes of sensible heat Q_H and latent heat Q_E are important components of the surface energy exchange in urban areas (Oke 1987). For this study, all three were obtained by *in-situ* observations. Chapter IV provides details on these and other surface energy balance components.

V.2.1 Measurement site

The study area is located in the 'Central Activities Zone' (CAZ) of London, UK (see Chapter IV for further details). At the Strand Campus of King's College London (KCL, 51°30' N, 0°7' W), two measurement towers, referred to as *KSS* and *KSK,* were located approximately 60 m apart (Figure V.1[12]).

Urban sites can be characterised using a number of techniques including image based classification (e.g. LCZ, Local Climate Zone, Stewart and Oke 2012) or simple models (e.g. UZE, Urban Zone for Energy partitioning, Loridan and Grimmond 2012) which provide expectations of the urban heat island intensity and energy flux partitioning. Around KCL, the LCZ is 'compact midrise' and the UZE is 'high density'. More detailed descriptions of surface cover, derived from source area modelling are presented in Section V.4.2. Sensors were mounted on the top of extendable towers (KSK: single tube mast, Clark Masts CSQ T97/HP; KSS: triangular tower, Aluma T45-H), with the towers installed on the top of buildings. At KSS (KSK) the measurement height above ground level (agl) was 49 m (39 m); a ratio of 2.2 (1.9) compared to mean building height z_h. The River Thames, in close vicinity of the sites (Figure V.1), experiences tidal differences of up to 6 m.

KCL Strand is located at a junction (*Aldwych*) of one of the main east-west roads through central London, *The Strand*. Taxis, private cars and buses (including several night bus routes) use this road with high frequency. In addition, vans and lorries deliver goods to businesses, shops, restaurants and hotels in the area. Especially during rush hour, substantial traffic emissions can be expected. To the southwest is a pedestrian courtyard within *Somerset House* (Figure V.1) and another busy road (*Waterloo Bridge*).

V.2.2 Data collection and processing

The turbulent fluxes of sensible and latent heat were observed using the eddy covariance (EC) method. Net all-wave radiation was measured directly and auxiliary meteorological observations

[12] Amendment of Kotthaus and Grimmond (2013b): added radial grid lines in 100 m intervals to Figure V.1.

and cloud cover were also observed at KCL Strand. In this paper, data collected between October 2008 and March 2012 are used. While turbulent heat fluxes were calculated based on 30 min intervals, all other data are available with a resolution of 15 min. At KSK, two *Kipp & Zonen* radiometers have been operational (Chapter IV, Table IV.1): a CNR1 (2008–2009) and CNR4 (2010-2012). Based on daily total incoming short-wave radiation, the estimates by the older sensor (CNR1) are higher by ~6%. This falls in the range of expected accuracy of ± 10% specified by the manufacturer for daily totals. Cloud cover percentage was estimated based on ceilometer backscatter information, aggregated to the same temporal resolution. All recording and data analysis was done in UTC (Universal Time Coordinated). This is local time in the winter and an hour earlier during the summer (daylight savings period). Further information on data collection, availability, and processing is provided in Chapter IV.

V.2.3 Source area calculations

Micrometeorological measurements characterise surface-atmosphere exchange as a function of the radiative properties, moisture availability, or anthropogenic activities etc. of the surface. With a complex surface the linkage between the measurement and instrumental source area becomes more challenging. Of particular interest in this study is the influence of surface controls in a

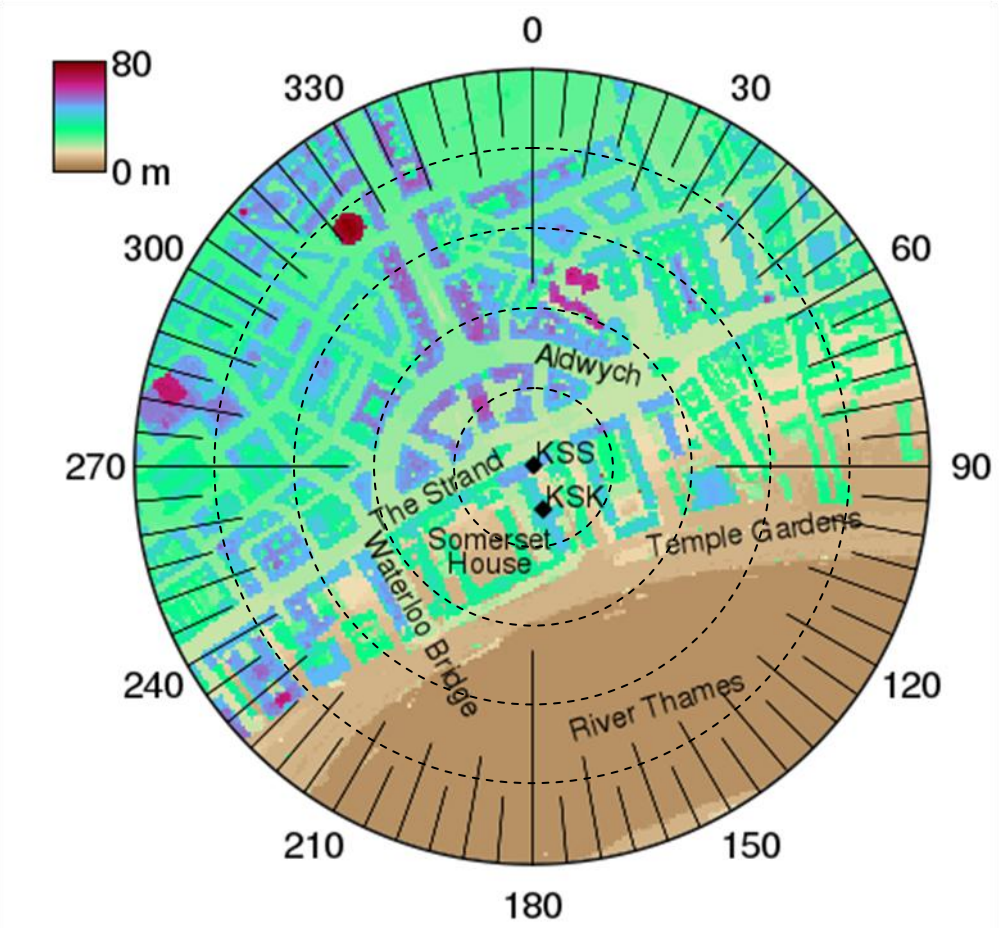

Figure V.1: Digital elevation model of ground and buildings (Lindberg and Grimmond 2010) for a 500 m radius around KCL Strand (centred on KSS site) in metres above sea level at 4 m spatial resolution. Radial coordinates according to BNG (British National Grid) north. Site locations and relevant places are labelled.[12]

dense urban setting. Approaches to source area modelling are described as context for the measurement methods used.

V.2.3.1 Turbulent flux footprint

The turbulent fluxes of latent and sensible heat change in time and space as a function of sensor position (height; e.g. Schmid and Lloyd 1999), atmospheric conditions (expressed by e.g. wind speed, wind direction, atmospheric stability; e.g. Kljun et al. 2002) and surface characteristics (expressed by e.g. terrain, surface roughness, material composition; e.g. Vesala et al. 2008).

Observed urban turbulent energy exchanges are commonly stratified by wind direction into sectors related to land cover (e.g. Järvi et al. 2009 compare roads, buildings and vegetation). This practice takes into account two very important aspects of the linkage between the surface and observed turbulent exchange: wind direction and broad variations in surface characteristics. However, it does not provide any insight in the effect of wind speed (e.g. related to mesoscale wind regimes, Lemonsu et al. 2004) or atmospheric stability. The latter is a major control on the extent of the source area (Kljun et al. 2002).

Footprint models of varying complexity have been developed to locate the probable surface area affecting turbulent flux measurements (see review in Vesala et al. 2010). After pioneering work on analytical footprint calculations (e.g. Gash 1986; Schuepp et al. 1990; Horst and Weil 1992), a 3D analytical model (scalar Flux Source Area Model, FSAM) was developed to aid interpreting eddy covariance measurements (Schmid 1994, 1997). This has been widely used in a variety of urban studies, e.g. supporting energy balance analysis in Marseille (Grimmond et al. 2004; Lemonsu et al. 2004), carbon dioxide flux observations in Essen (Kordowski and Kuttler 2010), and a series of turbulent flux measurements in Łódź (Offerle et al. 2006b; Pawlak et al. 2011; Fortuniak et al. 2012a).

Future computing capacity will make the applicability of Lagrangian stochastic dispersion models that can represent complex flow conditions more feasible. However, such sophisticated models have not yet been used in full for urban studies. A simple parameterisation (Kljun et al. 2004) of the backward trajectory Lagrangian stochastic footprint model of Kljun et al. (2002) has been applied to urban situations (e.g. Mårtensson et al. 2006; Hiller et al. 2011; Park et al. 2011). Hsieh et al.'s (2000) analytical footprint model, a parameterisation from a Lagrangian stochastic approach, aided interpretation of carbon dioxide fluxes in Florence (Gioli et al. 2012). The forward Lagrangian stochastic model of Göckede et al. (2006), based on an analytical method (FSAM), identified the probable source areas for small aperture scintillometers in a dense city centre (Pauscher 2010).

More sophisticated methods, such as Large Eddy Simulation (LES) or ensemble-averaged closure models (Rannik et al. 2012), tend to be computationally expensive and address restricted stability conditions. Hence, they remain minimally used in city studies. Vesala et al. (2008) apply

the model SCADIS (Sogachev and Lloyd 2004; Sogachev 2009) to a Helsinki site but only under neutral conditions for two wind directions, where they find an asymmetry of the source area in the approaching flow.

The relatively simple implementation of analytical footprint models provides clear advantages in computing time and ease of use, so they are often applied to gain a first order estimate of probable location and size of flux source areas (Rannik et al. 2012). Some uncertainty might arise from simplifications (van de Boer et al. 2011) as these models are not capable of formulating the whole complexity of the surface flow. Developed for flat surfaces they are not able to capture the impact of vertical variations of sources and sinks (Vesala et al. 2008a; Salmond et al. 2012). Nonetheless, the information gained from more elaborate models does not (yet) legitimise their complexity and time intensive implementation for large datasets. Thus, analytical models are usually chosen for the interpretation of long-term datasets. Recent examples of their application include the Kormann and Meixner (2001) model to interpret carbon dioxide fluxes (e.g. Vancouver, Christen et al. 2011; Baltimore, Crawford et al. 2011; Beijing, Liu et al. 2012), to improve understanding of turbulent energy transport (e.g. Helsinki, Nordbo et al. 2012; Basel, Salmond et al. 2012) and to match *in-situ* and remote sensing observations (e.g. Cairo, Frey and Parlow 2012).

The footprint calculated for individual time periods can be composited by time and space to provide, with an appropriate geographical information database, the sensor field of view or footprint climatology. Such an approach has been shown to be beneficial to the interpretation of urban fluxes (e.g. Christen et al. 2011).

In this study, footprint functions for both study sites for each 30 minute period were estimated with the Kormann and Meixner (2001) analytical footprint model. However, instead of calculating friction velocity (u*) according to equation (31) in Kormann and Meixner (2001), the measured value of u* at the respective site (KSK or KSS) was supplied to the footprint model as input, along with wind speed, wind direction, cross wind standard deviation σ_v and Obukhov length L. Roughness length for momentum z_0 and displacement height z_d were estimated using Macdonald et al.'s (1998) method based on the mean building height above ground z_h, plan area fraction λ_p and frontal area index λ_f. All three morphometric parameters were calculated from a digital elevation model (DEM) of ground and buildings at a spatial resolution of 4 m (Lindberg and Grimmond 2010).

Vegetation covers a small portion of the area around the study sites, thus its effect on surface roughness is assumed to be negligible. The topography of the area slopes from the lowest elevations at the river to highest in the north (Figure V.1). To incorporate these variations, mean ground height z_g as well as z_h, λ_p and λ_f were estimated as a function of wind direction. First, a database of morphometric parameters was created based on a 500 m radius and 1° intervals. These were then averaged based on mean sectors (defined by mean wind direction and cross

wind variability σ_v) to derive 'first-guess' estimates of roughness parameters z_0 and z_d for each time period. These were then used in the initial footprint calculation. New morphometric parameters were calculated for each identified source area, leading to new roughness parameters that provided the basis for more precise source area calculations. Finally, morphometric parameters and land cover fractions were obtained from this area for each observation period. In order to facilitate the analysis, these results have then been aggregated into 10° wind sectors. The measurement height z_m was adjusted during this iterative process to account for variations in ground height. This is crucial because the effective height $z' = z_m - z_d$ was used within the atmospheric stability parameter $\zeta = z'/L$ to classify unstable ($\zeta < -0.1$), near-neutral ($-0.1 \leq \zeta < 0.1$), and stable ($0.1 \leq \zeta$) conditions.

V.2.3.2 Radiometer footprint

Key to surface atmosphere exchanges are radiative fluxes. For Lambertian surfaces, the source area is mainly a function of measurement height. However, the complex three-dimensional structure of the urban surface causes shadow patterns and the combination of various materials with different radiative properties brings about spatial variability caused by the sun-surface geometry (Soux et al. 2004). High reflectance materials such as glass and metal are increasingly used in modern architecture, especially for commercial buildings, leading to distinct reflections of short-wave radiation. 'Reflection glare' can cause discomfort, and even danger, to the urban population (e.g. people working in offices, pedestrians or drivers, Iwata et al. 1991). Strong reflections of solar radiation from vertical facets, or even horizontal surfaces, increase short-wave (including UV) but also thermal energy gain to the object receiving the reflected beam (Shih and Huang 2001).

Measurement of surface albedo is impacted not only by surface materials and their spatial arrangement but also by the atmospheric transmissivity and solar geometry. As atmospheric transmissivity determines the relation between diffuse and direct solar irradiance (Lucht et al. 2000) the total surface albedo includes the reflection of diffuse (white-sky albedo) and direct (black-sky albedo) radiation. While the black-sky albedo can be expressed as a function of the solar elevation angle, the interaction of diffuse radiation with the surface should be independent of solar geometry (Lucht et al. 2000).

The footprints of EC and radiation measurements usually do not agree (Schmid 1997) as different processes control the respective energy transfer. Concentric circles describe isopleths of the source area of a radiometer (over a Lambertian surface) which do not vary temporarily. Their radii depend on the measurement height above the surface (Schmid 1997). For non-Lambertian surfaces, this source area model can provide a first approximation of the footprint for the case of diffuse irradiance when variations in directional reflectance of the surface have less impact. Under direct irradiance, however, heterogeneities in surface reflectance can represent great variations in the surface response, thereby inducing a complex pattern of source area weights that can no longer be represented by concentric circles. Here the footprint function should

incorporate the bidirectional reflectance distribution function (BRDF) of the surface as well as the sun geometry, which varies both spatially and temporally. In an urban setting, the BRDF needs to combine variations due to surface materials but also the three-dimensional form of buildings, vegetation, roads, and canyons. This is unique for every measurement site and sensor height, and very difficult to portray.

In this study, in order to visualise the impact of the urban surface on reflected short-wave radiation, locations of maximum specular reflection were calculated as a function of solar azimuth angle and distance of maximum reflection of solar irradiance

$$R_s = z_R/\tan(\Theta)$$

with sun elevation angle Θ and height of the pyranometer above the surface z_R. This formulation of the radius of maximum specular reflection R_s stems from rules of specular reflectance and basic geometry. Given the majority of the pyranometers' field of view (FOV) consisted of roof surfaces, the height above the surface z_R was assigned as an average value defined as the tower height above the roof reduced by 1 m to account for roof height variations and objects (such as elevated windows) close to the towers. Even though this measure assumes a flat surface and does not account for the complex, small-scale height variations around the measurement towers or close by canyons, it still provides useful location estimates for peak reflections in the radiometer's source area.

V.3 Spatial variability of reflected short-wave radiation

V.3.1 Observations

All four components of the net all-wave radiation were observed at KCL Strand. Their temporal variability and role in the surface energy balance in the dense urban study area are discussed in detail in Chapter IV. They also analyse how long-wave radiation is affected by a combination of atmospheric effects (cloud cover) and the urban surface, drawing on cloud cover fractions derived from ceilometer backscatter observations. Diffuse incoming short-wave radiation, measured with a sunshine pyranometer (SNP1, Delta-T Devices) over the period of Jan 2011–Mar 2012, has a clear relation to cloud cover fractions (not shown).

The urban impact on the observed radiation exchange is most apparent in the reflected short-wave radiation $K_\uparrow$ and hence the surface albedo. This is due to the immense heterogeneity of surface materials and geometry around the sites, which the following analyses illustrate.

The spatial distribution of reflected short-wave radiation observed at KSK (Oct 2008–Nov 2009; Figure V.2b) shows a clear response to objects in the source area of the down-facing pyranometer (Figure V.2a). Two flat roof windows south of the mast at KSK and a tilted roof window towards the southwest cause peak values of $K_\uparrow$. These appear as 'outliers' in the time series (Chapter IV, Figure IV.4). Averaged over a 15 m radius (80% FOV; solar elevation angle

≤ 29.8°) for times with clear sky conditions, the roof windows at KSK have a 25% increase in albedo compared to the surrounding roof area which is composed of various kinds of concrete as well as slate roofing shingles. In addition to the marked roof window areas, the spatial distribution of reflected short-wave radiation reveals the influence of generally darker surfaces towards the east of the mast. This can be explained by the three-dimensional structure of the roof itself which casts greater shadow areas when the sun is in the east. At KSS the composition of the source area is more complex so that no isolated objects can be mapped. No windows are located on this roof.

The spatial variations of reflected short-wave radiation, and hence surface albedo, are evident under clear sky conditions as detected from ceilometer measurements. In order to study the effect of diffuse radiation in conjunction with the sun-surface geometry, median albedo patterns were calculated as a function of solar elevation angle and cloud cover at KSS and KSK (Figure V.3a, c). Those for clear (cloud cover = 0%) and cloudy (overcast, cloud cover = 100%) conditions were stratified by azimuth (easterly E, westerly W) and shown as a function of solar elevation angle (Figure V.3b, d). To facilitate comparison between figures (Figure V.2b, Figure V.3), the distance of maximum reflection of specular solar irradiance R_s (Section V.2.3.2) is included in the upper x-axis in Figure V.3.

Cloud cover clearly affects the surface albedo estimates and determines its dependence on solar elevation angle (Figure V.3a, c), given the generally higher surface reflectance at low solar elevation angles results from increased specular reflectance. Accordingly, the surface albedo gradually decreases with rising solar elevation angle under clear sky conditions (0% cloud cover). The rugosity of the urban surface contributes to the lower albedo values at higher solar elevation

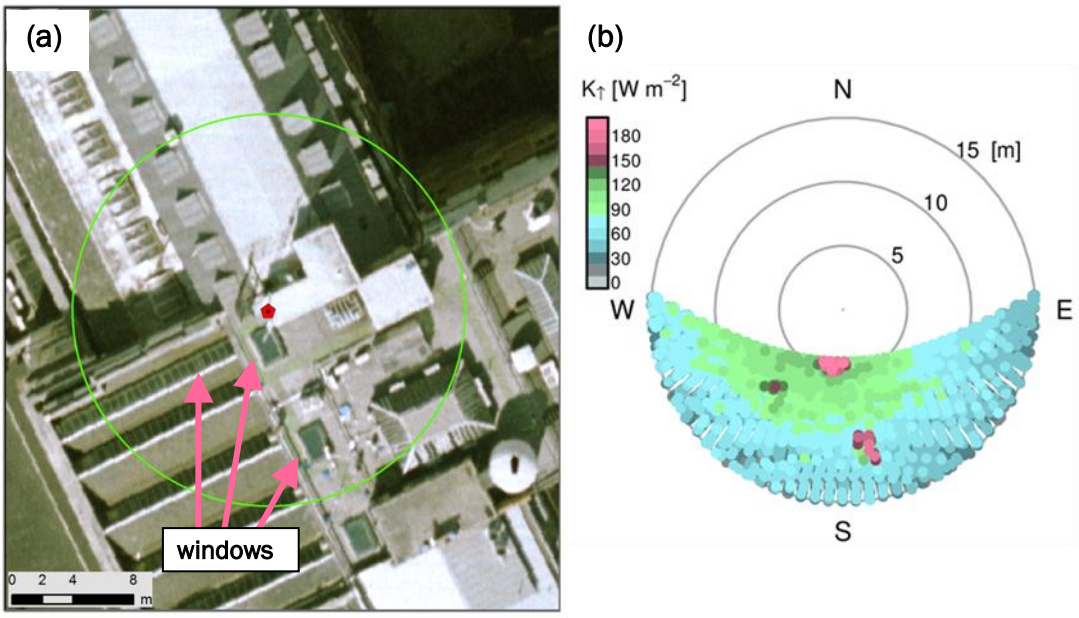

Figure V.2: (a) Aerial photo (NERC ARSF 2008) showing the 80 % source area (15.2 m radius) of the down-facing radiometer at KSK; (b) median reflected short-wave radiation observed at KSK in 2009, by solar azimuth angle and distance of maximum, specular reflection R_s. Height above roof surface z_R = 7.6 m = tower height offset by 1 m (to account for roof height variations).

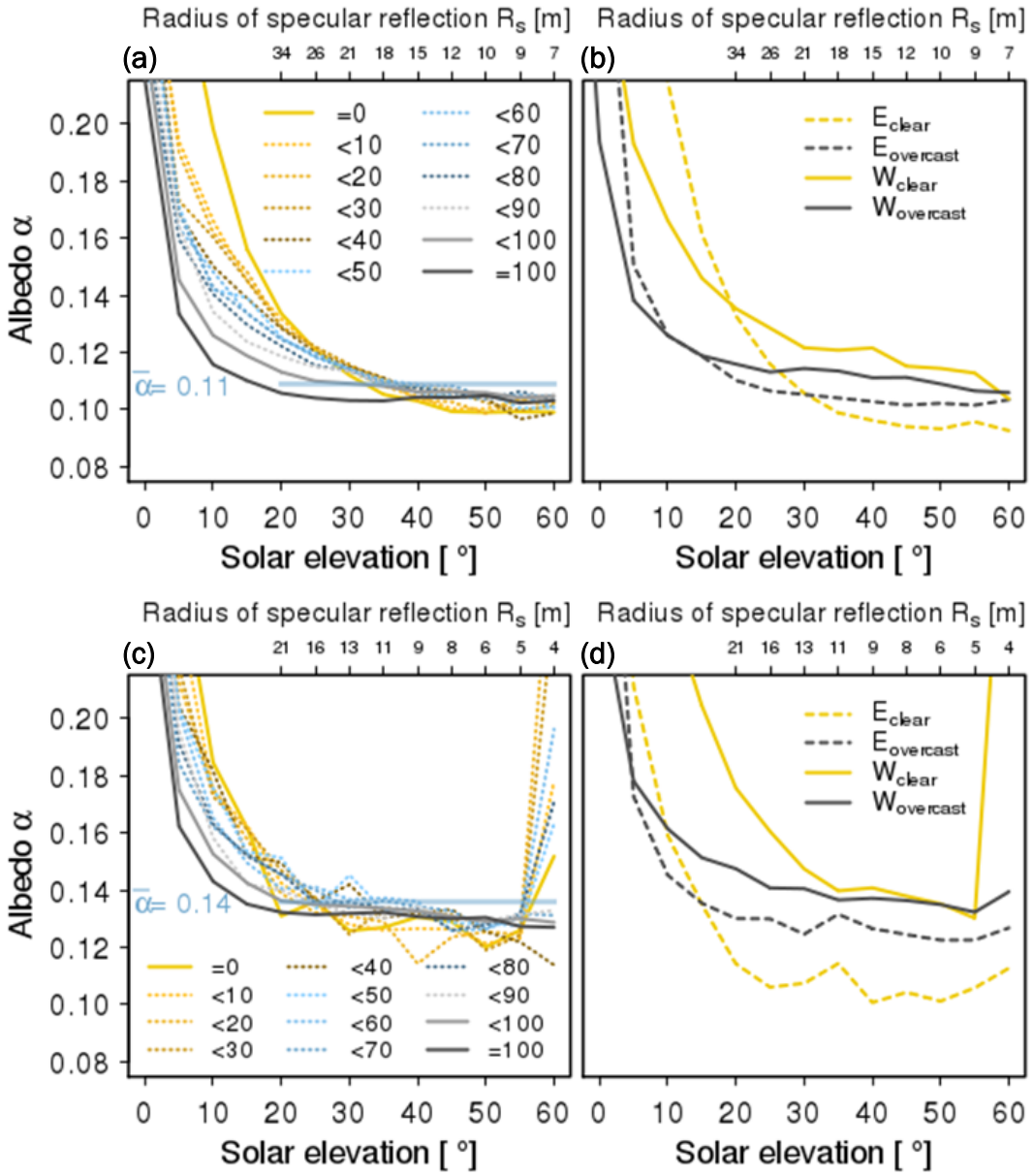

Figure V.3: Median surface albedo as function of solar elevation angle at (a, b) KSS and (c, d) KSK: (a, c) split by cloud cover [%]; (b, d) clear sky (cloud cover < 10%) and overcast conditions separated into E (sun in the East) and W (sun in the West). The bulk surface albedo $\bar{\alpha}$ is calculated as the mean of all values with a solar elevation angle of at least 20°. The additional axis (top) indicates the distance of maximum specular reflection of direct solar irradiance R_s from the respective tower location (see Section V.2.2).

angles as more short-wave radiation enters the street canyons (Christen and Vogt 2004) where it is trapped. The slope of surface albedo versus solar elevation angle flattens with increasing cloud cover, especially for elevation angles > 20°. Surface albedo does not vary with solar elevation angle under overcast conditions (100% cloud cover).

At KSS (Figure V.3a), the gradient from clear to cloudy values is mostly evident for solar elevation angles below 40°, while those with higher elevation angles and hence lower distance to maximum reflection R_s become more similar. In contrast, at KSK (Figure V.3c), the overall albedo exhibits high variability for all but overcast conditions (i.e. cloud cover < 100%). This could be

explained partly by the smaller amount of data at this site (Chapter IV, Table IV.1). However, since the fluctuation with distance to maximum reflection is stronger for times with more direct irradiance, it seems likely to be caused by high reflectance surfaces in the source area (Figure V.2). The window at $R_s \approx 5$ m southwest of KSK results in strong peaks of surface albedo. In addition to the high albedo surfaces, the presence of shadows increases the spatial variability of surface albedo under the influence of direct solar incoming radiation. Above 70% cloud cover, diffuse radiation gains importance and nearly removes the dependency on solar angles.

Despite the significant variability of albedo at the two sites and the uncertainties associated with measurements of this quantity, a bulk surface albedo can be estimated to summarise overall radiative characteristics. Here, it was calculated as the median of all observations with solar elevation angles of at least 20° (horizontal bar in Figure V.3a, c). As the larger source area for KSS included street canyons (to the north as well as to the southeast), the overall bulk surface albedo is lower ($\bar{\alpha} \approx 0.11$). Even though these observations did not cover the full range of facets in the area, this bulk albedo can be assumed to be more representative for the study area than the higher value of 0.14 measured at KSK where roof surfaces dominate. This again underlines the importance of sampling a representative composite of active urban facets to determine the radiation balance at the local-scale (Roberts 2010). At both sites the bulk surface albedo is best represented by observations under overcast conditions. On average for solar elevation angle > 20°, this white-sky albedo (diffuse radiation only) is a little lower (by 0.01) than the overall bulk albedo. The comparatively low albedo values observed in the current study (compared to e.g. Oke 1987) are in accordance with the discussion of Christen and Vogt (2004) who found similar surface characteristics (albedo around 0.1 at their sites in the city centre of Basel) and concluded that European cities might reflect less short-wave radiation than those studied in North America.

Albedo observed under clear sky conditions changes with solar azimuth angle (simplified here into E and W) in response to the three dimensional geometry of the surface. At KSS (Figure V.3b) the surface appears brighter (for solar elevation angle > 20°) when illumination comes from the west (W_{clear} in Figure V.3b) because flat roof surfaces made up most of the surface under the radiometer in a radius of about 20–30 m to the southwest of the tower (Chapter IV, Figure IV.1b). The canyon in the southeast, however, causes significant trapping of incoming solar radiation which lowers the observed surface albedo (E_{clear} in Figure V.3b). A small impact is even evident under overcast sky conditions ($E_{overcast} < W_{overcast}$ for solar elevation angle > 20°), indicating that the canyon absorbs diffuse radiation as well. While the clear-sky albedo in the roof-dominated area (W_{clear}) steadily increases with decreasing solar elevation angle, the canyon-dominated area appears darkest at solar elevation angles around 50°. This sun-surface geometry corresponds to a distance to maximum reflection of about 12 m, which roughly marks the edge of the KSS roof towards the southeast and hence the place where minimal radiation escapes towards the sensor from the canyon. For smaller distances the influence of the KSS roof on the observed reflected

short-wave radiation increases, and also more radiation reflected from the canyon reaches the sensor for larger distances.

At KSS, incoming short-wave radiation tends to be slightly lower in the morning hours (not shown) which could be a consequence of a not perfectly level sensor. Obviously this affects the observed albedo in addition to the surface structure in the source area. However, since a negative $K_{\downarrow}$ bias is associated with an overestimation of albedo, this (possibly measurement related) artefact acts to alleviative the observed E–W difference. Without this systematically higher incoming short-wave radiation for westerly solar positions the roof area would appear even brighter in comparison to the canyon. At the KSK site, no such asymmetry of incoming short-wave radiation with solar azimuth angle is detected. Again, clear-sky surface albedo is generally lower when the sun is in the east (E_{clear} Figure V.3d) where elevated roof structures cause apparent shadowing (Figure V.2a). The two roof windows detected (Figure V.2b) show up as distinct peaks in the median albedo curves of easterly ($R_s \approx 12$ m) and westerly ($R_s \approx 5$ m) solar positions, respectively. Again, under overcast conditions, the high fraction of diffuse radiation integrates the diverse effects of the heterogeneous surface so that albedo at KSK shows hardly any variability ($E_{overcast}$ and $W_{overcast}$ in Figure V.3d) dependant on sun-surface geometry (for elevation angles > 20°).

These observations demonstrate several important aspects characterising the urban surface and its anisotropic nature (also highlighted by Soux et al. 2004):

- High reflectance materials, which are increasingly found in modern urban architecture, significantly impact the surface albedo.
- Provided sufficient irradiance, these materials cause strong specular reflections or reflection glare.
- The surface deviates distinctly from Lambertian characteristics.
- Due to the heterogeneous composition of anthropogenic materials with various radiative properties, observations of the interaction between Sun, surface and atmosphere are highly dependent on the observational field of view or footprint (or source area).

V.3.2 Implications for source area models and siting

The anisotropic nature of the urban surface has implications for the description of radiometer source areas. The dependence of surface albedo on the relation between diffuse and direct illumination is linked to the spatial distributions of facets with different orientations in the source area. If the surface in the field of view of the radiometer covers walls and surfaces of a variety of orientations, and if these are similarly distributed by solar elevation and azimuth angles, the average albedo under clear sky conditions should be similar to the one observed during overcast periods (e.g. as seen at the central urban sites in Basel, Christen and Vogt 2004) because both estimates represent an integration over a representative distribution of sun-surface-sensor geometry settings.

The source area (field of view) of a down-facing pyranometer over uniform, Lambertian surfaces is well described by concentric source area isopleths (Schmid 1994). Here, the simple example of a highly reflective, forward scattering surface is considered to put the impact of the roof windows at the KSK site into a wider context.

Highly reflective, forward scattering surfaces in the pyranometer field of view can have enhanced impact on the observation of reflected short-wave radiation resulting in an overestimation of the local-scale flux if uniform source area weighting is applied. The latter is related to the distance of specular reflection R_s, and is dependent on the site latitude, the sensor height above the surface (in the current example the roof) and time (within year and day). To demonstrate this, R_s is shown for 70°N to 0° latitudes on the 21st of each month from June to December covering the range of possible solar positions (Figure V.4[13], reverse months for southern hemisphere and invert). For the northern hemisphere, the surface towards the south of the site influences the main part of

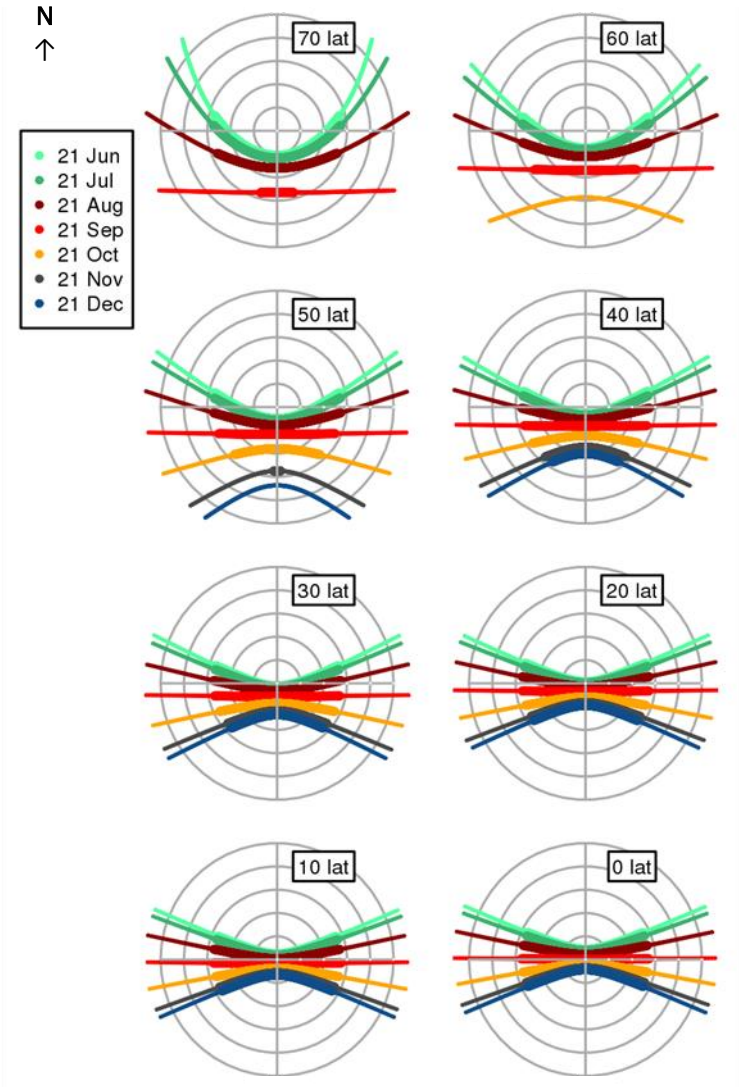

Figure V.4: Schematic illustration of location of maximum specular reflection at 0-70°N as a function of R_s (radial coordinate) and solar azimuth (angular coordinate) on the 21st of each month (Jul-Dec); for solar elevation ≥ 10° (solid lines), and ≥ 20° (bold lines). For southern hemisphere the dates are reversed and patterns inverted.

the source area for specular reflections. The area from which specular reflection can reach the sensor for solar elevation angles ≥ 20° (bold lines in Figure V.4) is closest to the tower at noon in June for latitudes down to 20°N. However, north of about 30°N the area right below the site does not contribute to any specular reflections. North of 50°N, specular reflections are only relevant for the period from March to September and a wider area can contribute during particularly long summer days.

The source area for specular reflections can be combined with the general field of view approach to ascertain which areas influence observations of reflected short-wave radiation. Using a site at 50°N (close to the KCL site latitude), the source area estimates are calculated with a sensor height of 5–30 m above the roof in 1 m intervals (Figure V.5). The FOV isopleths (dotted lines) do not vary with time, while the minimum distance of specular reflection (solid lines) depends on the day of year (same example days as in Figure V.4). The maximum distance reached (variable with time of day) is defined by the 20° solar elevation angle (grey shading marks the area of solar elevation angles ≥ 20° where specular reflection can occur).

Comparison of the direct and diffuse footprint indicators illustrates that different surface areas can be important for the reflection of the two components of incoming solar radiation. Based on the fixed source area formulation (Schmid 1994), it is possible to estimate the source area weighting of a flat 1 m² roof window at various distances from the site (squares in Figure V.5). The contribution is highest for low measurement heights and decreases with increasing sensor

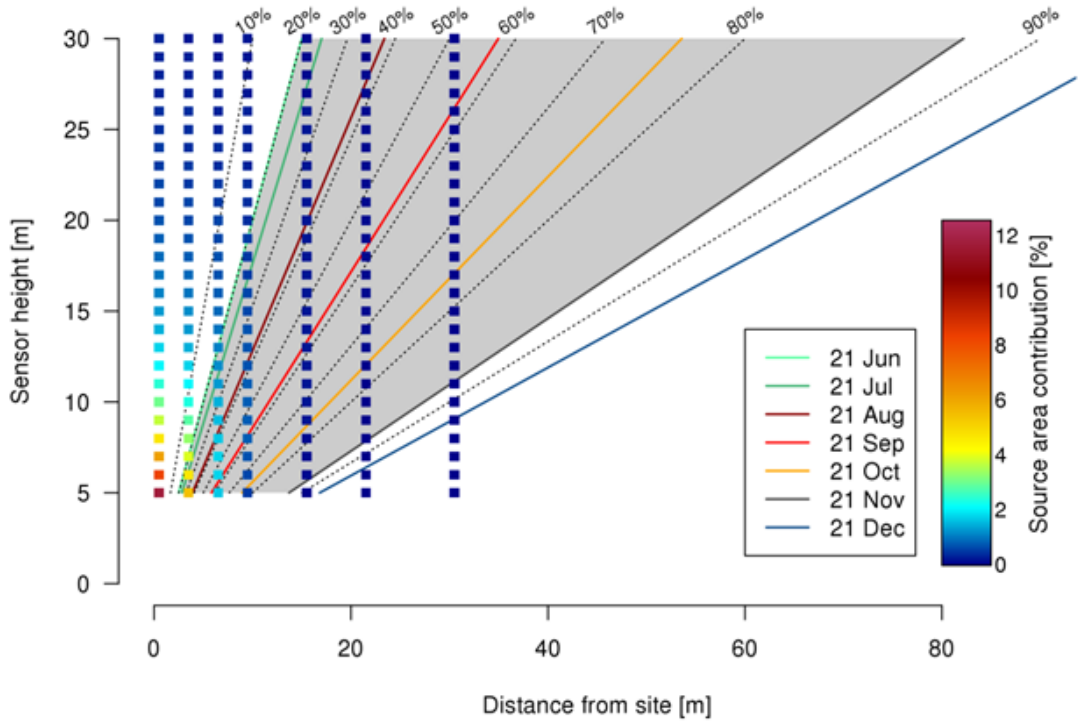

Figure V.5: Schematic of source area variations for a down-facing pyranometer depending on sensor height above roof and distance from site. Points give source area contribution of flat 1 m² roof window [%] according to concentric footprint isopleths (Schmid et al. 1991), indicated by dotted lines. Solid lines mark location of minimum radius of specular reflection R_s on the 21st of each month (Jun-Dec), calculated for a site at 50°N. See Section V.3.2.

height and distance from the site. However, highly reflective/ non-Lambertian surfaces are most likely to influence observations of reflected short-wave radiation (Figure V.2; Figure V.3) at some distance from the site. For example, a radiometer at 15 m above roof level can receive specular reflections from a flat roof window 30 m south of the site from about March till September. Depending on site location and measurement time (Figure V.4; Figure V.5), a window at a certain distance from the measurement site and at a certain bearing could have a much higher impact on the final measurement than one located right below the sensor. Due to the spatial and temporal variability of specular reflection locations, the source area for clear sky albedo observations is more complex to parameterise than for times with diffuse radiation. A full source area model needs to describe variations in illumination conditions as well as the BRDF of the surface.

In the context of surface energy balance observations, the aspect of siting of a radiometer and the associated source area obviously also needs to be considered with respect to the source area of the turbulent fluxes measured (Schmid 1997). It is a common issue for those observational datasets, that radiation sensors are often installed on top of the same towers as the EC sensors so that their FOV might only cover parts of the source area of the EC fluxes. At times, the footprint of radiative and turbulent fluxes might not overlap at all. Other than for studies of rural areas, where the observed surface is often sufficiently homogeneous to assume the radiative source area to represent the local-scale, outgoing radiative fluxes over the urban canopy may be affected by processes that may not be captured in the instantaneous source area of the turbulent fluxes, given the range of surface heterogeneities discussed. Hence, in addition to an improved understanding of the radiometer source area, new approaches in terms of siting might be advisable in order to ensure that a representative composition of facets is captured (Roberts 2010). Ideally radiometers would be mounted higher than turbulence sensors (Offerle et al. 2003; Roberts 2010). Often this may be unrealistic because of planning restrictions. Hence, an increased number of radiometers installed in various directions (e.g. predominant wind directions) could potentially provide a better spatial coverage. Obviously, with advances in surface remote sensing (Yang 2011), both in terms of spatial resolution and temporal coverage, observations from other non-tower based platforms might help to quantify radiative fluxes in the future, but these need to be viable across all cloud conditions.

V.4 Spatial variability of turbulent heat fluxes

V.4.1 Wind and surface morphology

Around the KCL Strand campus the morphology is complex (Figure V.1), street canyons dominate to the west and north, whereas to the south the River Thames has significantly lower surface roughness. This diversity impacts the roughness parameters: plan area fraction λ_p, frontal area index λ_f, mean building height z_h, roughness length for momentum z_0 and zero plane displacement height z_d (Figure V.6a, b).

On average (Table V.1), the KSS measurement height ($z_m \approx 2.2 \times z_h$) should be above the blending height, whereas the KSK observations may be within the roughness sublayer ($z_m \approx 1.9 \times z_h$). Still, based on morphometric parameters alone, it is difficult to locate the blending height. Hence it is not certain if/when observations at KSK rather represent the roughness sublayer. In Basel (Rotach et al. 2005) during the BUBBLE campaign, multiple levels of EC instruments on two urban and one suburban flux tower provided information about vertical variations in turbulent exchange from within the canyon up to a local-scale fetch (Christen 2005). Based on the vertical divergence of the sensible heat flux density at a central urban BUBBLE site, Christen and Vogt (2004) conclude that the main influence on measurements at the top (2.2 times the mean building height z_h) originates from the volume around roof height (> 0.8 x z_h and < 1.4 x z_h). Their findings also suggest that the blending height in the dense urban setting is reached at about 1.5 x z_h, above which vertical flux divergence vanishes.

At the two study sites, the mean building height is higher (lower) towards the northwest (southeast) with median values in the west and east (Figure V.1, Figure V.6a, b). The directional plan area fractions are clearly impacted by the river with $\lambda_p < 0.45$ in a sector 85–245° (85–235°) at KSS (KSK). The variability in displacement height z_d is primarily controlled by mean building height, and then λ_p (Macdonald et al. 1998). Thus it is reduced in the south to southeast, with a z_d/z_h minimum of 0.42 (0.36) at 180° for KSS (KSK). As all these components are required for the roughness length calculation (Section V.2.3.1), z_0 varies between 1 m at KSS (0.8 m at KSK) and 2.8 m. Surface roughness is particularly high in the southwest and northwest, while the relatively high displacement height (compared to z_h) in the west and east lowers the surface drag. Roughness estimates for KSK and KSS are generally in agreement by direction, but the lower measurement height at KSK causes a small/different footprint (Section V.4.2). This may explain why the clear increase in surface roughness to the north is evident for KSS

Table V.1: Site and source area characteristics at KSK and KSS calculated as averages over all available observations based on the individual turbulent source area estimates. Heights specified in m above ground level (agl).

		KSK	KSS
Height [m agl]	Mean building height z_h	21.0	22.0
	Roughness length z_0	1.7	1.9
	Displacement height z_d	13.8	14.2
	Sensor height z_m	38.8	48.9
	Height of building hosting tower	30.2	35.6
Height [m]	Tower height above roof	8.6	13.3
Turbulent source area [km²]	Including 50% of footprint	0.1	0.2
	Including 90% of footprint	3.0	5.3
Distance X_{max} from site to footprint maximum [m]	Unstable atm. conditions	67	95
	Neutral atm. conditions	101	147
Land cover fraction in source area [%]	Roads	43	43
	Buildings	40	38
	Water	13	14
	Vegetation	4	5

(Figure V.6a) but less pronounced for KSK (Figure V.6b). In addition to the diversity of surface roughness elements in the study area, the underlying topography (Figure V.1) adds complexity to the source area calculations. As it is not flat, the measurement height z_m was calculated as a function of wind direction (Section V.2.3.1).

The wind-rose, based on all available EC observations (Section V.2.2), shows which wind sectors are most frequently observed by the flux sites. The prevailing wind direction (45% of all observations) at KSS is from the southwest (175–265°; Figure V.6c); the secondary sector (18%) is the opposite from the northeast (355–45°). As the measurements at KSK (Figure V.6d) cover a longer period (Chapter IV, Table IV.1), the absolute frequency values are higher than for KSS. Although the two dominant wind sectors can be identified for KSK, they are slightly shifted towards the west (southerly) and east (northerly), respectively. Given the KSK sensor height was lower (Table V.1) surface roughness elements in the immediate surroundings can impact the

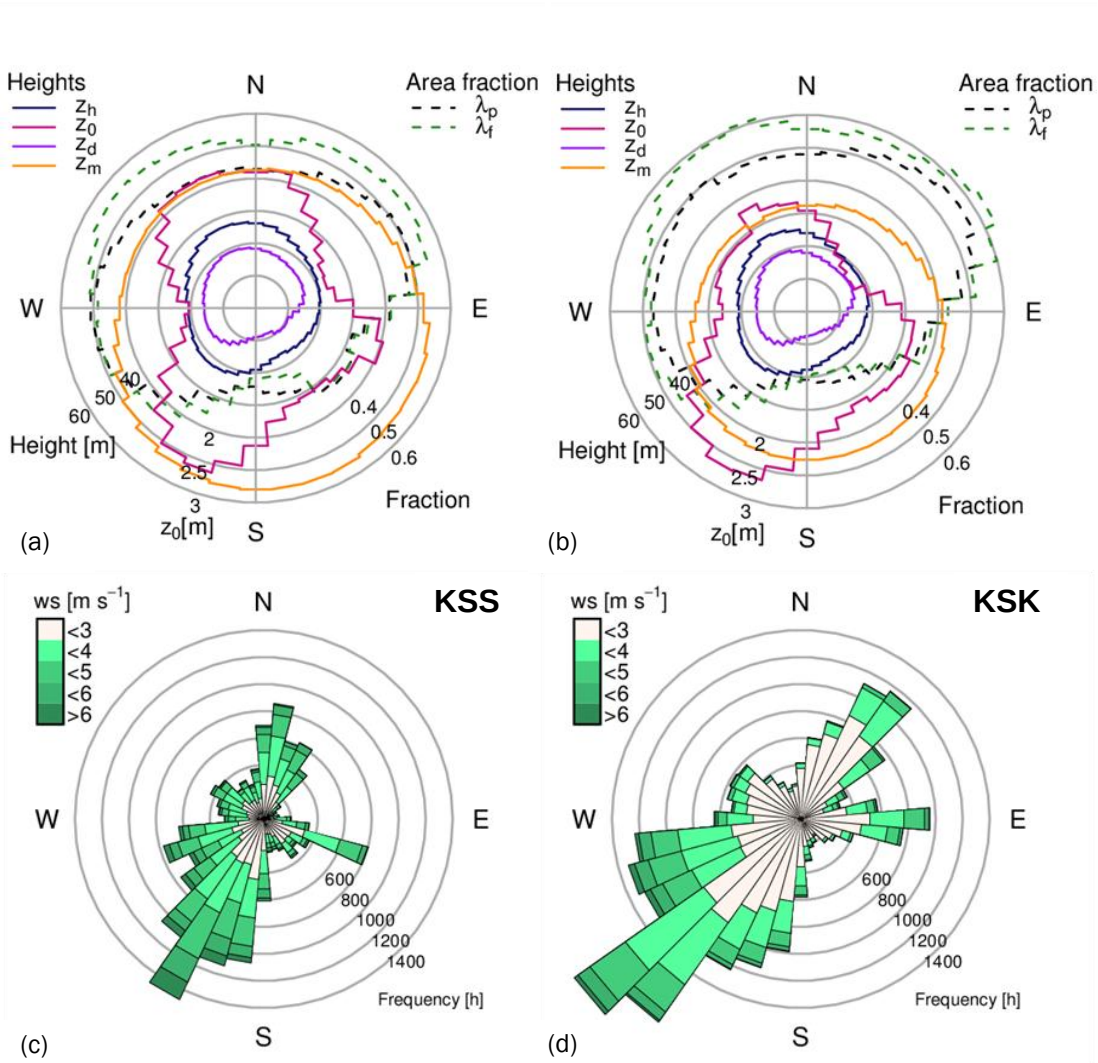

Figure V.6: Directional characteristics at (a, c) KSS and (b, d) KSK, separated into 10° intervals: (a, b) Average surface characteristics based on individual source areas maps: Building height z_h, roughness length z_0, displacement height z_d and measurement height z_m, plan area fraction λ_p and frontal area fraction λ_f. (c, d) Frequency distribution of wind speed by wind direction.

observed turbulent flow and thus the dispersive fluxes (Raupach and Shaw 1982) might have an influence. The northeast-southwest oriented building north of KSK (i.e. the one hosting the KSS site, Figure V.1) likely caused sheltering effects and thus explains the difference in wind direction distribution compared to KSS. The wind speed distribution (shading in Figure V.6c, d) corroborates this observation. Higher wind speeds occurred at the higher KSS sensor (61% of all observations with ≥ 3 m s^{-1}) and a stronger decelerating effect of the surface roughness is seen at KSK (62% with ≤ 3 m s^{-1}). At both sites, stronger winds occurred from around 240° where more than 60% (50% at KSK) of the data show wind velocities > 3 m s^{-1}.

Further, frequencies are slightly higher between 105–115° (Figure V.6c) with about 4% of all observations. These directions coincide with the alignment of River Thames to the east of the site (Chapter IV, Figure IV.1), indicating that channelling might impact the flow from this direction. These easterly wind directions, however, are often coincidently observed at London airports (e.g. Heathrow, City, and Luton, MetOffice 2012a; not shown), which probably rules out them being induced by local-scale, site specific flow distortion by the urban canopy in the site's source areas.

V.4.2 Modelled source areas of turbulent fluxes

The local-scale source areas, estimated for each observation period using Kormann and Meixner's (2001) model (Section V.2.3.1), have uncertainties caused by the complex environment that need to be kept in mind during interpretation. The spatial variability of roughness elements by direction for each EC site (Figure V.6a, b) was used to calculate the appropriate morphometric parameters and roughness characteristics (Section V.2.3.1) for each individual time period's source area. Atmospheric stability plays a major role in the determination of source area locations (Kormann and Meixner 2001), the footprint area increases with increasing stability as does the distance from the site to the maximum footprint contribution. At KSS (KSK), atmospheric conditions are predominantly unstable (neutral), with about a third (60%) of all observation periods classified as neutral. At both sites, stable stratification is rarely observed (Chapter IV). The overall source area characteristics of both sites are listed in Table V.1.

Here, the KSS site results are analysed for neutral and unstable atmospheric conditions. Through aggregation of the individual source area weights (Figure V.7a, b) a footprint climatology has been derived. Wind direction distributions differ slightly for the two stability regimes, as is reflected in the overall shapes of the source areas (compare Figure V.7a and b; see, for example, the low probability of south-easterly flow under neutral stratification). A larger (smaller) surface area influences the flux observations under neutral (unstable) conditions with the area contributing 50% to the footprint (shading in Figure V.7a, b) extending on average to about 410 m (250 m) to the southwest and 330 m (180 m) to the northeast. To determine the average surface composition influencing exchanges, the individual source areas were used to weight the land cover fractions in 10° sectors using the individual 30 min mean wind direction (Figure V.7c, d). Consistently, vegetation (e.g. grass and shrubs) and trees (here counted separately) are a small portion of the source area (Table V.1) with maximum coverage (total of 11%) towards the

east. Here, a small park (*Temple Gardens*, Figure V.1) and street trees are located within the 80% footprint isopleth (Figure V.7a, b). Generally, impervious surfaces dominate with buildings and roads forming more than 80% of the source area (Table V.1). Roads have a slightly larger plan area than buildings, except to the northeast where this is reversed. For the west to northeast (245–55°), where impervious surfaces make up more than 90%, surface cover fractions within the source area show little difference with atmospheric stability. Given the vicinity of the River Thames (Figure V.1), open water contributes to the source areas in a broad sector between 75° and 245°, with substantial fractions (>40 % for unstable conditions) from 105° to 205°. To the northwest, the maximum source area contribution (not shown) aligns with a major road (*The Strand*, Figure V.1) where anthropogenic heat emissions from traffic are presumably substantial (Iamarino et al. 2012). The overall source area climatology indicates a strong influence from the *Aldwych* junction (Section V.2.1) at the 50% level (Figure V.7a), again with shorter extent for unstable conditions.

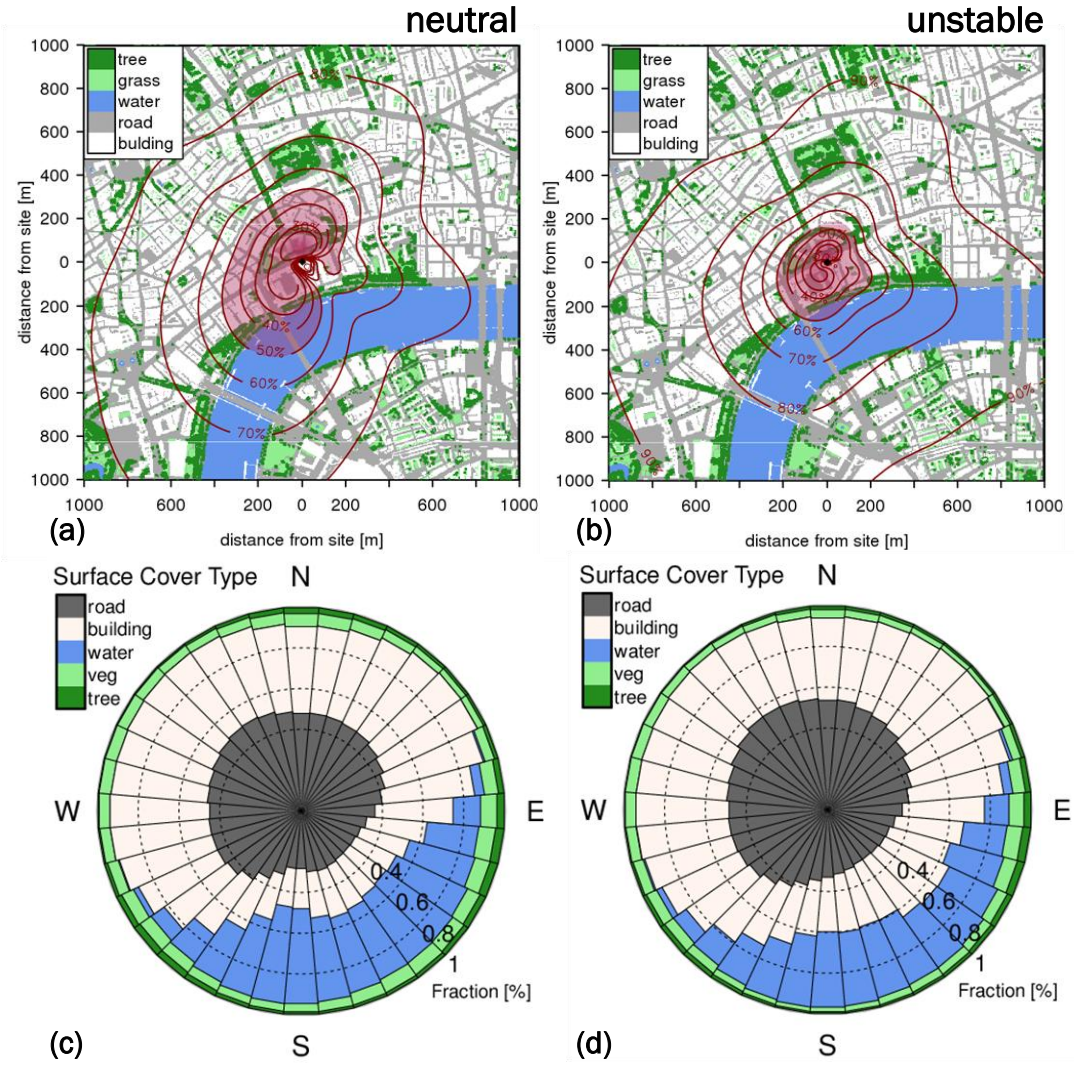

Figure V.7: Spatial and directional characteristics at KSS for (a, c) neutral and (b, d) unstable atmospheric stability: (a, b) Accumulated source area weights. Area contributing up to 50% of the source area is shaded. Underlying map of land cover types, 4 m resolution (based on OS MasterMap and vegetation data from Lindberg and Grimmond 2011). Maps are centred on the tower. (c, d) Accumulated surface cover fraction per 10° intervals, normalised by total amount of observations within each interval.

For northerly wind directions, some influence from traffic emissions can be expected. However, for the prevailing wind direction from the southwest (Section V.4), source area characteristics are very diverse. The climatological 50% isopleths include a large pedestrian courtyard (*Somerset House*, Figure V.1), busy roads (*Waterloo Bridge*), and many tall buildings alongside open water (*River Thames*). This diversity complicates the interpretation of turbulent surface exchange based on the modelled source area.

In general, the modelled fetch at KSK (not shown) does not reach as far and has a slightly different alignment (as expected from the wind rose comparison in Figure V.6). This shift of the wind roses in conjunction with the slight spatial displacement of the two sites of about 60 m (Chapter IV) can result in situations where the eddies observed at the two sites might have been influenced by quite different sinks and sources. Especially for unstable conditions, when source areas are small, observations at the KSK site might have been affected more by nearby roofs and canyons rather than a footprint at the local-scale. Still, even in the roughness sublayer, fluxes are related to surface controls. For example, Kanda et al. (2006) investigated the spatial variability of turbulent fluxes in the roughness sublayer during a winter period where sensible heat flux observations from sites influenced by different source areas were successfully explained by variations in vegetation surface cover. On average, the 50% isopleths for KSK do not include the river towards the south (potential moisture source) and only a small fraction of the busy *Aldwych* junction (potential heat source). The modelled source areas for KSK are probably inappropriate for the times that the measurements are within the roughness sublayer as the fundamental assumptions of the footprint model are not fulfilled. Thus, the footprint analysis (Section V.4.3) is concerned with the KSS site only.

V.4.3 Analysis of footprint surface-atmosphere exchanges

Based on source area characteristics, the relation between surface forcing and observed energy exchange is examined. The turbulent latent and sensible heat fluxes clearly have variations at seasonal and diurnal scales (Chapter IV, Figure IV.6), which, combined with systematic temporal variations in wind direction (for example, northerly winds were more frequent during winter months, not shown), could potentially confuse the investigation of surface controls. In order to minimise this effect, turbulent fluxes were normalised by the incoming radiative fluxes ($Q_{\downarrow} = K_{\downarrow} + L_{\downarrow}$). Median energy flux ratios $Q_H/Q_{\downarrow}$ and $Q_E/Q_{\downarrow}$ are analysed by wind direction (aggregated into 10° intervals) and surface cover percentage (Figure V.8). Furthermore, precipitation clearly affects the Bowen ratio (Chapter IV, Figure IV.9) and is most often associated with frontal systems of mid-latitude cyclones approaching London from the southwest (Met Office 2012a). Hence, fluxes are shown for all conditions (all, Figure V.8[14]) and restricted to measurements with no rainfall within the preceding 12 h (dry) in order to alleviate a potential directional bias caused by precipitation.

[14] Comment on Kotthaus and Grimmond (2013b): Uncertainty of results from Figure V.8 is discussed in Appendix V.A based on the respective inter-quartile range statistics.

Sensible heat flux (Figure V.8a) is strongest from 205–85°, where median Q_H usually makes up at least 22% of $Q_{\downarrow}$, compared to southerly and southeasterly directions, where most median estimates are below 20% $Q_{\downarrow}$. In the first instance, this contrast reflects variations in surface cover characteristics given the energy flux ratio is higher in areas where impervious surfaces dominate (> 80%). However, a series of variations can be identified which illustrate that surface controls on the fluxes are more complex and not driven by the surface cover types alone. For instance, areas with almost complete impervious cover (> 90%) are not associated with higher fluxes than those with small amounts of vegetation (80–90% impervious). Rather, the flux ratios are highest for the latter in an area north of the site between 335–45°. Furthermore, even very low median values of Q_H (< 10% $Q_{\downarrow}$) occur for periods with dominant impervious fractions in the flux source area, namely between 105–145° and 165–205°. Sensible heat flux ratios within these two wind direction regions do not indicate a clear response to surface cover fractions of roads and buildings (ranging from 40–100%), rather they are constantly low. These directional patterns, both to the N and to the SE/S, suggest that other effects, besides the impervious surface cover fractions, need to be considered when interpreting the fluxes observed.

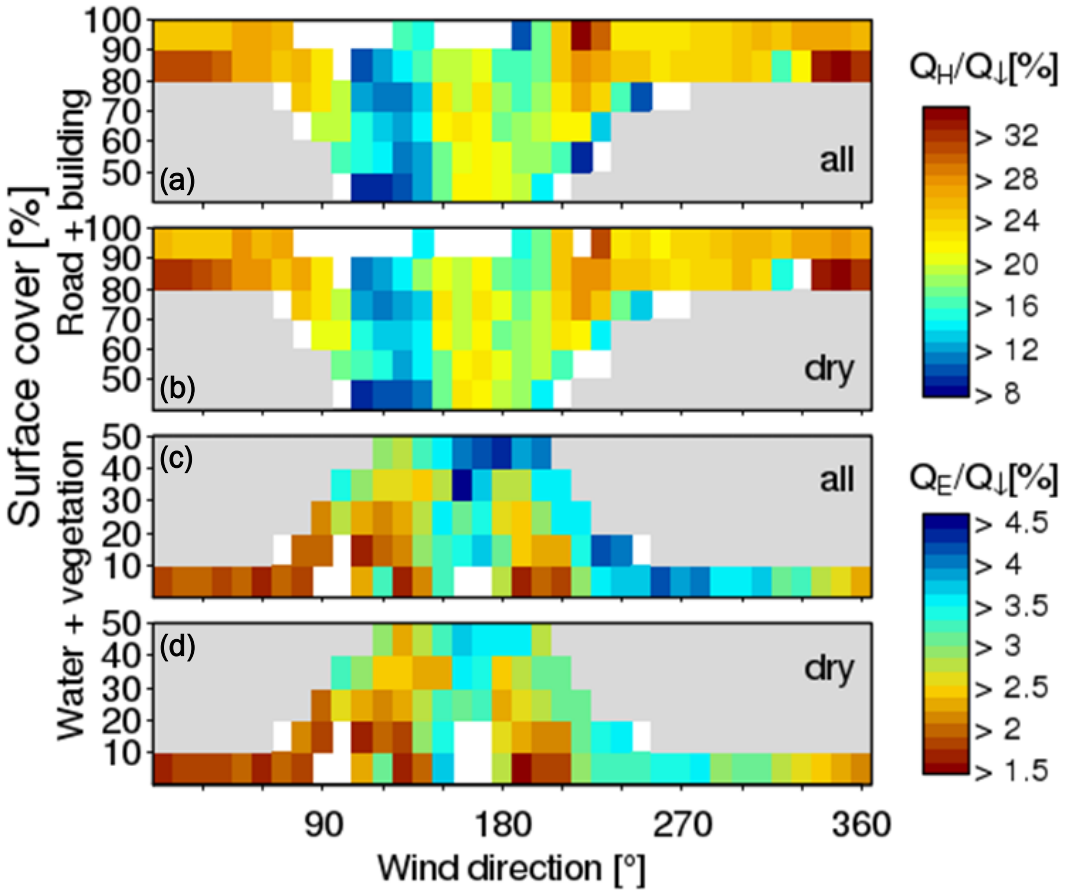

Figure V.8: Median heat flux (a, b) Q_H and (c, d) Q_E at KSS normalised by incoming radiation $Q_{\downarrow}$ by wind direction and surface cover; (a, c) all conditions; (b, d) restricted to periods with no rain within the preceding 12 h. Minimum number of measurements available to calculate the median for each interval (a, b) 15; (c, d) 20 (white – insufficient data). Grey shading indicates land cover/wind direction combinations that cannot occur.[14]

The impact of surface roughness variations in the complex CBD setting can be expected to account for some of the directional patterns seen in the energy flux ratios (Figure V.8). The surface drag is reduced for wind directions aligned with the River Thames (not shown), i.e. in the south (185–205°) and the southeast (115–140°). Wood et al. (2013) found enhanced flow relative to the flux tower sites along the river at this location. Horizontal gradients of temperature and moisture (such as seen in Marseille, Pigeon et al. 2007) could play a role. These regions coincide with those of reduced sensible heat flux (Figure V.8a, b) which suggests that variations in turbulent statistics and momentum transport could explain some of the variability of the turbulent latent and sensible heat fluxes observed. However, given the complex nature of the area surrounding the site, a comprehensive analysis is required to understand the nature of turbulence influencing these measurements. This is beyond the scope of the current study and will be presented elsewhere. These turbulence characteristics may, however, indicate that the reduced sensible heat fluxes (and momentum fluxes, not shown), especially from SE directions, are also associated with larger scale advection which single EC towers are not able to capture. In cases of horizontal advection, the fluxes observed are driven by spatial differences in local-scale surface controls which are not well addressed in the commonly applied EC source area models (Section V.2.3). The fact that normalised sensible heat fluxes do not seem to respond to the amount of impervious surface cover estimated by the footprint model, could suggest that the observed fluxes indeed do not represent the calculated local-scale source area from directions 105–140°.

Modelling approaches incorporating the three dimensional nature of the surface (possibly with back trajectories) would be required to understand the 'history' of the observed atmospheric conditions. Advection has long been recognised to impact EC observations under complex conditions (e.g. Aubinet et al. 2003). Still, there are no simple tools to address the issue of advection (e.g. Feigenwinter et al. 2008; Aubinet et al. 2010). Typically extensive observations are required to be combined with numerical modelling (e.g. Pigeon et al. 2007). Ideally, EC sites should be installed where advection effects are minimal. This requirement, however, is difficult to meet when studying the patchy urban landscape, with areas of varying building density interspersed with areas of very different materials (e.g. parks, rivers and lakes). Advection effects caused by these characteristic urban components need to be addressed during the observation and modelling of urban climate conditions. As cities are retrofitted and built to be more "livable" this patchiness will likely increase further. Thus there is a need to develop appropriate tools to ensure that measurements are appropriately understood and that model performance is evaluated adequately before being utilised for decision making.

In addition, there are meso-scale effects that influence the meteorological conditions observed in central London when the flow is coming from the east. As seen in the KSS wind rose (Figure V.6c), about 4% of the observations are from around 110°, which aligns with the River Thames. Tidal effects might affect the overall roughness of the urban area of Greater London as a whole. Moreover, this wind direction is associated with sea breezes (Bohnenstengel et al. 2011; Chemel

and Sokhi 2012). Further investigation is required in order to understand the relation of local-scale surface controls and synoptic scale conditions as forcing for the observed turbulent surface fluxes.

Overall, the impact of precipitation and associated wet surfaces is not particularly strong on the sensible heat flux (Figure V.8b). On some occasions rainfall results in a reduced Q_H, mostly for the region 190–250°, but this sector already had smaller heat fluxes. As expected, the moisture input has a much stronger influence on the latent heat flux (Figure V.8c, d). For southerly and westerly flow, which represent typical conditions for frontally induced precipitation in the UK, the occurrence of Q_E > 3.5% $Q_{\downarrow}$ is obviously higher when the urban fabric is wet. Still, even when those times are excluded from the analysis (Figure V.8d), the latent heat flux shows a clear signal of higher fluxes from a broad south-westerly range of wind directions (150–280°). This could be an artefact of the way 'dry' surface conditions are defined here. Possibly, the effect of increased evaporation fluxes due to moisture supply by wet surfaces after rainfall occurs for more than 12h, even though its impact on the Bowen ratio clearly decreases after this period of time (Chapter IV). This is not surprising, given the turbulent flux of latent heat observed in this CBD is considerably smaller than that of sensible heat, so the impact on Q_E needs to be substantial to show up in the ratio of energy partitioning. No effect of rainfall is detected under northerly wind conditions where median normalised evaporation is consistently low (< 2.5% $Q_{\downarrow}$).

As for the sensible heat flux, the relation of latent heat flux ratios to surface cover fractions in the source area is complex (Figure V.8d). Median latent heat fluxes range between 2–3.8% of $Q_{\downarrow}$ over the whole range of vegetation and water surface cover (0–50%). Very low fluxes (< 2% $Q_{\downarrow}$) occur for some areas where those surface fractions make up less than 30%. The river, which according to the footprint analysis (Figure V.7c) contributes significantly to the source area between 105–205°, does not have a distinct signature in the latent heat fluxes. It could be argued that the open water surface supplies moisture for evaporation in a region between 175–215° where the latent heat flux ratio appears to indicate an increase of fluxes with water (+ vegetation) surface cover. However, given that the wind directions of increased rainfall and considerable open water surface cover overlap, it is not possible to separate the impact of the two surface moisture sources completely (based on the data available).

In addition to the surface cover types, the three dimensional structure of the surface can give insight into mechanisms governing surface controls on the evaporation flux observed. The river introduces rather abrupt changes in surface roughness (Figure V.1) to the urban canopy which presumably initiate internal boundary layers (IBL) at the river banks. Thermal effects driven by the temperature differences between the water body and the urban fabric may play a role at times. Given the vicinity of the site to the open water surface (< 200 m) and the relative height (59.1 m above sea level, tides ± 3 m), the IBL characterised by the river might be too shallow to reach the sensors. Extensive measurements and/or a high-resolution model would be required to capture the nature of this potential IBL. According to a simple parameterisation (Elliott 1958; assuming a

roughness length of 0.1 m for the river surface which includes boats etc), an IBL initiated at the rough-to-smooth transition at the south bank of the river would probably develop to a height of 35–50 m when reaching the north bank (river width ≈ 300 m). Therefore the IBL height would remain below the KSS measurement level under southerly flow directions. Thus the surface characteristics south of the river would impact the sensor which may explain the lack of large increase in latent heat flux from these directions. Source area models currently available for the interpretation of EC fluxes, such as the analytical model used here (Section V.2.3.1), are not able to capture such complex structures.

Vegetated areas add complexity to the interpretation of potential moisture sources for the maintenance of latent heat fluxes. These may also contribute to prolonged moisture supply after rainfall. Overall, urban vegetation has a comparatively small presence and no large variations with wind direction (Figure V.7c). There are a few more street trees immediately north of the site and slightly more trees and vegetated areas beside the riverbanks (e.g. Temple gardens), but their close proximity to the open water makes it very difficult to separate their effect on the observed surface energy exchange. Further, the small magnitude of the turbulent latent heat fluxes observed in this dense urban environment may mean that the differences between fluxes from certain wind directions are within the observational uncertainty of eddy covariance. Still, despite the small magnitudes of the latent heat flux ratios with incoming radiative energy, the analysis (Figure V.8c, d) suggests that rainfall is the most important moisture source for evaporation in the CBD studied.

The variations of both turbulent fluxes presented suggest that surface cover type alone does not characterise sufficiently the surface controls on surface energy exchanges, rather the impact of surface roughness seems to be significant at various scales. Further aspects to be considered are the spatial patterns of the storage heat flux and the locations of anthropogenic heat and moisture sources in the CBD which are not necessarily captured in the map of land cover types used for the current footprint analysis (Figure V.7a). For example, the latter does not account for the potential effect of anthropogenic moisture sources in areas of impervious land cover (Chapter III) and does not distinguish between busy roads and pedestrian areas (e.g. the *Somerset House* courtyard). For this reason, auxiliary data from an anthropogenic heat flux model (Iamarino et al. 2012) have been incorporated into the energy balance analysis for the current study area (Chapter IV) as an attempt to account for anthropogenic activities around the site. In Chapter IV source area estimates from this analysis are used to spatially align the modelled flux with the EC observations.

V.4.4 Inter-site comparison

Instruments at KSK were lower than at KSS (Table V.1), hence the roughness parameters (Section V.4.1) and source area characteristics differ. As the KSK measurements were within the roughness sublayer at times, the immediate surroundings (buildings and canyons at KCL Strand) would have strongly influenced the turbulent surface exchanges observed. Evidence of the

impact of the surface roughness elements on the flow at KSK has been found in the wind direction frequency distribution, as it is shifted relative to that observed at KSS (Section V.4.1, Figure V.6). Thus to compare simultaneous observations at the two sites, the analysis here is based on the KSS wind direction (dir_{KSS}) and the deviation observed at KSK (dir_{KSS}–dir_{KSK}; Figure V.9). As the simultaneous measurements of latent heat flux observations are limited (Chapter IV, Table IV.1), and the flux is generally of small magnitude, Q_E is not plotted. The shaded area (dir_{KSS} ≈ 39–97°) marks the region where micro-scale anthropogenic emissions have been detected at KSS (Chapter III) or flow distortion induced by the instrumental setup (sensor mountings) might have occurred. No obvious distortion effects are evident in this region of wind direction. However, given the frequency of observations from this sector is low and further diminished due to quality control restrictions (Chapter III), it is not discussed in the comparison of KSK and KSS observations. No numerical requirements have been applied to the observations in each wind direction bin, in order to display the full range of observations (Figure V.9a). However, this should be considered in the analysis of the median ratios of the atmospheric variables (e.g. wind speed,

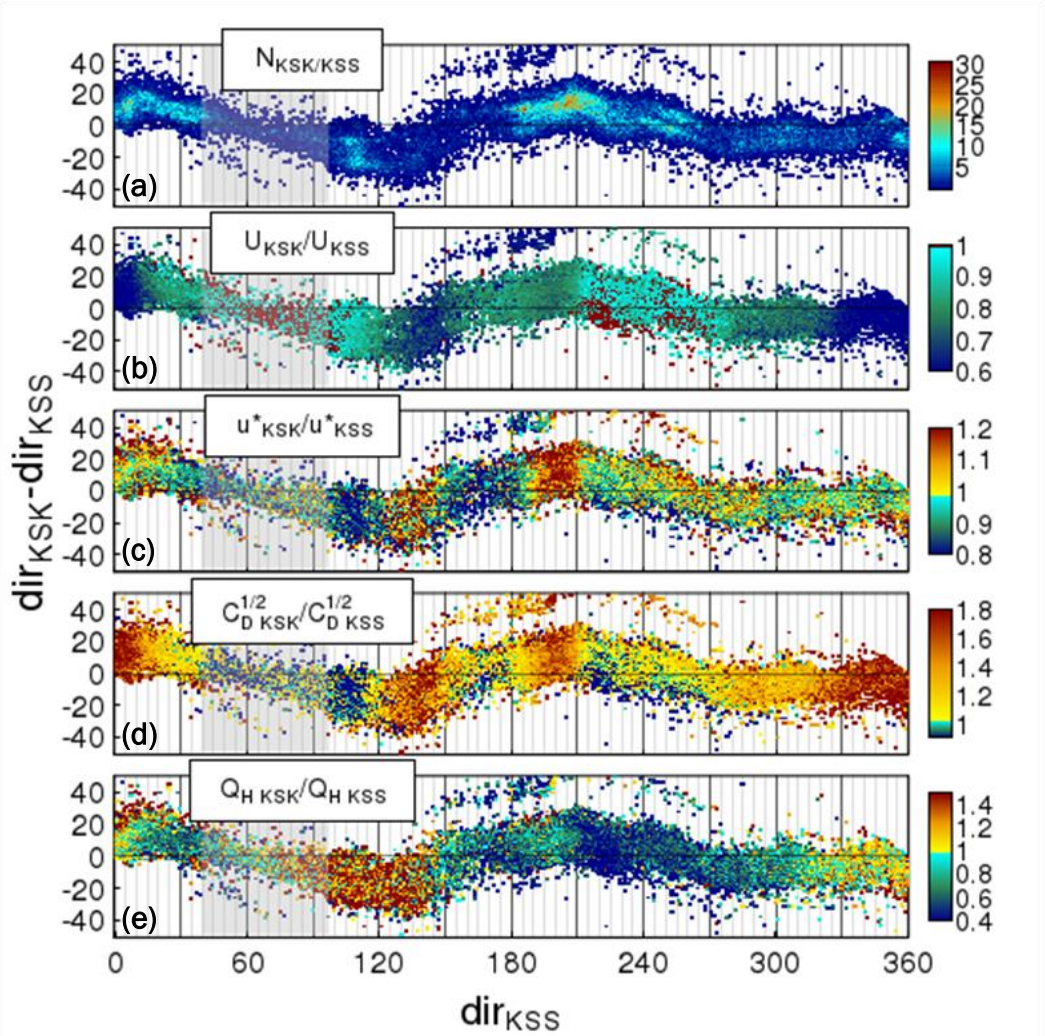

Figure V.9: Median ratio of observations at KSK and KSS of (b) wind speed U, (c) friction velocity u*, (d) drag coefficient $C_D^{1/2}$, and (e) sensible heat flux Q_H by KSS wind direction and the deviation of wind direction at KSK from that at KSS; (a) the number of measurement periods analysed is shown for wind speed ratio (b). dir_{KSK}-dir_{KSS} is restricted to an absolute deviation of 50°. (grey shading; 39–97°) Sector affected by micro-scale anthropogenic sources (IMAS; Chapter III) at KSS and potentially flow distortion effects from the mountings.

Figure V.9a). From the observed wind roses (Figure V.6c, d), it is evident that KSK wind is slightly distorted to the right (resulting in higher wind direction values compared to KSS) for winds from the southwest and northeast and to the left (lower wind direction values) from the west/northwest and east/southeast (Figure V.9). Despite precise instrument-alignment and assessment against an independent reference (wind direction observations at London Heathrow Airport, MetOffice 2012a) some of the deviation may be related to measurement inaccuracies. However, as both negative and positive deviations are detected a simple bias due to misalignment does not explain the differences.

Wind speed, friction velocity and surface drag coefficient ($C_D^{1/2} = u^*/U$) give useful insight into the influence of roughness elements on the observations at KSK when put into relation to those at KSS (Figure V.9b-d). These variables are discussed first, in order to provide the context for interpreting the sensible heat flux patterns (Figure V.9e). As the wind roses (Section V.4) showed, overall winds are stronger at the higher measurement level at KSS (Figure V.9b). Friction velocity is often of similar magnitude at the measurement locations (Figure V.9c); however, there are regions where u* values observed at one clearly exceed those at the other. The surface drag coefficient is generally higher at KSK (Figure V.9d) with only two exceptions, i.e. wind directions 100–115° and partly around 225° (dir_{KSS}).

The most consistent and 'homogeneous' fetch for the two EC sites at KCL is located in the north to north-westerly directions (Figure V.7c, d). Here, height variations have presumably less impact than to the south (Figure V.1). For a broad range of wind directions ($dir_{KSS} \approx 280–40°$) wind speeds are, as expected, considerably higher at KSS (Figure V.9b), thus the lower surface drag coefficient (Figure V.9d) at this higher measurement level. From these directions, the flow observed at the two sites appears to be systematically related. Wind speeds at KSK are, on average under neutral conditions, 0.6 (330–10°) to 0.7 (285–320°) times lower. This suggests a slightly stronger increase of wind speed with height/wind shear than would be described by a neutral logarithmic wind profile. From this, mean wind speed at KSK should be about 0.8 times that at KSS (for $dir_{KSS} \approx 330–10°$ as well as $dir_{KSS} \approx 285–320°$) for neutral stratification periods using the first order roughness parameters (Section 4.1). Hence, it could be argued that observations from these wind directions represent conditions similar to the well-blended surface layer. This agrees with the dense urban canopy in this fetch which makes skimming flow more probable so that mixed turbulence could be observed, even though from these directions both measurement levels are probably below the rule of thumb estimate (2 x the mean building height) of the blending height (Section V.4.1). These findings support the expectation that in densely built areas the blending height will be lower (e.g. Mulhearn and Finnigan 1978; Raupach et al. 1980), as seen in the observations of Christen and Vogt (2004). It further underlines the need to evaluate morphometeric parameterisations under these conditions.

A small sector of wind directions (around $dir_{KSS} \approx 110°$), apparent in both wind roses (Figure V.6c, d) and discussed in the footprint analysis of KSS observations (Section V.4.3), indicates

channelling by the nearby river. Here, the KSK wind speed has a local maximum so that observations are very similar to those at KSS (often $U_{KSK}/U_{KSS} > 0.9$). Wind directions of $dir_{KSS} \approx 100–115°$ represent the only region where both friction velocity and surface drag coefficient are clearly higher at KSS compared to KSK, with ratios of about 0.8 and 0.9, respectively. The DEM around the sites (Figure V.1) shows the ground and building height variations at KCL Strand. The orientation of the building hosting the KSK mast, suggests that bluff body effects could influence the flow observed at this lower measurement height towards the southeast. Further, flow is potentially separated to bypass the bluff body, which would introduce wake flow into the turbulence observed at KSK. This bluff body might cause acceleration of the flow around it, explaining the relatively higher wind speeds, reduced friction velocities and surface drag discussed for directions of $dir_{KSS} \approx 100–115°$ (Figure V.9b-d).

As noted (Section V.4.3), the surface drag and u* observed at the higher KSS tower (not shown) are reduced for wind directions aligned with the River Thames ($dir_{KSS} \approx 115–140°$ and 185–205°). Friction is higher for the region in between ($dir_{KSS} \approx 155–175°$), where the fetch of open water is considerably smaller and the sharp increase in surface roughness at the north bank of the River Thames might cause some bluff body-type impacts on the flow from these directions. The u* variation at KSS is evident in the observed ratios (Figure V.9b, c). The intra-site comparison (Figure V.9) has the bluff body effects of the KSK building (possibly affecting the flow for $dir_{KSS} \approx 100–195°$) and the river-roughness variations seen at KSS ($dir_{KSS} \approx 110–210°$) superimposed. For example, to the west of KSK, increased wind speeds and decreased surface drag may be expected, similar to those at $dir_{KSS} \approx 100–115°$, but they are obscured by the KSS signature (Figure V.9b-d).

Wind speeds at the two heights are similar between $dir_{KSS} \approx 210–280°$ (Figure V.9b): the median ratio of observations at the two locations is close to unity and some KSK wind speeds are even slightly higher than those at KSS (maximum $U_{KSK}/U_{KSS} = 1.01$; cf. compared to the mean of 0.9 for neutral conditions calculated using the log–law based on average initial morphometric parameters for all directions). These south-westerly directions are probably where the KSK tower encounters the least roof-induced roughness in the immediate surroundings and the flow observed at KSS is influenced mainly by roads and buildings (rather than the open water). The surface drag is mostly higher (factor of ≈1.2) at the KSK site (Figure V.9d). However, the stronger winds at KSK (Figure V.9b) for some wind direction combinations impact the surface drag coefficient (Figure V.9d). In the south-westerly region, wind speed (Figure V.9b) and friction velocity (Figure V.9c) variations are correlated with the wind direction deviations ($dir_{KSK}–dir_{KSS}$, Figure V.9), but the ratio of friction velocity in this region is very complex. Again, a more in-depth analysis of turbulence characteristics might lead to a better understanding of processes governing the flow from these directions observed at the two heights.

Within $dir_{KSS} \approx 280–40°$ there are low wind speed ratios to the north ($dir_{KSS} \approx 325–10°$; Figure V.9b) potentially caused by bluff body effects. The KSK tower is only 1.5 m taller than the building

hosting the KSS tower (Figure V.1), so flow distorted around this building from both its westerly and easterly sides, affects the deviations at $dir_{KSS} \approx 280–320°$ and $dir_{KSS} \approx 10–40°$, respectively. Winds observed at KSK are slightly accelerated compared to the northerly region ($dir_{KSS} \approx 325–10°$) as is evident in the wind speed ratio (Figure V.9b). Given the southwest–northeast orientation of the building (Figure V.1), the edge effect is sharper at the easterly end, where the redirection of the KSK wind direction appears more pronounced than at the westerly edge (dir_{KSS}-dir_{KSK}, Figure V.9).

For most wind directions, higher turbulent sensible heat fluxes are recorded at KSS (on average $Q_{H\,KSK}/Q_{H\,KSS} \approx 0.6$). However, a clear response to the flow characteristics discussed is evident (Figure V.9e). As noted (Section V.4.3), channelling along the river and possible horizontal advection may influence the observations when wind is from the south ($dir_{KSS} \approx 185–205°$) and the southeast ($dir_{KSS} \approx 115–140°$). However, as this direction has been rarely observed at KSK and associated with low sensible heat fluxes at KSS (cf. Figure V.8), this results in values close to 1 (Figure V.9e). From the southeast ($dir_{KSS} \approx 90–145°$), sensible heat fluxes are smaller at KSS than at KSK. Any bluff body effect impacting the flow at KSK would play a role ($dir_{KSS} \approx 100–115°$), but higher wind speeds usually do not favour buoyancy. We speculate the higher Q_H at KSK may be induced by the nearby building facets. The sensible heat fluxes are more similar for the southerly directions ($dir_{KSS} \approx 185–205°$) so that the heat flux remains higher than that observed at the lower measurement level, with ratios around $Q_{H\,KSK}/Q_{H\,KSS} \approx 0.7$ (Figure V.9e). Sensible heat flux at KSK is about half that of KSS for westerly flow conditions, where surface drag and wind speed at the two heights were found to be very similar ($dir_{KSS} \approx 210–280°$). For northerly directions ($dir_{KSS} \approx 330–10°$), where wind speed (Figure V.9b) and friction velocity (Figure V.9c) indicate a systematic vertical wind profile, the sensible heat fluxes are nearly identical (also when comparing individual values, not shown). Here, the median ratio is close to unity.

Obviously, variations in anthropogenic heat sources and net storage heat flux relate to the urban canopy structure, and will impact the turbulent sensible heat fluxes observed. The canopy structure influences both the blending height, and the ability to transport heat, momentum, moisture and other constituents above the roughness sub layer. The latter is illustrated by the example of horizontal advection, induced by the channelling along the river. Such surface variations have been found to affect the flow in the surface layer elsewhere. For example, an inter-site comparison by Schmid et al. (1991) revealed that rather small surface variations can significantly impact the turbulent fluxes measured, even when the measurement height is likely above the roughness sublayer and the heterogeneity of the urban surface is classified as well-mixed at the local-scale. In their study, local-scale differences were of nearly comparable order of magnitude to urban-rural differences found elsewhere. Accordingly, the differences found between KSK and KSS could provide an estimate of the expected variations within the local-scale.

V.5 Implications for turbulent source area models and siting of EC systems

The results presented illustrate the challenges micrometeorological research faces in the complex, dense urban environments. Observations at the higher measurement level (KSS) were influenced by regional to local-scale advection, and local-scale roughness elements and bluff body effects of the urban surface. The micro-scale features were more evident in the measurements at the lower level (KSK) indicating it was within the roughness sublayer. The internal boundary layers that develop over the nearby river surface have likely not developed to sufficient height to reach the flux towers, so the latent heat fluxes remained small. The low vegetation cover, the complex arrangement of anthropogenic (heat and moisture) emissions and probably most importantly the immense variability of the three dimensional structure of the urban canopy (affecting radiation fluxes, heat storage flux, surface roughness and flow conditions) all make it difficult to interpret the observed quantities simply.

As is well known for surface energy balance measurements, in order to measure turbulent fluxes representative at the local-scale, a homogeneous fetch is considered a crucial requirement. Further, it is recommended to choose a sensor height well above the blending height. Measurements should be located far away from any object with bluff body characteristics, far away from chimneys and other micro-scale sources of anthropogenic emissions, and be sufficiently distant from large-scale surface changes that might induce horizontal advection. Obviously, every effort should be made by those using eddy covariance for local-scale turbulent exchanges to follow those guidelines. However, in cities, and especially their dense centres, it is often challenging to find these 'ideal', suitable locations, simply due to the heterogeneous nature of the urban canopy and/or due to logistical constraints (e.g. access etc.).

Still, the patchiness of surface form and materials are the reality of cities and hence of specific interest. In order to adequately capture such aspects, measurement strategies need to be designed carefully and properly adapted to the urban setting. Where ideal measurement locations cannot be chosen, it may be advisable to operate a series of sites in proximity. As the current study shows, a second tower, even with a lower sensor height within the roughness sublayer, has the potential to add useful information for the interpretation of fluxes measured. And, as indicated with respect to radiative source areas (Section V.2.3.2), multiple measurements would improve the spatial representativeness. In addition to profile measurements (EC observations at different height/horizontal distances) other measurement approaches (such as surface or atmospheric remote sensing) obviously can add useful information for the interpretation of the fluxes measured.

Data need to be analysed in combination with adequate footprint models that can treat the complex urban areas appropriately. The site described in this study illustrates some of the more sophisticated requirements that need to be incorporated into future footprint models. Where surface heterogeneities are low, it is probably acceptable to rely on simple wind direction sector

analysis. However, over patchy surfaces, such as those including larger parks or river surfaces, the application of simple models provides only very first order results as likely internal boundary layers and advective fluxes are not accounted for. Such features will need to be addressed by footprint models aiming to be applicable to the real urban surface. However, such models need to be computationally efficient and address the range of atmospheric stability, most notably urban areas' unstable conditions.

V.6 Conclusions

Urban climate observations are often constrained by logistics (e.g. safety, planning, economic, operations, maintenance, access etc.). This results in few sensors being installed and typically only in restricted locations. Modelling of surface atmosphere exchanges are also challenged by urban environments, especially in complex central business districts (CBD). Nevertheless, it is critical to understand the atmospheric processes within these areas, given this is where many people live and work. The analysis of fluxes observed at two nearby sites in central London allows some conclusions to be drawn about urban surface energy exchanges. Moreover, it demonstrates methodological challenges of research in CBD that have clear implications for future studies.

Radiation measurements are impacted by the anisotropic nature of the urban surface and the high reflectance materials increasingly being used in buildings. With sufficient irradiance, the surface albedo is influenced by strong specular reflections or reflection glare. The surface deviates distinctly from Lambertian characteristics. This highlights the need to consider the source area of radiometers in terms of both diffuse and direct irradiance. Accounting for reflections of direct irradiance, which depend on the solar position relative to the site (i.e. latitude, time), sensor height, and the BRDF of the observed surface (described by a combination of conditions at various scales from material properties to three-dimensional canopy structure) allows apparently anomalous reflected short-wave radiation to be explained.

Spatial patterns of surface albedo suggest that the lower bulk surface albedo observed at the site with the greater measurement height ($\overline{\alpha}$ = 0.11 at KSS) better represents the local-scale area, whereas instruments located at a lower elevation show a bias towards roof surfaces ($\overline{\alpha}$ = 0.14 at KSK). Under overcast conditions at both sites, the bulk surface albedo is close to these median albedo values (higher by 0.01). Using cloud cover information, it is shown that the impact of specular reflections on surface albedo measurements is highly accentuated under clear sky conditions and decreases with increasing cloud cover. In London, above 70% cloud cover, diffuse radiation mostly dominates over the direct flux.

An analytical footprint model was used to relate the observed turbulent fluxes of sensible and latent heat to surface controls from different land cover types. Land cover fractions derived from this modelled turbulent flux source area indicated that dominant[15] turbulent sensible heat fluxes occur where impervious surface fractions are particularly high. However, the modelled source

[15] Amendment of Kotthaus and Grimmond (2013b): 'high' replaced by 'dominant'

area characteristics did not fully explain the spatial variations of the turbulent fluxes. Sensible heat flux was lower from directions potentially affected by a nearby open water surface, the River Thames. However, this did not seem to be related to the moisture supplied and its potential impact on the partitioning of available energy, as there is no clear increase in turbulent latent heat fluxes. Rather, the river has a decrease in surface roughness, so the decrease in sensible heat fluxes was explained by channelling of the flow and potential horizontal advection. The impact of the river on the observed fluxes might have been further limited if the internal boundary layers that form over the water surface do not develop to the height of the flux towers. Such effects are not captured by the analytical footprint model. Probably, detailed LES modelling could provide some insights.

It has not been possible to quantify precisely the role of vegetation as a moisture source for the latent heat fluxes, given its generally small surface coverage. While no clear signal was found in the latent heat flux corresponding to the nearby water surface (presumably due to the formation of internal boundary layers) or the sparse vegetation, rainfall appeared to be a key driving-factor for evaporation in this dense urban environment. When the urban fabric was wet, mostly associated with south-westerly flow (i.e. frontal systems connected to mid-latitude cyclones), the generally small latent heat flux magnitude did increase. However, the response to rainfall could not be isolated from the influence of the vegetated areas and their soil moisture content.

While only limited conclusions could be drawn from the source area analysis, because of the spatial distribution of the land cover types (e.g. no area with particularly high vegetation in the flux footprint) and the applicability of the model under such complex conditions (e.g. three dimensional building form, advection along the river), the analysis of flow patterns proved more suitable. Comparison of the two measurement heights suggested the spatial variations of the sensible heat flux observed were related to changes in surface roughness. Measurements at the higher level clearly picked up the larger scale channelling induced by the riverbed, while bluff body effects explained variations at the lower level. Where the source areas were most homogeneous (areas with greatest built density), flow conditions were vertically consistent. The wind velocity profile was similar to the log–law and sensible heat flux appeared to be invariant with height, even if initial morphometric parameters suggested the measurements may be below the blending height. These findings indicate that the investigation of turbulence statistics may be more informative in the interpretation of turbulent fluxes than detailed calculations of surface cover fractions without detailed 3D information incorporated. Also, it highlights that parameterisations of morphometric characteristics need to be further evaluated for such complex settings.

This work demonstrates, even in this complex setting, observations provide useful information about processes governing surface-atmosphere exchange that must be understood in the context of global urbanisation and climate change adaptation strategies. Detailed analysis and careful interpretation do allow us to describe and move towards quantifying atmospheric conditions in

the CBD. This study identified limitations to some current observational approaches, including critical aspects of instrument siting in complex urban settings and where more detailed, better adapted footprint models are required. All fluxes of the surface energy balance are highly scale dependant, which needs to be considered when interpreting measured (as well as modelled) energy fluxes in relation to each other. Both for radiometer and EC flux measurements, it is suggested that simultaneous operation of two nearby sites can greatly benefit the analysis. Multiple radiation sensors could be combined to be more representative of the turbulent flux footprint. The results provide an example of how observations within the roughness sublayer can be interpreted, also with respect to the impact of bluff bodies. Clearly more measurements are needed from such settings, but this work underlines the requirement for careful directional analysis and interpretation of such datasets.

Measurement and modelling approaches may be pushed to their limits in dense urban settings, but if urban climate research is to contribute to the challenges of real cities those limits have to be addressed. To manage cities sustainably and smartly, currently and into the future under changing climates, measurements and models must also consider central urban areas where interactions of humans with the environment are particularly concentrated. Surface heterogeneities that have proven to challenge both measurements and modelling techniques in this study are at the scale where urban planning strategies are implemented (e.g. usage of high reflectance materials, orientation of buildings, etc.). Measurements will allow improved understanding of the processes, enhanced modelling skill and better forecasting with data assimilation to help make cities more resilient places.

Acknowledgements

This study was funded by EUFP7 Grant agreement no. 211345 (BRIDGE) and NERC ClearfLo (NE/H003231/1), EPSRC (EP/I00159X/1, EP/I00159X/2) Materials Innovation Hub and KCL. We thank Dr Andreas Christen (UBC, 2010) for use of his IDL based implementation of the footprint model; Dr Brian Offerle and Dr Fredrik Lindberg for use of their script for morphometric parameter calculations; Dr Arnold Moene at Wageningen University for providing the ECpack software and for all advice regarding its usage; Dr Jiangping He for support of our data archive; Dr Catherine Souch for her comments; all people/students at KCL who contributed to the data collection; KCL Directorate of Estates & Facilities for giving us the opportunity to operate the various measurement sites. We appreciate the constructive comments and suggestions of both reviewers, which proved very helpful in the development of this work.

Appendix V.A Uncertainty in analysis of footprint surface-atmosphere exchange

Surface controls on the turbulent fluxes of sensible heat Q_H and latent heat Q_E were analysed as a function of surface cover fractions, by wind direction (Section V.4.3; Figure V.8). To account for seasonal and diurnal variations, these energy fluxes were normalised by total incoming radiation $Q_{\downarrow}$. Still, there may be variability of the turbulent exchanges not captured by the median statistics presented (Figure V.8). The respective inter-quartile range (IQR) statistics (Figure V.A.1) reveal particularly high uncertainties for the flux of evaporation (Figure V.A.1c, d): for this flux, the IQR describes similar spatial patterns as the median statistics (Figure V.8c, d). This is in agreement with the analysis presented (Chapter IV; Chapter V) because latent heat fluxes observed at the central urban sites are rather small with their temporal and spatial variations in a similar order of magnitude as their absolute values. The variability of the normalised sensible heat fluxes (Figure V.A.1a, b) relative to their absolute values (Figure V.8a, b) is a little lower and spatial patterns less similar. For this flux, the IQR statistics do not show particular dependence to wind direction and or land cover fractions. Only in the sector where fluxes appear diminished by effects of horizontal advection (105–135°), the variability shows a tendency for slightly lower values as well.

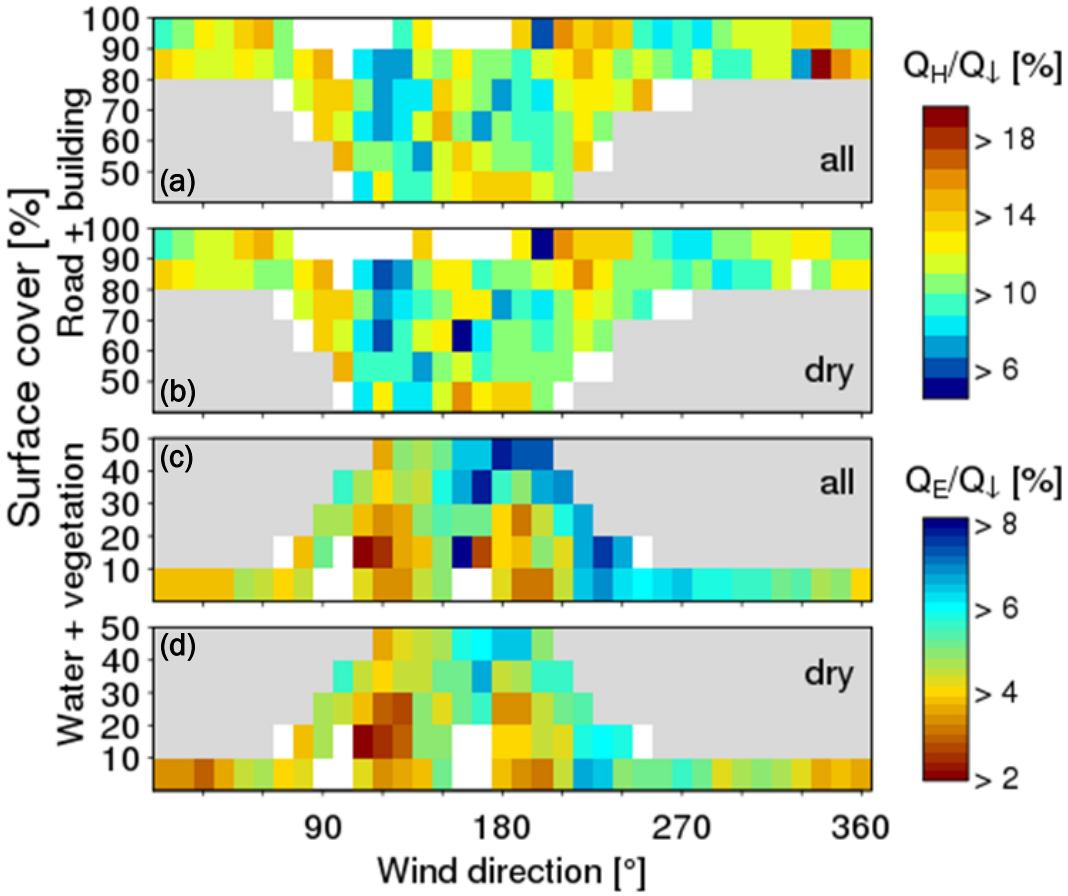

Figure V.A.1: As for Figure V.8 but showing inter-quartile-range instead of median statistics.

VI Conclusions

VI.1 Introduction

This study advances the understanding of energy exchange processes in the dense urban environment through analysis of measured and modelled components of the surface energy balance for an area in the central business district (CBD) of London, UK. The methods and analyses presented in the study are relevant at temporal and spatial scales (Figure VI.1) – ranging from the order of minutes to decades, and from individual facets to neighbourhoods.

Key aspects of the study and findings include:

A The spectral radiative responses of impervious urban materials (Chapter II) characterises the building structures and facets in terms of their material composition, which usually remain similar over several years or decades.

B Broadband radiation fluxes at different heights above the urban canopy are influenced by a combination of surface characteristics (composition and geometry) and variable atmospheric conditions (Chapter IV; Chapter V). The latter can change relatively rapidly (e.g. cloud cover) or reflect longer cycles (e.g. solar elevation). The outgoing radiative fluxes are clearly related to the sun-surface-sensor geometry. In this study the influence of different canopy structures is analysed, from single building facets such as windows, to buildings and urban canyons.

C Micro-scale anthropogenic emissions of heat, moisture and CO_2 (Chapter III) reflect human activities at the (sub-)building scale. While their impact on local-scale turbulent fluxes is mostly short-lived (depending on atmospheric conditions, of the order of minutes to hours or days), micro-scale fluxes reflect the diurnal as well as the seasonal trends of anthropogenic activities.

D The role of local-scale anthropogenic heat flux in the urban surface energy balance is documented to be substantial all year. At temporal (spatial) scales it varies in response to atmospheric conditions (surface structure/cover).

E The turbulent fluxes of sensible and latent heat, respond most directly to variations in available energy and moisture. Hence they vary at scales closely linked to those controlling radiation fluxes and anthropogenic emissions (and also the storage heat flux), and further to those related to moisture supply (e.g. rain water at temporal scales from minutes to hours/ days).

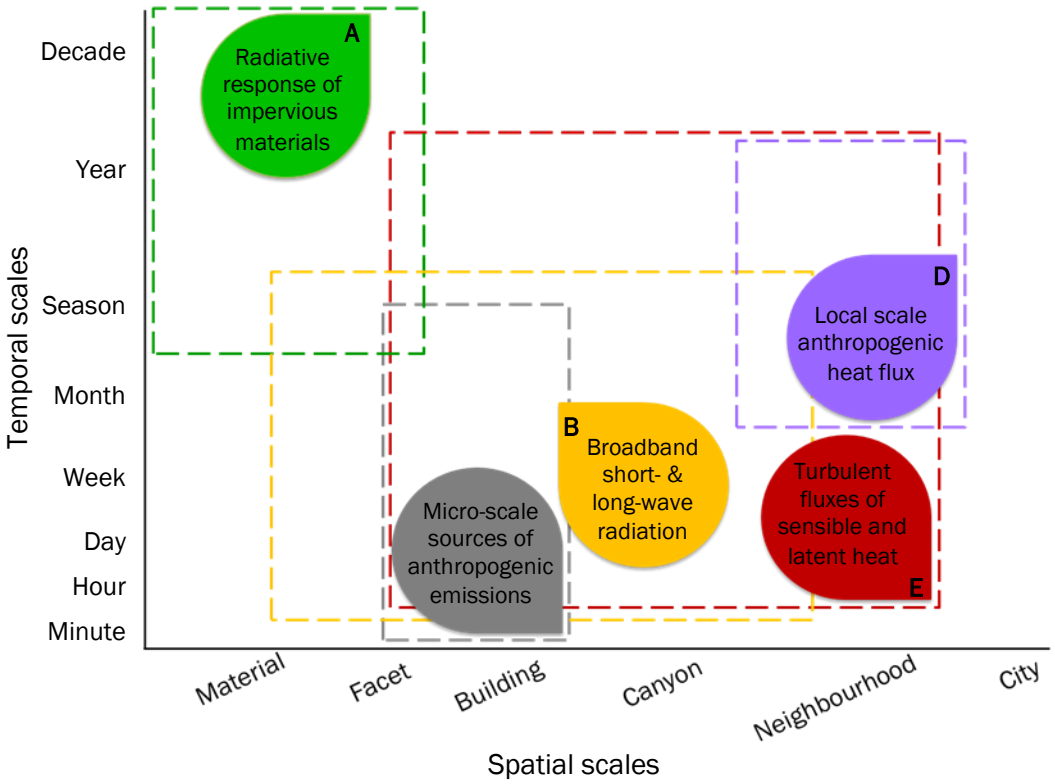

Figure VI.1: Aspects of the urban surface energy balance investigated in this study indicating their relevance at spatial and temporal scales (dashed lines).

These findings provide new insights concerning radiative processes (Section VI.2), the contribution of anthropogenic emissions (Section VI.3), and the turbulent fluxes of latent heat and sensible heat (Section VI.4) in an environment where energy exchange processes strongly influence climate conditions at different scales. Further, the work identifies issues important to be addressed by future urban climate studies (Section VI.5). Suggestions are made with respect to the development and applicability of the various methods used and the processes/ characteristics of surface energy exchanges that may require special attention.

VI.2 Radiation exchange

Different controls governing radiation exchanges in the CBD of London are investigated. First, the potential of spectrally detailed information covering the long-wave infrared (LWIR) region to better characterise impervious urban surface materials is considered. A spectral library is derived through emittance and reflectance spectroscopy (Chapter II), also including visible to short-wave infrared (VIS-SWIR) wavelengths. Second, long-term (3.5 years) measurements of the broadband components of the radiation balance, i.e. incoming and outgoing short- ($K_{\downarrow}$ & $K_{\uparrow}$; again covering VIS-SWIR) and long-wave ($L_{\downarrow}$ & $L_{\uparrow}$) radiation, are presented. These reveal key aspects of the temporal (Chapter IV) and spatial variations (Chapter V) of radiative energy exchanges.

VI.2.1 Radiative response at the scale of materials

Recent advances in thermal infrared remote sensing include increased availability of multi- and hyperspectral information covering the long-wave infrared (LWIR) region. This is expected to greatly enhance the study of urban environments where thermal characteristics are of special interest and the surface materials are particularly diverse. To support interpretation of such data, LWIR emissivity spectra of relevant materials are required as a reference. In this study, one of the first spectral libraries of impervious urban materials covering both the short-wave (VIS-SWIR; 300–2500 nm) and the long-wave infrared (8–14 μm) spectral regions (Appendix A) was derived from observations. Data were collected using field-portable spectrometers in controlled laboratory conditions with methodologies mostly applicable also to an outdoor setup. Some useful information was gathered during prior outdoor field observations (Appendix B).

The new spectral library of impervious urban materials is available from the London Urban Micromet data Archive (LUMA; Appendix C ; *http://londonclimate.info/LUMA/SLUM.html*).

- Short- and long-wave response of 74 samples, with meta-data and pictures (Appendix A), are categorised into ten classes based on usage and material composition.
- Short descriptions of the ten material classes summarise their dominant absorption characteristics (Appendix II.B).
- The short-wave response of composite construction materials varies greatly, while long-wave response is more consistent within a single material class.
- As many construction materials consist of minerals, which often have distinct reststrahlen and absorption features in the LWIR, hyper-spectral information in this spectral region has great potential to characterise these constituents.
- Metals have the most diverse radiative response in both the short- and long-wave region. They remain under-represented in spectral libraries and should receive special attention in future studies.

Despite numerous samples being measured, the compiled spectral library does not fully represent the diverse range of materials found in urban areas. Ground truth observations should be performed to support imagery collected from airborne and space-borne platforms. With new materials and coatings being developed, characterisation of urban spectral radiative response is an on-going and dynamic process. Hence, the current work focuses on the methodology to measure radiative properties with field-portable spectrometers to provide suggestions for future studies. While short-wave reflectance observations are widely used for ground-based remote sensing, LWIR spectroscopy until recently has been confined to specialised laboratories. Hence, a detailed framework for spectral emissivity measurements using a field-portable Fourier Transform InfraRed (FTIR) spectrometer is developed in this study:

- It is demonstrated how uncertainties linked to the instrumental setup and radiometric calibration can be assessed using a thermal imaging device and auxiliary observations from independent radiation sources.

- To ensure a suitable signal-to-noise ratio, targets observed under laboratory conditions need to be heated substantially above room temperature immediately prior to the spectral sampling (unnecessary outdoors).

The methodology and setup is evaluated by measuring a sample of known composition. Errors from radiometric calibration and system performance are comparable to uncertainties of the method applied to separate the temperature and emissivity signature of the target.

VI.2.2 Radiation balance at the micro- to local scale

Long-term radiation balance observations at two CBD sites (*KSS, KSK*) with different measurement heights above the canopy are analysed in the context of meteorological and cloud cover conditions. The findings illustrate processes at different scales:

- At night under clear sky conditions up to 35% more energy leaves the urban surface than is received via long-wave radiation. As cloud cover increases, this percentage decreases, so that for an overcast sky $L_{\uparrow}$ and $L_{\downarrow}$ are nearly equal. Cloud cover diminishes nocturnal cooling rates of the urban surface, so that outgoing long-wave radiation decreases by only 5% over the course of a night for overcast conditions compared to 7% for clear nights. During daytime, outgoing long-wave radiation drops to 40% of the total incoming radiative energy under clear sky conditions, remaining higher for overcast periods (about 70%). Although, not an urban characteristic, the relations have important impacts on the surface temperatures and therefore the energy balance as a whole.
- Radiation measurements are impacted by the anisotropic nature of the urban surface and the high reflectance materials increasingly being used as building materials. With sufficient irradiance, the surface albedo is influenced by strong direct reflections or reflection glare and the surface deviates distinctly from Lambertian characteristics. This highlights the need to consider the source area of radiometers in terms of both diffuse and direct irradiance. Accounting for reflections of direct irradiance, which depend on the solar position relative to the site (i.e. latitude, time), sensor height, and the bidirectional reflectance distribution function (BRDF) of the observed surface (described by a combination of conditions at various scales from material properties to three-dimensional canopy structure) allows apparently anomalous reflected short-wave radiation to be explained.
- Spatial patterns of surface albedo suggest that the lower bulk surface albedo observed at the site with the greater measurement height ($\overline{\alpha}$ = 0.11 at KSS) better represents the local-scale area, whereas instruments located at a lower elevation show a bias towards roof surfaces ($\overline{\alpha}$ = 0.14 at KSK). Under overcast conditions at both sites, the bulk surface albedo is close to these median albedo values (higher by 0.01). Using cloud cover information, it is shown that the impact of specular reflections on surface albedo measurements is highly accentuated under clear sky conditions and decreases with increasing cloud cover. In London, above 70% cloud cover diffuse radiation mostly dominates over the direct flux.

VI.3 Anthropogenic emissions at the micro- and local scale

Using a new analysis approach (Chapters III and IV) anthropogenic emissions were measured at the micro-scale, and modelling (Chapter IV) was undertaken to quantify fluxes at the local scale.

The new analysis, termed here IMAS, used the long-term (3.5 years) eddy covariance (EC) measurements at two nearby CBD flux-towers (*KSS, KSK*). This procedure identifies extreme events in sonic temperature, water vapour and carbon dioxide concentrations, and enables separation of micro-scale emissions from local scale fluxes. This new filtering technique was tested and then verified using observations that could be attributed to anthropogenic sources located near the instruments. Analysis of the IMAS processed data, where significant emissions sources were present, found:

- The results have physically reasonable diurnal patterns.
- The impact on friction velocity, sensible heat, latent heat and carbon dioxide fluxes can be explained physically and there is consistent behaviour in a direct comparison of L1 (no filter) and L2 (with IMAS filter) results and for the overall frequency distributions.
- Overall the filter reduces the surface fluxes but analysis by wind direction shows the fluxes to be enhanced when the flow is from the directions of the sources and the percentage of identified data points (event frequency γ_E) has this directional behaviour.
- Evaluation at the two proximal sites shows comparable functionality.

The IMAS processed turbulent surface fluxes, provide a direct estimate of the anthropogenic heat fluxes originating from building scale emissions (Q_{Fb}).

- Quantitative analysis suggested that sensible heat and carbon dioxide fluxes are influenced strongly.
- For all results, the magnitude of micro-scale induced fluxes can be explained by temporal variability of human activities and variations in approaching flow direction.
- The long-term averages have magnitudes that are comparable to model estimates of Q_{Fb}.

Analysis of modelled (Iamarino et al. 2012) monthly local scale anthropogenic heat flux for the study area and air temperature observations indicate:

- In central London, modelled building anthropogenic heat fluxes are constant when mean daily air temperature exceeds a threshold (≈ 17.5°C).
- Anthropogenic heat contributes significantly to the surface energy balance throughout the year. Q_F is the dominant energy source during winter and ranges in the same order of magnitude as net all-wave radiation during summer (mean daily basis).

VI.4 Turbulent fluxes of latent and sensible

Analysis of the EC observations of the turbulent fluxes of latent (Q_E) and sensible heat (Q_H) at the two CBD sites (*KSS*, *KSK*) covers a range of meteorological conditions (e.g. very dry winter months, warm spring periods, wet summer periods) from which the following conclusions are drawn (Chapters IV; Chapter V).

- Sensible heat fluxes are positive all year round, even at night, sustained by a combination of storage and anthropogenic heat fluxes. Monthly median nocturnal fluxes (50-100 W m^{-2}) are amongst the highest observed but are not unexpected given the building densities and activities in this central city area. Turbulent sensible heat flux systematically exceeds the input from net all-wave radiation.
- A monthly time scale analysis of energy balance closure, initially gives a constantly positive residual (0.7-8.9 MJ d^{-1} m^{-2}); whereas accounting for a measurement underestimation of the EC fluxes (20%) and an over-estimation of Q_F (26%) the mean annual residual is effectively zero.
- The strong positive Q_H inhibits stable atmospheric stratification but atmospheric stability is mostly controlled by the friction velocity over the rough urban surface. Neutral stratification (about a third of the time at KSS) has peak frequencies in the early evening associated with the diurnal cycles of momentum and sensible heat fluxes.
- Turbulent latent heat fluxes are very small, so Bowen ratios are mostly larger than one (mean β = 6.4 at KSS) and decrease through the day as higher evaporation rates occur in the afternoon (probably induced by a higher vapour pressure deficit and increased turbulent transport). The daytime mean Bowen ratio is independent of averaging time duration.
- Due to small surface cover fractions of vegetation, its role as a moisture source is not detectable in the weak evaporation signal and phenological variations are accordingly not evident.
- Variations in the evaporation observed are controlled by rainfall (beyond the available energy). The Bowen ratio immediately following rainfall is depressed. Values of between 1–2.5 dominate for a period 1 to 6 h after the event; then the ratio increases given impervious surfaces remove surface water efficiently. The effect of most precipitation events is limited to a period between 12–18 h after the rain has stopped.
- An analytical footprint model was used to relate the observed turbulent fluxes of sensible and latent heat to surface controls from different land cover types. The derived land cover fractions indicate the high turbulent sensible heat fluxes are associated with high impervious fractions. However, the modelled source area characteristics do not fully explain the spatial variations of the turbulent fluxes. Although the sensible heat fluxes are lower from directions potentially affected by a nearby open water surface (River Thames) this does not seem to be related to moisture supplied as there is no clear increase in turbulent latent heat fluxes. Rather, the low surface roughness of the river indicates that channelling of the flow and potential horizontal advection may be responsible for the relatively low sensible heat fluxes observed under certain conditions. Further, the impact of the river on the

observed turbulent fluxes may be limited if internal boundary layers forming over the water surface do not develop to the height of the flux towers.

- While only limited conclusions can be drawn from the source area analysis, because of the spatial distribution of the land cover types (e.g. no area with particularly high vegetation in the flux footprint) and model applicability under such complex conditions (e.g. three dimensional building form, advection along the river), the analysis of flow patterns proved more suitable. Comparison of the two measurement heights suggests the spatial variations of the sensible heat flux observed are related to changes in surface roughness. These findings indicate that the investigation of turbulence statistics may be more informative to the interpretation of turbulent fluxes than detailed calculations of surface cover fractions that do not incorporate detailed 3D information.

This work demonstrates, even in this complex setting, observations provide useful information about processes governing surface-atmosphere exchanges that must be understood in the context of global urbanisation and climate change adaptation strategies. Radiation fluxes have direct impact on human thermal comfort as well as the energy budget of buildings with implications for energy consumption and hence are linked to the flux of anthropogenic heat. Both these fluxes feed turbulent energy exchanges between the urban surface and the atmosphere. The turbulent fluxes of sensible and latent heat greatly impact temperature and humidity levels which urban inhabitants are exposed to. Further, they determine the growths of the urban boundary layer and hence the atmospheric volume in which pollutants and exhaust gases are dispersed. It is crucial to be able to quantify these fluxes and to understand the underlying processes that determine their magnitudes to be able to assess current urban climate conditions but also to evaluate the climate impact of urban planning strategies.

In this work it is shown that human activities play an important role with respect to the sustainability of urban areas through processes across all relevant scales. In the CBD, which is dominated by very high day-time populations and commercial (rather than residential) activities, anthropogenic emissions of energy and exhaust gases have a clear impact on climate conditions. To inform decision making, the activities that are most relevant need to be identified. These relate to day-to-day activities and urban design through the type of materials used in construction of buildings, roads and pavements. The findings illustrate the choice of material has implications through for, e.g.:

- **Reflection of solar radiation:** specular reflections from glass surfaces are associated with reflection glare that can be dangerous to people or damage materials exposed to the reflected beam. It can cause large variations in surface albedo, which plays a key role in the absorption of solar energy, and hence the surface energy budget.
- **Absorption of long-wave radiation:** many construction materials are composed of minerals with high values of LWIR emissivity, which modifies the absorption of long-wave radiation and heat storage within the urban canopy. It is one important driver of the urban heat island phenomenon. Quantification of this effect aids the prediction of human

thermal comfort, which is especially beneficial given increased future heat waves are predicted. Risk management strategies require air temperature and humidity levels to be reasonably accurately to be able to implement appropriate support measures.

- **Storage of heat:** impervious materials dominating the CBD study area greatly restrict moisture availability. Given their low natural moisture content, compared to vegetation and open soil, the sensible heat flux is usually favoured in the partitioning of energy. Even with rainfall increasing evaporation significantly, excess moisture is removed relatively rapidly by efficient runoff so increased latent heat fluxes are restricted to time scales of less than a day. Given evaporation processes can help to cool down the atmosphere and often improve levels of thermal comfort, additional vegetation and/ or open ground areas incorporated into cities can aid in providing a healthier environment.

Detailed analysis and careful interpretation allow not only for a qualitative description of atmospheric conditions in the CBD but also a move towards quantifying various aspects. This study identified limitations to some current observational approaches, including critical aspects of instrument siting in complex urban settings and where more detailed, better adapted footprint models are required. All fluxes of the surface energy balance are highly scale dependant, which needs to be considered when interpreting measured (as well as modelled) energy fluxes in relation to each other. Both for radiometer and EC flux measurements, it is suggested that simultaneous operation of two nearby sites can greatly benefit the analysis. Multiple radiation sensors could be combined to be more representative of the turbulent flux footprint. The results provide an example of how observations within the roughness sublayer can be interpreted, also with respect to the impact of bluff bodies. Clearly more measurements are needed from such settings, but this work underlines the requirement for careful directional analysis and interpretation of such datasets.

VI.5 Implications for future work

The findings of this study (Sections VI.2-VI.4) suggest areas for future micrometeorological research. Notably in dense urban settings, methods need to be improved/ adapted to increase their applicability:

- More work is needed to better characterise the radiative response of the urban surface. The work presented demonstrates that information covering the LWIR region can enhance material classification in urban areas. It is shown that quality LWIR emissivity spectra can be obtained from field-portable FTIR spectrometer observations. The developed methodology is applicable to future ground-truth data collection studies to support the new generation of multi-/ hyperspectral LWIR imagers on air- and space-borne platforms and to collect new library spectra.
- In terms of (spectral) radiative response of impervious materials, metals used in buildings need to be characterised better. Their specular reflectance in the VIS-SWIR and diversity in

albedo and emissivity observed are not yet sufficiently described. Metals and new material classes (e.g. PVC) are particularly under-represented in existing spectral libraries.

- Spectral reflectance and hence broadband albedo can have strong variations between impervious materials and even within one material class. At larger scales, the geometry of buildings and canyons influences the directional dependence of reflected radiation. Studies at the scales at which albedo as a material property becomes less important than albedo resulting from the geometry of the canopy are needed. Remotely sensed imagery could provide useful insight.
- Given fluxes of outgoing short-wave radiation are extremely scale dependent and can show strong variations with viewing geometry, more work is needed to study spatial variations of this flux. How point measurements can be integrated to represent the scale of interest should be studied along with more sophisticated source area modelling for pyranometers (and pyrgeometers) deployed over heterogeneous surfaces.
- Special attention should be given to the impact of materials with generally high albedo and strong specular reflectance, because they
    a) significantly impact the radiation balance
    b) are increasingly used in urban construction, even at large scales (skyscrapers)
    c) are considered a powerful tool for climate mitigation efforts.
- The role of anthropogenic emissions on the fluxes of latent and sensible heat (and also CO_2) is significant in the CBD, however, it is not yet sufficiently understood. In dense urban settings the vertical distribution of anthropogenic emission sources particularly warrants attention. Those located at elevated heights (e.g. chimneys) are a) difficult to capture by commonly used turbulent flux measurements (such as single-tower EC) and b) may affect local-scale fluxes in the form of micro-scale signatures. The IMAS filter developed in this study could be a useful tool to address these emissions in other locations.
- Observations of turbulent EC fluxes should be interpreted with respect to their source area. In order to better account for the complexity of the urban surface in terms of roughness and land cover materials, including sources of heat and moisture, more sophisticated footprint models are needed, that are still computationally fast enough to be used for a range of conditions and long-term datasets.
- It is critical to understand the impact of rivers on the climate of city centres. Both measurement and modelling studies are needed to address this complex, but common urban surface component.

Evaluation of urban land surface (and other) models requires representative measurements for a neighbourhood at the local scale or larger area. Flux measurements for short periods do not address the diversity of weather conditions experienced in any setting. The more complex urban areas, such as CBDs, are insufficiently studied. Measurement and modelling approaches may be pushed to their limits in dense urban settings, but if urban climate research is to contribute to the challenges of real cities those limits have to be addressed. To manage cities sustainably and smartly, currently and into the future under changing climates, measurements and models must

also consider central urban areas where interactions of humans with the environment are particularly concentrated. Surface heterogeneities are challenging at the scale where urban planning strategies are implemented (e.g. usage of high reflectance materials, orientation of buildings, etc.). Using appropriate methodologies, measurements will allow improved understanding of the processes, enhanced modelling skill and better forecasting with data assimilation to help make cities more resilient places.

References

Abrams, M. J., and S. J. Hook, 2013: NASA's Hyperspectral Infrared Imager (HyspIRI). *Thermal Infrared Remote Sensing*, C. Kuenzer and S. Dech, Eds., Springer Netherlands, 117–130.

Adam, E., O. Mutanga, and D. Rugege, 2010: Multispectral and hyperspectral remote sensing for identification and mapping of wetland vegetation: a review. *Wetl. Ecol. Manag.*, **18**, 281–296.

Akbari, H., and L. S. Rose, 2008: Urban Surfaces and Heat Island Mitigation Potentials. *J. Human-Environ. Sys.*, **11(2)**, 85–101.

Akbari, H., S. Menon, and A. Rosenfeld, 2009: Global cooling: increasing world-wide urban albedos to offset CO2. *Clim. Chang.*, **94**, 275–286.

Akbari, H., H. Damon Matthews, and D. Seto, 2012: The long-term effect of increasing the albedo of urban areas. *Environ. Res. Lett.*, **7**, 024004, doi:10.1088/1748-9326/7/2/024004.

Allen, L., F. Lindberg, and C. S. B. Grimmond, 2011: Global to city scale urban anthropogenic heat flux: model and variability. *Int. J. Clim.*, **31**, 1990–2005, doi:10.1002/joc.2210.

Andreou, C., V. Karathanassi, and P. Kolokoussis, 2011: Investigation of hyperspectral remote sensing for mapping asphalt road conditions. *Int. J. Remote Sens.*, **32**, 6315–6333.

Arnfield, A. J., 2003: Two decades of urban climate research: A review of turbulence, exchanges of energy and water, and the urban heat island. *Int. J. Clim.*, **23**, 1–26.

Arnold, S. J., H. ApSimon, J. Barlow, S. Belcher, M. Bell, J. W. Boddy, R. Britter, H. Cheng, R. Clark, R. N. Colvile, S. Dimitroulopoulou, A. Dobre, B. Greally, S. Kaur, A. Knights, T. Lawton, A. Makepeace, D. Martin, M. Neophytou, S. Neville, M. Nieuwenhuijsen, G. Nickless, C. Price, A. Robins, D. Shallcross, P. Simmonds, R. J. Smalley, J. Tate, A. S. Tomlin, H. Wang, P. Walsh,, 2004: Introduction to the DAPPLE Air Pollution Project. *Sci. Total environ.*, **332**, 139–153, doi:10.1016/j.scitotenv.2004.04.020.

Atkins, P. W., 2006: *Physical Chemistry*. W.H. Freeman, Ed. Oxford University Press, 1008p.

Atkinson, B. W., 1969: A Further Examination of the Urban Maximum of Thunder Rainfall in London, 1951-60. *Trans. Inst. Br. Geog.*, 97–119, doi:10.2307/621493.

Aubinet, M., B. Heinesch, and M. Yernaux, 2003: Horizontal and Vertical Co2 Advection In A Sloping Forest. *Boundary-Layer Meteorol.*, **108**, 397–417, doi:10.1023/A:1024168428135.

Aubinet, M., C. Feigenwinter, B. Heinesch, C. Bernhofer, E. Canepa, A. Lindroth, L. Montagnani, C. Rebmann, P. Sedlak, E. Van Gorsel, 2010: Direct advection measurements do not help to solve the night-time CO2 closure problem: Evidence from three different forests. *Agric. For. Meteorol.*, **150**, 655–664, doi:10.1016/j.agrformet.2010.01.016.

Baldridge, A. M., S. J. Hook, C. I. Grove, and G. Rivera, 2009: The ASTER spectral library version 2.0. *Remote Sens. Environ.*, **113**, 711–715, doi:10.1016/j.rse.2008.11.007.

Barata, M., E. Ligeti, G. De Simone, T. Dickinson, D. Jack, J. Penney, M. Rahman, and R. Zimmerman, 2011: Climate change and human health in cities. *Climate Change and Cities: First Assessment Report of the Urban Climate Change Research Network*, C. Rosenzweig, W.D. Solecki, S.A. Hammer, and S. Mehrotra, Eds., Cambridge University Press, Cambridge, UK, 179–213.

Bassani, C., R. M. Cavalli, F. Cavalcante, V. Cuomo, A. Palombo, S. Pascucci, and S. Pignatti, 2007: Deterioration status of asbestos-cement roofing sheets assessed by analyzing hyperspectral data. *Remote Sens. Environ.*, **109**, 361–378, doi:10.1016/j.rse.2007.01.014.

Ben-Dor, E., N. Levin, and H. Saaroni, 2001: A spectral based recognition of the urban environment using the visible and near-infrared spectral region (0.4-1.1 μm). A case study over Tel-Aviv, Israel. *Int. J. Remote Sens.*, **22**, 2193–2218, doi:10.1080/01431160117759.

Blake, R., A. Grimm, T. Ichinose, R. Horton, S. Gaffin, S. Jiong, D. Bader, and L. D. Cecil, 2011: Urban Climate: Processes, Trends, and Projections. *Climate Change and Cities: First Assessment Report of the Urban Climate Change Research Network*, C. Rosenzweig, D.W. Solecki, S.A. Hammer, and S. Mehrotra, Eds., Cambridge University Press, Cambridge, UK, 43–81.

Bohnenstengel, S. I., S. Evans, P. A. Clark, and S. E. Belcher, 2011: Simulations of the London urban heat island. *Quart. J. R. Met. Soc.*, **137**, 1625–1640, doi:10.1002/qj.855.

Borel, C. C., 1998: Surface emissivity and temperature retrieval for a hyperspectral sensor. *IGARSS 98 Sensing and Managing the Environment*, Vol. 1 of, IEEE International Geoscience and Remote Sensing Symposium, No98CH36174.

Bowen, B. B., B. A. Martini, M. A. Chan, and W. T. Parry, 2007: Reflectance spectroscopic mapping of diagenetic heterogeneities and fluid-flow pathways in the Jurassic Navajo Sandstone. *Am. Assoc. Pet. Geol. Bull.*, **91**, 173–190, doi:10.1306/08220605175.

Breen, C. F. Clegg, M. M. Herron, G. P. Hild, S. Hillier, T. L. Hughes, T. G. J. Jones, A. Matteson, J. Yarwood, 2008: Bulk mineralogical characterisation of oilfield reservoir rocks and sandstones using Diffuse Reflectance Infrared Fourier Transform Spectroscopy and Partial Least Squares analysis. *J. Pet. Sci. Eng.*, **60**, 1–17, doi:10.1016/j.petrol.2007.05.001.

Bretz, S., H. Akbari, and A. Rosenfeld, 1998: Practical issues for using solar-reflective materials to mitigate urban heat islands. *Atmos. Environ.*, **32**, 95–101, doi:10.1016/S1352-2310(97)00182-9.

Brook, A., and E. Ben-Dor, 2011: Reflectance spectroscopy as a tool to assess the quality of concrete in situ. *J. Civ. Eng. Constr. Technol.*, **2**, 168–188.

Brys, G., M. Hubert, and A. Struyf, 2004: A Robust Measure of Skewness. *J. Comput. Graph. Stat.*, **13**, 996–1017, doi:10.1198/106186004X12632.

Carslaw, D. C., and K. Ropkins, 2011: Openair: Open-source tools for the analysis of air pollution data. R package.

Chemel, C., and R. S. Sokhi, 2012: Response of London's Urban Heat Island to a Marine Air Intrusion in an Easterly Wind Regime. *Bound. Lay. Met.*, **144**, 65–81, doi:10.1007/s10546-012-9705-x.

Cheng, J. C. J., Q. X. Q. Xiao, X. L. X. Li, Q. L. Q. Liu, Y. D. Y. Du, and A. N. A. Nie, 2007: Evaluation of five algorithms for extracting soil emissivity from hyperspectral FTIR data. *IEEE International Geoscience and Remote Sensing Symposium*.

Christen, A., 2005: Atmospheric turbulence and surface energy exchange in urban environments. University of Basel, 142p.

Christen, A., and R. Vogt, 2004: Energy and Radiation Balance of a Central European City. *Int. J. Clim.*, **24**, 1395–1421.

Christen, A., E. van Gorsel, and R. Vogt, 2007: Coherent structures in urban roughness sublayer turbulence. *Int. J. Clim.*, **27**, 1955–1968.

Christen, A. N. C. Coops, B. R. Crawford, R. Kellett, K. N. Liss, I. Olchovski, T. R. Tooke, M. van der Laan, and J. A. Voogt, 2011: Validation of modeled carbon-dioxide emissions from an urban neighborhood with direct eddy-covariance measurements. *Atmos. Environ.*, **45**, 6057–6069, doi:10.1016/j.atmosenv.2011.07.040.

Christensen, P. R., J. L. Bandfield, V. E. Hamilton, D. A. Howard, M. D. Lane, J. L. Piatek, S. W. Ruff, and W. L. Stefanov, 2000: A thermal emission spectral library of rock-forming minerals. *J. Geophys. Res.*, **105**, 9735, doi:10.1029/1998JE000624.

Clark, R. N., 1999: Spectroscopy of Rocks and Minerals, and Principles of Spectroscopy. *Manual of Remote Sensing, Remote Sensing for the Earth Sciences*, A.N. Rencz, Ed., John Wiley and Sons, New York, 3–58.

Clark, R. N., G. A. Swayze, R. Wise, E. Livo, T. Hoefen, and S. J. Kokaly, R., Sutley, 2007: USGS digital spectral library splib06a. *U.S. Geol. Surv. Digit. Data Ser. 231*. http://speclab.cr.usgs.gov/spectral.lib06/.

Clarke Annez, P., G. Huet, and G. E. Peterson, 2008: *Lessons for the Urban Century*. World Bank Publications, 92p.

Cleugh, H. A., and T. R. Oke, 1986: Suburban-rural energy balance comparisons in summer for Vancouver, B.C. *Bound. Lay. Met.*, **36(4)**, 351–369.

Cloutis, E. A., 1989: Spectral reflectance properties of hydrocarbons: remote-sensing implications. *Science*, **245**, 165–168, doi:10.1126/science.245.4914.165.

Cloutis, E. A., M. A. Craig, R. V Kruzelecky, W. R. Jamroz, A. Scott, F. C. Hawthorne, and S. A. Mertzman, 2008: Spectral reflectance properties of minerals exposed to simulated Mars surface conditions. *Icarus*, **195**, 140–168, doi:10.1016/j.icarus.2007.10.028.

Coutts, A. M., J. Beringer, and N. J. Tapper, 2007: Impact of Increasing Urban Density on Local Climate: Spatial and Temporal Variations in the Surface Energy Balance in Melbourne, Australia. *J. Appl. Meteor. Clim.*, **46**, 477–493.

Crawford, B., C. S. B. Grimmond, and A. Christen, 2011: Five years of carbon dioxide fluxes measurements in a highly vegetated suburban area. *Atmos. Environ.*, **45**, 896–905.

Culf, A. D., T. Foken, and J. H. C. Gash, 2004: The energy balance closure problem. *A new perspective on an interactive system*, P. Kabat, M. Claussen, and P.A. Dirmeyer, Eds., Springer, Berlin, Heidelberg, 159–166.

Damtoft, J. S., J. Lukasik, D. Herfort, D. Sorrentino, and E. M. Gartner, 2008: Sustainable development and climate change initiatives. *Cem. Concr. Res.*, **38**, 115–127.

Dash, A., F.-M. Goettsche, F.-S. Olesen, and H. Fischer, 2002: Land surface temperature and emissivity estimation from passive sensor data: theory and practice-current trends. *Int. J. Remote Sens.*, **23**, 2563–2594.

Deaton, B. C., and W. L. Balsam, 1991: Visible Spectroscopy--A Rapid Method for Determining Hematite and Goethite Concentration in Geological Materials. *J. Sediment. Pet.*, **61(4)**, 628–632.

Deer, W. A., R. A. Howie, and J. Zussman, 1992: *An introduction to the rock-forming minerals*. 2nd ed. Longman Scientific & Technical, 528p.

Deng, J.-S., K. Wang, J. Li, and Y.-H. Deng, 2009: Urban Land Use Change Detection Using Multisensor Satellite Images. *Pedosphere*, **19(1)**, 96–103.

Department for Communities and Local Government, 2013: *Next steps to zero carbon homes - Allowable Solutions*.

De Sherbinin, A., A. Schiller, and A. Pulsipher, 2007: The vulnerability of global cities to climate hazards. *Environ. Urban.*, **19**, 39–64, doi:10.1177/0956247807076725.

Dewan, A. M., and Y. Yamaguchi, 2009: Land use and land cover change in Greater Dhaka, Bangladesh: Using remote sensing to promote sustainable urbanization. *Appl. Geogr.*, **29**, 390–401, doi:10.1016/j.apgeog.2008.12.005.

Dragoni, D., H. P. Schmid, C. S. B. Grimmond, and H. W. Loescher, 2007: Uncertainty of annual net ecosystem productivity estimated using eddy covariance flux measurements. *J. Geophys. Res.*, **112**, 1–9, doi:10.1029/2006JD008149.

Dyer, A. J., 1974: A review of flux-profile relationships. *Bound. Lay. Met.*, **7**, 363–372, doi:10.1007/BF00240838.

Elliott, W. P., 1958: The growth of the atmospheric internal boundary layer. *Trans. Am. Geophys. Un.*, **39**, 1048, doi:10.1029/TR039i006p01048.

Feigenwinter, C. and Coauthors, 2008: Comparison of horizontal and vertical advective CO2 fluxes at three forest sites. *Agric. For. Meteorol.*, **148**, 12–24, doi:10.1016/j.agrformet.2007.08.013.

Feigenwinter, C., R. Vogt, and A. Christen, 2012: Eddy Covariance Measurements Over Urban Areas. *Eddy Covariance: A Practical Guide to Measurement and Data Analysis*, M. Aubinet, T. Vesala, and D. Papale, Eds., Springer Atmospheric Sciences, 377–397.

Ferrier, G., C. A. Hecker, T. E. L. Smith, C. MacLellan, S. Kemp, A. Ganas, and R. Pope, 2014: Challenges in the use of field-based Fourier Transform Infrared Spectroscopy for geological applications. *Remote Sens.*, in press.

Finnigan, J., 1999: A comment on the paper by Lee (1998): "On micrometeorological observations of surface-air exchange over tall vegetation." *Agric. For. Meteorol.*, **97**, 55–64, doi:10.1016/S0168-1923(99)00049-0.

Flerchinger, G. N., W. Xaio, D. Marks, T. J. Sauer, and Q. Yu, 2009: Comparison of algorithms for incoming atmospheric long-wave radiation. *Water Resour. Res.*, **45**, W03423, doi:10.1029/2008WR007394.

Foken, T., 2003: *Angewandte Meteorologie - Mikrometeorologische Methoden*. Springer, 289p.

Foken, T., 2006: 50 Years of the Monin–Obukhov Similarity Theory. *Bound. Lay. Met.*, **119**, 431–447, doi:10.1007/s10546-006-9048-6.

Foken, T., 2008: The energy balance closure problem: an overview. *Ecol. Appl.*, **18**, 1351–1367.

Foken, T., and B. Wichura, 1996: Tools for Quality Assessment of Surface-Based Flux Measurements. *Agric. For. Meteorol.*, **78**, 83–105.

Foken, T., M. Göckede, M. Mauder, L. Mahrt, B. D. Amiro, and J. W. Munger, 2004: Post-Field Data Quality Control. *Handbook of Micrometeorology: A Guide for Surface Flux Measurement and Analysis*, Kluwer Dordrecht, 181–208.

Foken, T., F. Wimmer, M. Mauder, C. Thomas, and C. Liebethal, 2006: Some Aspects of the Energy Balance Closure Problem. *Atmos. Chem. Phys.*, **6**, 4395–4402.

Fortuniak, K., W. Pawlak, and M. Siedlecki, 2012a: Integral Turbulence Statistics Over a Central European City Centre. *Bound. Lay. Met.*, **146**, 257–276, doi:10.1007/s10546-012-9762-1.

Fortuniak, K., W. Pawlak, M. Siedlecki, and M. Zieliński, 2012b: Urban flux measurements in Łódź, central Poland. *FLUXLETTER, Newsl. FLUXNET*, **5**, 14–20.

Franke, J., D. A. Roberts, K. Halligan, and G. Menz, 2009: Hierarchical Multiple Endmember Spectral Mixture Analysis (MESMA) of hyperspectral imagery for urban environments. *Remote Sens. Environ.*, **113**, 1712–1723.

Frey, C. M., and E. Parlow, 2012: Flux Measurements in Cairo. Part 2: On the Determination of the Spatial Radiation and Energy Balance Using ASTER Satellite Data. *Remote Sens.*, **4**, 2635–2660, doi:10.3390/rs4092635.

Frey, C. M., E. Parlow, R. Vogt, M. Harhash, and M. M. Abdel Wahab, 2011: Flux measurements in Cairo. Part 1: in situ measurements and their applicability for comparison with satellite data. *Int. J. Clim.*, **31**, 218–231, doi:10.1002/joc.2140.

Gaffey, S. J., 1985: Reflectance spectroscopy in the visible and near-infrared (0.35-2.55 μm): Applications in carbonate petrology. *Geology*, **13**, 270–273, doi:10.1130/0091-7613(1985)13.

Gash, J. H. C., 1986: A Note on Estimating the Effect of a Limited Fetch on Micrometeorological Evaporation Measurements. *Bound. Lay. Met.*, **35**, 409–413.

Gillespie, A., S. Rokugawa, T. Matsunaga, J. S. Cothern, S. Hook, and A. B. Kahle, 1998: A temperature and emissivity separation algorithm for Advanced Spaceborne Thermal Emission and Reflection Radiometer (ASTER) images. *IEEE T. Geosci. Remote*, **36**, 1113–1126, doi:10.1109/36.700995.

Gioli, B., P. Toscano, E. Lugato, A. Matese, F. Miglietta, A. Zaldei, and F. P. Vaccari, 2012: Methane and carbon dioxide fluxes and source partitioning in urban areas: the case study of Florence, Italy. *Environ. Pollut.*, **164**, 125–131, doi:10.1016/j.envpol.2012.01.019.

GLA, 2011: The London Plan. www.london.gov.uk/publication/londonplan (Accessed 05/05/2013).

GLA, 2012: Daytime Population, Borough. http://data.london.gov.uk/datastore/package/daytime-population-borough (Accessed 11/02/2013).

Göckede, M., T. Markkanen, C. B. Hasager, and T. Foken, 2006: Update of a Footprint-Based Approach for the Characterisation of Complex Measurement Sites. *Bound. Lay. Met.*, **118**, 635–655, doi:10.1007/s10546-005-6435-3.

Goldbach, A., and W. Kuttler, 2012: Quantification of turbulent heat fluxes for adaptation strategies within urban planning. *Int. J. Clim.*, **33**, 143–159, doi:10.1002/joc.3437.

Goulden, M. L., J. W. Munger, S.-M. Fan, B. C. Daube, and S. C. Wofsy, 1996: Measurements of carbon sequestration by long-term eddy covariance: methods and a critical evaluation of accuracy. *Glob. Chang. Biol.*, **2**, 169–182, doi:10.1111/j.1365-2486.1996.tb00070.x.

Griffiths, P. R., 1983: Fourier transform infrared spectrometry. *Science*, **222**, 297–302.

Grimmond, C. S. B., 1992: The suburban energy balance: methodological considerations and results for a mid-latitude west coast city under winter and spring conditions. *Int. J. Clim.*, **12**, 481–497.

Grimmond, C. S. B., 2006: Progress in Measuring and Observing the Urban Atmosphere. *Theor. Appl. Clim.*, **84**, 3–22.

Grimmond, C. S. B., and T. R. Oke, 1995: Comparison of heat fluxes from summertime observations in the suburbs of four North American cities. *J. Appl. Meteor.*, **34**, 873–889.

Grimmond, C. S. B., and T. R. Oke, 1999a: Heat Storage in Urban Areas: Local-Scale Observations and Evaluation of a Simple Model. *J. Appl. Meteor.*, **38**, 922–940.

Grimmond, C. S. B., and T. R. Oke, 1999b: Aerodynamic Properties of Urban Areas Derived from Analysis of Surface Form. *J. Appl. Meteor.*, **38**, 1262–1292.

Grimmond, C. S. B., and T. R. Oke, 2002: Turbulent Heat Fluxes in Urban Areas: Observations and a Local-Scale Urban Meteorological Parameterization Scheme (LUMPS). *J. Appl. Meteor.*, **41**, 792–810.

Grimmond, C. S. B., H. A. Cleugh, and T. R. Oke, 1991: An Objective Urban Heat Storage Model and Its Comparison with Other Schemes. *Atmos. Environ.*, **25B**, 311–326.

Grimmond, C. S. B., J. A. Salmond, T. R. Oke, B. Offerle, and A. Lemonsu, 2004: Flux and turbulence measurements at a dense urban site in Marseille: Heat, Mass (water, carbon dioxide) and Momentum. *JGR Atmos.*, **109**, 19pp.

Grimmond, C. S. B., M. Roth, T. R. Oke, Y. C. Au, M. Best, R. Betts, G. Carmichael, H. Cleugh, W. Dabberdt, R. Emmanuel, E. Freitas, K. Fortuniak, S. Hanna, P. Klein, L. S. Kalkstein, C. H. Liu, A. Nickson, D. Pearlmutter, D. Sailor, and J. Voogt, J., 2010: Climate and More Sustainable Cities: Climate Information for Improved Planning and Management of Cities (Producers/Capabilities Perspective). *Proc. Environ. Sci.*, **1**, 247–274, doi:10.1016/j.proenv.2010.09.016.

Guardian, T., 2013: Walkie Talkie architect 'didn't realise it was going to be so hot'. http://www.theguardian.com/artanddesign/2013/sep/06/walkie-talkie-architect-predicted-reflection-sun-rays. (Accessed 14/11/2013)

Hamilton, I. G., M. Davies, P. Steadman, A. Stone, I. Ridley, and S. Evans, 2009: The significance of the anthropogenic heat emissions of London's buildings: A comparison against captured shortwave solar radiation. *Build. Environ.*, **44**, 807–817.

Harrison, R. M. M. Dall'Osto, D. C. S. Beddows, A. J. Thorpe, W. J. Bloss, J. D. Allan, H. Coe, J. R. Dorsey, M. Gallagher, C. Martin, J. Whitehead, P. I. Williams, R. L. Jones, J. M. Langridge, A. K. Benton, S. M. Ball, B. Langford, C. N. Hewitt, B. Davison, D. Martin, K. F. Petersson, S. J. Henshaw, I. R. White, D. E. Shallcross, J. F. Barlow, T. Dunbar, F. Davies, E. Nemitz, G. J. Phillips, C. Helfter, C. F. Di Marco, and S. Smith, 2012: Atmospheric chemistry and physics in the atmosphere of a developed megacity (London): an overview of the REPARTEE experiment and its conclusions. *Atmos. Chem. Phys.*, **12**, 3065–3114, doi:10.5194/acp-12-3065-2012.

Haugen, D. A., J. C. Kaimal, and E. F. Bradley, 1971: An Experimental Study of Reynolds Stress and Heat Flux in the Atmospheric Surface Layer. *Quart. J. R. Met. Soc.*, **97**, 168–180.

Hecker, C. A., T. E. L. Smith, B. R. da Luz, and M. J. Wooster, 2013: Thermal Infrared Spectroscopy in the Laboratory and Field in Support of Land Surface Remote Sensing. *Thermal Infrared Remote Sensing*, C. Kuenzer and S. Dech, Eds., Springer Netherlands, 43–67.

Heiden, U., S. Roessner, K. Segl, and H. Kaufmann, 2001: Analysis of spectral signatures of urban surfaces for their identification using hyperspectral HyMap data. *Remote Sensing and Data Fusion over Urban Areas, IEEE/ISPRS Joint Workshop 2001*, 173–177.

Heiden, U., K. Segl, S. Roessner, and H. Kaufmann, 2007: Determination of robust spectral features for identification of urban surface materials in hyperspectral remote sensing data. *Remote Sens. Environ.*, **111**, 537–552.

Helfter, C., D. Famulari, G. J. Phillips, J. F. Barlow, C. R. Wood, C. S. B. Grimmond, and E. Nemitz, 2011: Controls of carbon dioxide concentrations and fluxes above central London. *Atmos. Chem. Phys.*, **11**, 1913–1928, doi:10.5194/acp-11-1913-2011.

Herold, M., 2007: Spectral characteristics of asphalt road surfaces. *Remote Sensing of Impervious Surfaces*, Q. Weng, Ed., Boca Raton, Florida: CRC Press, 237–247.

Herold, M., M. Gardner, and D. A. Roberts, 2003: Spectral Resolution Requirements for Mapping Urban Areas. *IEEE T. Geosci. Remote*, **41(9)**, 1907–1919.

Herold, M., D. A. Roberts, M. E. Gardner, and P. E. Dennison, 2004: Spectrometry for urban area remote sensing - Development and analysis of a spectral library from 350 to 2400 nm. *Remote Sens. Environ.*, **91**, 304–319.

Hiller, R., J. McFadden, and N. Kljun, 2011: Interpreting CO2 Fluxes Over a Suburban Lawn: The Influence of Traffic Emissions. *Bound. Lay. Met.*, **138**, 215–230, doi:10.1007/s10546-010-9558-0.

Hollinger, D. Y., and A. D. Richardson, 2005: Uncertainty in eddy covariance measurements and its application to physiological models. *Tree Physiol.*, **25**, 873–885.

Hook, S. J., and A. B. Kahle, 1996: The micro fourier transform interferometer (μFTIR) — A new field spectrometer for acquisition of infrared data of natural surfaces. *Remote Sens. Environ.*, **56**, 172–181, doi:10.1016/0034-4257(95)00231-6.

Hook, S. J., W. R. Johnson, and M. J. Abrams, 2013: NASA's Hyperspectral Thermal Emission Spectrometer (HyTES). *Thermal Infrared Remote Sensing*, C. Kuenzer and S. Dech, Eds., Springer Netherlands, 93–115.

Horst, T. W., and J. C. Weil, 1992: Footprint estimation for scalar flux measurements in the atmospheric surface layer. *Bound. Lay. Met.*, **59**, 279–296, doi:10.1007/BF00119817.

Horton, K. A., J. R. Johnson, and P. G. Lucey, 1998: Infrared Measurements of Pristine and Disturbed Soils 2. Environmental Effects and Field Data Reduction. *Remote Sens. Environ.*, **64**, 47–52, doi:10.1016/S0034-4257(97)00167-3.

Howard, L., 1833: *The Climate of London, Vols. I-III*. Harvey and Darton, London, 383p.

Hsieh, C., G. Katul, and T. Chi, 2000: An approximate analytical model for footprint estimation of scalar fluxes in thermally stratified atmospheric flows. *Adv. Water Resour.*, **23**, 765–772.

Hubert, M., and E. Vandervieren, 2008: An adjusted boxplot for skewed distributions. *Comput. Stat. Data An.*, **52**, 5186–5201, doi:10.1016/j.csda.2007.11.008.

Hubert, M., and S. Van der Veeken, 2008: Outlier detection for skewed data. *J. Chemom.*, **22**, 235–246, doi:10.1002/cem.1123.

Hunt, G. R., 1977: Spectral signatures of particulate minerals in the visible and near infrared. *Geophysics*, **42**, 501–513, doi:10.1190/1.1440721.

Hunt, G. R., and J. W. Salisbury, 1971: Visible and near infrared spectra of minerals and rocks II. Carbonates. *Mod. Geol.*, **2**, 23–30.

Hunt, J. M., M. P. Wisherd, and L. C. Bonham, 1950: Infrared Absorption Spectra of Minerals and other Inorganic Compounds. *Anal. Chem.*, **22**, 1478–1497.

Hunter, L. J., G. T. Johnson, and I. D. Watson, 1992: An investigation of three-dimensional characteristics of flow regimes within the urban canyon. *Atmos. Environ. Part B. Urban Atmos.*, **26**, 425–432, doi:10.1016/0957-1272(92)90049-X.

Iamarino, M., S. Beevers, and C. S. B. Grimmond, 2012: High-resolution (space, time) anthropogenic heat emissions: London 1970-2025. *Int. J. Clim.*, **32**, 1754–1767, doi:10.1002/joc.2390.

Ichinose, T., L. Lee, F. Matsumoto, Y. Shiraki, and I. Harada, 2009: Mechanism of Mmitigation of Atmospheric Environmentby a Large Restauration of inner-City River (Cheong-Gye Stream in Seoul). *seventh Int. Conf. Urban Clim.*, 2–5.

Iwata, T., K.-I. Kimura, M. Shukuya, and K. Takano, 1991: Discomfort caused by wide-source glare. *Energ. Build.*, **15**, 391–398, doi:10.1016/0378-7788(90)90013-9.

Järvi, J. and Coauthors, 2009: The urban measurement station SMEAR III: Continuous monitoring of air pollution and surface–atmosphere interactions in Helsinki, Finland. *Boreal Env. Res.*, **14 (suppli**, 86–109.

Joseph, G., 2005: *Fundamentals of Remote Sensing*. Universities Press, 486p.

Kahle, A. B., and R. E. Alley, 1992: Separation of temperature and emittance in remotely sensed radiance measurements. *Remote Sens. Environ.*, **42**, 107–111.

Kaimal, J. C., and J. J. Finnigan, 1994: *Atmospheric Boundary Layer Flows: Their Structure and Measurement*. Oxford University Press, New York, 289p.

Kalanda, B. D., T. R. Oke, and D. L. Spittlehouse, 1980: Suburban Energy Balance Estimates for Vancouver, B.C., Using the Bowen Ratio-Energy Balance Approach. *J. Appl. Meteor.*, **19**, 791–802.

Kanda, M., R. Moriwaki, and F. Kasamatsu, 2006: Spatial variability of both turbulent fluxes and temperature profiles in an urban roughness layer. *Bound. Lay. Met.*, **121**, 339–350.

Karra, S., L. Malki-Epshtein, and M. Neophytou, 2011: The Dispersion of Traffic Related Pollutants Across a Non-Homogeneous Street Canyon. *Proc. Environ. Sci.*, **4**, 25–34, doi:10.1016/j.proenv.2011.03.004.

Kastner-Klein, P., and M. W. Rotach, 2004: Mean Flow and Turbulence Characteristics in an Urban Roughness Sublayer. *Bound. Lay. Met.*, **111**, 55–84.

Kerekes, J. P., K.-E. Strackerjan, and C. Salvaggio, 2008: Spectral reflectance and emissivity of man-made surfaces contaminated with environmental effects. *Opt. Eng.*, **47**, 106201.

Kikegawa, Y., Y. Genchi, H. Yoshikado, and H. Kondo, 2003: Development of a numerical simulation system toward comprehensive assessments of urban warming countermeasures including their impacts upon the urban buildings' energy-demands. *Appl. Energ.*, **76**, 449–466, doi:10.1016/S0306-2619(03)00009-6.

King, T. V. V., and R. N. Clark, 1989: Reflectance Spectroscopy (0.2 to 20μm) As An Analytical Method For The Detection of Organics. *Soils: Proceedings First International Symposium: Field Screening Methods for Hazardous Waste Site Investigations*, EPA, 485–488.

Kljun, N., M. W. Rotach, and H. P. Schmid, 2002: A Three-Dimensional Backward Lagrangian Footprint Model For A Wide Range Of Boundary-Layer Stratifications. *Bound. Lay. Met.*, **103**, 205–226, doi:10.1023/A:1014556300021.

Kljun, N., P. Calanca, M. W. Rotach, and H. P. Schmid, 2004: A Simple Parameterisation for Flux Footprint Predictions. *Bound. Lay. Met.*, **112**, 503–523.

Korb, A. R., P. Dybwad, W. Wadsworth, and J. W. Salisbury, 1996: Portable Fourier transform infrared spectroradiometer for field measurements of radiance and emissivity. *Appl. Opt.*, **35**, 1679–1692, doi:10.1364/AO.35.001679.

Kordowski, K., and W. Kuttler, 2010: Carbon dioxide fluxes over an urban park area. *Atmos. Environ.*, **44**, 2722–2730, doi:10.1016/j.atmosenv.2010.04.039.

Kormann, R., and F. X. Meixner, 2001: An Analytical Footprint Model for Non-Neutral Stratification. *Bound. Lay. Met.*, **99**, 207–224.

Kotthaus, S., and C. S. B. Grimmond, 2012: Identification of Micro-scale Anthropogenic CO2, heat and moisture sources – Processing eddy covariance fluxes for a dense urban environment. *Atmos. Environ.*, **57**, 301–316, doi:10.1016/j.atmosenv.2012.04.024.

Kotthaus, S., and C. S. B. Grimmond, 2013a: Energy exchange in a dense urban environment – Part II: impact of spatial heterogeneity of the surface. *Urban Clim.*, doi:doi:10.1016/j.uclim.2014.10.001.

Kotthaus, S., and C. S. B. Grimmond, 2013b: Energy exchange in a dense urban environment – Part I: temporal variability of long-term observations in central London. *Urban Clim.*, doi:doi:10.1016/j.uclim.2014.10.002.

Kotthaus, S., T. E. L. Smith, M. J. Wooster, and C. S. B. Grimmond, 2014: Derivation of an urban materials spectral library through emittance and reflectance spectroscopy. *in review*.

Kovats, R. S., and S. Hajat, 2008: Heat stress and public health: a critical review. *Annu. Rev. Publ. Heal.*, **29**, 41–55, doi:10.1146/annurev.publhealth.29.020907.090843.

Kuenzer, C., and S. Dech, 2013: *Thermal Infrared Remote Sensing: Sensors, Methods, Applications*. C. Kuenzer and S. Dech, Eds. Springer, 544p.

Kusaka, H., H. Kondo, Y. Kikegawa, and F. Kimura, 2001: A Simple Single-Layer Urban Canopy Model For Atmospheric Models: Comparison With Multi-Layer And Slab Models. *Bound. Lay. Met.*, **101**, 329–358.

Lagouarde, J. P., M. Irvine, J. M. Bonnefond, C. S. B. Grimmond, N. Long, T. Oke, J. Salmond, and B. Offerle, 2006: Monitoring the sensible heat flux over urban areas using large aperture scintillometry: case study of Marseille city during the ESCOMPTE experiment. *Bound. Lay. Met.*, **118**, 449–476.

Langford, B., E. Nemitz, E. House, G. J. Phillips, D. Famulari, B. Davison, J. R. Hopkins, A. C. Lewis, and C. N. Hewitt, 2010: Fluxes and Concentrations of Volatile Organic Compounds Above Central London, Uk. *Atmos. Chem. Phys.*, **10**, 627–645.

Lee, X., J. J. Finnigan, and K. T. P. U, 2004: Handbook of Micrometeorology : A guide for Surface Flux Measurement and Analysis. X. Lee, W. Massman, and B. Law, Eds., Kluwer Academic Publishers, Dordrecht, p. 250.

Lemonsu, A., C. S. B. Grimmond, and V. Masson, 2004: Modeling the Surface Energy Balance of the Core of the Old Mediterranean City: Marseille. *J. Appl. Meteorol.*, **43**, 312–327.

Li, Z., and L. Moreau, 1996: Alteration of Atmospheric Solar Absorption by Clouds: Simulation and Observation. *J. Appl. Meteorol.*, **35**, 653–670, doi:10.1175/1520-0450(1996)035<0653:AOASAB>2.0.CO;2.

Lindberg, F., and C. S. B. Grimmond, 2010: Continuous sky view factor from high resolution urban digital elevation models. *Clim. Res.*, **42(3)**, 177–183.

Lindberg, F., and C. S. B. Grimmond, 2011: The influence of vegetation and building morphology on shadow patterns and mean radiant temperatures in urban areas: model development and evaluation. *Theor. Appl. Clim.*, **105**, 311–323, doi:10.1007/s00704-010-0382-8.

Lindberg, F., C. Grimmond, N. Yogeswaran, S. Kotthaus, J. He, L. Allen, and M. Iamarino, 2013: Impact of urban changes and weather on anthropogenic heat flux in Europe 1995-2015. *Urban Clim.*, **4**, 1–15, doi:http://dx.doi.org/10.1016/j.uclim.2013.03.002.

Lindermeir, E., P. Haschberger, V. Tank, and H. Dietl, 1992: Calibration of a Fourier transform spectrometer using three blackbody sources. *Appl. Opt.*, **31**, 4527, doi:10.1364/AO.31.004527.

Liu, H. Z., J. W. Feng, L. Järvi, and T. Vesala, 2012: Four-year (2006–2009) eddy covariance measurements of CO2 flux over an urban area in Beijing. *Atmos. Chem. Phys.*, **12**, 7881–7892, doi:10.5194/acp-12-7881-2012.

Loridan, T., and C. S. B. Grimmond, 2012: Characterization of Energy Flux Partitioning in Urban Environments: Links with Surface Seasonal Properties. *J. Appl. Meteor. Clim.*, **51**, 219–241, doi:10.1175/JAMC-D-11-038.1.

Loridan, T., F. Lindberg, O. Jorba, S. Kotthaus, S. Grossman-Clarke, and C. S. B. Grimmond, 2013: High Resolution Simulation of the Variability of Surface Energy Balance Fluxes Across Central London with Urban Zones for Energy Partitioning. *Bound. Lay. Met.*, **147**, 493–523, doi:10.1007/s10546-013-9797-y.

Lucht, W., C. B. Schaaf, and A. H. Strahler, 2000: An algorithm for the retrieval of albedo from space using semiempirical BRDF models. *IEEE T. Geosci. Remote*, **38**, 977–998, doi:10.1109/36.841980.

Lyon, R. J. P., 1964: *Evaluation of Infrared Spectrophotometry for Compositional Analysis of Lunar and Planetary Soils,* Part II: Rough and Powdered Surfaces: NASA Contractor Report CR-100, 262p.

Macdonald, R. W., R. F. Griffiths, and D. J. Hall, 1998: An improved method for the estimation of surface roughness of obstacle arrays. *Atmos. Environ.*, **32**, 1857–1864, doi:10.1016/S1352-2310(97)00403-2.

Mårtensson, E. M., E. D. Nilsson, G. Buzorius, and C. Johansson, 2006: Eddy covariance measurements and parameterisation of traffic related particle emissions in an urban environment. *Atmos. Chem. Phys.*, **6**, 769–785, doi:10.5194/acp-6-769-2006.

Masson, V., L. Gomes, G. Pigeon, C. Liousse, V. Pont, J.-P. Lagouarde, J. Voogt, J. Salmond, T. R. Oke, J. Hidalgo, D. Legain, O. Garrouste, C. Lac, O. Connan, X. Briottet, S. Lachérade, P. Tulet, 2008: The Canopy and Aerosol Particles Interactions in TOulouse Urban Layer (CAPITOUL) experiment. *Meteorol. Atmos. Phys.*, **102**, 135–157, doi:10.1007/s00703-008-0289-4.

Matzarakis, A., F. Rutz, and H. Mayer, 2010: Modelling radiation fluxes in simple and complex environments: basics of the RayMan model. *Int. J. Biometeorol.*, **54**, 131–139.

Mauder, M., S. P. Oncley, R. Vogt, T. Weidinger, L. Ribeiro, Ch. Bernhofer, T. Foken, W. Kohsiek, H. A. R. de Bruin, and H. Liu, 2007: The energy balance experiment EBEX-2000. Part II: Intercomparison of eddy-covariance sensors and post-fiels data processing methods. *Bound. Lay. Met.*, **123**, 29–54.

Met Office, 2012a: Regional Climates: Southern England. http://www.metoffice.gov.uk/climate/uk/so/ (Accessed 05/05/2013).

Met Office, 2012b: Met Office Integrated Data Archive System (MIDAS) Land and Marine Surface Stations Data (1853-current). *NCAS Br. Atmos. Data Cent.* http://badc.nerc.ac.uk/browse/badc/ukmo-midas (Accessed 16/07/2013).

Met Office, 2013: Meeting on UK's run of unusual seasons. *Met Office news*, 16/06/2013. http://metofficenews.wordpress.com/2013/06/ (Accessed 18/07/2013).

Meyer, R. F., and W. de Witt, 1990: Definition and World Resources of Natural Bitumens. *U.S. Geol. Surv. Bull.*, **1944**, 1–14.

Michel, D., R. Philipona, C. Ruckstuhl, R. Vogt, and L. Vuilleumier, 2008: Performance and Uncertainty of CNR1 Net Radiometers during a One-Year Field Comparison. *J. Atmos. Ocean. Tech.*, **25**, 442–451, doi:10.1175/2007JTECHA973.1.

Mills, G., 2007: Cities as agents of global change. *Int. J. Clim.*, **27**, 1849–1857, doi:10.1002/joc.1604.

Mills, G., 2008: Luke Howard and The Climate of London. *Weather*, **63**, 153–157, doi:10.1002/wea.195.

Moffat, A. M., D. Papale, M. Reichstein, D. Y. Hollinger, Y. David, A. D. Richardson, A. G. Barr, C. Beckstein, B. H. Braswell, G. Churkina, A. R. Desai, E. Falge, J. H. Gove, M. Heimann, D. Hui, A. J. Jarvis, J. Kattge, A. Noormets, and V. J. Stauch, 2007: Comprehensive comparison of gap-filling techniques for eddy covariance net carbon fluxes. *Agric. For. Meteorol.*, **147**, 209–232, doi:10.1016/j.agrformet.2007.08.011.

Moncrieff, J. B., R. Clement, J. J. Finnigan, and T. Meyers, 2004: Averaging and de-trending. *Handbook of Micrometeorology*, and B.L. Lee, X., W. Massman, Ed., Kluwer Acad. Publ., Dordrecht, 7–31.

Moore, C. J., 1986: Frequency Response Corrections for Eddy Correlation Systems. *Bound. Lay. Met.*, **37**, 17–35.

Moriwaki, R., and M. Kanda, 2004: Seasonal and Diurnal Fluxes of Radiation, Heat, Water Vapor, and Carbon Dioxide over a Suburban Area. *J. Appl. Meteor.*, **43**, 1700–1710.

MPA Cement, 2012: Mineral Products Association (MPA) Cement. http://cement.mineralproducts.org/cement/manufacture/types_of_cement.php (Accessed 10/07/2013).

Mulhearn, P. J., and J. J. Finnigan, 1978: Turbulent flow over a very rough, random surface. *Bound. Lay. Met.*, **15**, 109–132, doi:10.1007/BF00165509.

Münkel, C., N. Eresmaa, J. Räsänen, and A. Karppinen, 2006: Retrieval of mixing height and dust concentration with lidar ceilometer. *Bound. Lay. Met.*, **124**, 117–128, doi:10.1007/s10546-006-9103-3.

Nordbo, A., L. Järvi, S. Haapanala, J. Moilanen, and T. Vesala, 2012: Intra-City Variation in Urban Morphology and Turbulence Structure in Helsinki, Finland. *Bound. Lay. Met.*, **146**, 469–496, doi:10.1007/s10546-012-9773-y.

NREL, National Renewable Energy Laboratory, 2000: ASTM G173-03. http://rredc.nrel.gov/solar/spectra/am1.5/#about (Accessed 27/05/2013).

Offerle, B., C. S. B. Grimmond, and T. R. Oke, 2003: Parameterization of Net All-Wave Radiation for Urban Areas. *J. Appl. Meteorol.*, **42**, 1157–1173.

Offerle, B., C. S. B. Grimmond, and K. Fortuniak, 2005a: Heat storage and anthropogenic heat flux in relation to the energy balance of a central European city centre. *Int. J. Clim.*, **25(10)**, 1405–1419.

Offerle, B., P. Jonsson, I. Eliasson, and C. S. B. Grimmond, 2005b: Urban Modification of the Surface Energy Balance in the West African Sahel: Ouagadougou, Burkina Faso. *J. Appl. Meteor.*, **18**, 3983–3995.

Offerle, B., C. S. B. Grimmond, K. Fortuniak, K. Klysik, and T. R. Oke, 2006a: Temporal variations in heat fluxes over a central European city centre. *Theor. Appl. Clim.*, **84**, 103–115.

Offerle, B., C. S. B. Grimmond, K. Fortuniak, and W. Pawlak, 2006b: Intraurban Differences of Surface Energy Fluxes in a Central European City. *J. Appl. Meteor.*, **45**, 125–136.

ONS, Office for National Statistics, 2012: Annual Mid-year Population Estimates for England and Wales, Mid 2011. http://www.ons.gov.uk/ons/rel/pop-estimate/population-estimates-for-england-and-wales/mid-2011--2011-census-based-/stb---mid-2011-census-based-population-estimates-for-england-and-wales.html (Accessed 14/11/2012).

Oke, T. R., 1982: The Energetic Basics of the Urban Heat Island. *Quart. J. R. Met. Soc.*, **108**, 1–24.

Oke, T. R., 1987: *Boundary Layer Climates*. 2nd editio. co-published by Routledge, London and John Wiley & Sons, New York, 435 pp.

Oke, T. R., R. Spronken-Smith, E. Jauregui, and C. S. B. Grimmond, 1999: The energy balance of central Mexico City during the dry season. *Atmos. Environ.*, **33**, 3919–3930.

Park, C., G. W. Schade, and I. Boedeker, 2011: Characteristics of the flux of isoprene and its oxidation products in an urban area. *J. Geophys. Res.*, **116**, D21303, doi:10.1029/2011JD015856.

Pascucci, S., C. Bassani, A. Palombo, M. Poscolieri, and R. Cavalli, 2008: Road Asphalt Pavements Analyzed by Airborne Thermal Remote Sensing: Preliminary Results of the Venice Highway. *Sensors*, **8**, 1278–1296, doi:10.3390/s8021278.

Patino, J. E., and J. C. Duque, 2012: A review of regional science applications of satellite remote sensing in urban settings. *Comput. Environ. Urban Syst.*, doi:10.1016/j.compenvurbsys.2012.06.003.

Pauscher, L., 2010: Scintillometer Measurements above the Urban Area of London. Universität Bayreuth, Diploma Thesis, 95p.

Pauscher, L., M. Gouvea, S. Kotthaus, C. R. Wood, J. F. Barlow, P. D. Smith, and S. Grimmond, 2012: Large aperture scintillometer measurements in London. *ICUC8, Dublin, Ireland, 6-10 August 2012*, (T22/260, Poster).

Paw U, K. T., D. D. Baldocchi, T. P. Meyers, and K. B. Wilson, 2000: Correction Of Eddy-Covariance Measurements Incorporating Both Advective Effects And Density Fluxes. *Bound. Lay. Met.*, **97**, 487–511.

Pawlak, W., K. Fortuniak, and M. Siedlecki, 2011: Carbon dioxide flux in the centre of Lodz, Poland - analysis of a 2-year eddy covariance measurement data set. *Int. J. Clim.*, **31**, 232–243, doi:10.1002/joc.2247.

Pearlmutter, D., P. Berliner, and E. Shaviv, 2007: Integrated modeling of pedestrian energy exchange and thermal comfort in urban street canyons. *Build. Environ.*, **42**, 2396–2409, doi:10.1016/j.buildenv.2006.06.006.

Peixoto, J. P., and A. H. Oort, 1992: *Physics of Climate*. American Institute of Physics, 520p.

Pengelly, L. D., M. E. Campbell, C. S. Cheng, C. Fu, S. E. Gingrich, and R. Macfarlane, 2007: Anatomy of heat waves and mortality in Toronto: lessons for public health protection. *Can. J. Public Heal. Rev. Can. Sante Publique*, **98**, 364–368.

Pigeon, G., A. Lemonsu, C. S. B. Grimmond, P. Durand, O. Thouron, and V. Masson, 2007: Divergence of Turbulent Fluxes in the Surface Layer: Case of a Coastal City. *Bound. Lay. Met.*, **124**, 269–290.

Planck, M., 1901: Über das Gesetz der Energieverteilung im Normalspectrum. *Ann. Phys.*, **309**, 553–563, doi:10.1002/andp.19013090310.

Price, J. C., 1995: Examples of high resolution visible to near-infrared reflectance spectra and a standardized collection for remote sensing studies. *Int. J. Remote Sens.*, **16**, 993–1000, doi:10.1080/01431169508954459.

Quah, A. K. L., and M. Roth, 2011: Diurnal and weekly variation of anthropogenic heat emissions in a tropical city, Singapore. *Atmos. Environ.*, **46**, 92–103.

R Development Core Team, 2005: R: A language and environment for statistical computing.

Rannik, Ü., A. Sogachev, T. Foken, M. Göckede, N. Kljun, M. Y. Leclerc, and T. Vesala, 2012: Footprint Analysis. *Eddy Covariance: A Practical Guide to Measurement and Data Analysis*, M.A. et Al., Ed., Springer Atmospheric Sciences, 212–261.

Raupach, M. R., and R. H. Shaw, 1982: Averaging procedures for flow within vegetation canopies. *Bound. Lay. Met.*, **22**, 79–90, doi:10.1007/BF00128057.

Raupach, M. R., A. S. Thom, and I. Edwards, 1980: A Wind-Tunnel Study of Turbulent Flow Close to Regularly Arrayed Rough Surfaces. *Bound. Lay. Met.*, **18**, 373–397.

Raupach, M. R., J. J. Finnigan, and Y. Brunei, 1996: Coherent eddies and turbulence in vegetation canopies: The mixing-layer analogy. *Bound. Lay. Met.*, **78**, 351–382, doi:10.1007/BF00120941.

Revercomb, H. E., H. Buijs, H. B. Howell, D. D. Laporte, W. L. Smith, and L. A. Sromovsky, 1988: Radiometric calibration of IR Fourier transform spectrometers - Solution to a problem with the High-Resolution Interferometer Sounder. *Appl. Opt.*, **27**, 3210–3218.

Rivard, B., R. E. Arvidson, I. J. Duncan, M. Sultan, and B. Elkaliouby, 1992: Varnish, Sediment, and Rock Controls on Spectral Reflectance of Outcrops in Arid Regions. *Geology*, **20**, 295–298, doi:10.1130/0091-7613(1992)020<0295:vsarco>2.3.co;2.

Roberts, D. A., D. A. Quattrochi, G. C. Hulley, S. J. Hook, and R. O. Green, 2012: Synergies between VSWIR and TIR data for the urban environment: An evaluation of the potential for the Hyperspectral Infrared Imager (HyspIRI) Decadal Survey mission. *Remote Sens. Environ.*, **117**, 83–101, doi:10.1016/j.rse.2011.07.021.

Roberts, S. M., 2010: Three-dimensional radiation flux source areas in urban areas. University of British Columbia, PhD Thesis, 214p.

Robins, A., 2008: DAPPLE (dispersion of air pollution and its penetration into the local environment) experiments and modelling. *HPA Chem. Hazards Poisons Rep.*, **13**, 24–28.

Robinson, I., and A. Mac Arthur, 2012: The FSF Post Processing Toolbox User Guide: Post processing spectral data in MATLAB, 1–26. http://www.mathworks.com/matlabcentral/fileexchange/31547 (Accessed 27/11/2013)

Rodriguez, M. A., M. J. Liso, F. Rubio, J. Rubio, and J. L. Oteo, 1999: Study of the reaction of γ – methacryloxypropyltrimethoxysilane (γ – MPS) with slate surfaces. *J. Mater. Sci.*, **34**, 3867–3873, doi:10.1023/A:1004666621479.

Roessner, S., K. Segl, U. Heiden, and H. Kaufmann, 2001: Automated Differentiation of Urban Surfaces Based on Airborne Hyperspectral Imagery. *IEEE T. Geosci. Remote*, **39**, 1525–1532.

Rossel, R. A. V., R. N. McGlynn, and A. B. McBratney, 2006: Determining the composition of mineral-organic mixes using UV - vis - NIR diffuse reflectance spectroscopy. *Geoderma*, **137**, 70–82, doi:10.1016/j.geoderma.2006.07.004.

Rotach, M., 1995: Profiles of Turbulence Statistics in and above an urban street canyon. *Atmos. Environ.*, **29(13)**, 1473–1486.

Rotach, M. W., R. Vogt, C. Bernhofer, E. Batchvarova, A. Christen, A. Clappier, B. Feddersen, S.-E. Gryning, G. Martucci, H. Mayer, V. Mitev, T. R. Oke, E. Parlow, H. Richner, M. Roth, Y.-A. Roulet, D. Ruffieux, J. A. Salmond, M. Schatzmann, J. A. Voogt, 2005: BUBBLE - an Urban Boundary Layer Meteorology Project. *Theor. Appl. Clim.*, **81**, 231–261.

Roth, M., 2000: Review of atmospheric turbulence over cities. *Q. J. R. Meteorol. Soc.*, **126**, 941–990.

Ruff, S. W., P. R. Christensen, P. W. Barbera, and D. L. Anderson, 1997: Quantitative thermal emission spectroscopy of minerals: A laboratory technique for measurement and calibration. *J. Geophys. Res.*, **102**, 14899–14913, doi:10.1029/97JB00593.

Sailor, D. J., 2011: A review of methods for estimating anthropogenic heat and moisture emissions in the urban environment. *Int. J. Clim.*, **31**, 189–199, doi:10.1002/joc.2106.

Sailor, D. J., and L. Lu, 2004: A top-down methodology for developing diurnal and seasonal anthropogenic heating profiles for urban areas. *Atmos. Environ.*, **38**, 2737–2748.

Salisbury, J. W., and D. M. D'Aria, 1992: Emissivity of terrestrial materials in the 8–14 μm atmospheric window. *Remote Sens. Environ.*, **42**, 83–106, doi:10.1016/0034-4257(92)90092-X.

Salmond, J. A., T. R. Oke, C. S. B. Grimmond, S. Roberts, and B. Offerle, 2005: Venting of Heat and Carbon Dioxide from Urban Canyons at Night. *J. Appl. Meteor.*, **44**, 1180–1194, doi:10.1175/JAM2260.1.

Salmond, J. A., M. Roth, T. R. Oke, A. Christen, and J. A. Voogt, 2012: Can Surface-Cover Tiles Be Summed to Give Neighborhood Fluxes in Cities? *J. Appl. Meteor. Clim.*, **51**, 133–149.

Savitzky, A., and M. J. E. Golay, 1964: Smoothing and differentiation of data by simplified least squares procedures. *Anal. Chem.*, **36**, 1627–1639, doi:10.1021/ac60214a047.

Schäfer, K., S. Emeis, H. Hoffmann, and C. Jahn, 2006: Influence of mixing layer height upon air pollution in urban and sub-urban areas. *Meteorol. Z.*, **15**, 12, doi: 10.1127/0941-2948/2006/0164.

Schmid, H. P., 1994: Source Areas for Scalars and Scalar Fluxes. *Bound. Lay. Met.*, **67**, 293–318.

Schmid, H. P., 1997: Experimental design for flux measurements: matching scales of observations and fluxes. *Agric. For. Meteorol.*, **87**, 179–200, doi:10.1016/S0168-1923(97)00011-7.

Schmid, H. P., 2002: Footprint Modeling for Vegetation Atmosphere Exchange Studies: A Review and Perspective. *Agric. For. Meteorol.*, **113**, 159–183.

Schmid, H. P., and C. R. Lloyd, 1999: Spatial representativeness and the location bias of flux footprints over inhomogeneous areas. *Agric. For. Meteorol.*, **93**, 195–209, doi:10.1016/S0168-1923(98)00119-1.

Schmid, H. P., H. A. Cleugh, C. S. B. Grimmond, and T. R. Oke, 1991: Spatial variability of energy fluxes in suburban terrain. *Bound. Lay. Met.*, **54**, 249–276.

Schmid, H. P., H.-B. Su, C. S. Vogel, and P. S. Curti, 2003: Ecosystem-atmosphere exchange of carbon dioxide over a mixed hardwood forest in northern lower Michigan. *J. Geophys. Res.*, **108**, 4417, doi:10.1029/2002JD003011.

Schotanus, P., F. T. M. Nieuwstadt, and H. A. R. de Bruin, 1983: Temperature Measurements with a Sonic Anemometer and its Application to Heat and Moisture Fluxes. *Bound. Lay. Met.*, **26**, 81–93.

Schueler, T. R., 1994: The importance of imperviousnes. *Watershed Prot. Tech.*, **1(3)**, 100–111.

Schuepp, P. H., M. Y. Leclerc, J. I. MacPherson, and R. L. Desjardins, 1990: Footprint prediction of scalar fluxes from analytical solutions of the diffusion equation. *Bound. Lay. Met.*, **50**, 355–373, doi:10.1007/BF00120530.

Shafri, H., E. Taherzadeh, S. Mansor, and R. Ashurov, 2012: Hyperspectral Remote Sensing of Urban Areas: An Overview of Techniques and Applications. *Res. J. Appl. Sci., Eng. Technol.*, **4(11)**, 1557–1565.

Shih, N.-J., and Y.-S. Huang, 2001: An analysis and simulation of curtain wall reflection glare. *Build. Environ.*, **36**, 619–626, doi:10.1016/S0360-1323(00)00034-2.

Small, C., 2006: Comparative analysis of urban reflectance and surface temperature. *Remote Sens. Environ.*, **104(2)**, 168–189.

Sobrino, J. A., R. Oltra-Carrió, J. C. Jiménez-Muñoz, Y. Julien, G. Sòria, B. Franch, and C. Mattar, 2012: Emissivity mapping over urban areas using a classification-based approach: Application to the Dual-use European Security IR Experiment (DESIREX). *Int. J. Appl. Earth Obs. Geoinf.*, **18**, 141–147, doi:10.1016/j.jag.2012.01.022.

Soegaard, H., and L. Moller-Jensen, 2003: Towards a spatial CO2 budget of a metropolitan region based on textural image classification and flux measurements. *Remote Sens. Environ.*, **87**, 283–294.

Sogachev, A., 2009: A Note on Two-Equation Closure Modelling of Canopy Flow. *Bound. Lay. Met.*, **130**, 423–435, doi:10.1007/s10546-008-9346-2.

Sogachev, A., and J. Lloyd, 2004: Using a One-and-a-Half Order Closure Model of the Atmospheric Boundary Layer for Surface Flux Footprint Estimation. *Bound. Lay. Met.*, **112**, 467–502, doi:10.1023/B:BOUN.0000030664.52282.ee.

Soux, A., J. A. Voogt, and T. R. Oke, 2004: A Model to Calculate what a Remote Sensor `Sees' of an Urban Surface. *Bound. Lay. Met.*, **111**, 109–132.

Sparks, N., and R. Toumi, 2010: Remote sampling of a CO2 point source in an urban setting. *Atmos. Environ.*, **44**, 5287–5294, doi:10.1016/j.atmosenv.2010.07.048.

Spronken-Smith, R. A., M. Kossmann, and P. Zawar-Reza, 2006: Where does all the energy go? Surface energy partitioning in suburban Christchurch under stable wintertime conditions. *Theor. Appl. Clim.*, **84**, 137–149, doi:10.1007/s00704-005-0151-2.

Steemers, K., N. Baker, D. Crowther, J. Dubiel, and M. Nikolopoulou, 1998: Radiation absorption and urban texture. *Build. Res. Inf.*, **26**, 103–112, doi:10.1080/096132198370029.

Stewart, I. D., and T. R. Oke, 2012: "Local Climate Zones" for urban temperature studies. *Bull. Amer. Meteor. Soc.*, **93**, 1879–1900, doi:10.1175/BAMS-D-11-00019.1.

Stull, R. B., 1988: *An Introduction to Boundary Layer Meteorology*. Kluwer Acad. Publ., Dordrecht, 688p.

A. Le Tertre, A. Lefranc, D. Eilstein, C. Declercq, S. Medina, M. Blanchard, B. Chardon, P. Fabre, L. Filleul, J.-F. Jusot, L. Pascal, H. Prouvost, S. Cassadou, and M. Ledrans, 2006: Impact of the 2003 heatwave on all-cause mortality in 9 French cities. *Epidemiol. Cambridge Mass*, **17**, 75–79.

Testa, S. M., 1995: Chemical Aspects Of Cold-Mix Asphalt Incorporating Contaminated Soil. *J. Soil Contam.*, **4**.

Townshend, J., C. Justice, W. Li, C. Gurney, and J. McManus, 1991: Global land cover classification by remote sensing: present capabilities and future possibilities. *Remote Sens. Environ.*, **35**, 243–255, doi:10.1016/0034-4257(91)90016-Y.

UN-HABITAT, 2010: *State of the World's Cities 2010/2011*. UN-HABITAT, 224p.

UN-HABITAT, 2012: *State of the World's Cities 2012/2013*. UN-HABITAT, 142p.

UN-HABITAT, 2013: Time to think urban. *24th Session Governing Council, 20p.*

Van de Boer, A., A. Graf, A. F. Moene, and D. Schüttemeyer, 2011: Uncertainty analysis of analytical flux footprint models. *Geophys. Res. Abstr., EGU General Assembly*, Vol. 13, EGU2011–6384.

Van der Meer, F. D., and S. M. Jong, 2002: *Imaging spectrometry: basic principles and prospective applications*. Kluwer Academic, 425p.

Van Dijk, A., A. F. Moene, and H. A. R. de Bruin, 2004: The Proinciples of Surface Flux Physics: Theory, Practice and Description of the ECPACK library. *Intern. Report, Meteorol. Air Qual. Group, Wageningen Univ. Wageningen, Netherlands*, 99p.

Velasco, E., and M. Roth, 2010: Cities as Net Sources of CO2: Review of Atmospheric CO2 Exchange in Urban Environments Measured by Eddy Covariance Technique. *Geogr. Compass*, **4**, 1238–1259, doi:10.1111/j.1749-8198.2010.00384.x.

Velasco, E., S. Pressley, E. Allwine, H. Westberg, and B. Lamb, 2005: Measurements of CO2 fluxes from the Mexico City urban landscape. *Atmos. Environ.*, **39**, 7433–7446.

Vesala, T. L. Jarvi, S. Launiainen, A. Sogachev, U. Rannik, I. Mammarella, E. Siivola, P. Keronen, J. Rinne, A. Riikonen, E. Nikinmaa, 2008a: Surface-atmosphere interactions over complex urban terrain in Helsinki, Finland. *Tellus*, **60B**, 188–199.

Vesala, T. N, Kljun, U, Rannik, J. Rinne, A. Sogachev, T. Markkanen, K. Sabelfeld, Th. Foken, and M. Y. Leclerc, 2008b: Flux and concentration footprint modelling: state of the art. *Environ. Pollut.*, **152**, 653–666, doi:10.1016/j.envpol.2007.06.070.

Vesala, T., N. Kljun, Ü. Rannik, A. Sogachev, T. Markkanen, K. Sabelfeld, T. Foken, and M. Y. Leclerc, 2010: Flux and concentration footprint modelling. *Modelling of pollutants in complex environmental systems*, G. Hanrahan, Ed., ILM Publications, St Albans, 339–355.

Voogt, J. A., and T. R. Oke, 1991: Validation of an urban canyon radiation model for nocturnal long-wave fluxes. *Bound. Lay. Met.*, **54**, 347–361, doi:10.1007/BF00118866.

Voogt, J. A., and C. S. B. Grimmond, 2000: Modeling Surface Sensible Heat Flux Using Surface radiative Temperatures in a Simple Urban Area. *J. Appl. Meteorol.*, **1681**, 1669–1679.

Voogt, J. A., and T. R. Oke, 2003: Thermal Remote Sensing of Urban Climates. *Remote Sens. Environ.*, **86**, 370–384.

Wan, Z., D. Ng, and J. Dozier, 1994: Spectral emissivity measurements of land-surface materials and related radiative transfer simulations. *Adv. Sp. Res.*, **14**, 91–94, doi:10.1016/0273-1177(94)90197-X.

Ward, H. C., J. G. Evans, and C. S. B. Grimmond, 2013: Multi-season eddy covariance observations of energy, water and carbon fluxes over a suburban area in Swindon, UK. *Atmos. Chem. Phys.*, **13**, 4645–4666, doi:10.5194/acp-13-4645-2013.

Webb, E. K., G. I. Pearman, and R. Leuning, 1980: Correctionof the flux measurements for density effects due to heat and water vapour transfer. *Quart. J. R. Met. Soc.*, **106**, 85–100.

Weber, S., and K. Kordowski, 2010: Comparison of atmospheric turbulence characteristics and turbulent fluxes from two urban sites in Essen, Germany. *Theor. Appl. Clim.*, **102**, 61–74.

Weng, Q., 2009: Thermal Infrared Remote Sensing for Urban Climate and Environmental Studies: Methods, applications, and Trends. *ISPRS J. Photogramm.*, **64**, 335–344.

Weng, Q., 2012: Remote sensing of impervious surfaces in the urban areas: Requirements, methods, and trends. *Remote Sens. Environ.*, **117**, 34–49, doi:10.1016/j.rse.2011.02.030.

Wilczak, J., S. Oncley, and S. A. Stage, 2001: Sonic Anemometer Tilt Correction Algorithms. *Bound. Lay. Met.*, **99**, 127–150.

Winton, M., 2006: Surface Albedo Feedback Estimates for the AR4 Climate Models. *J. Clim.*, **19**, 359–365, doi:10.1175/JCLI3624.1.

Wood, C. R. A. Lacser, J. F. Barlow, A. Padhra, S. E. Belcher, E. Nemitz, C. Helfter, D. Famulari, D and C. S. B. Grimmond, 2010: Turbulent Flow at 190 m Height Above London During 2006–

2008: A Climatology and the Applicability of Similarity Theory. *Bound. Lay. Met.*, **137**, 77–96.

Wood, C. R., L. Pauscher, H. C. Ward, S. Kotthaus, J. F. Barlow, M. Gouvea, S. E. Lane, and C. S. B. Grimmond, 2013: Wind observations above an urban river using a new lidar technique, scintillometry and anemometry. *Sci. Total environ.*, **442**, 527–533, doi:10.1016/j.scitotenv.2012.10.061.

Wooster, M. J., P. H. Freeborn, S. Archibald, C. Oppenheimer, G. J. Roberts, T. E. L. Smith, N. Govender, M. Burton, and I. Palumbo, 2011: Field determination of biomass burning emission ratios and factors via open-path FTIR spectroscopy and fire radiative power assessment: headfire, backfire and residual smouldering combustion in African savannahs. *Atmos. Chem. Phys.*, **11**, 11591–11615, doi:10.5194/acp-11-11591-2011.

Wray, C., and H. Akbari, 2008: The effects of roof reflectance on air temperatures surrounding a rooftop condensing unit. *Energ. Build.*, **40**, 11–28.

Wyngaard, J. C., O. R. Coté, and Y. Izumi, 1971: Local Free Convection, Similarity and the Budgets of Shear Stress and Heat Flux. *J. Atmos. Sci.*, **28**, 1171–1182.

Xu, W., M. J. Wooster, and C. S. B. Grimmond, 2008: Modelling of urban sensible heat flux at multiple spatial scales: A demonstration using airborne hyperspectral imagery of Shanghai and a temperature-emissivity separation approach. *Remote Sens. Environ.*, **112**, 3493–3510, doi:10.1016/j.rse.2008.04.009.

Yaghoobian, N., and J. Kleissl, 2012: Effect of Reflective Pavements on Building Energy Use. *Urban Clim.*, **2**, 25–42, doi:10.1016/j.uclim.2012.09.002.

Yaghoobian, N., J. Kleissl, and E. S. Krayenhoff, 2010: Modeling the Thermal Effects of Artificial Turf on the Urban Environment. *J. Appl. Meteorol. Clim.*, **49**, 332–345, doi:10.1175/2009JAMC2198.1.

Yamamoto, Y., 2005: Measures to Mitigate Urban Heat Islands. *Distribution*, **18**, 65–83.

Yang, X., 2011: *Urban Remote Sensing: Monitoring, Synthesis and Modeling in the Urban Environment*. X. Yang, Ed. Wiley-Blackwell, Chichester, UK, 388p.

Zilitinkevich, S. S., E. E. Fedorovich, and M. V Shabalova, 1992: Numerical Model of a Non-steady Atmospheric Planetary Boundary Layer, Based on Similarity Theory. *Bound. Lay. Met.*, **59**, 387–411.

ZINC, 2003: Zinc applications. *Zinc Info Centre*,

http://www.zincinfocentre.org/zinc_applications.html (Accessed 27/11/2013).

Appendix A Spectral Library of Impervious Urban Materials

A.1 Introduction

The London Urban Micromet Data Archive (LUMA) Spectral Library of impervious Urban Materials (SLUM) is organised by material class (Chapter II, Table II.3). The methodologies used during the measurements and data processing are described in Chapter II, where meta information are provided (Table II.C.1).

Here, further information on all 74 material samples are presented in form of standardised data sheets. The latter are first introduced and details on the materials are listed by material class (Table A.1).

Table A.1: Content of the LUMA library of impervious urban materials.

MATERIAL CLASSSAMPLE-ID

For most material samples, a

zoomed

image is shown.

Picture of the sample

Class	
Material	
Colour	
Status	
Dimension [mm]	

VNIR/SWIR reflectance spectra

- Availability provided, all samples collected in the field and in the laboratory (lab) are shown together with the average across the respective samples. The latter depicts the final result.
- Spectra measured in the field do not provide data across the atmospheric absorption windows. Hence, laboratory spectra are used in the analysis.

TIR emissivity spectra

- All samples collected in the laboratory (lab) are shown together with their average. The latter depicts the final result.

QUARTZITE$_{X001}$

Class	Quartzite conglomerate
Material	Quartzite
Colour	Beige/brown/black/red
Status	New
Dimension [mm]	360 x 4 x 220

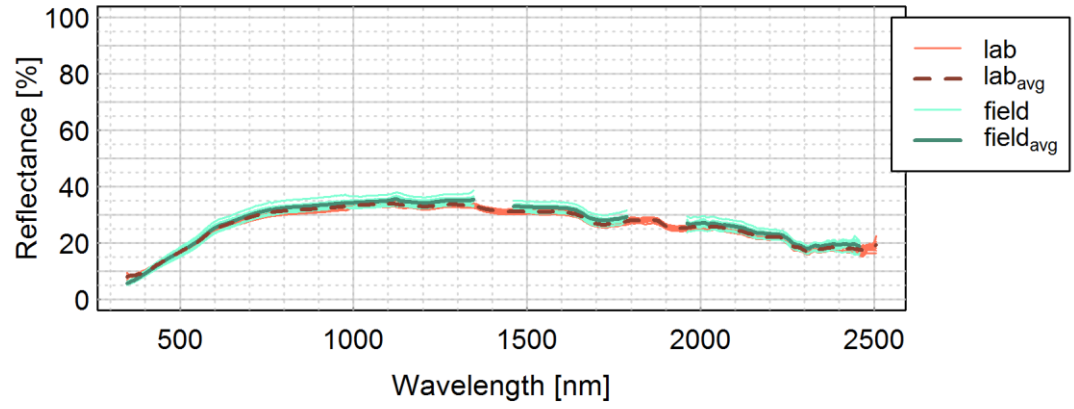

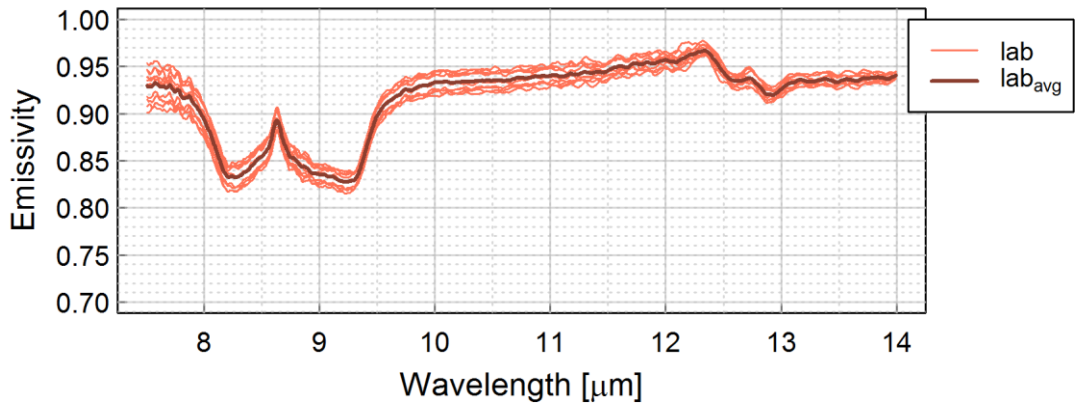

QUARTZITE$_{x002}$

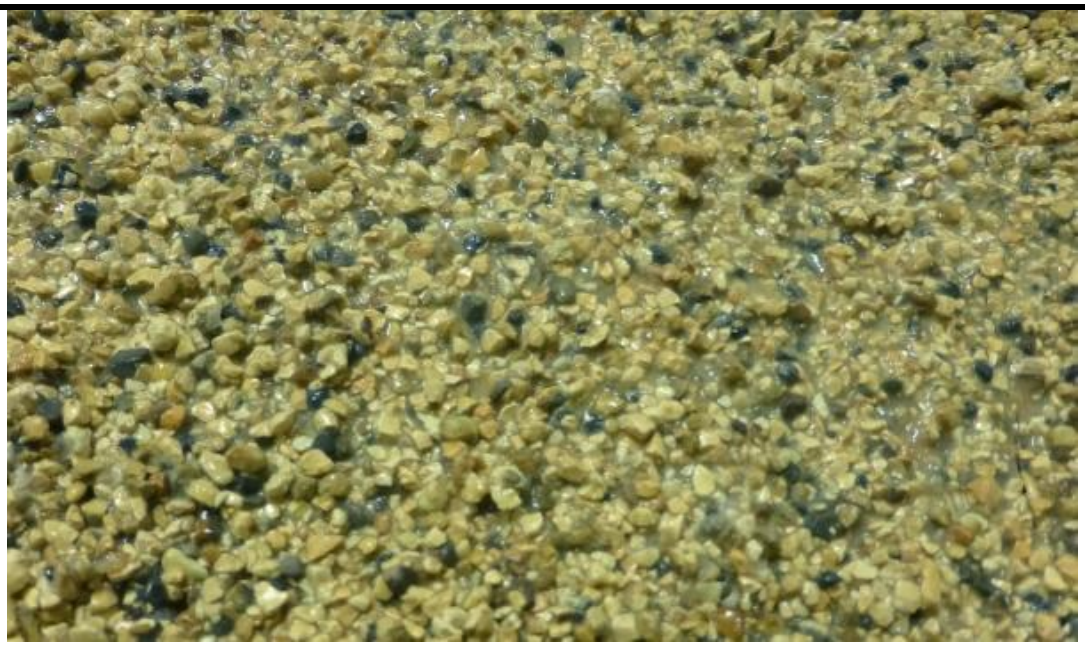

Class	Quartzite conglomerate
Material	Quartzite
Colour	Beige/brown/black
Status	New
Dimension [mm]	360 x 4 x 220

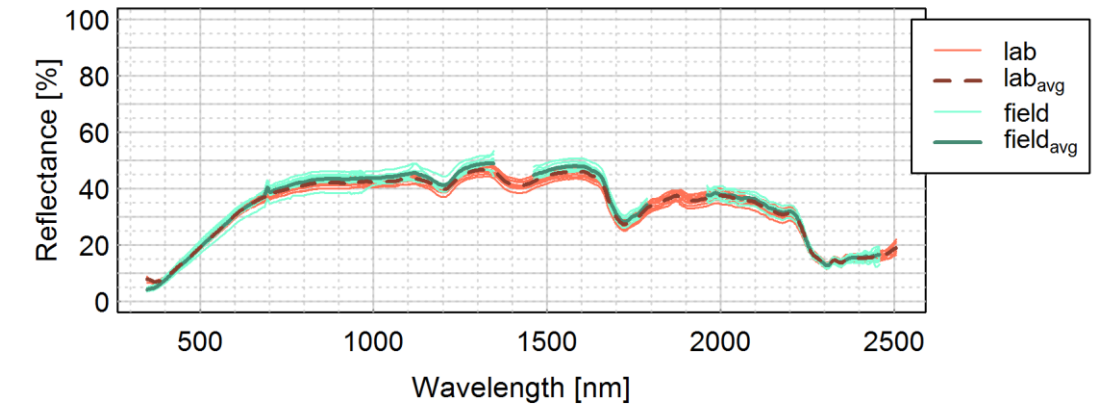

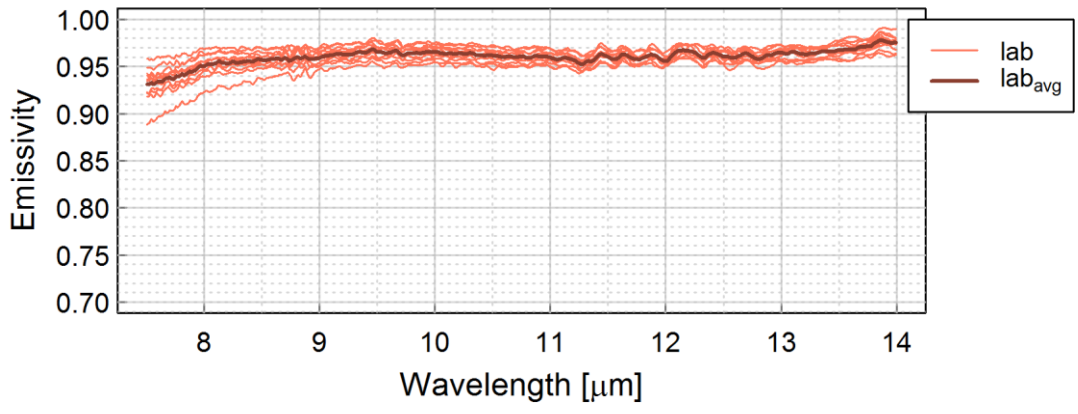

QUARTZITE$_{x003}$

Class	Quartzite conglomerate
Material	Quartzite
Colour	Beige/brown/black/red
Status	New
Dimension [mm]	360 x 4 x 220

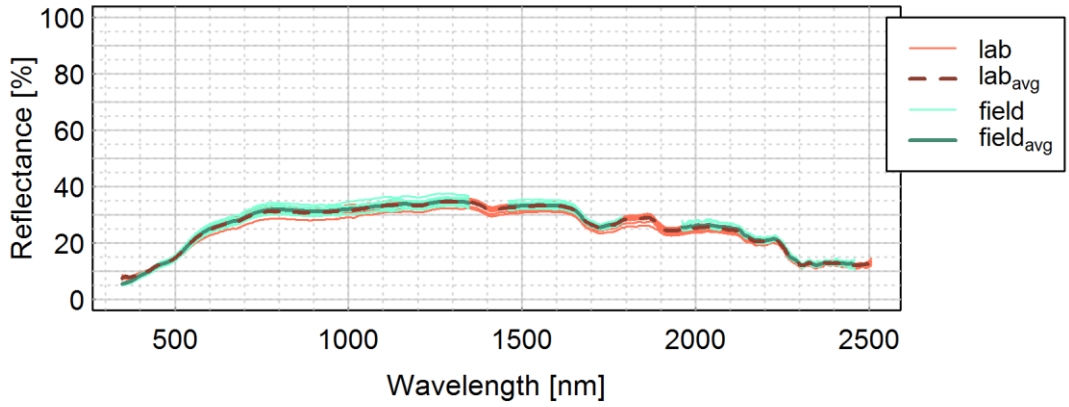

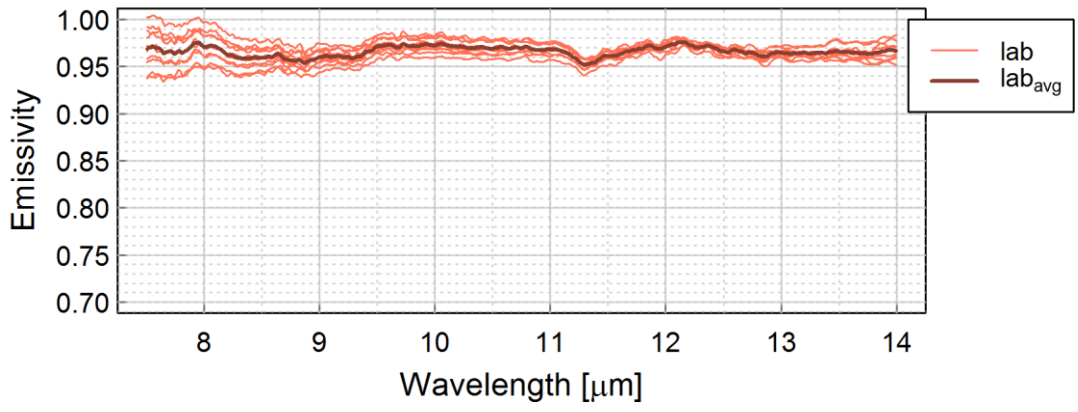

STONE$_{S001}$

Class	Stone
Material	Sandstone
Colour	Beige
Status	Weathered
Dimension [mm]	215 x 35 x 105

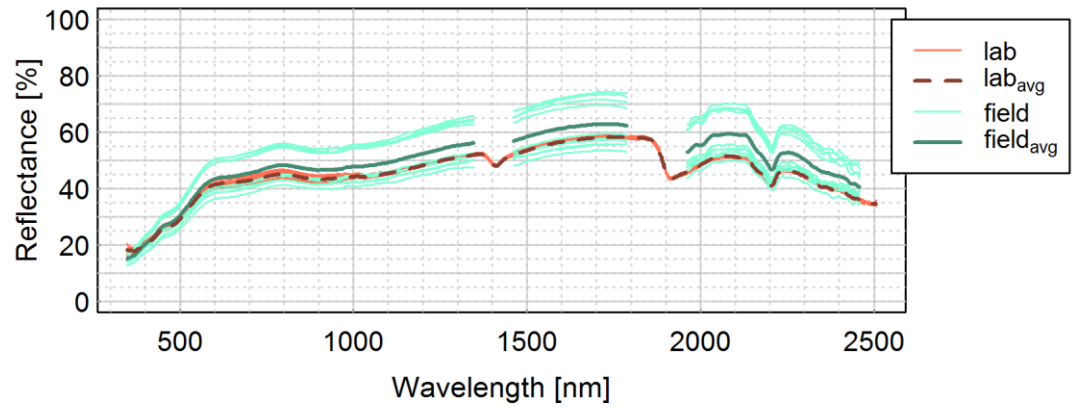

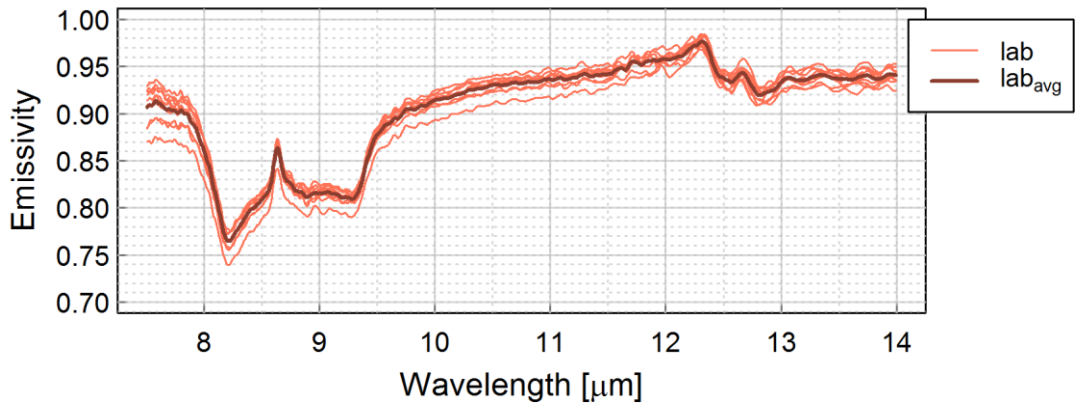

STONE$_{S002}$

Class	Stone
Material	Carboniferous coral limestone
Colour	Grey
Status	Weathered
Dimension [mm]	210 x 19 x 90

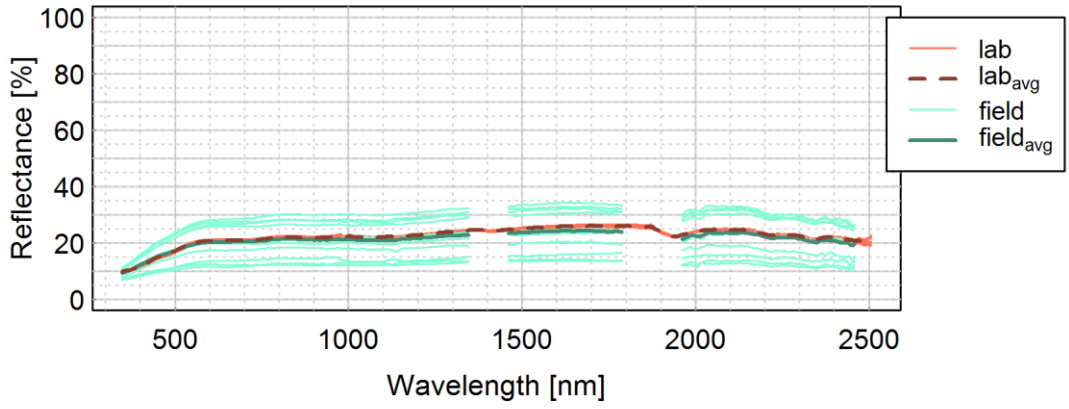

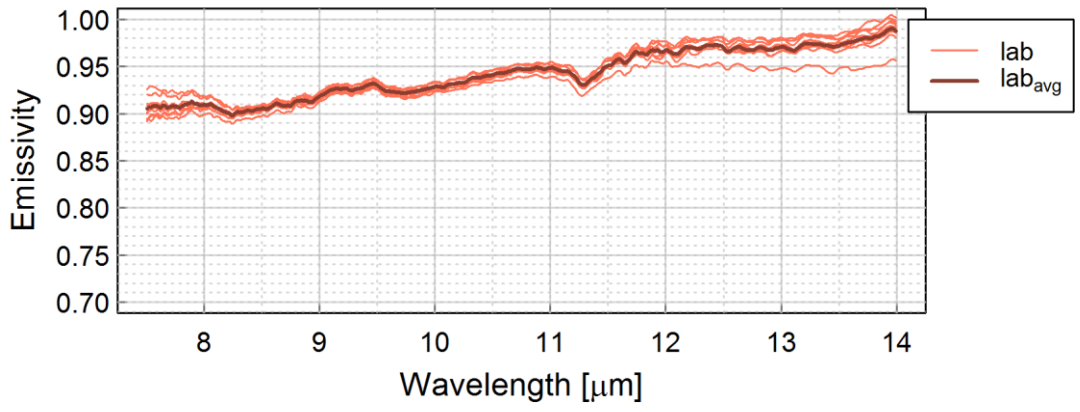

STONE$_{S003}$

Class	Stone
Material	Sandstone
Colour	Ochre
Status	Weathered
Dimension [mm]	70 x 55 x 25

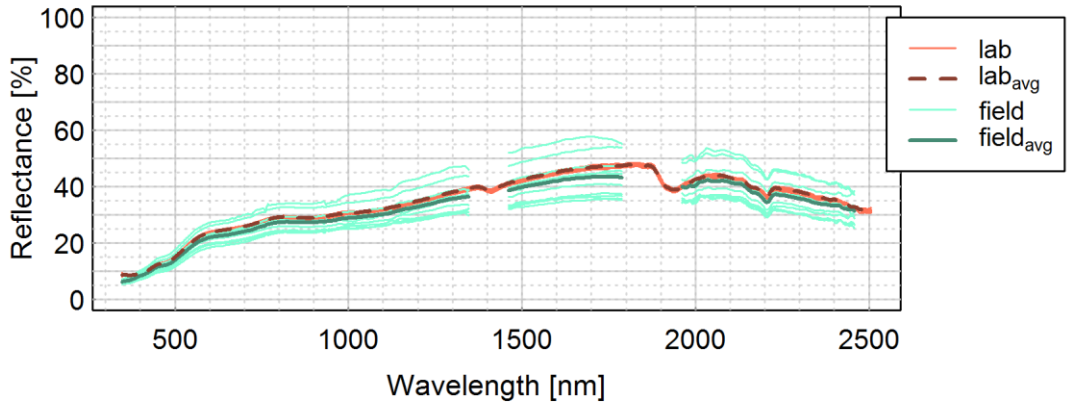

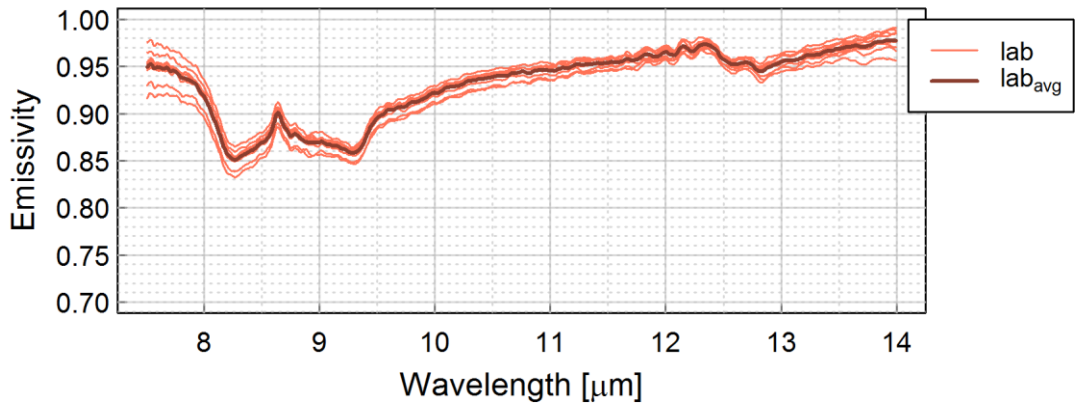

STONE$_{S004}$

Class	Stone
Material	Limestone
Colour	Beige
Status	Weathered
Dimension [mm]	70 x 55 x 25

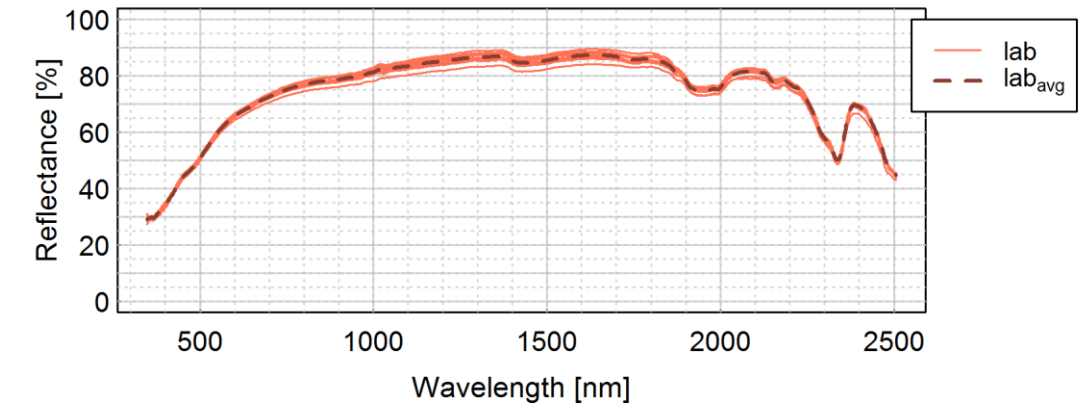

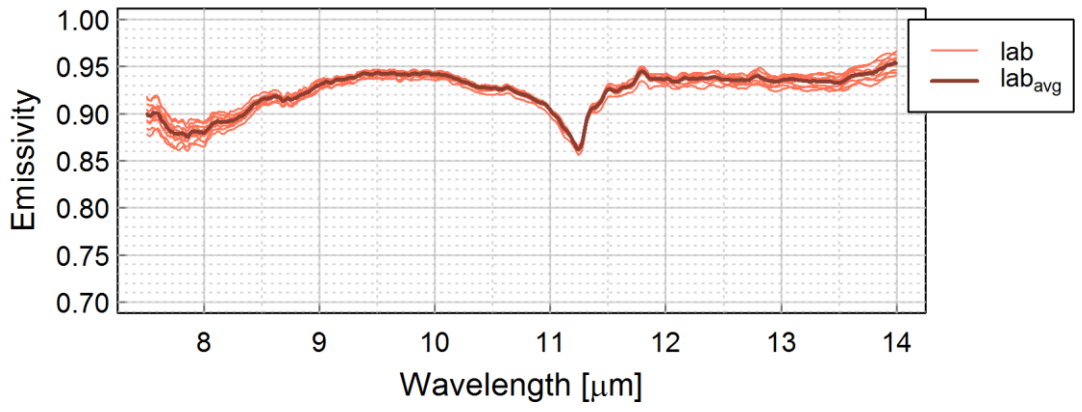

STONE$_{S005}$

Class	Stone
Material	Sandstone
Colour	Light grey
Status	Weathered
Dimension [mm]	28 x 75 x 180

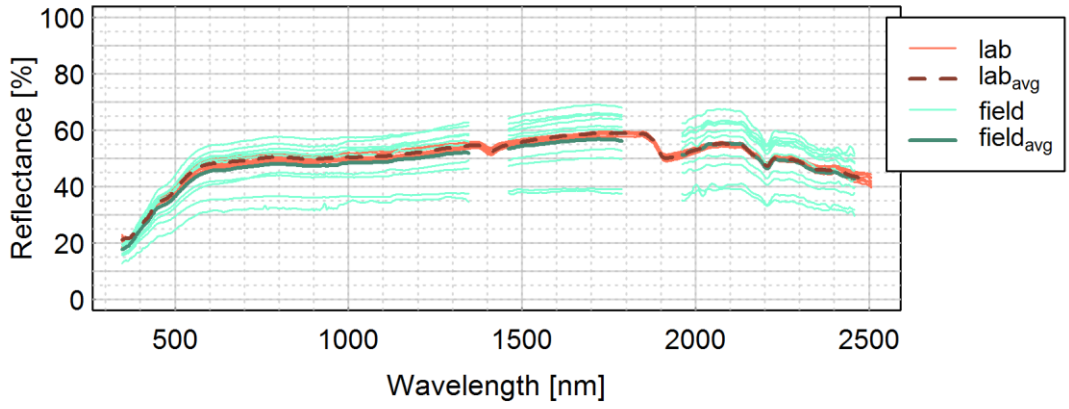

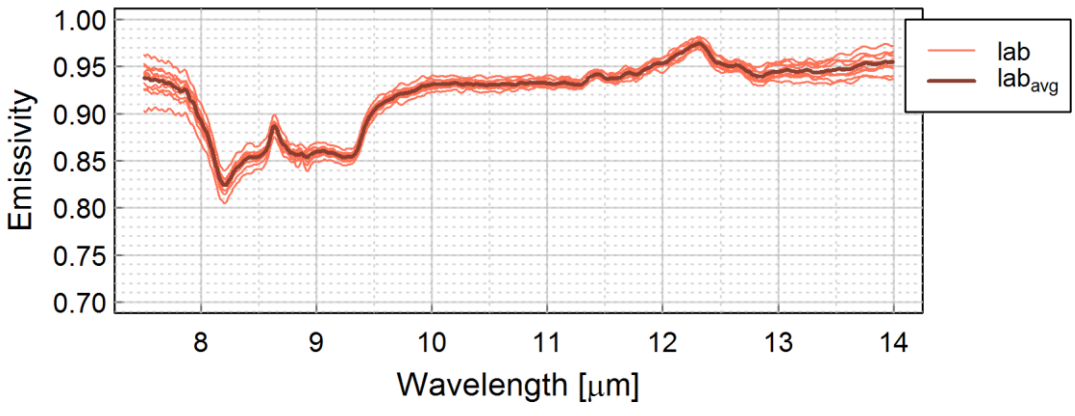

GRANITE$_{G001}$

Class	Granite
Material	Granite
Colour	White/black
Status	New, rough
Dimension [mm]	142 x 56 x 52

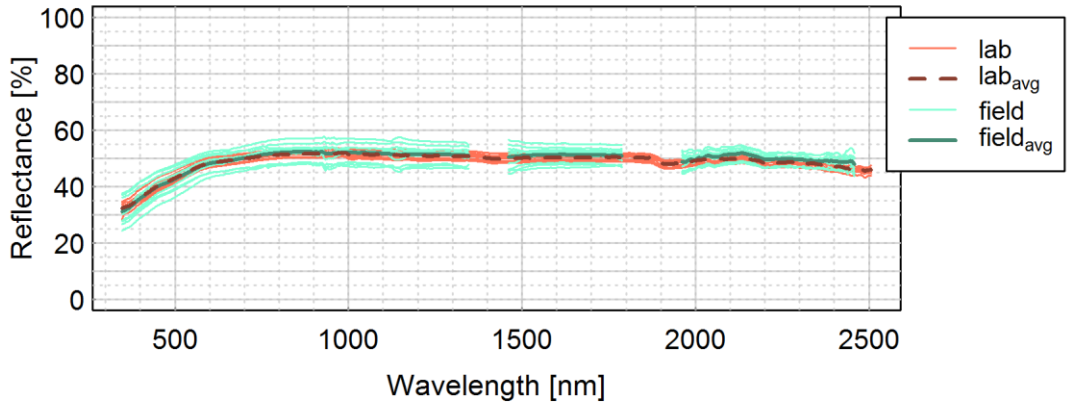

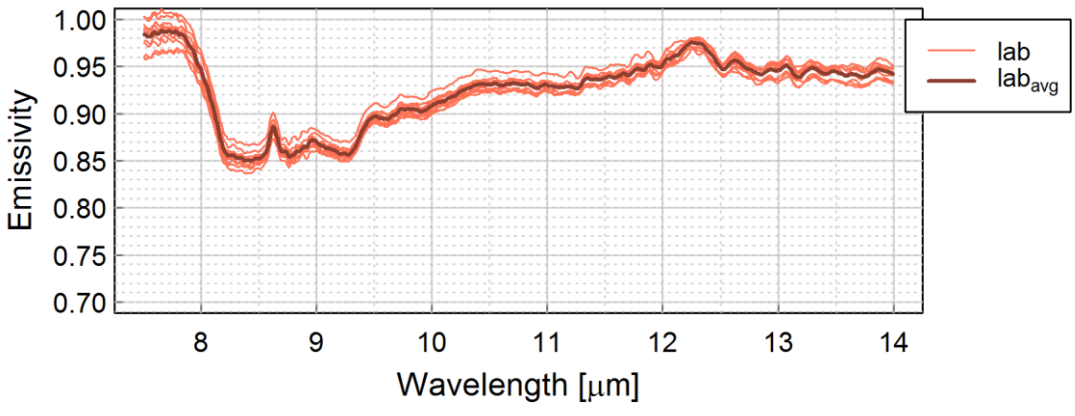

GRANITE$_{G002}$

Class	Granite
Material	Granite with cement
Colour	White/red
Status	Weathered
Dimension [mm]	101 x 95 x 88

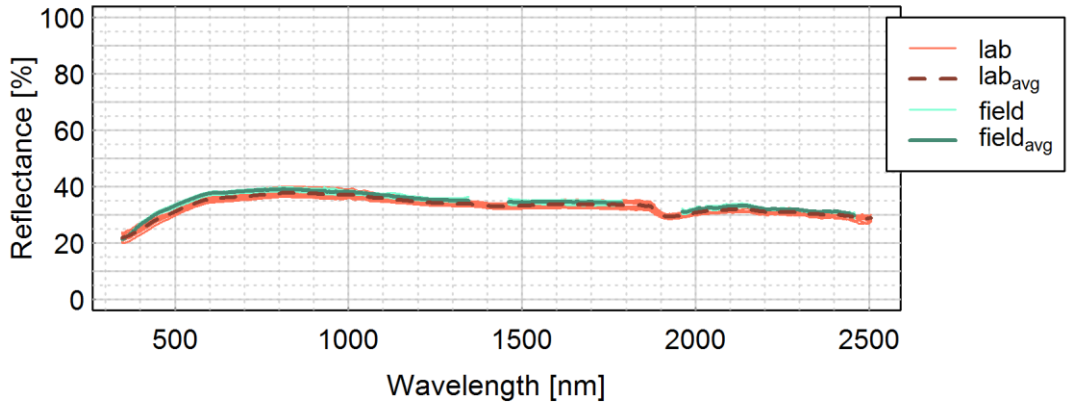

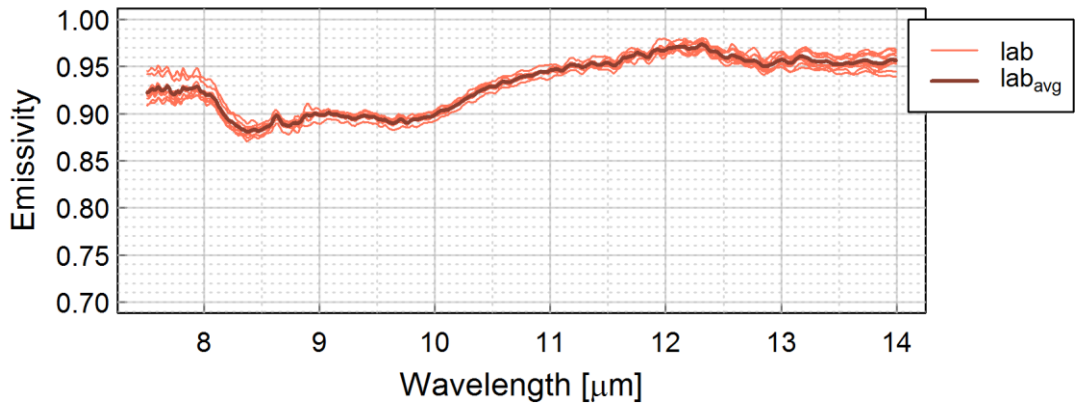

GRANITE$_{G003}$

Class	Granite
Material	Granite with cement
Colour	White/black
Status	Weathered
Dimension [mm]	215 x 57 x 105

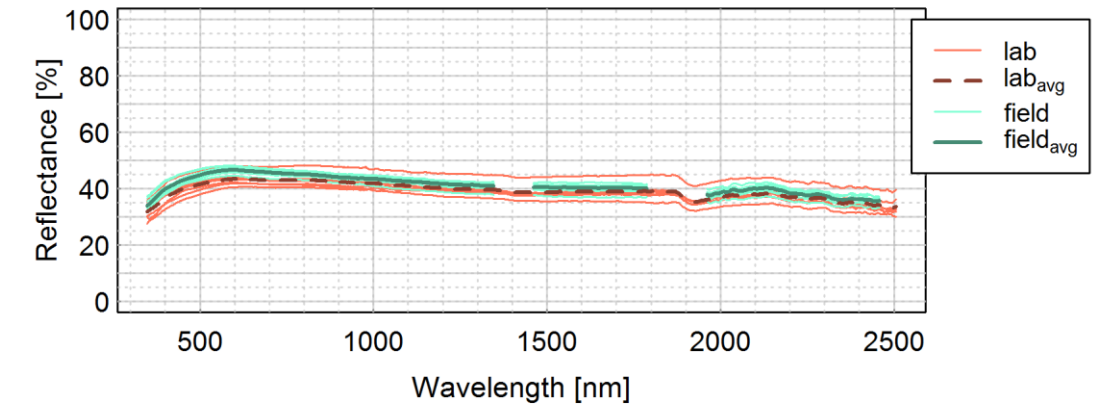

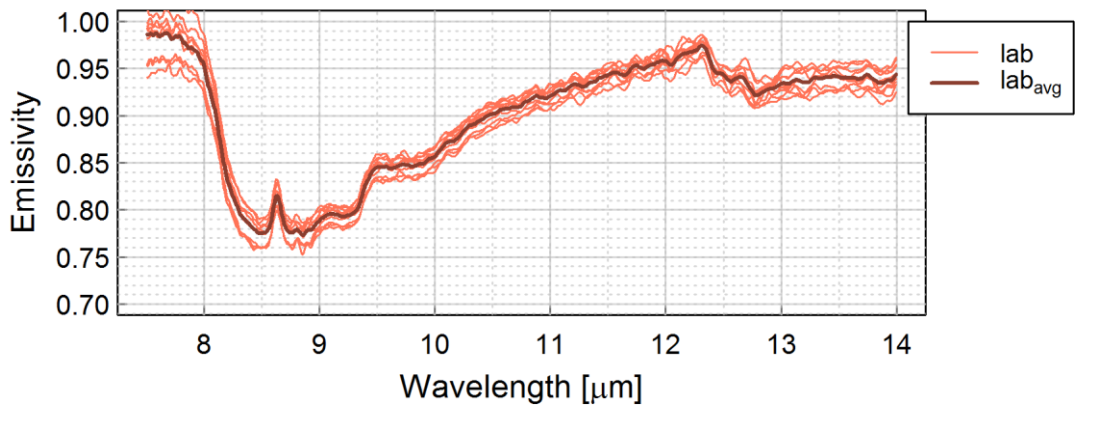

GRANITE$_{G004}$

Class	Granite
Material	Granite
Colour	White/red/black
Status	New, dusty
Dimension [mm]	233 x 60 x 78

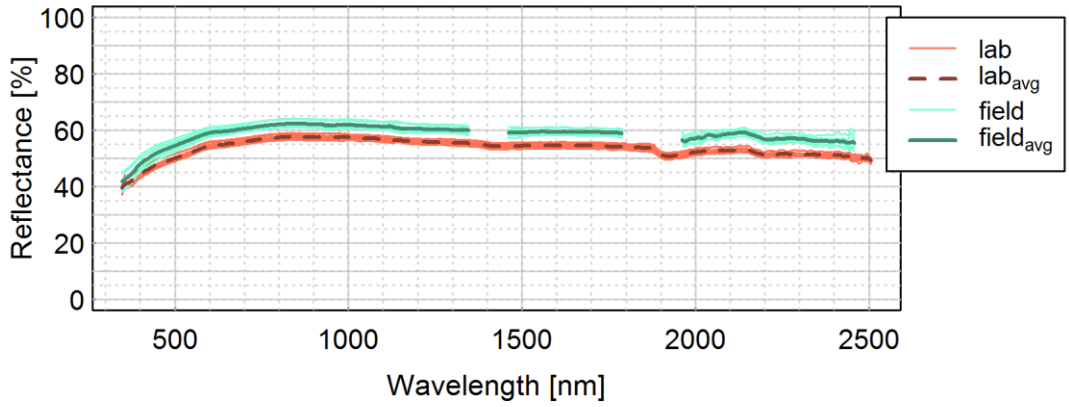

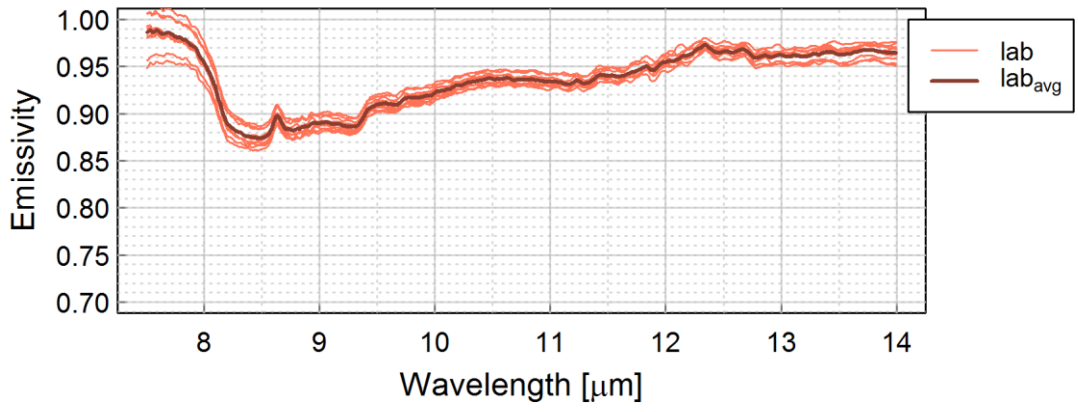

GRANITE$_{G005}$

Class	Granite
Material	Granite
Colour	Red/black
Status	New
Dimension [mm]	125 x 50 x 111

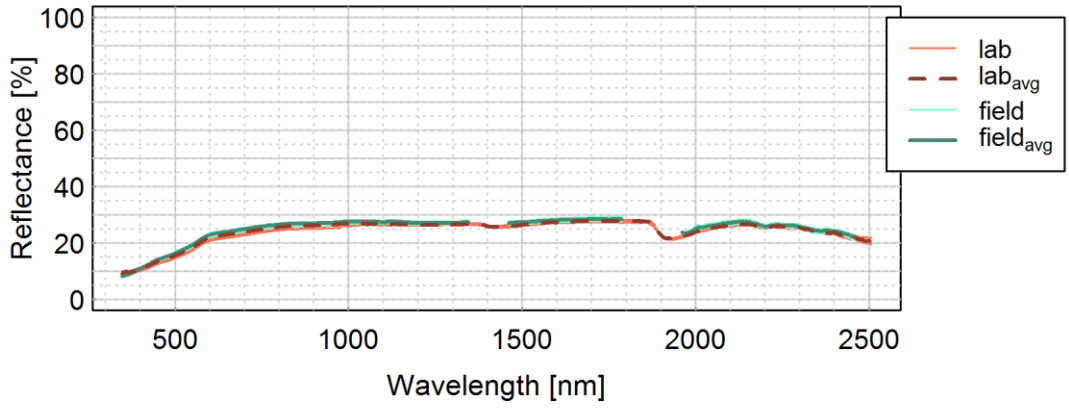

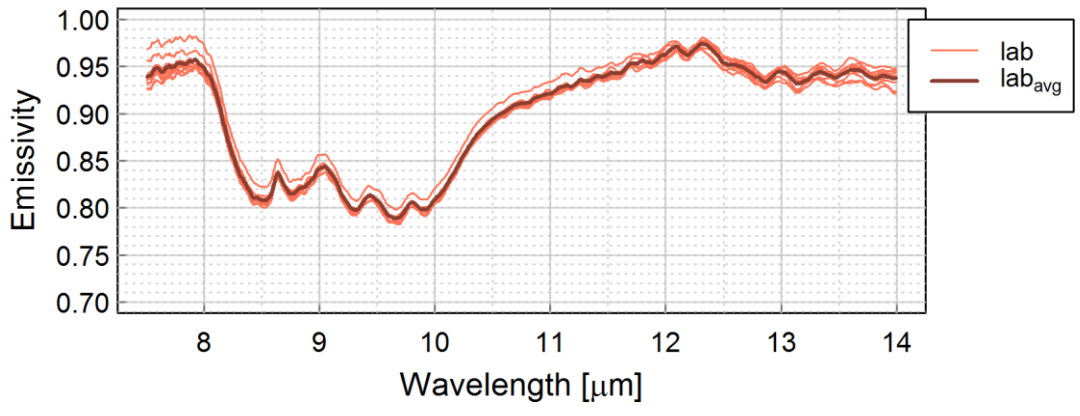

ASPHALT A001

Class	Road asphalt
Material	Asphalt with stone aggregate
Colour	Black/grey
Status	Weathered
Dimension [mm]	190 x 83 x 68

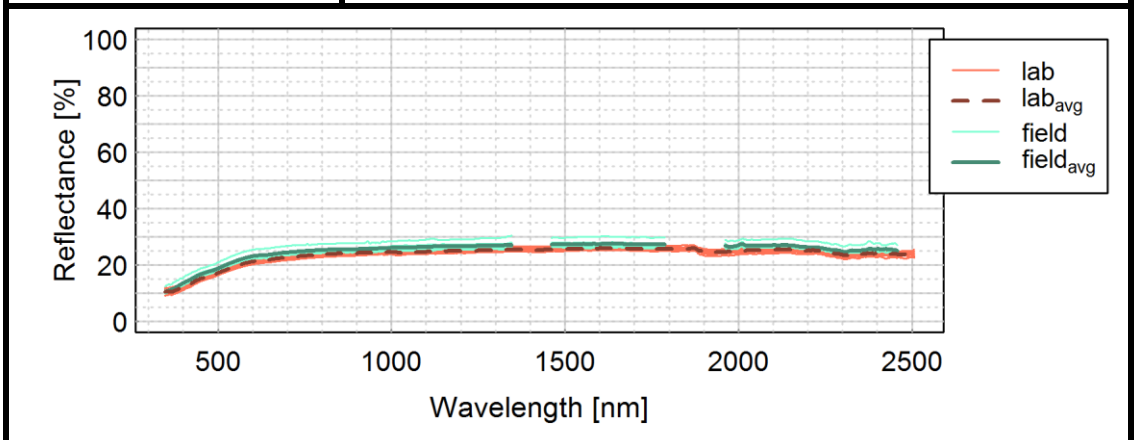

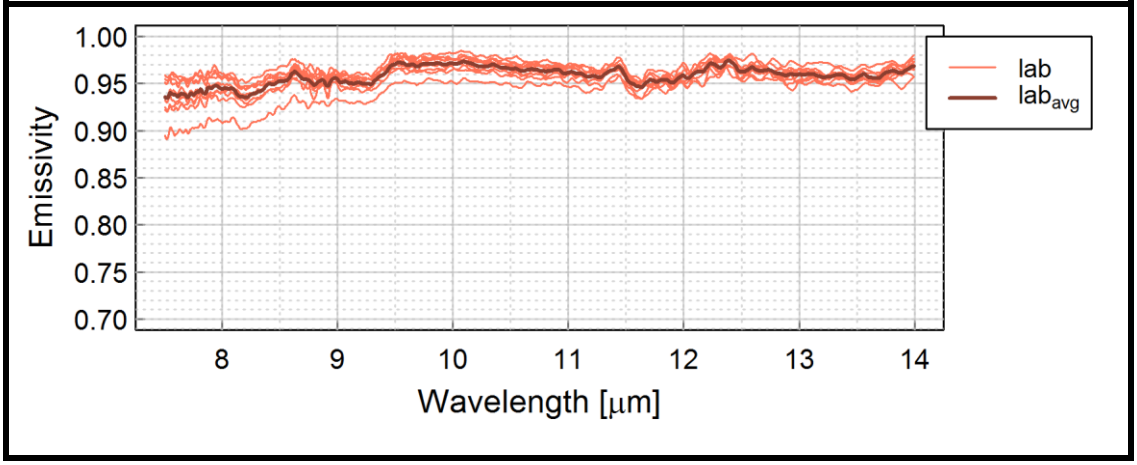

ASPHALT A002

Class	Road asphalt
Material	Asphalt with stone aggregate
Colour	Black/grey
Status	Weathered
Dimension [mm]	60 x 100 x 200

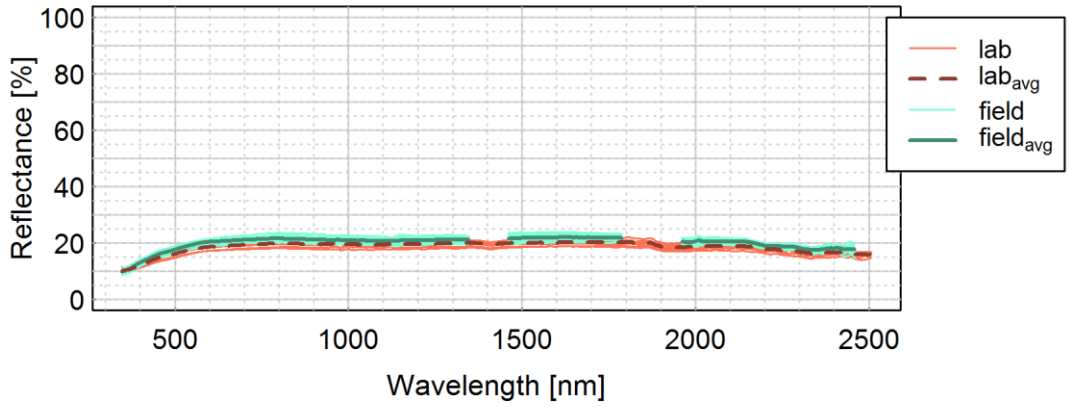

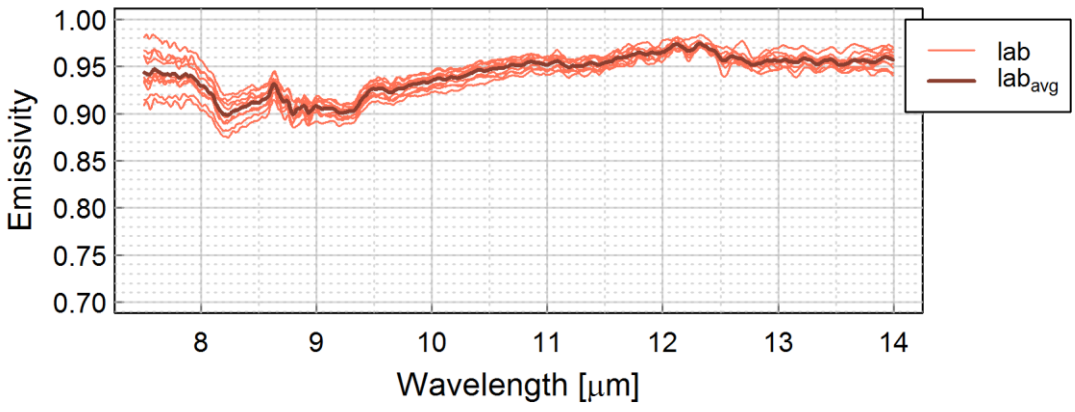

ASPHALT A003

Class	Road asphalt
Material	Asphalt with stone aggregate
Colour	Black/grey
Status	Weathered
Dimension [mm]	60 x 90 x 150

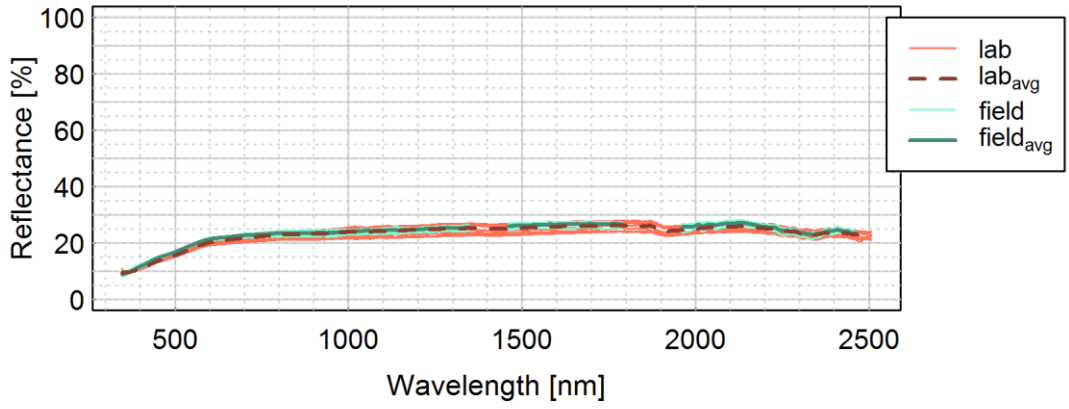

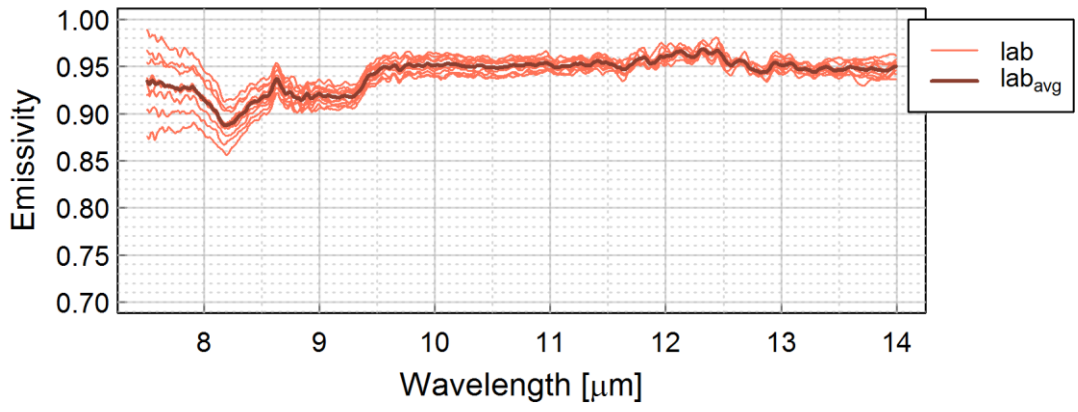

ASPHALT A004

Class	Road asphalt
Material	Asphalt with stone aggregate
Colour	Black/grey
Status	Weathered
Dimension [mm]	120 x 50 x 170

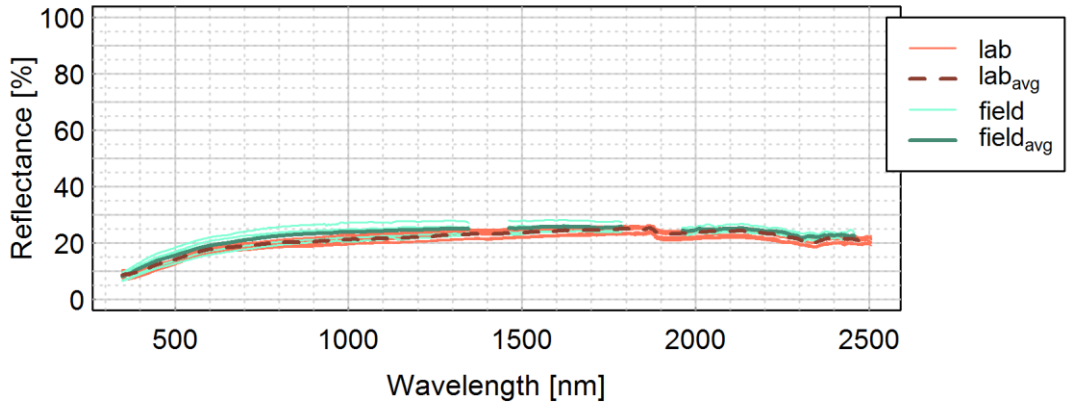

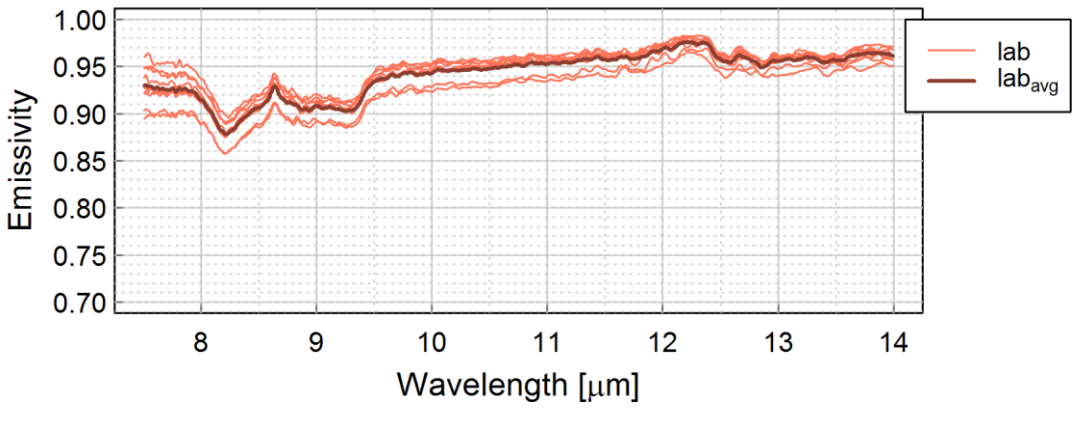

ASPHALT A005

Class	Road asphalt
Material	Asphalt with stone aggregate
Colour	Black/grey
Status	Weathered
Dimension [mm]	55 x 75 x 130

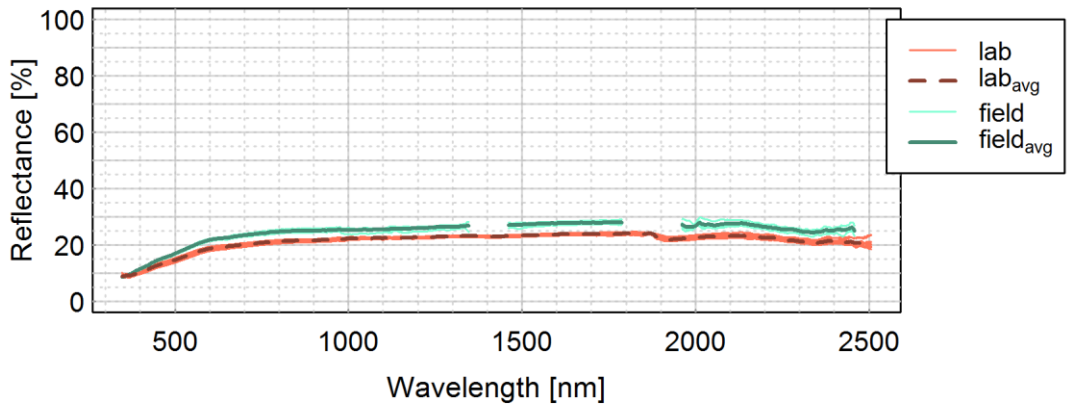

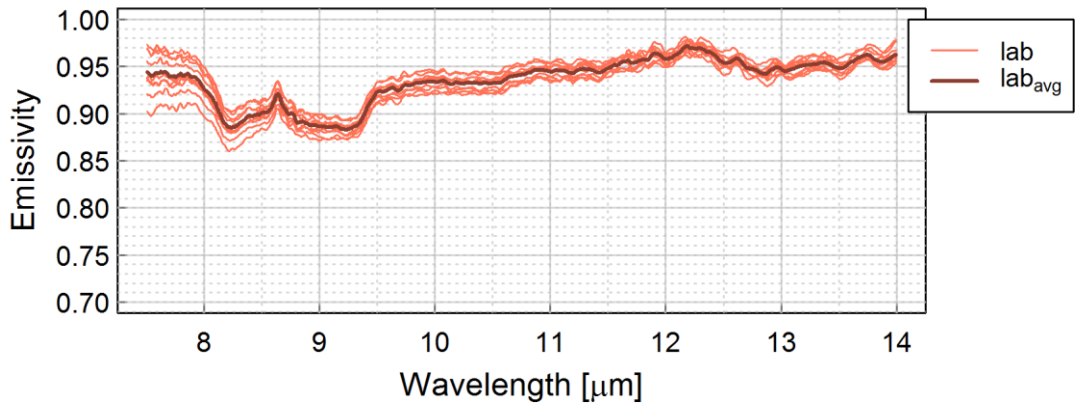

ASPHALT A006

Class	Road asphalt
Material	Asphalt with stone aggregate
Colour	Black/grey
Status	Weathered
Dimension [mm]	30 x 145 x 180

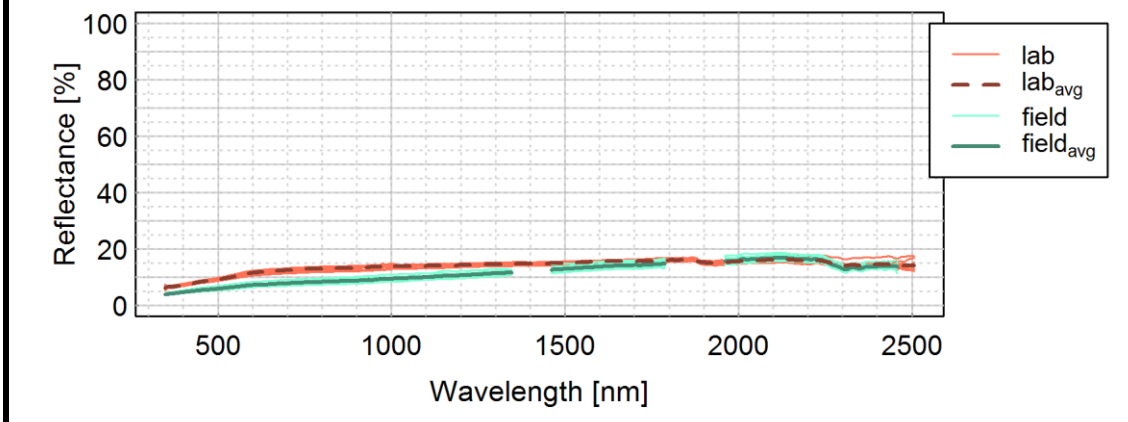

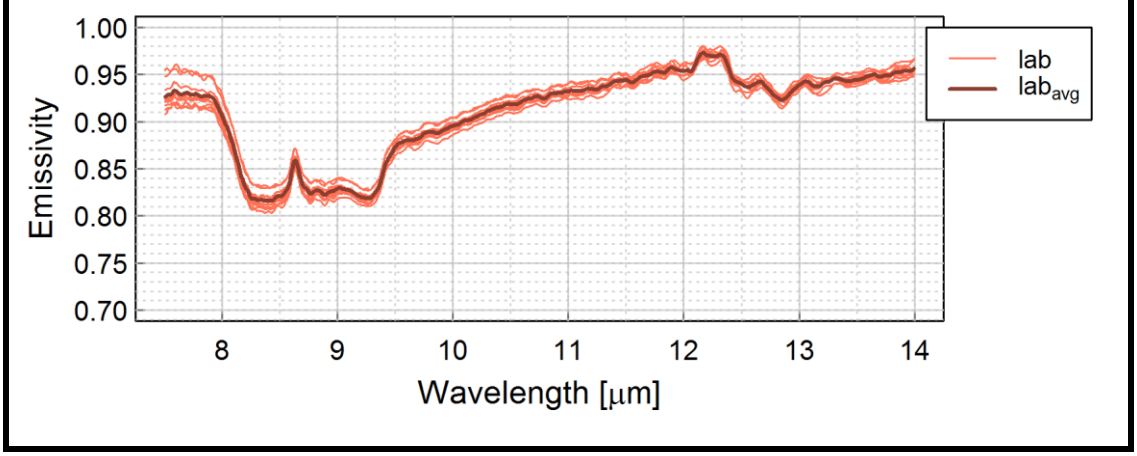

ASPHALT A007

Class	Asphalt roofing
Material	Asphalt roofing shingle with slate chippings
Colour	Grey
Status	New
Dimension [mm]	165 x 3 x 170

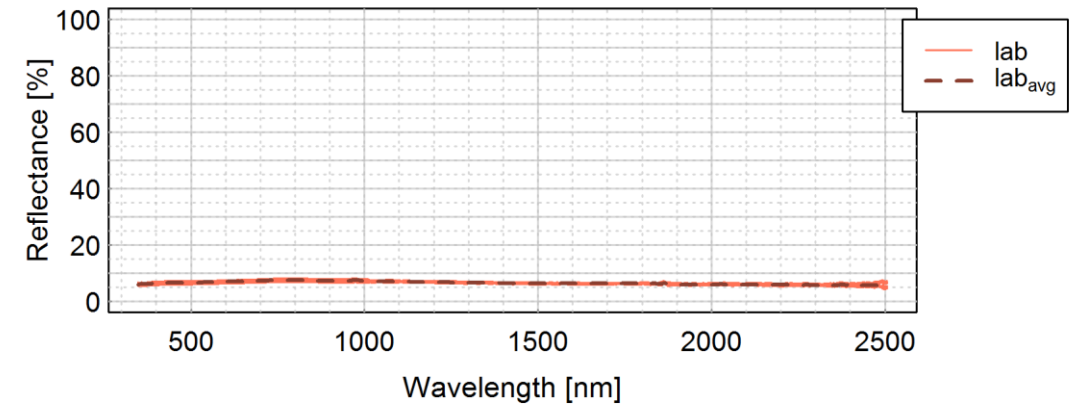

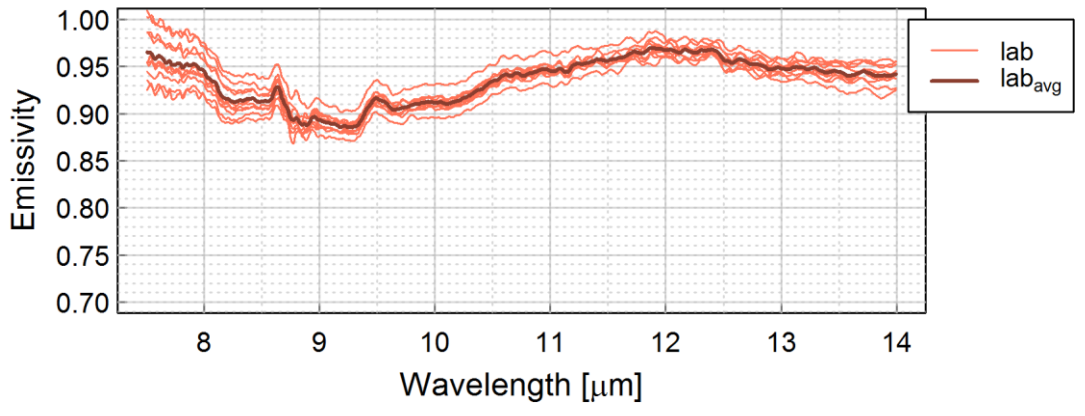

ASPHALT A008

Class	Road asphalt
Material	Tarmac
Colour	Black
Status	Weathered
Dimension [mm]	140 x 25 x 140

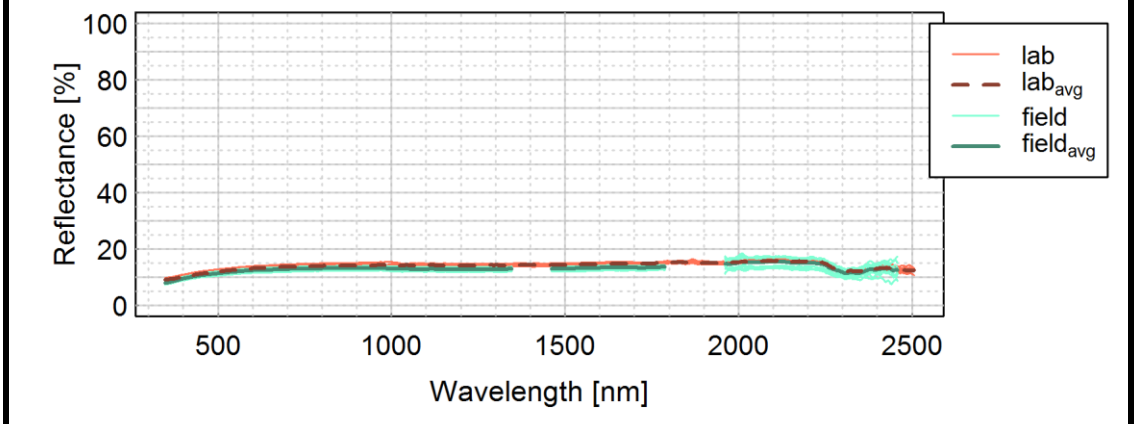

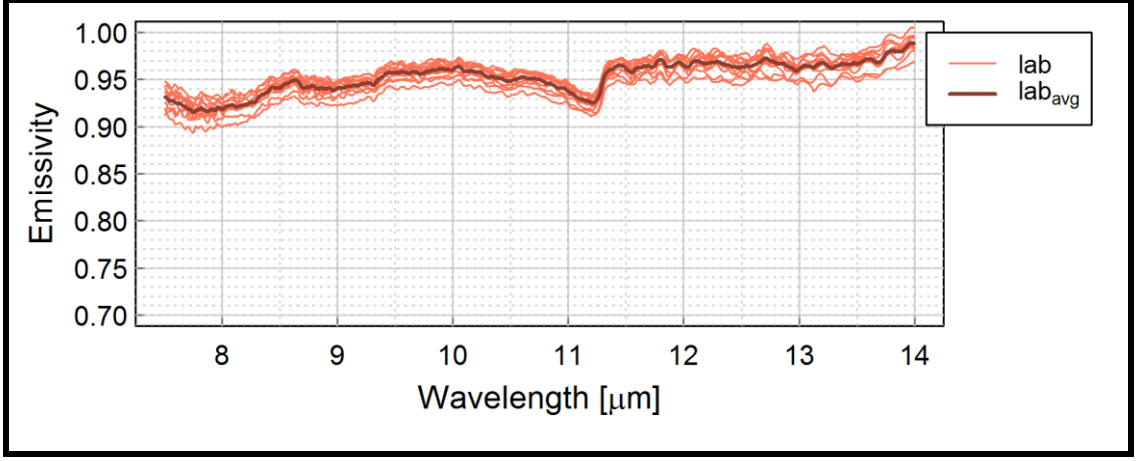

ASPHALT A009

Class	Road asphalt
Material	Tarmac
Colour	Black
Status	Weathered
Dimension [mm]	60 x 21 x 85

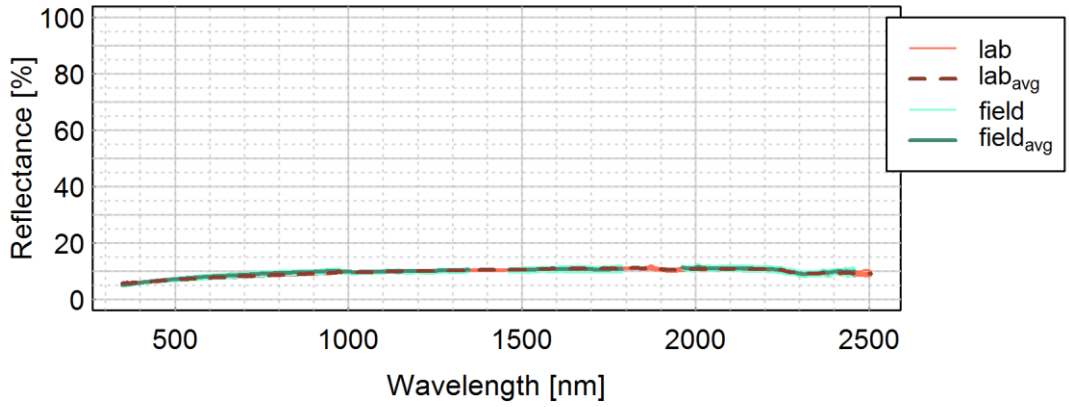

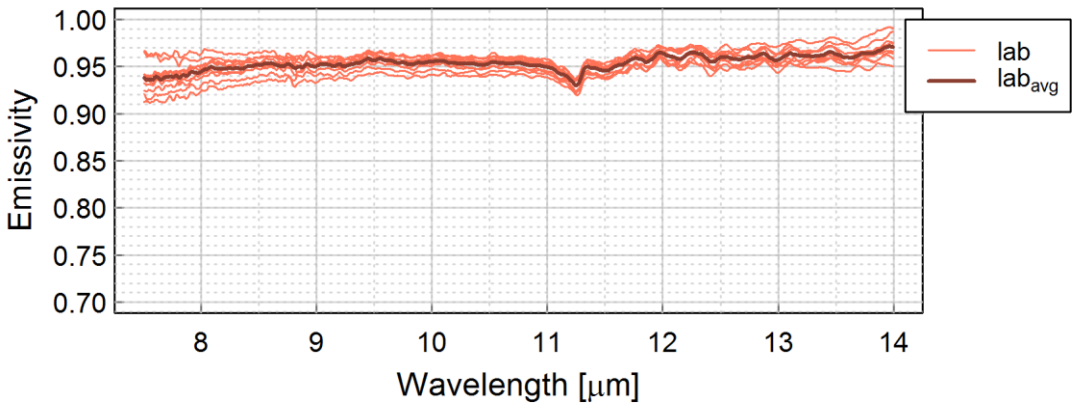

ASPHALT A010

Class	Road asphalt
Material	Tarmac
Colour	Black
Status	Weathered
Dimension [mm]	65 x 21 x 80

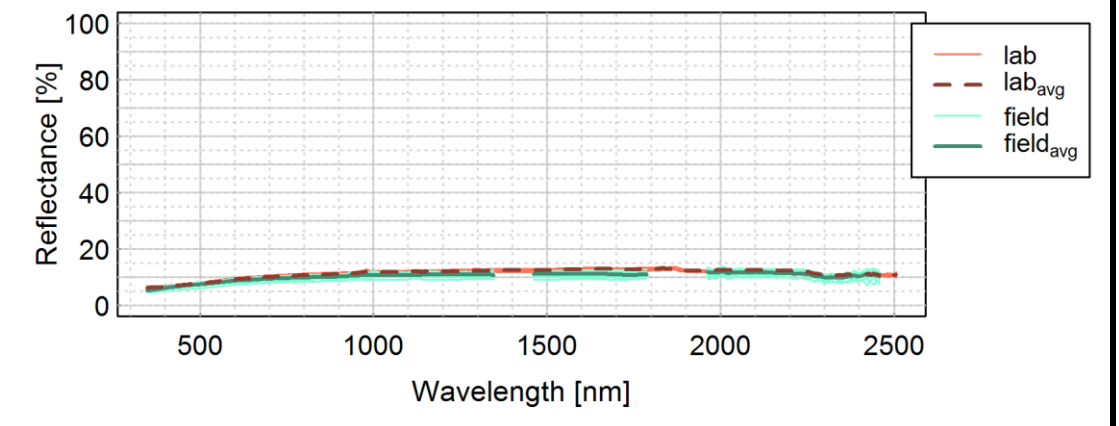

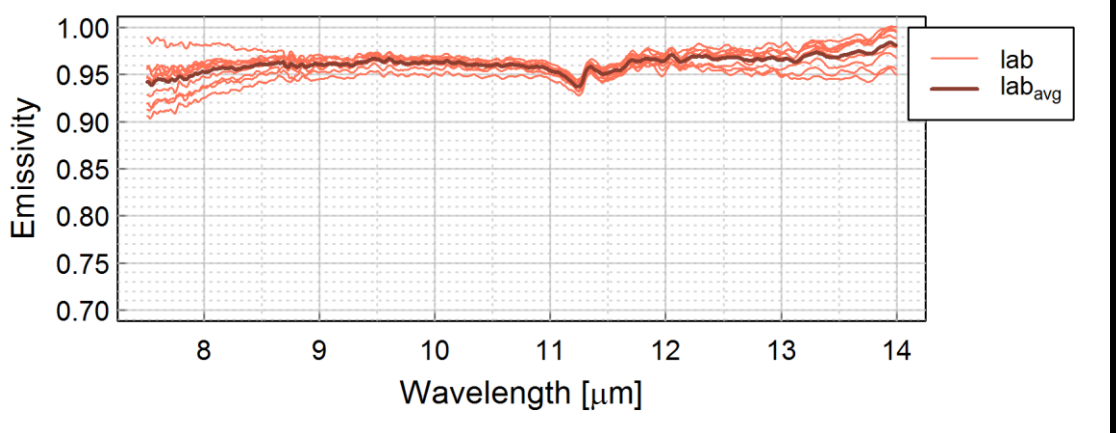

CONCRETE/CEMENT C001

Class	Cement
Material	Cement
Colour	Grey/ochre
Status	Weathered
Dimension [mm]	367 x 60 x 140

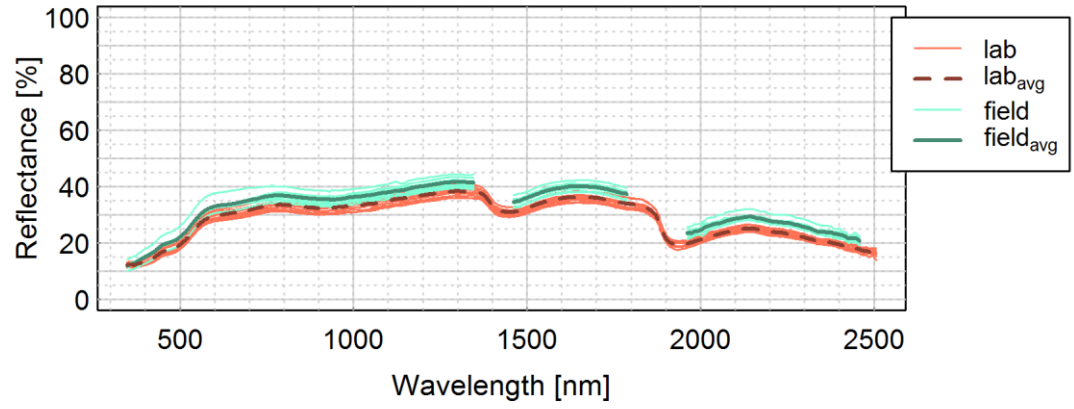

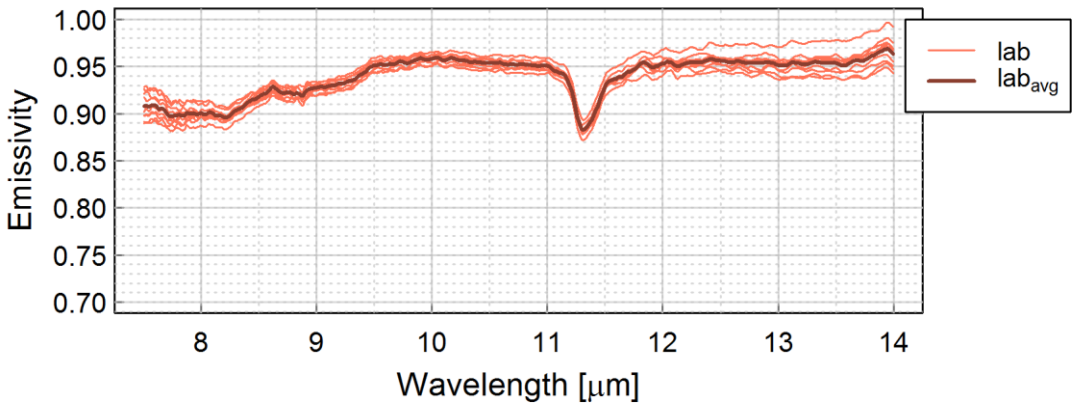

CONCRETE/CEMENT C002

Class	Concrete
Material	Concrete with small aggregate
Colour	Grey/white
Status	New
Dimension [mm]	198 x 53 x 100

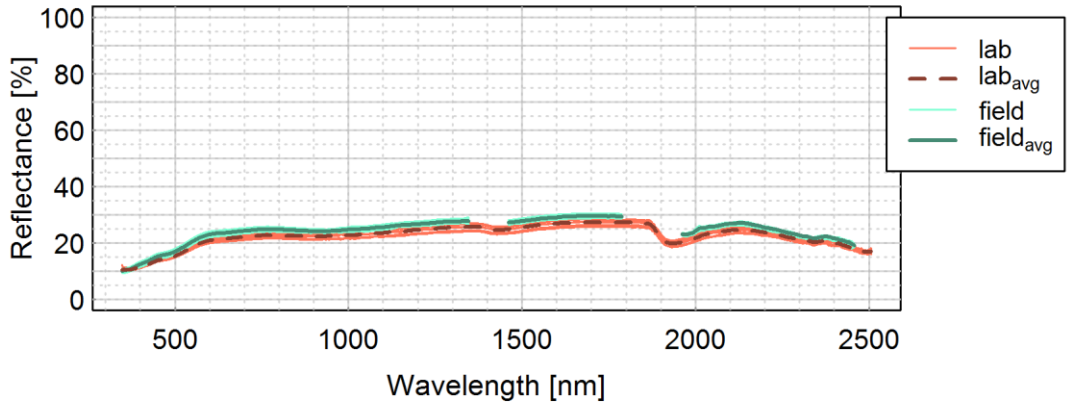

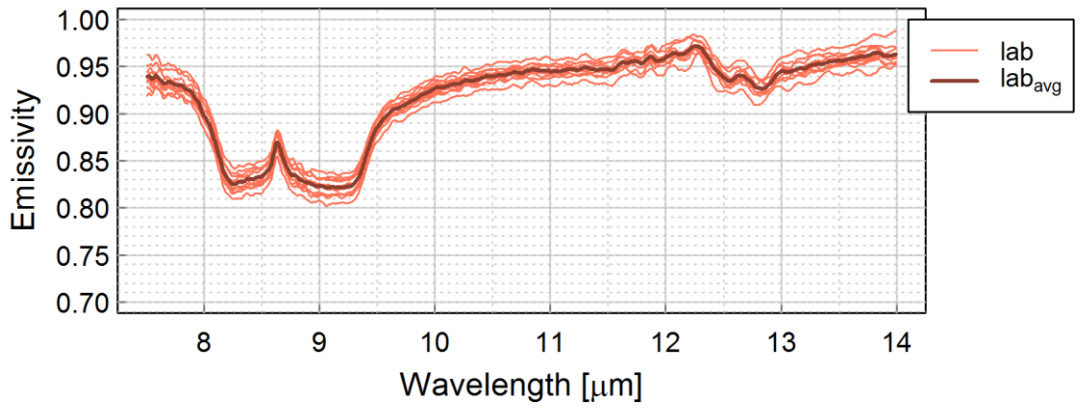

CONCRETE/CEMENT C003

Class	Cement
Material	Cement
Colour	Grey
Status	Weathered
Dimension [mm]	268 x 44 x 148

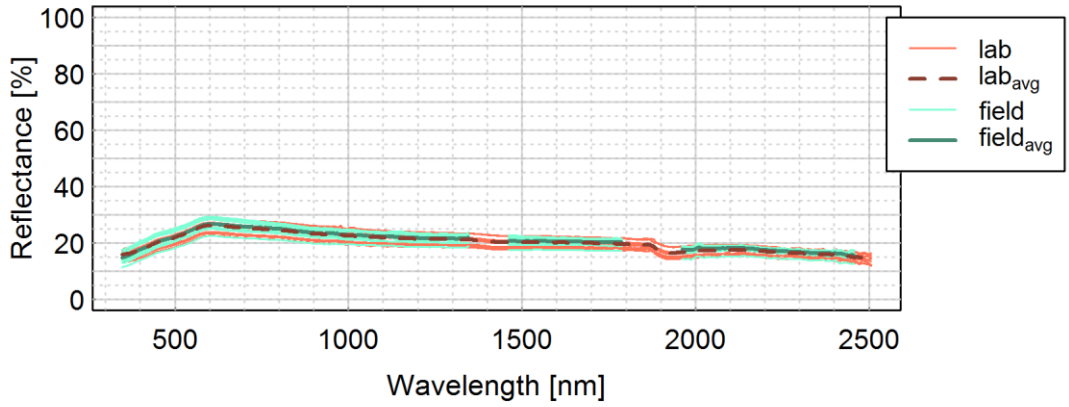

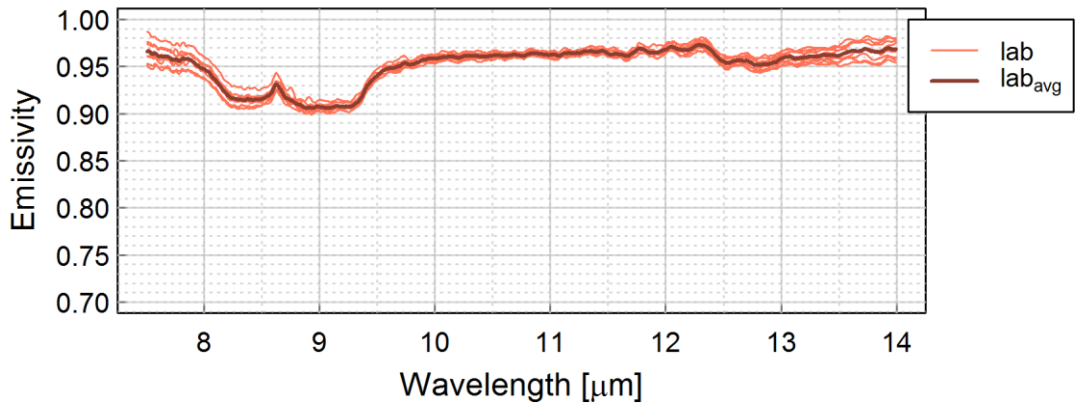

CONCRETE/CEMENT C004

Class	Concrete
Material	Concrete with small stone aggregate
Colour	Grey
Status	Weathered
Dimension [mm]	110 x 72 x 85

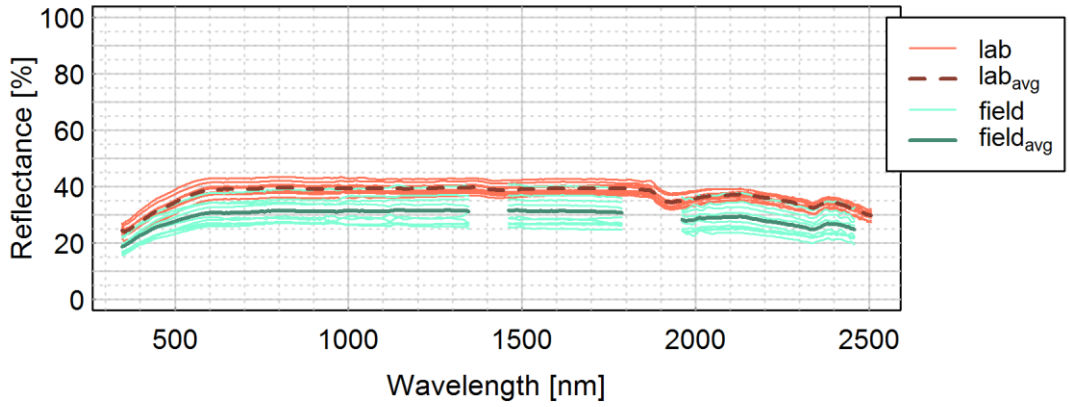

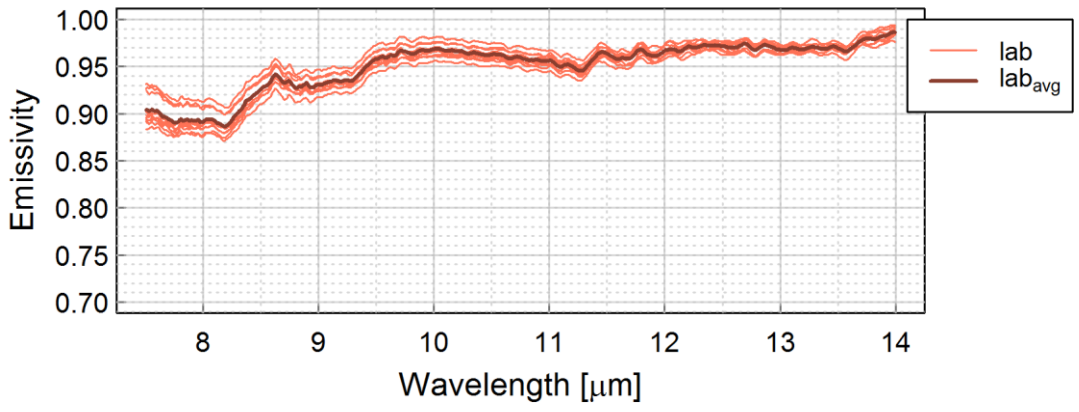

CONCRETE/CEMENT C005

Class	Cement
Material	Cement
Colour	Grey
Status	Weathered
Dimension [mm]	80 x 45 x 115

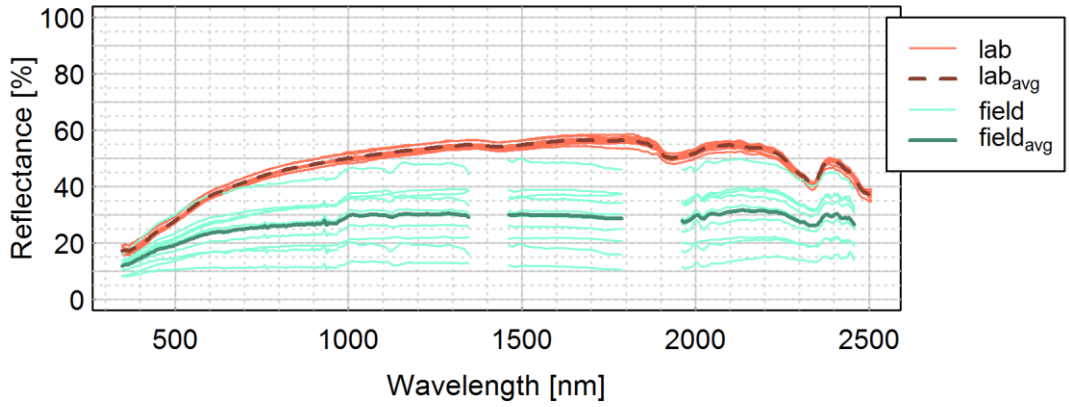

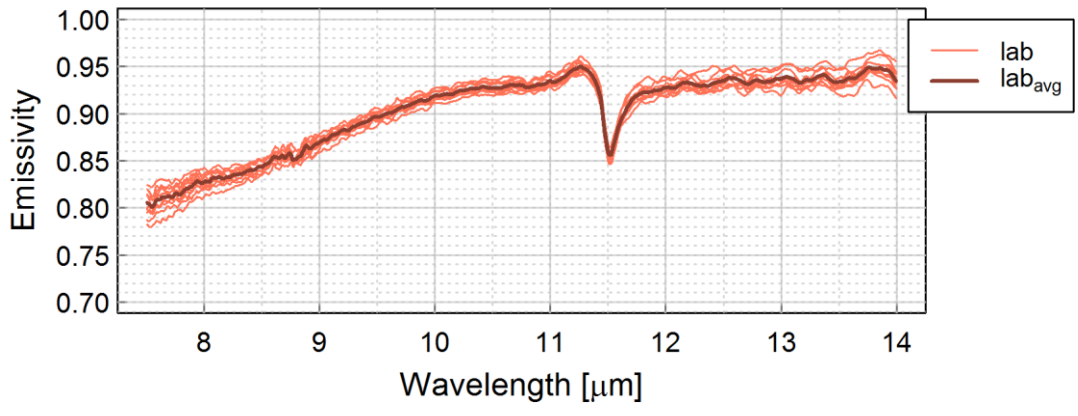

CONCRETE/CEMENT C006

Class	Concrete
Material	Concrete with small stone aggregate
Colour	White
Status	Weathered
Dimension [mm]	90 x 150 x 250

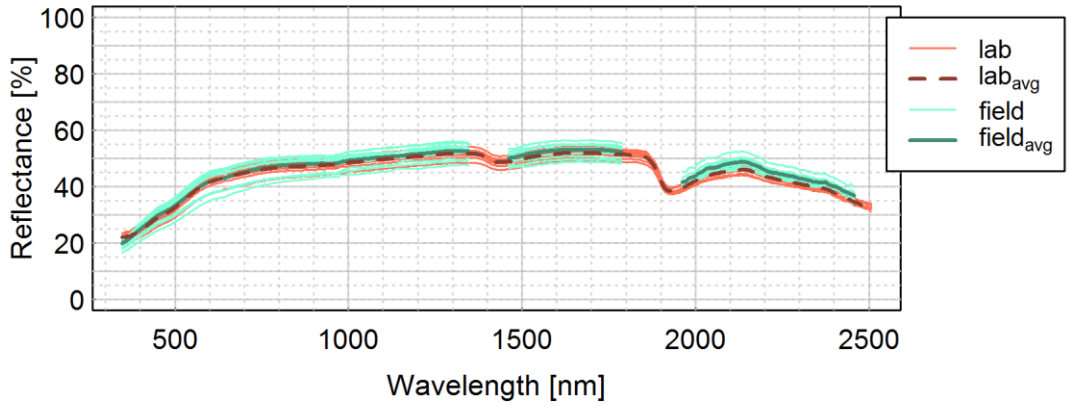

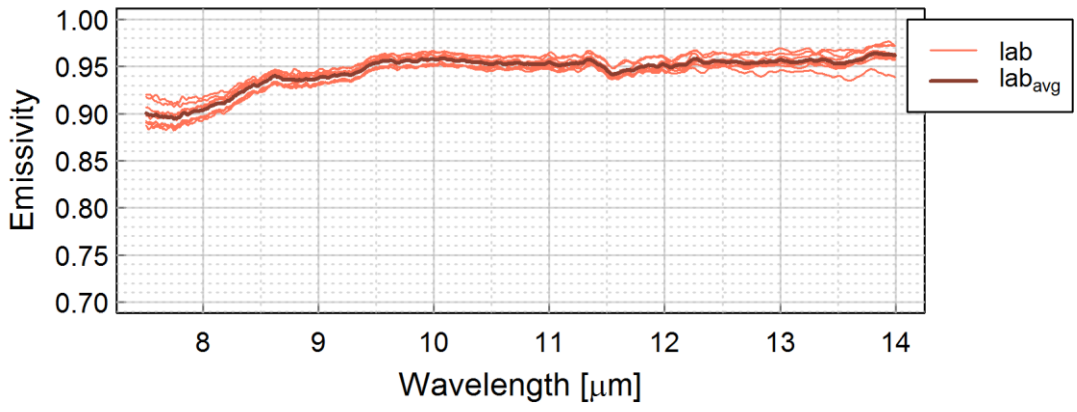

CONCRETE/CEMENT C008

Class	Concrete
Material	Concrete
Colour	Grey
Status	Weathered/rough
Dimension [mm]	120 x 20 x 108

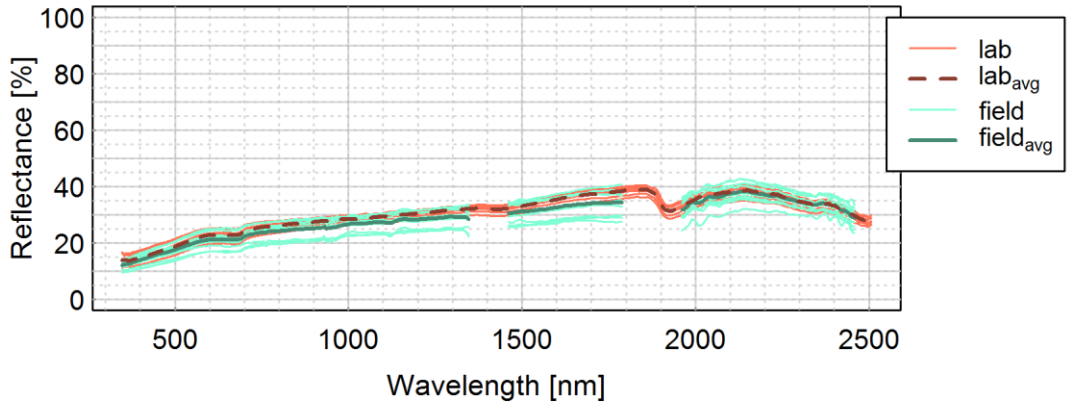

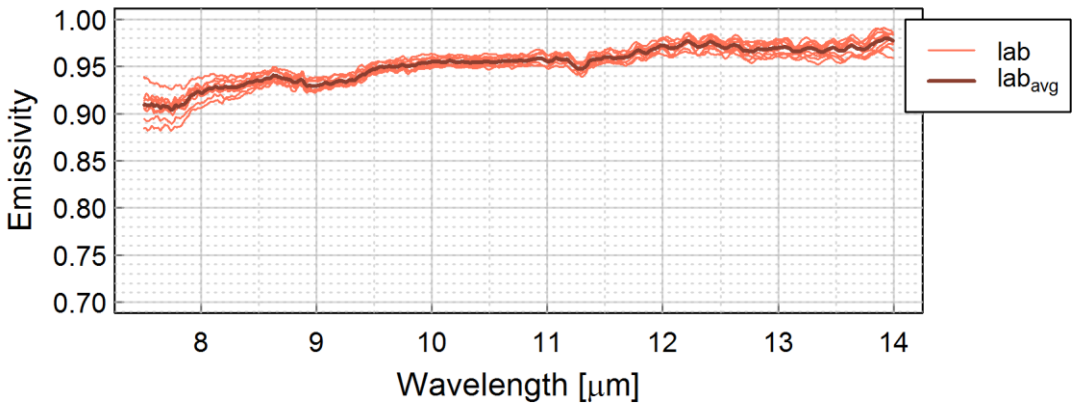

BRICK$_{B001}$

Class	Cement brick
Material	Cement
Colour	Yellow
Status	New
Dimension [mm]	200 x 60 x 100

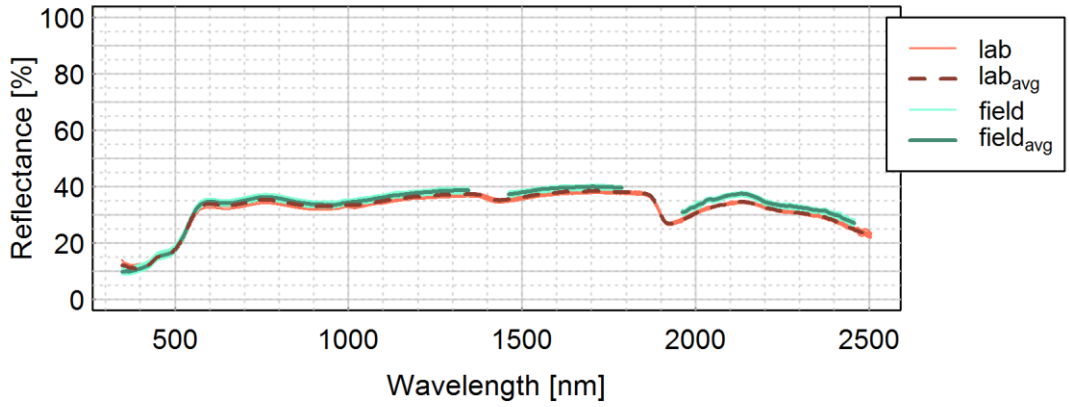

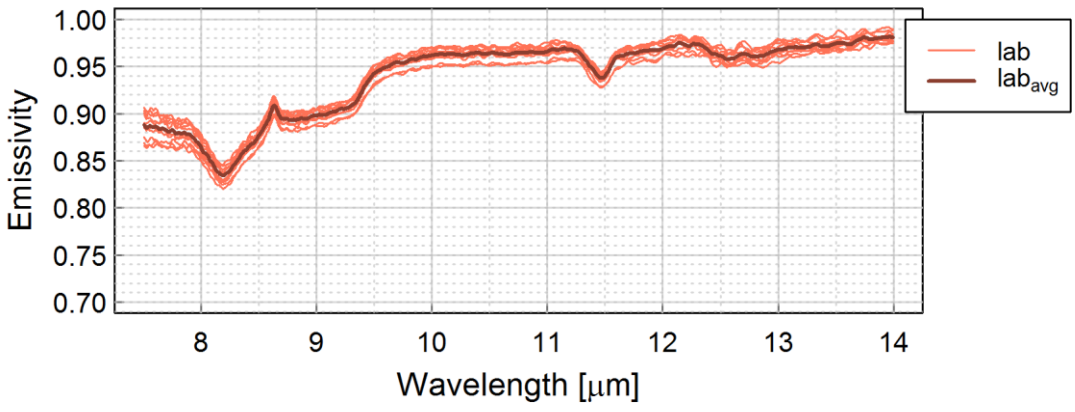

BRICK$_{B002}$

Class	Cement brick
Material	Cement
Colour	Black/light grey
Status	New, sandy
Dimension [mm]	200 x 58 x 98

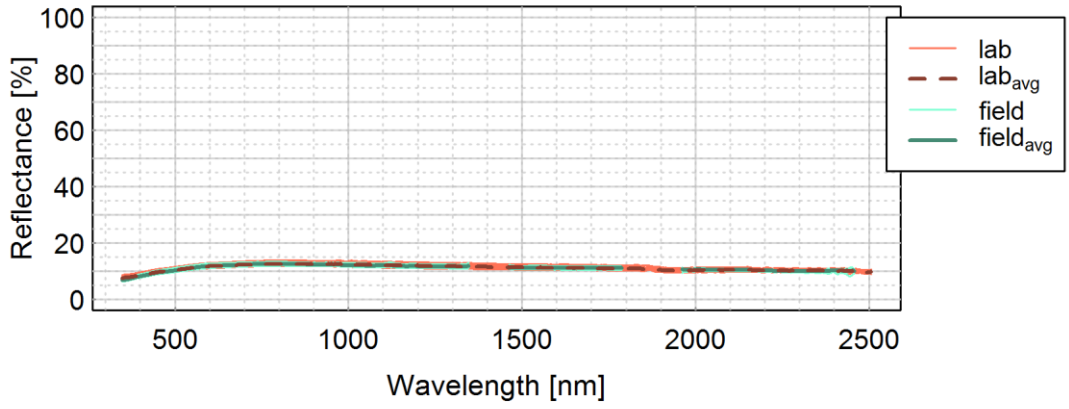

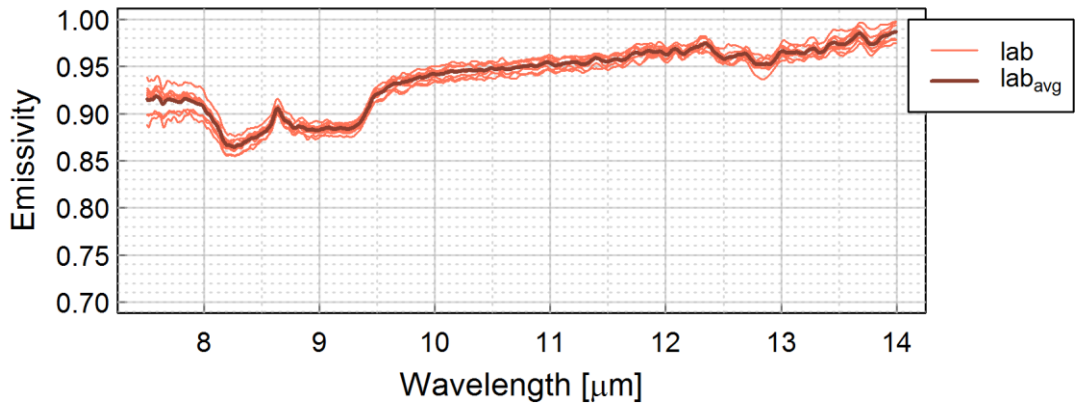

BRICK$_{B003}$

Class	Cement brick
Material	Cement
Colour	Black
Status	New
Dimension [mm]	195 x 52 x 98

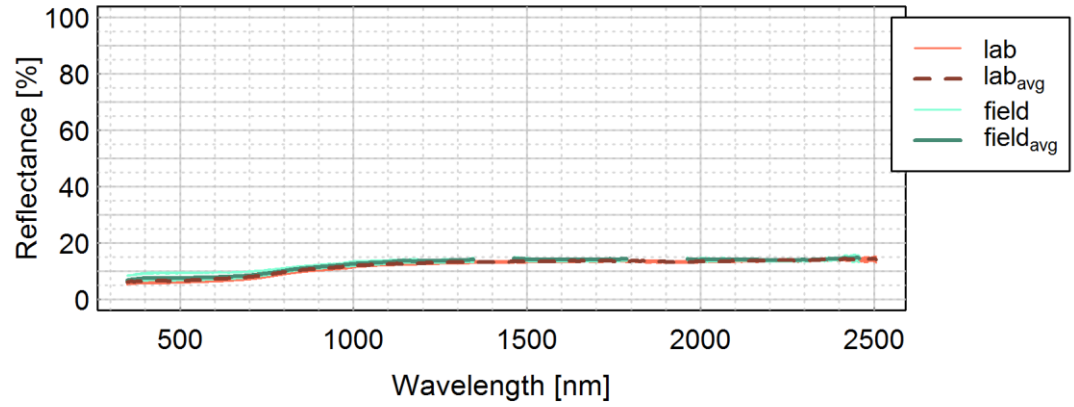

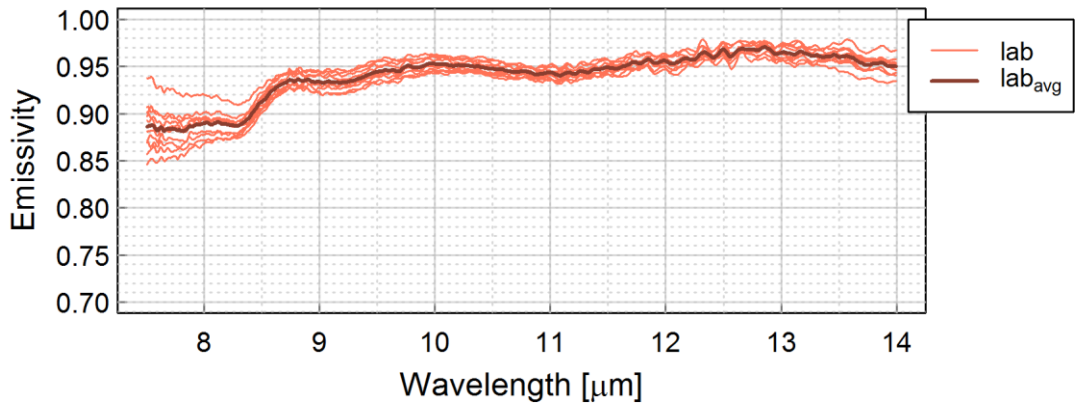

BRICK$_{B004}$

Class	Ceramic brick
Material	Ceramic with cement
Colour	Red
Status	Weathered
Dimension [mm]	62 x 35 x 52

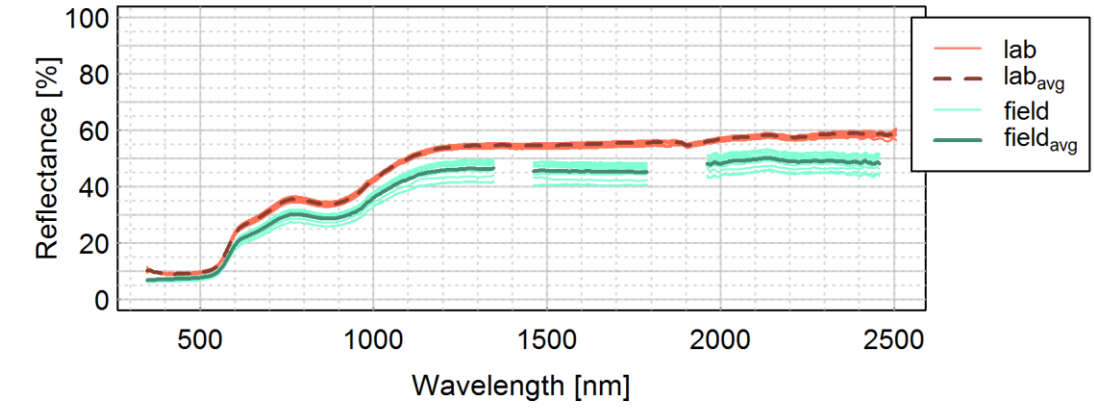

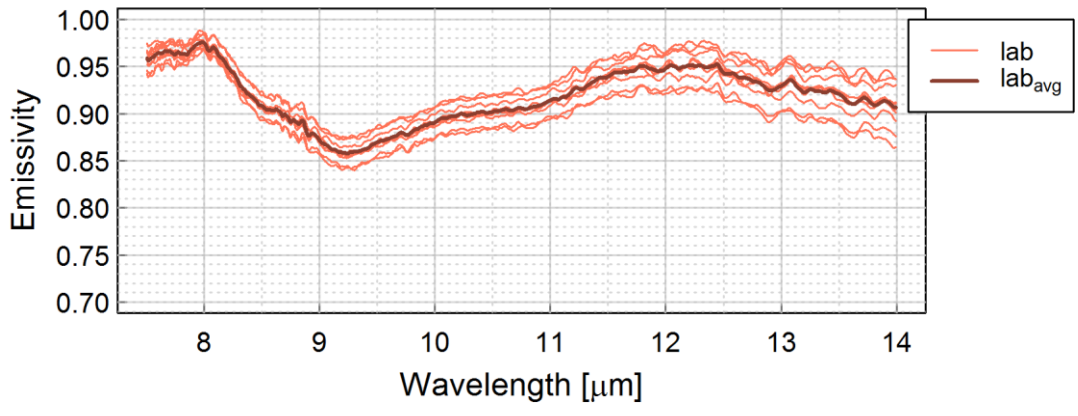

BRICK$_{B005}$

Class	Cement brick
Material	Cement
Colour	Red
Status	Weathered
Dimension [mm]	138 x 60 x 100

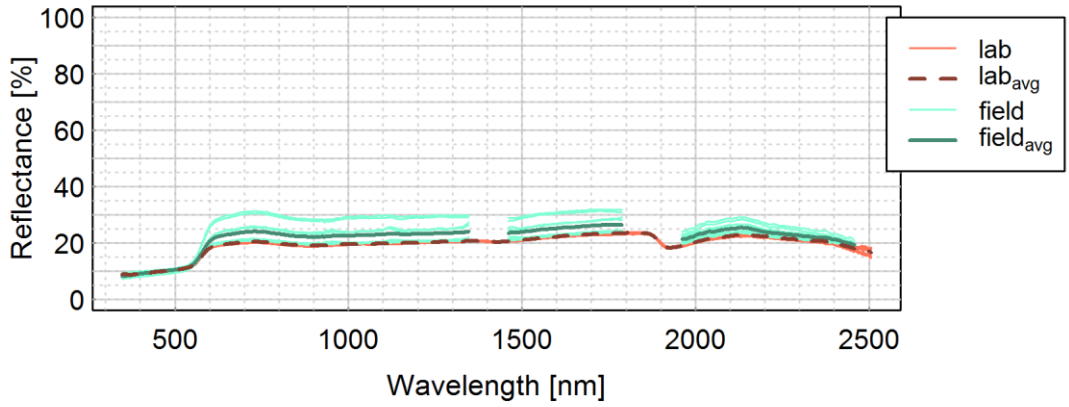

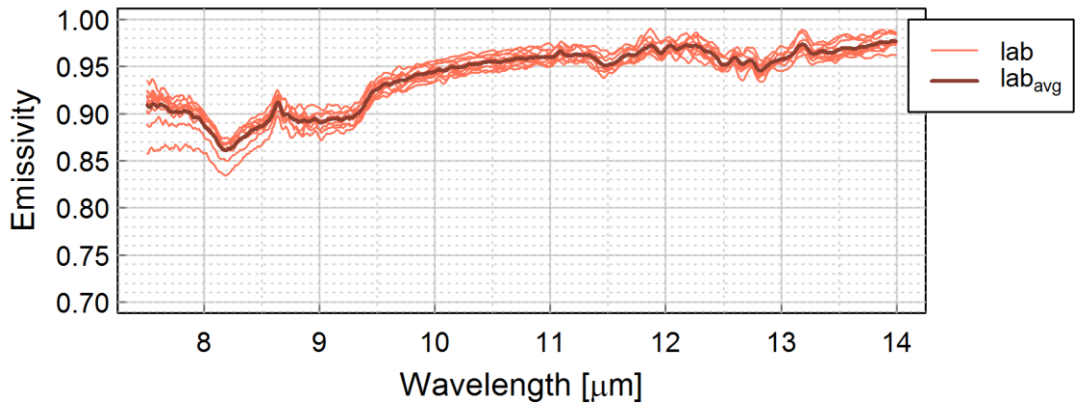

BRICK$_{B006}$

Class	Cement brick
Material	Cement
Colour	Black
Status	Sandy
Dimension [mm]	200 x 60 x 100

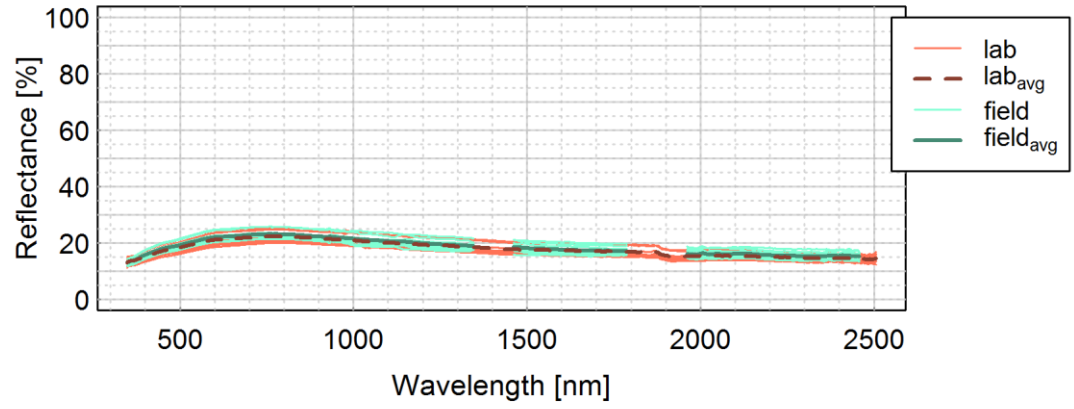

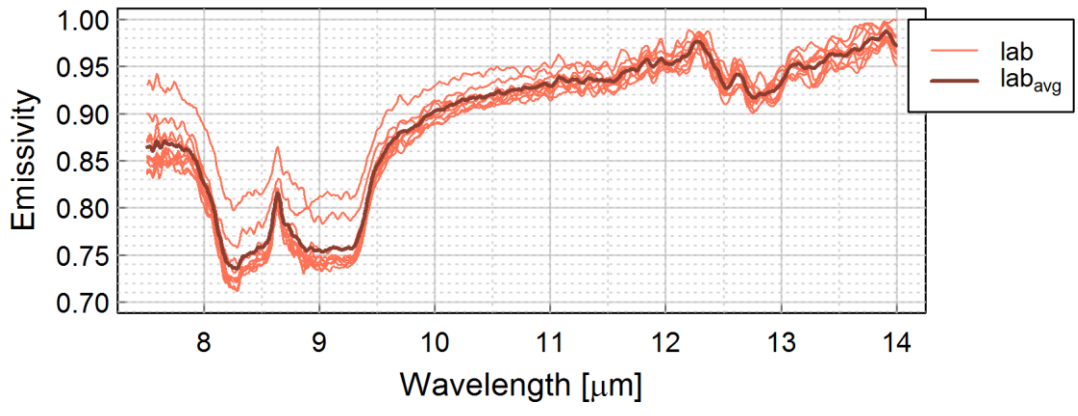

BRICK$_{B007}$

Class	Cement brick
Material	Cement
Colour	Light red
Status	New
Dimension [mm]	200 x 60 x 100

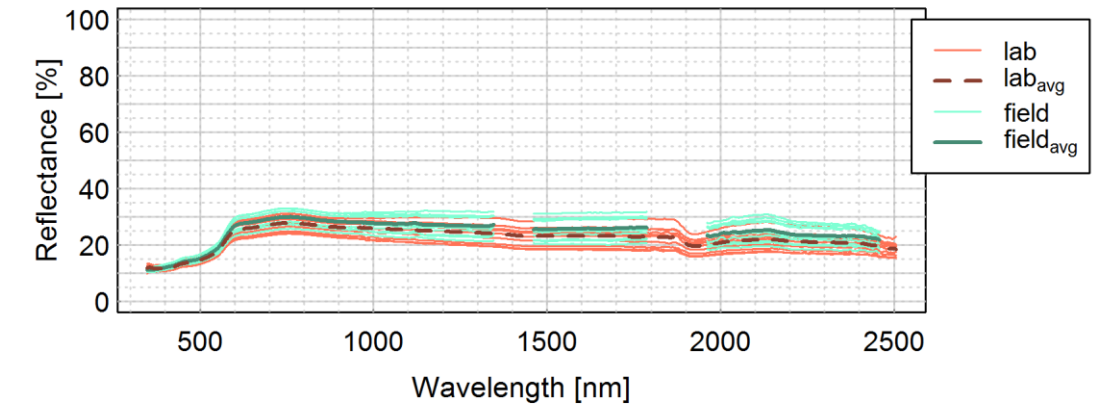

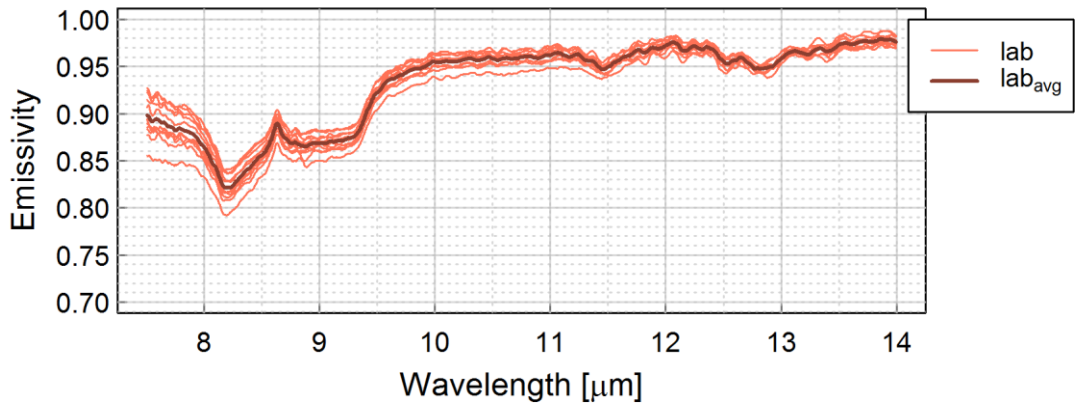

BRICK$_{B008}$

Class	Ceramic brick
Material	Ceramic
Colour	Light red
Status	New
Dimension [mm]	212 x 63 x 100

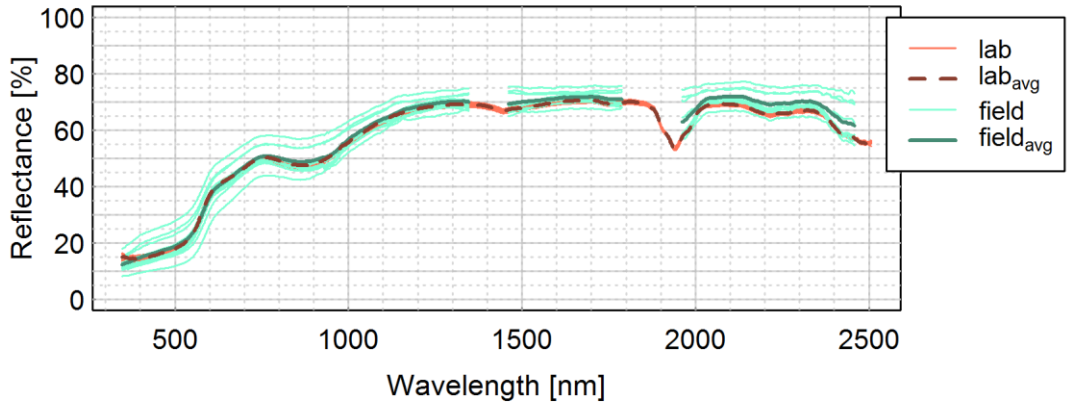

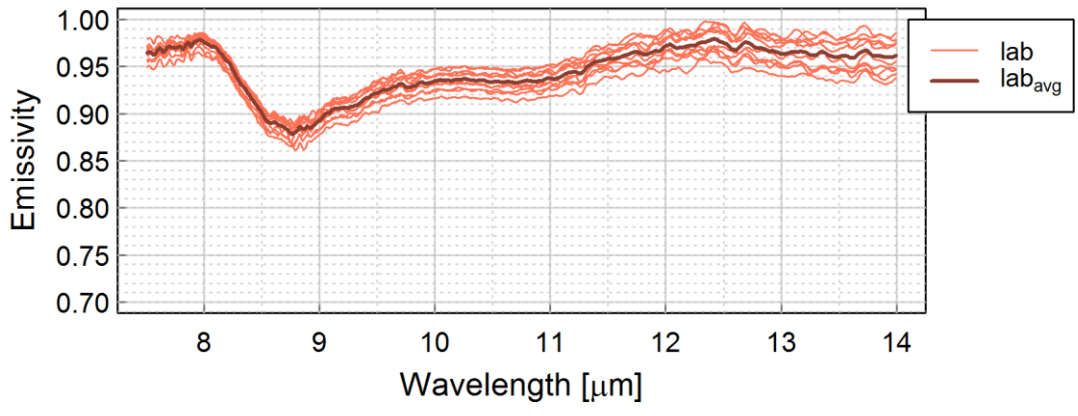

BRICK$_{B009}$

Class	Cement brick
Material	Cement
Colour	Red
Status	Weathered
Dimension [mm]	110 x 63 x 105

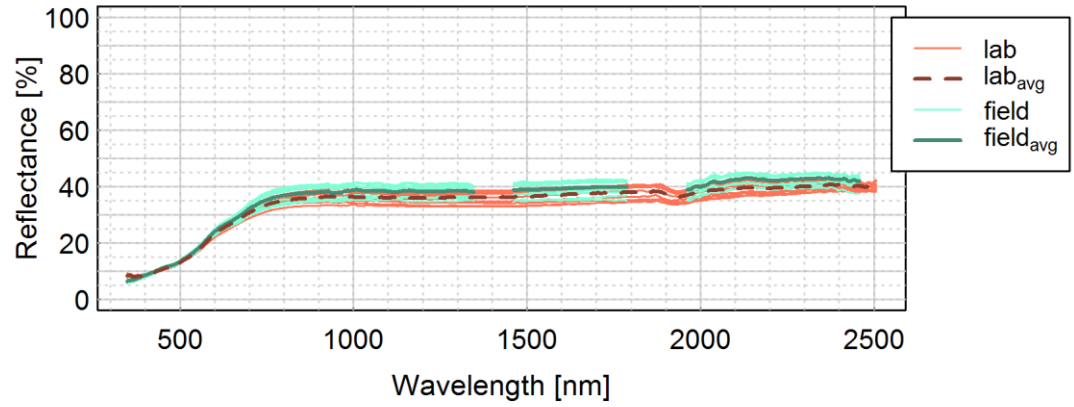

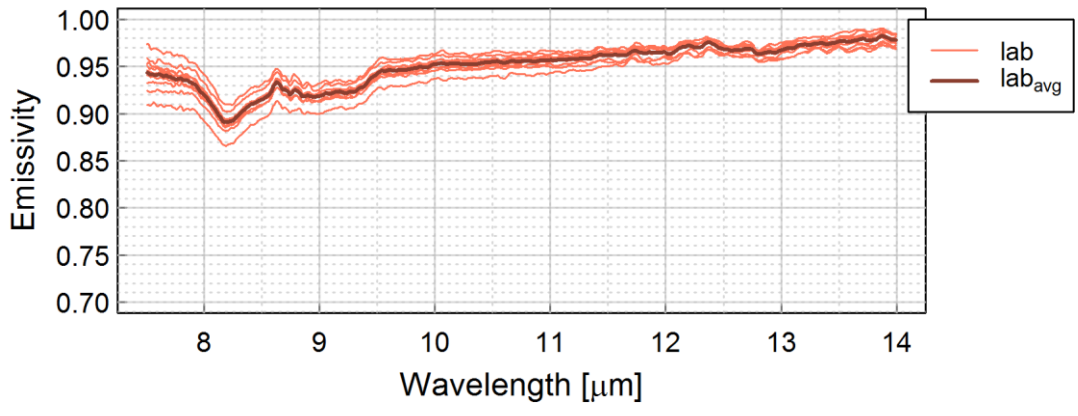

BRICK$_{B010}$

Class	Ceramic brick
Material	Ceramic with paint
Colour	Red with beige and grey paint
Status	Weathered
Dimension [mm]	110 x 80 x 100

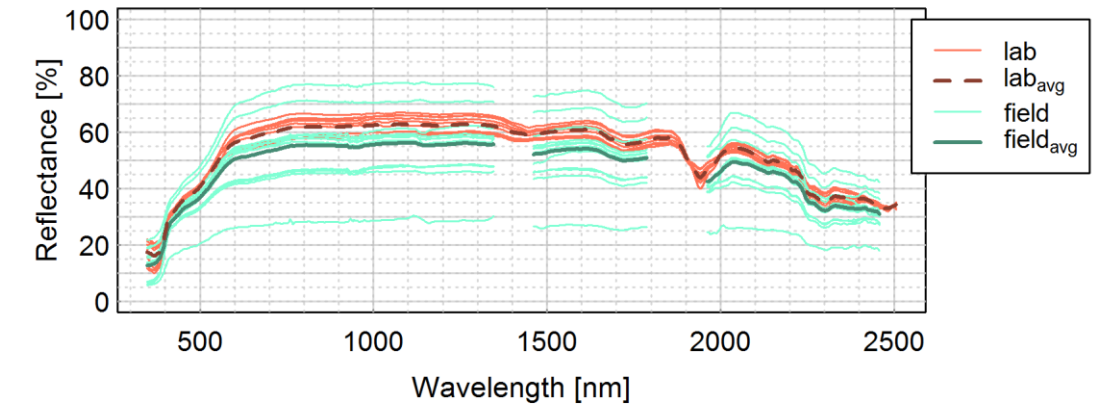

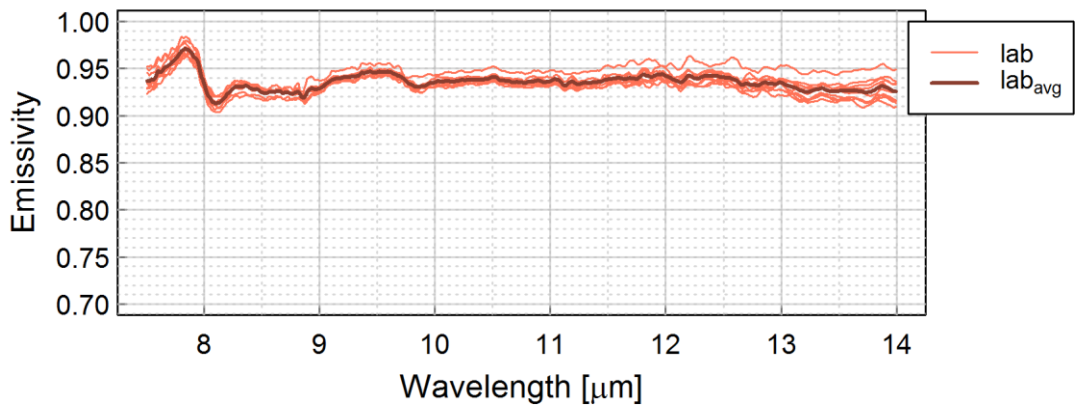

BRICK$_{B011}$

Class	Ceramic brick
Material	Ceramic brick with cement
Colour	Red/grey
Status	Weathered
Dimension [mm]	230 x 63 x 100

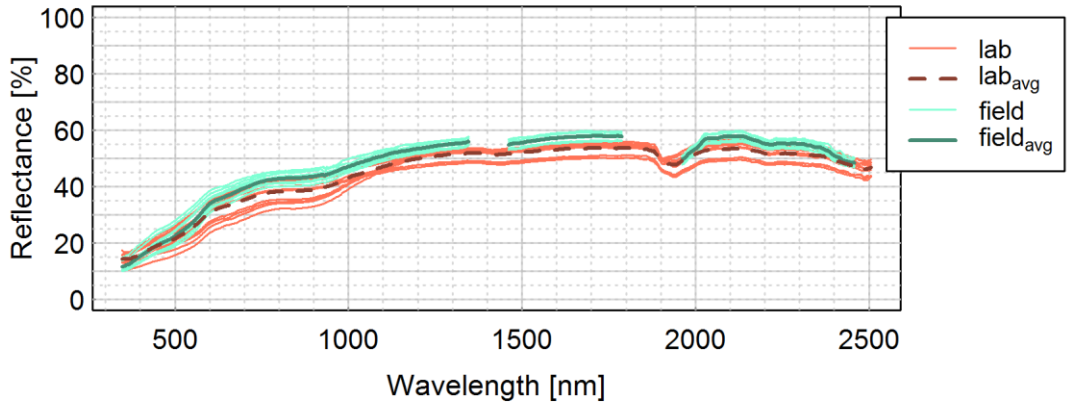

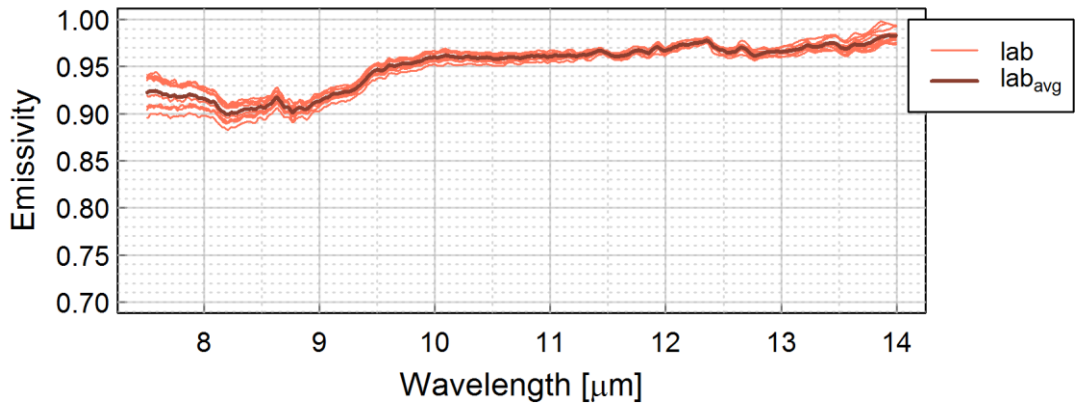

BRICK$_{B012}$

Class	Ceramic brick
Material	Ceramic brick with paint
Colour	Red with white paint
Status	Weathered
Dimension [mm]	112 x 70 x 107

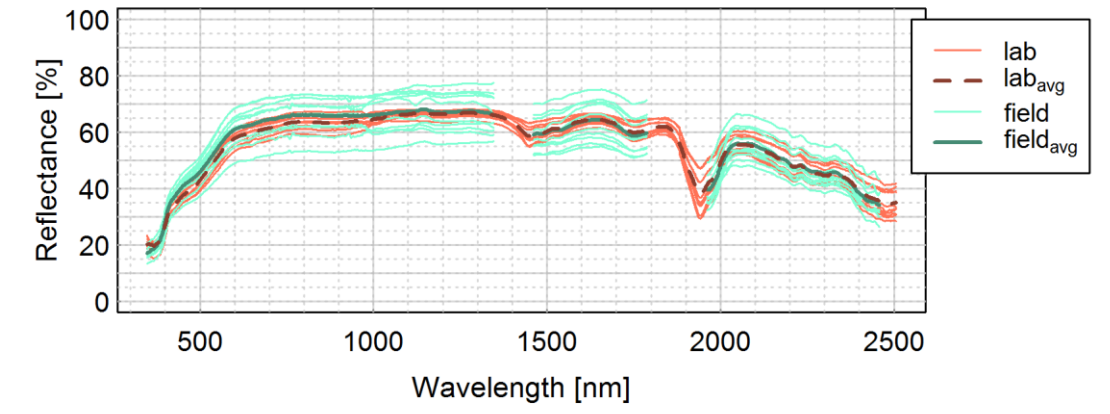

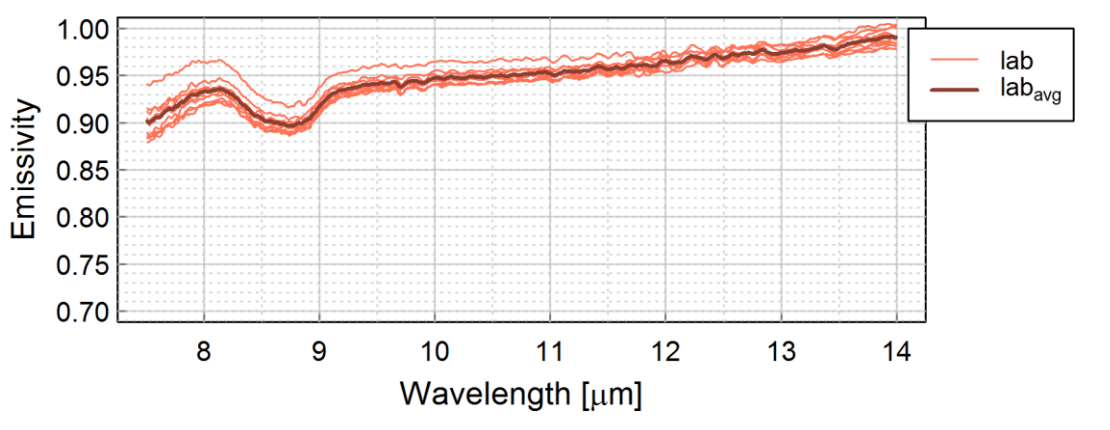

BRICK$_{B013}$

Class	Ceramic brick
Material	Ceramic brick
Colour	Red
Status	Weathered
Dimension [mm]	46 x 60 x 100

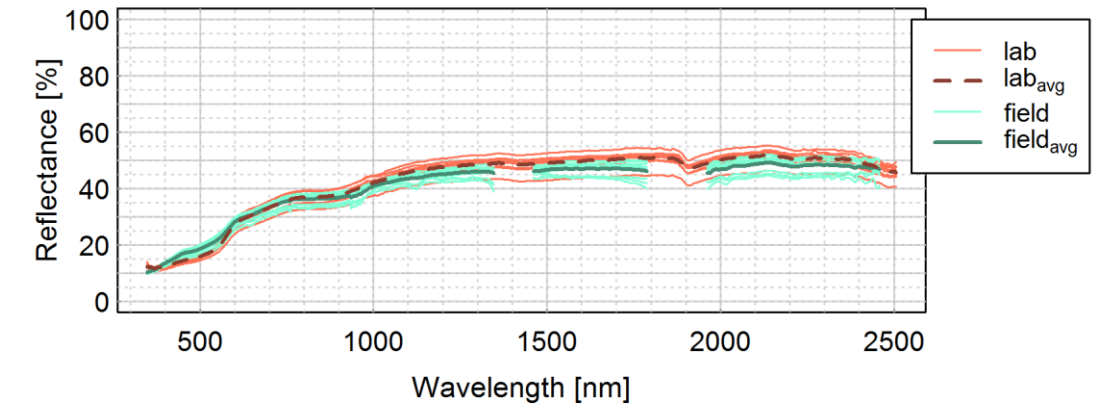

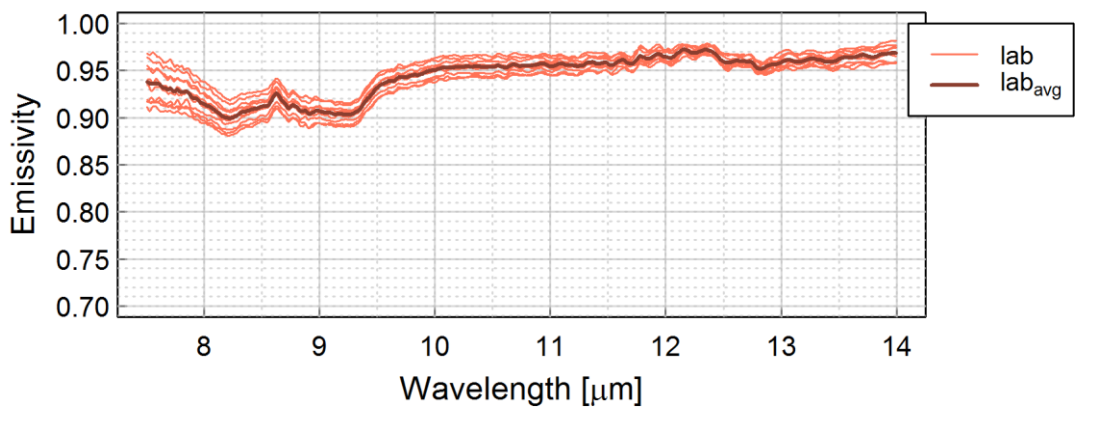

BRICK$_{B014}$

Class	Ceramic brick
Material	Ceramic brick
Colour	Yellow/grey
Status	Weathered
Dimension [mm]	130 x 68 x 90

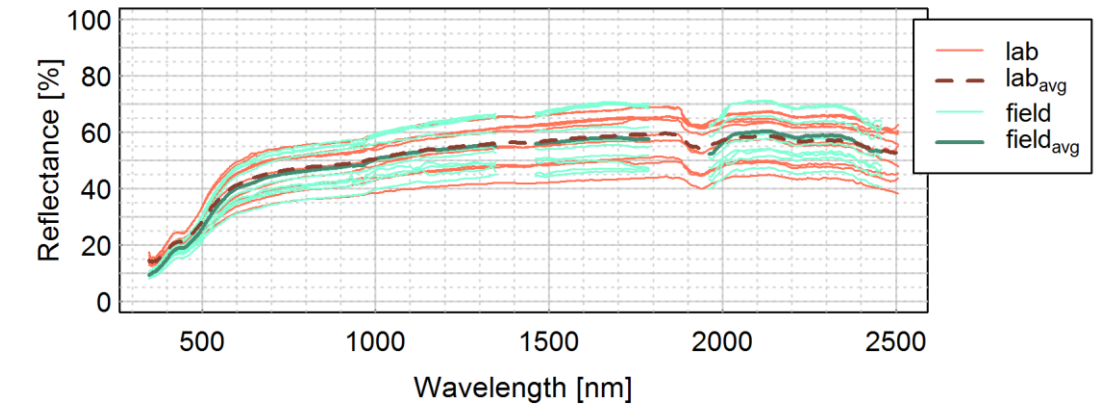

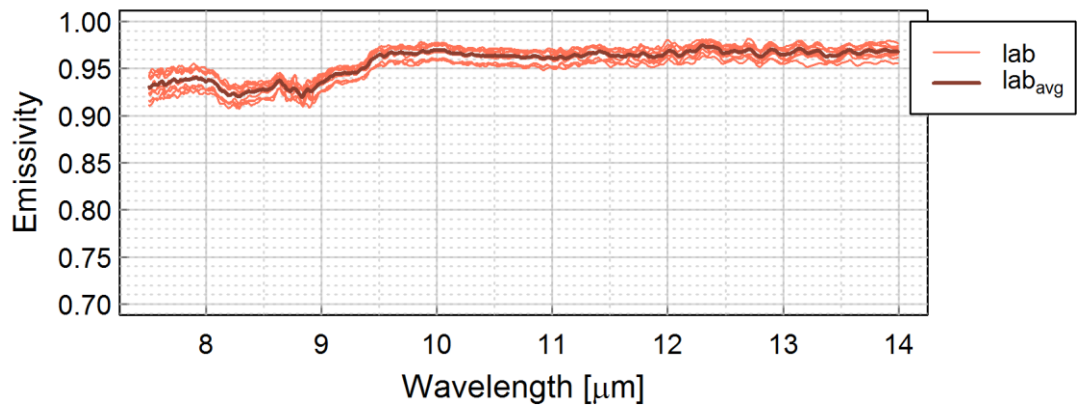

ROOFING SHINGLE$_{L001u}$

Class	Roofing shingle
Material	Slate roofing shingle
Colour	Grey
Status	Weathered
Dimension [mm]	255 x 3 x 210

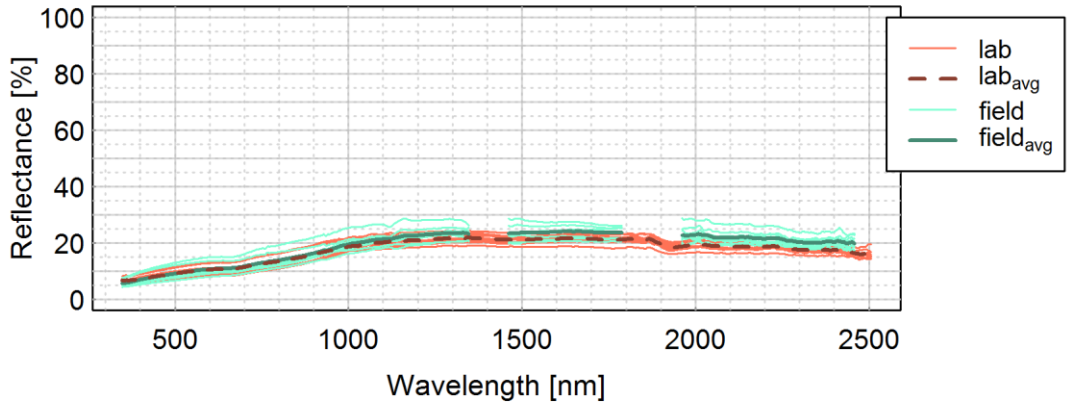

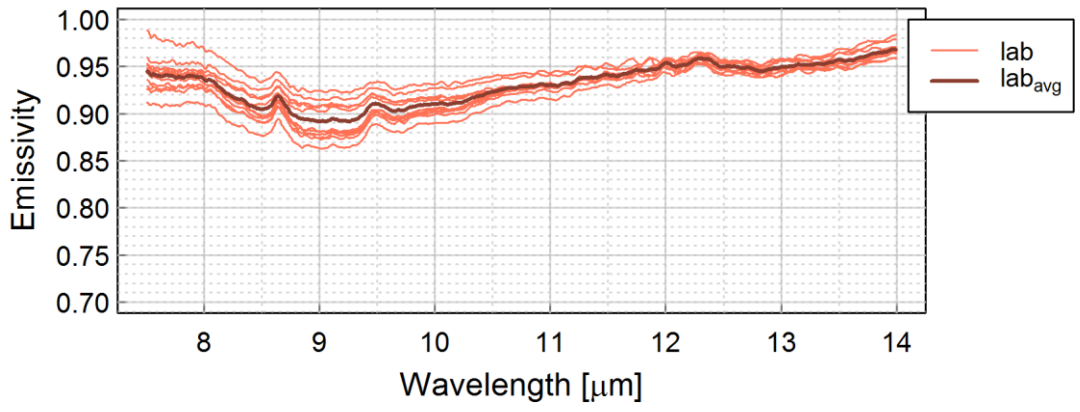

ROOFING SHINGLE$_{L001d}$

Class	Roofing shingle
Material	Slate
Colour	Grey
Status	Clear
Dimension [mm]	255 x 3 x 210

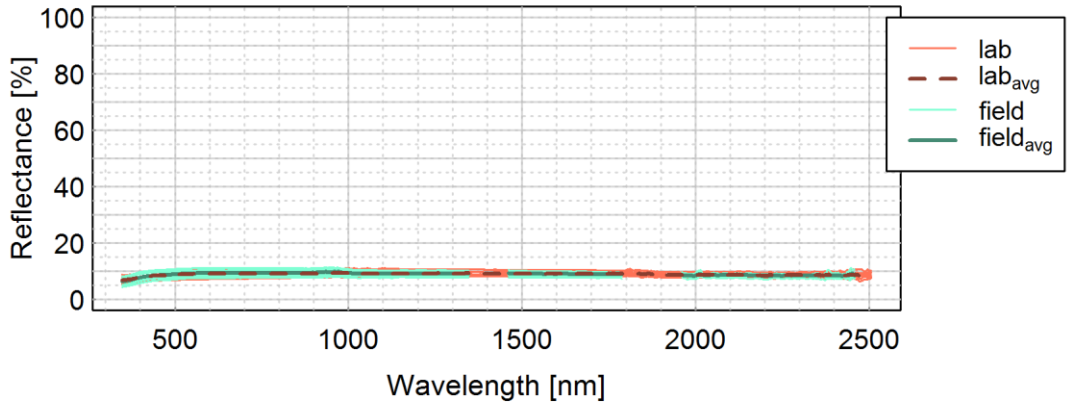

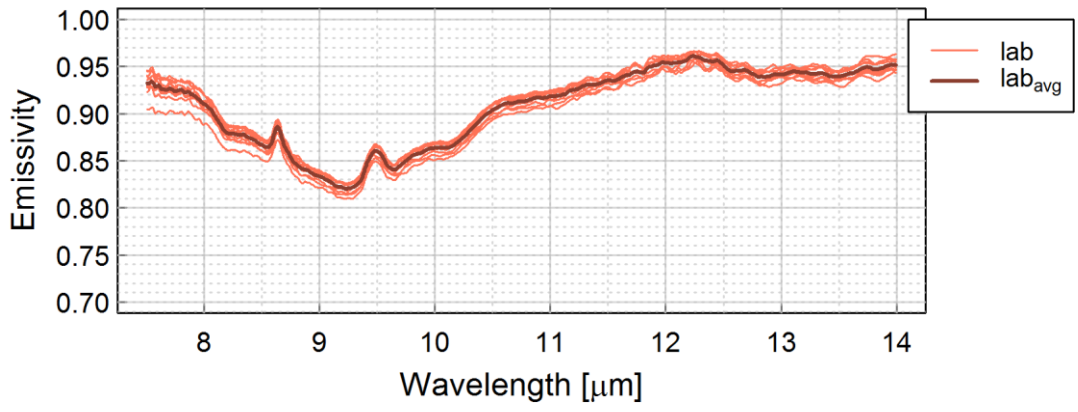

ROOFING SHINGLE$_{L002}$

Class	Roofing shingle
Material	Fibre cement
Colour	Black
Status	Weathered
Dimension [mm]	232 x 3 x 241

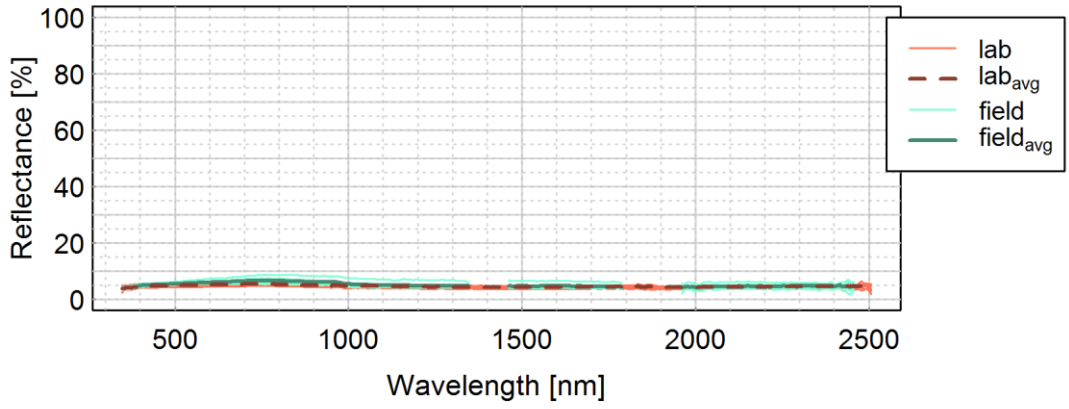

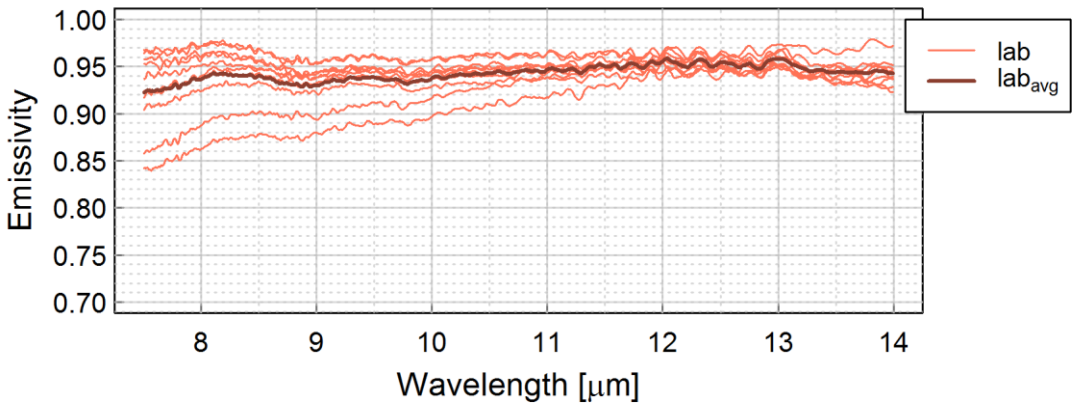

ROOFING SHINGLE$_{L003}$

Class	Roofing shingle
Material	Fibre cement
Colour	Black
Status	Weathered
Dimension [mm]	230 x 3 x 207

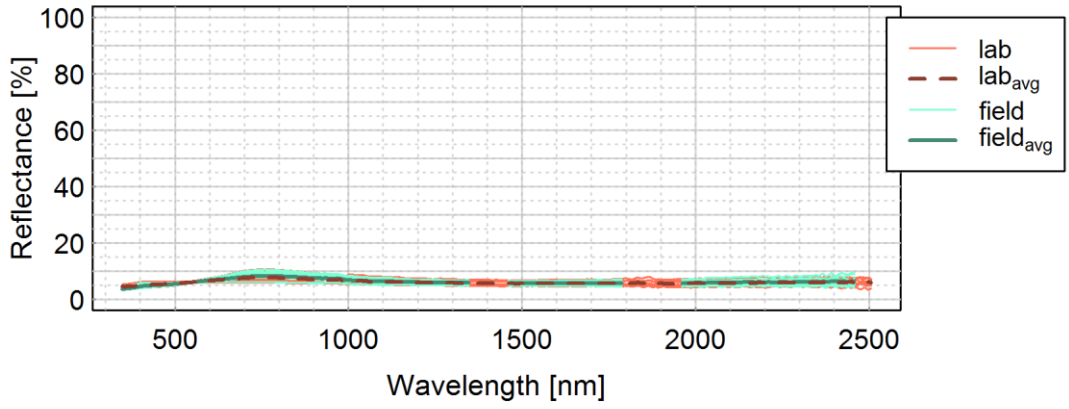

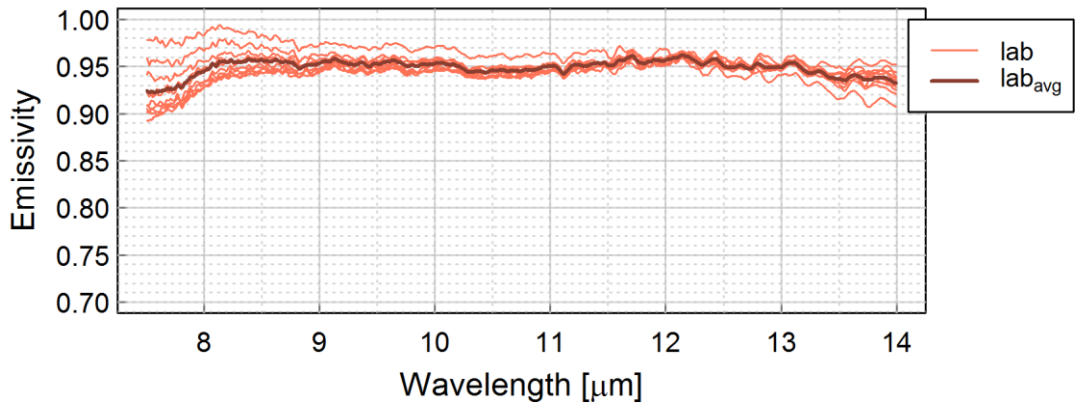

ROOFING TILE R001

Class	Roofing tile
Material	Ceramic
Colour	Black
Status	New
Dimension [mm]	150 x 11 x 150

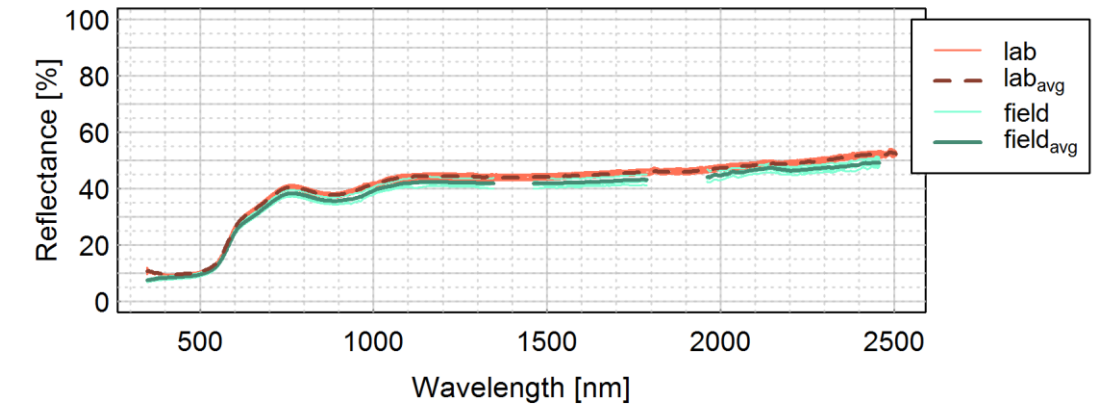

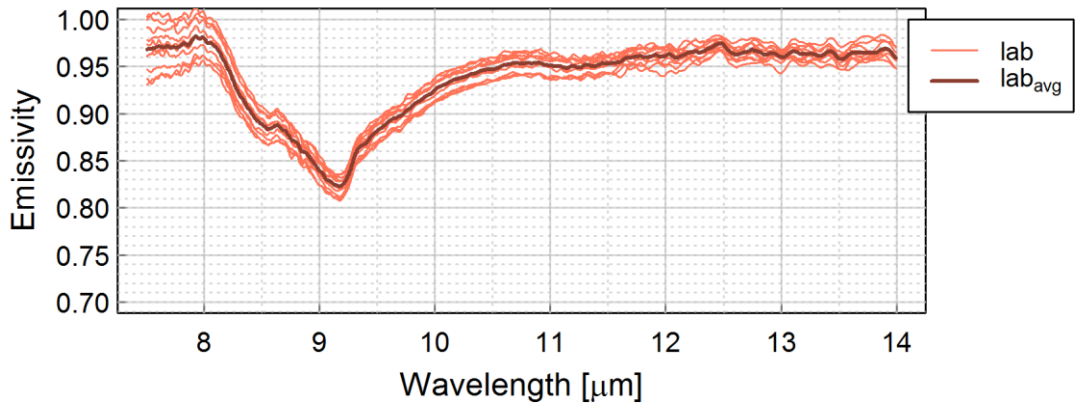

ROOFING TILE$_{R002}$

Class	Roofing tile
Material	Ceramic
Colour	Brown
Status	New
Dimension [mm]	300 x 10 x 200

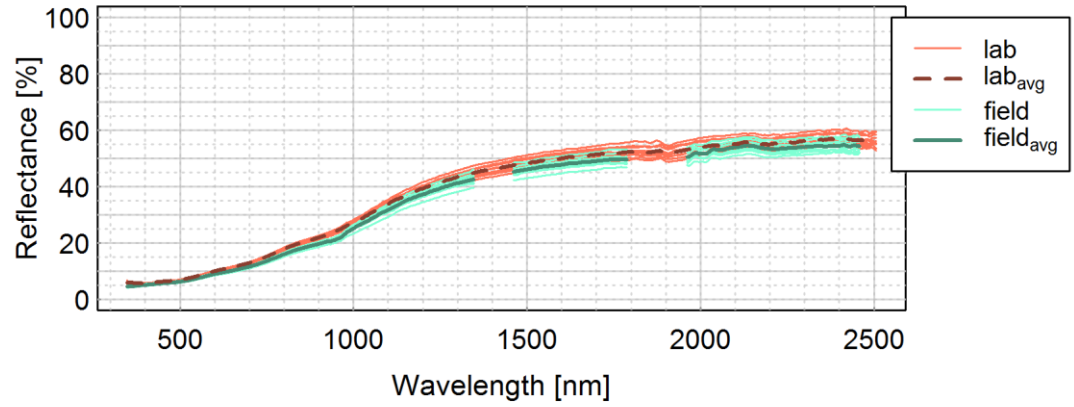

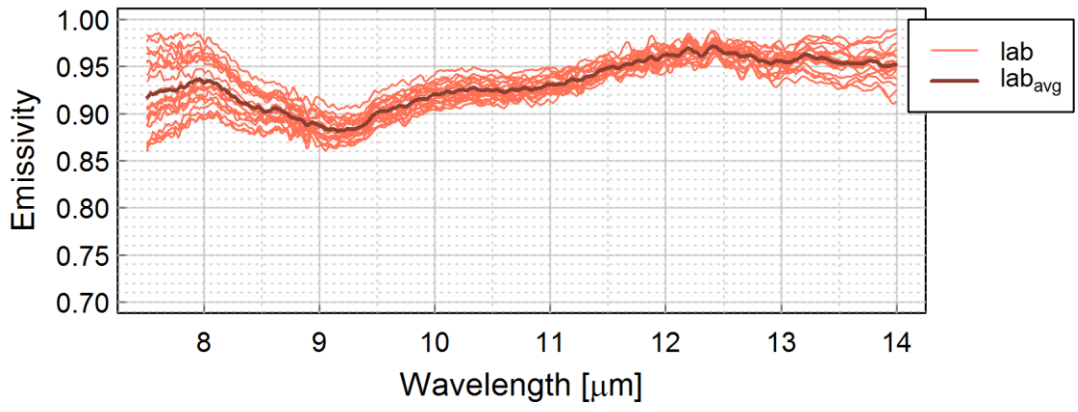

ROOFING TILE$_{R003}$

Class	Roofing tile
Material	Cement
Colour	Rustic red
Status	New
Dimension [mm]	270 x 12 x 170

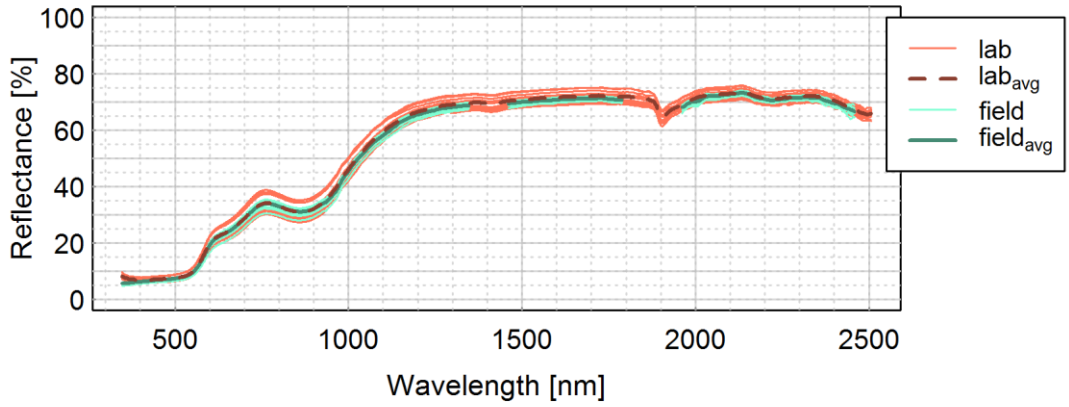

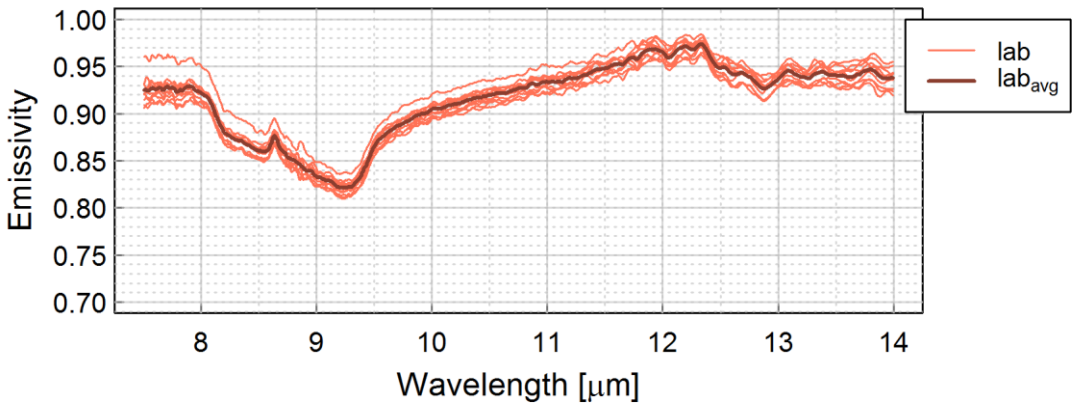

ROOFING TILE$_{R004}$

Class	Roofing tile
Material	Ceramic
Colour	Burnt red
Status	New
Dimension [mm]	300 x 13 x 200

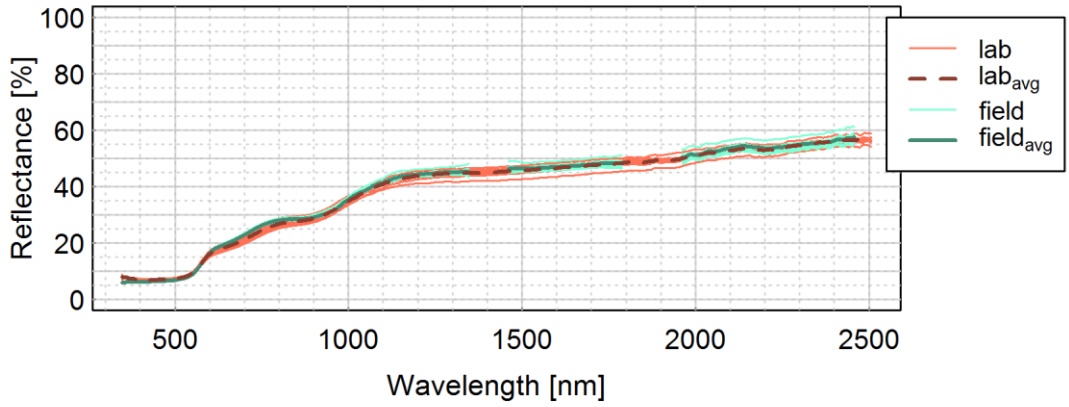

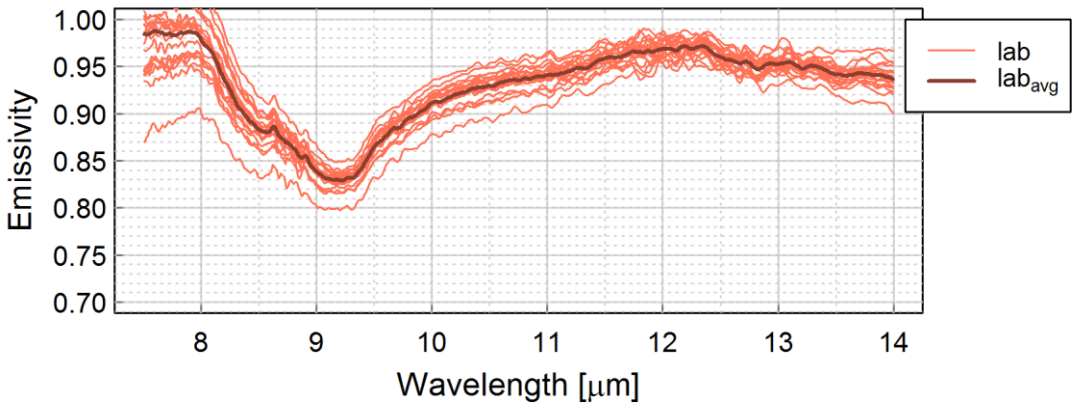

ROOFING TILE$_{R005}$

Class	Roofing tile
Material	Cement
Colour	Rustic red/black shading
Status	New/shiny
Dimension [mm]	260 x 12 x 165

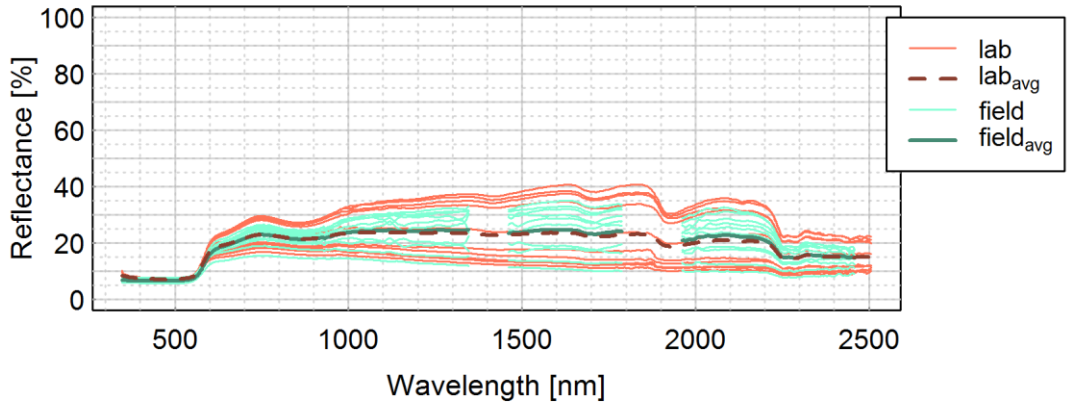

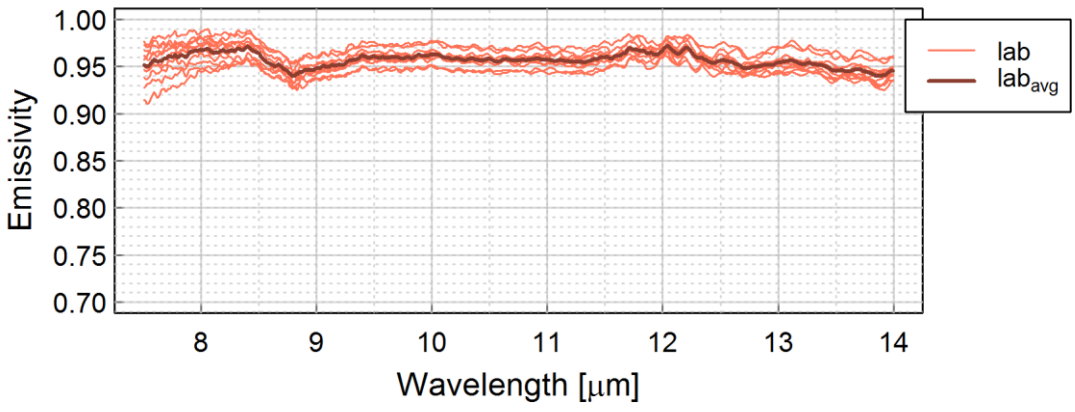

ROOFING TILE R006

Class	Roofing tile
Material	Cement
Colour	Slate grey
Status	New
Dimension [mm]	265 x 11 x 165

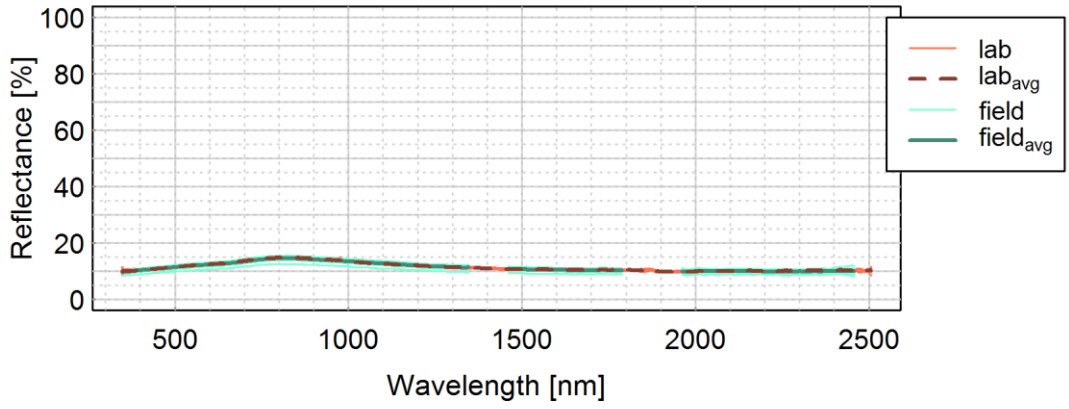

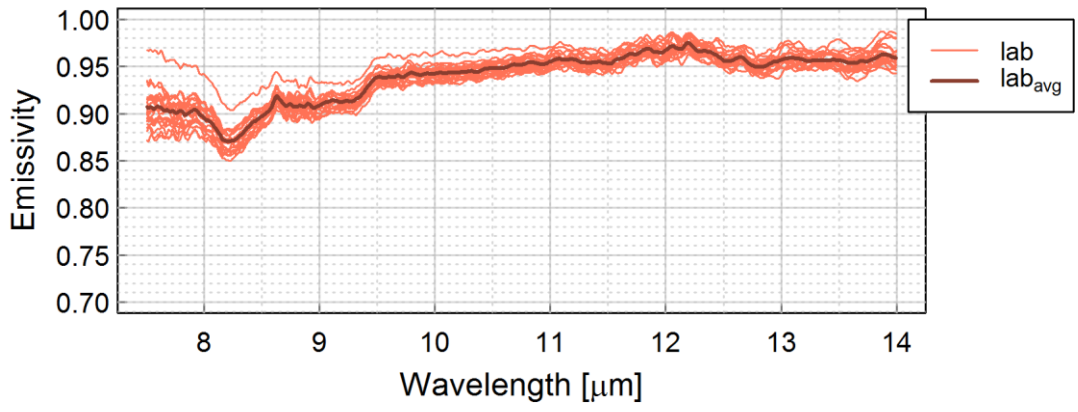

ROOFING TILE$_{R007}$

Class	Roofing tile
Material	Ceramic
Colour	Black
Status	New
Dimension [mm]	410 x 15 x 320

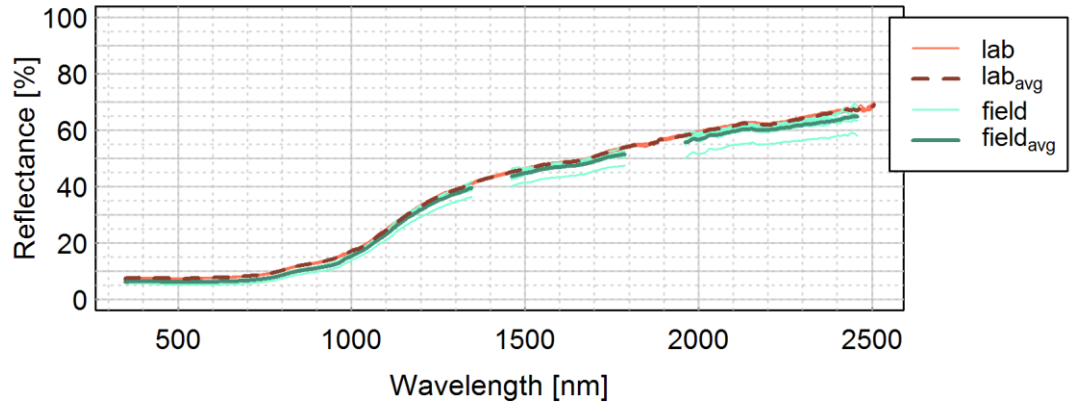

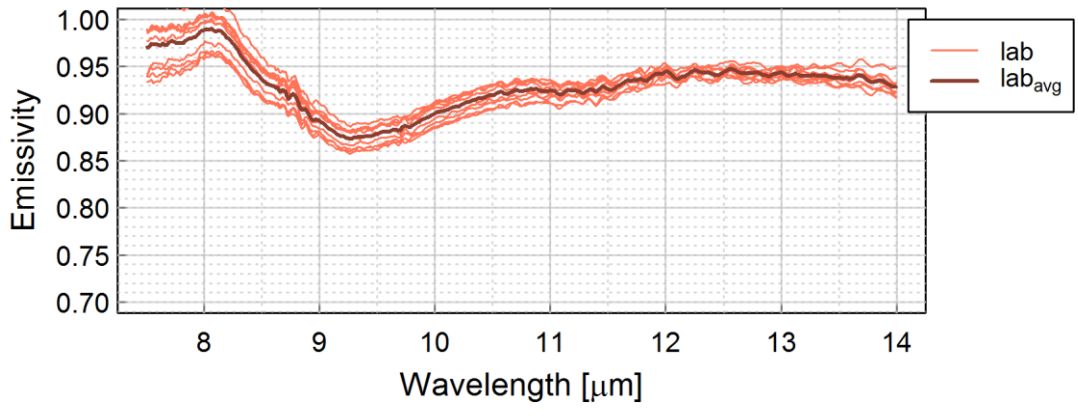

ROOFING TILE$_{R008}$

Class	Roofing tile
Material	Cement
Colour	Rustic red
Status	New
Dimension [mm]	260 x 12 x 165

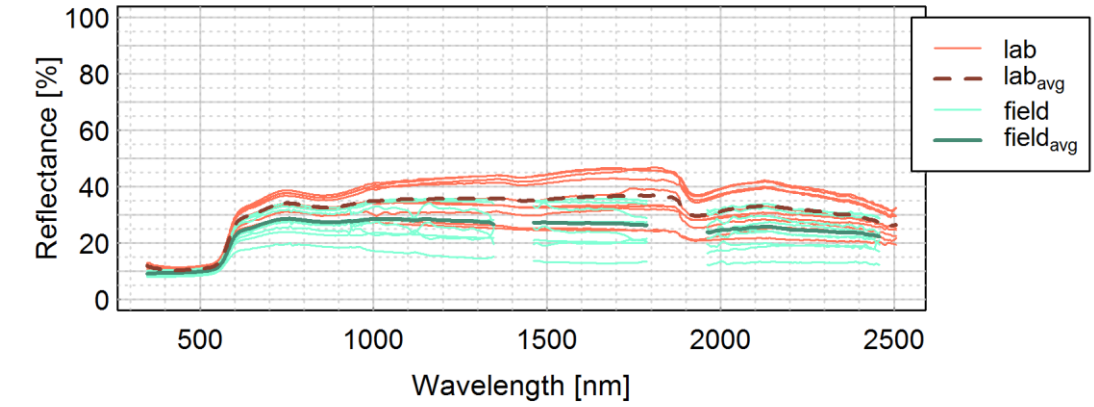

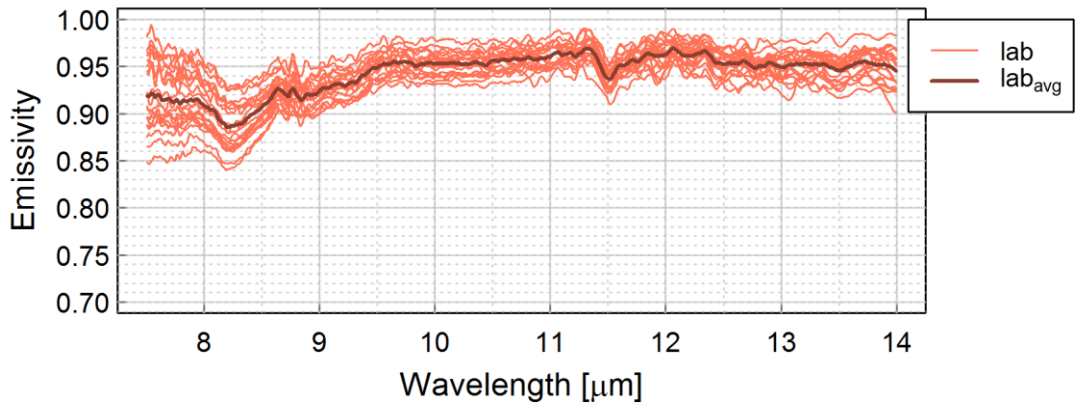

ROOFING TILE$_{R009}$

Class	Roofing tile
Material	Cement
Colour	Autumn red
Status	New/rough
Dimension [mm]	260 x 12 x 165

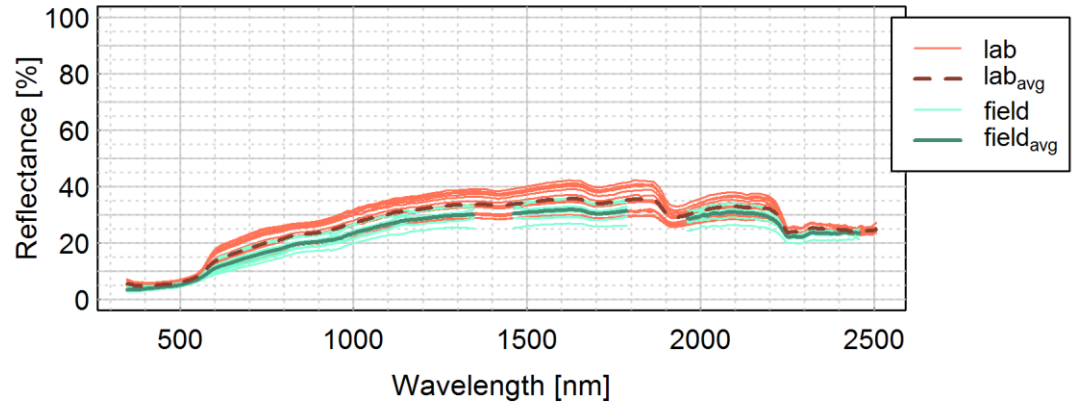

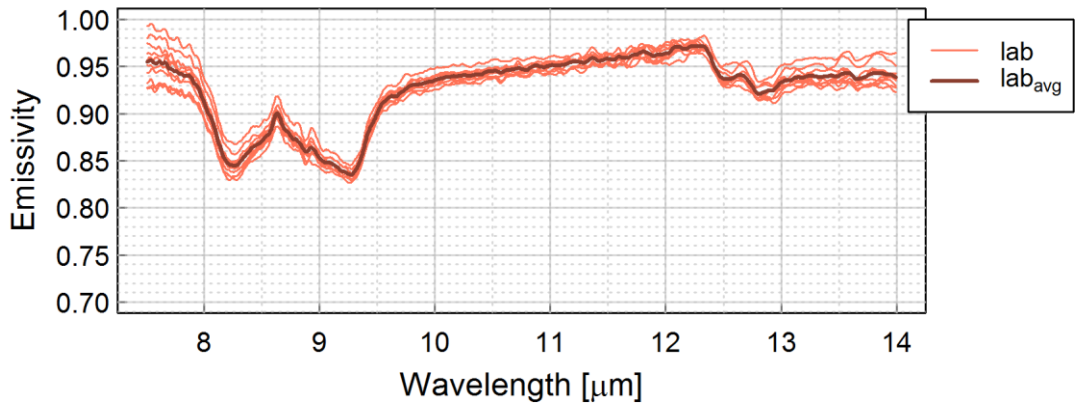

ROOFING TILE R010

Class	Roofing tile
Material	Ceramic
Colour	Red
Status	Weathered
Dimension [mm]	130 x 10 x 165

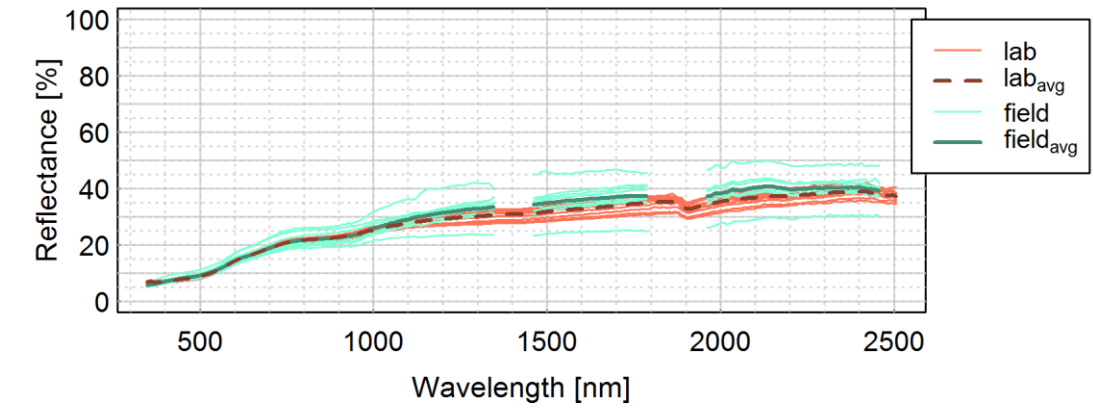

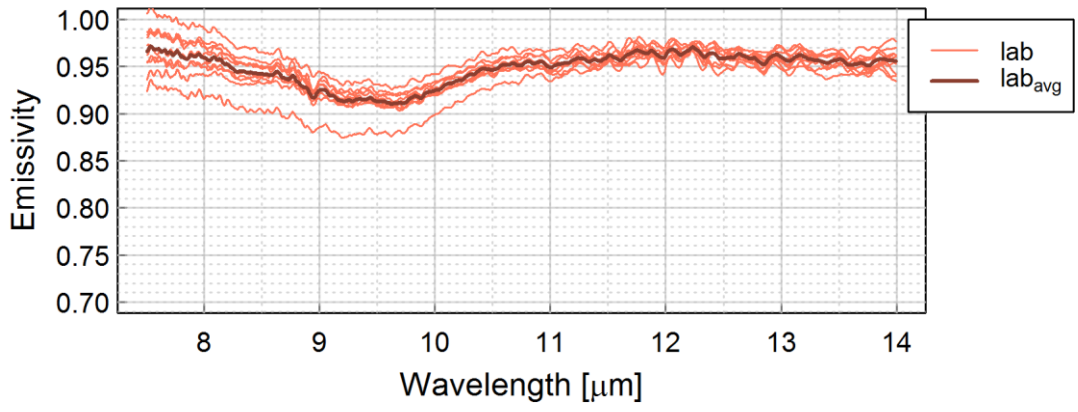

ROOFING TILE R012

Class	Roofing tile
Material	Ceramic
Colour	Red
Status	Weathered
Dimension [mm]	90 x 12 x 195

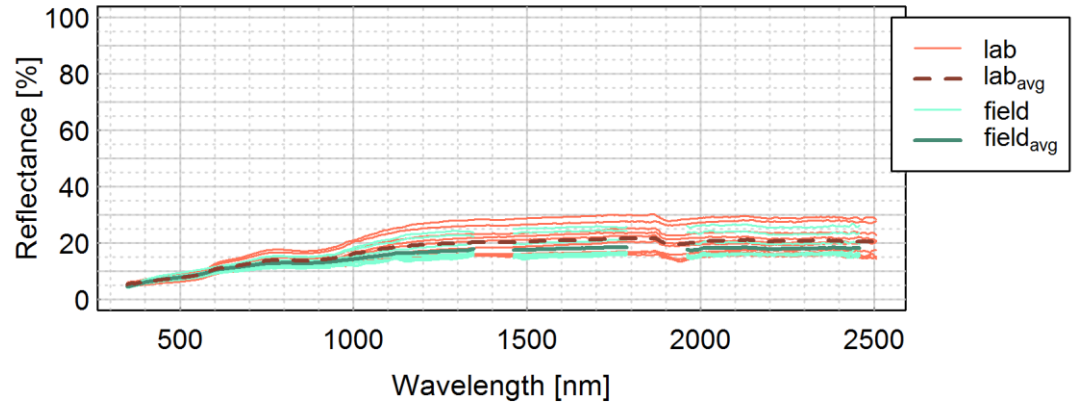

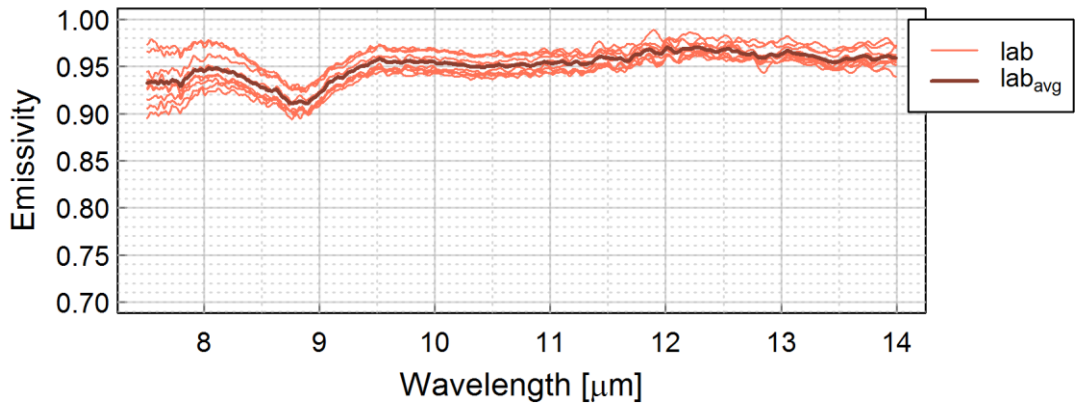

ROOFING TILE$_{R013}$

Class	Roofing tile
Material	Ceramic
Colour	Red
Status	Weathered
Dimension [mm]	115 x 12 x 130

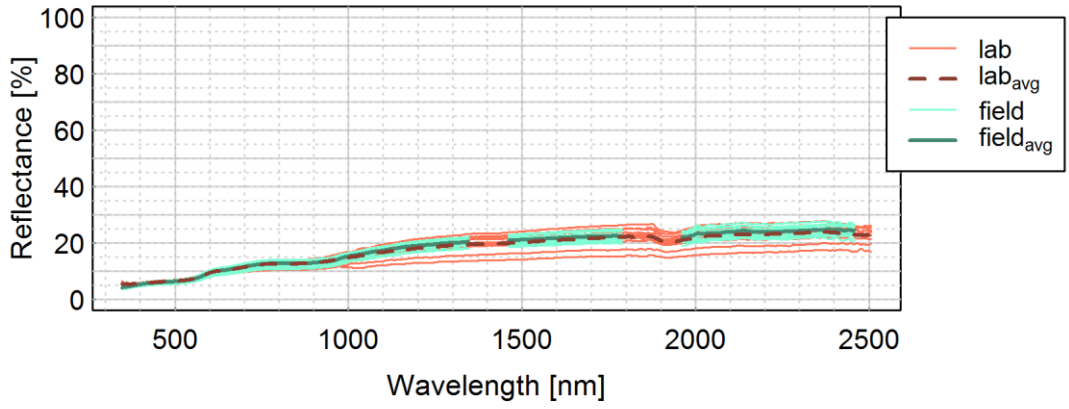

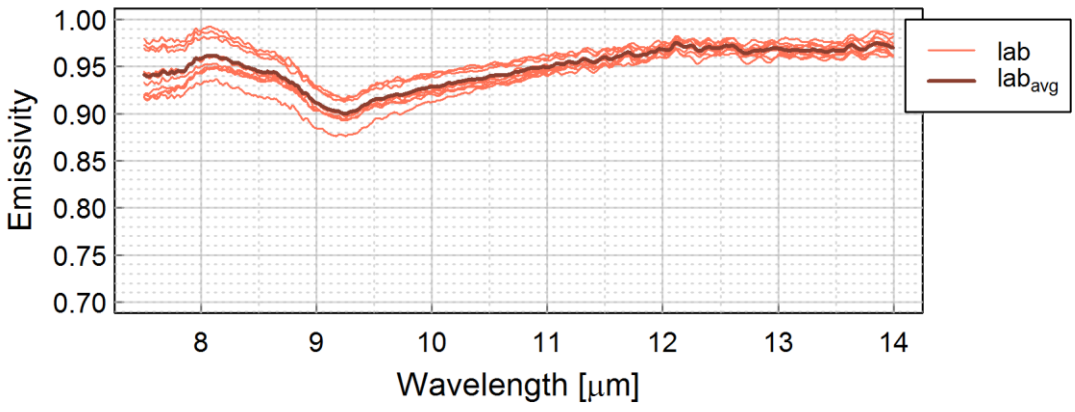

METAL$_{Z001}$

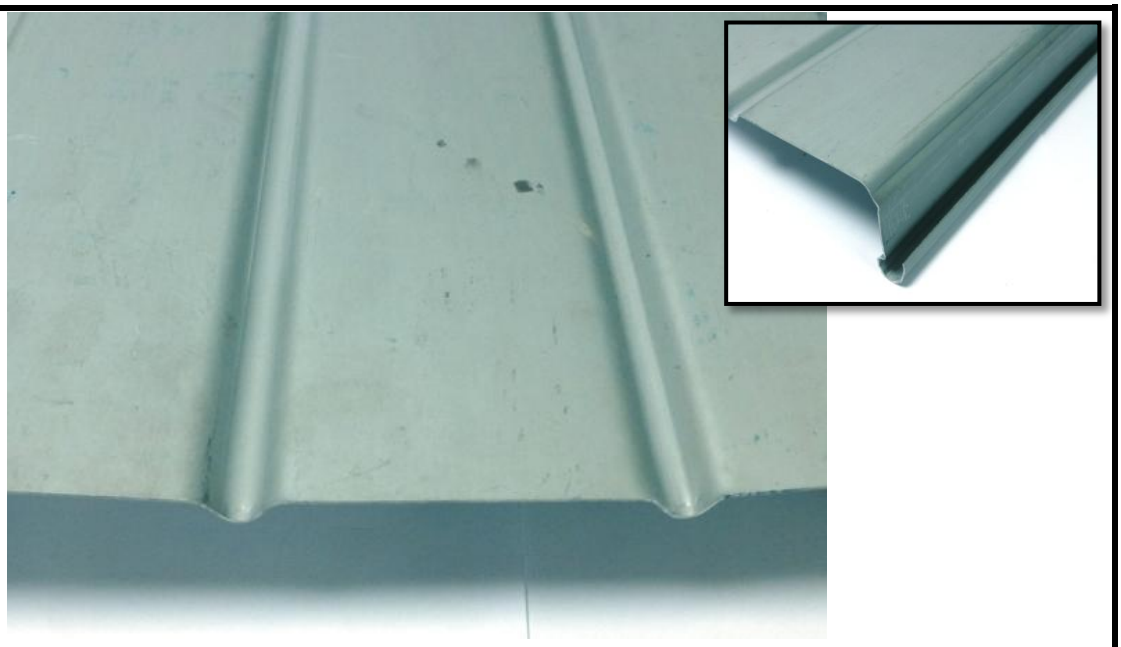

Class	Metal
Material	Aluminium plus zinc
Colour	Dull grey
Status	New
Dimension [mm]	390 x 1 x 295

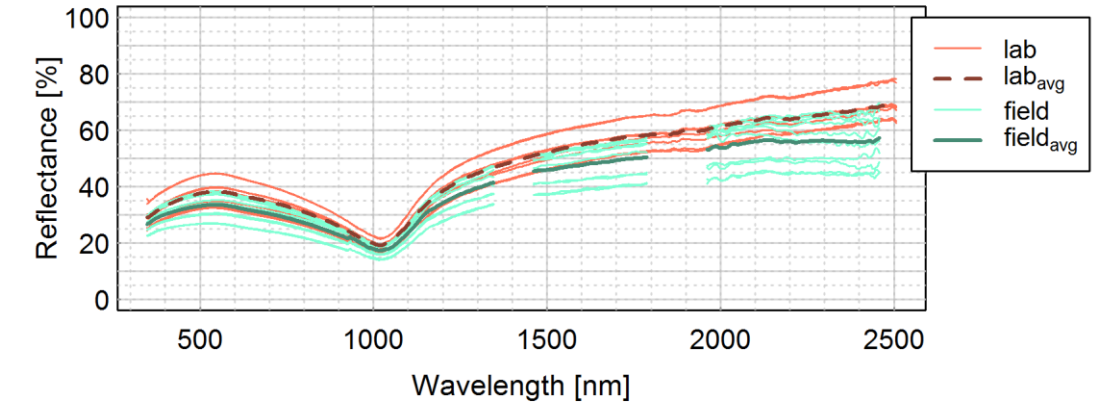

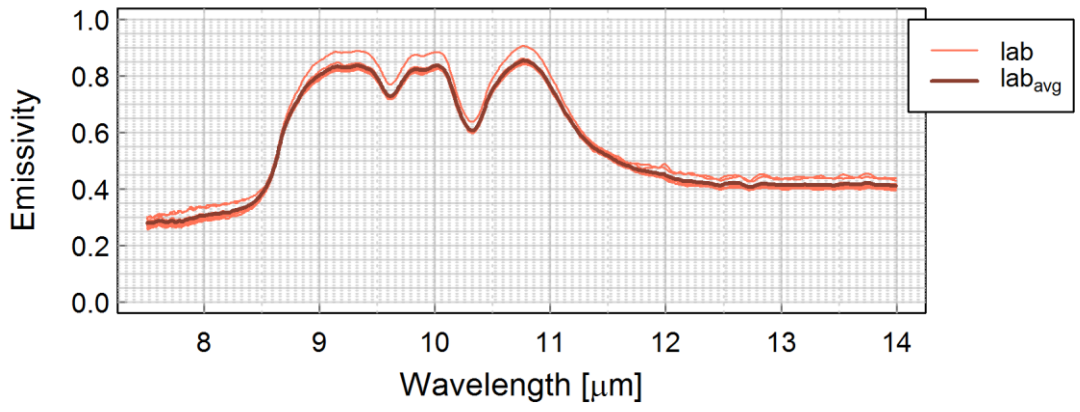

METAL$_{Z002}$

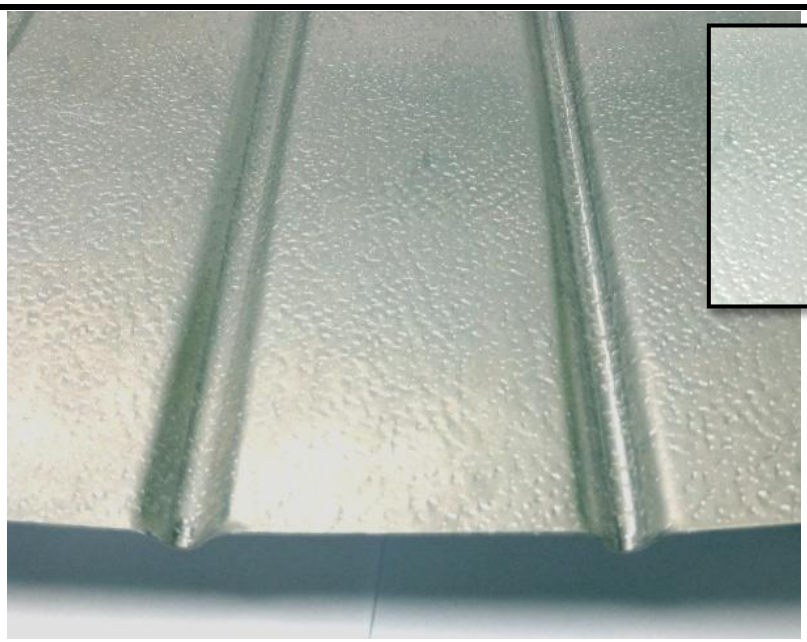

Class	Metal
Material	Aluminium, stucco
Colour	Shiny grey
Status	New
Dimension [mm]	380 x 1 x 295

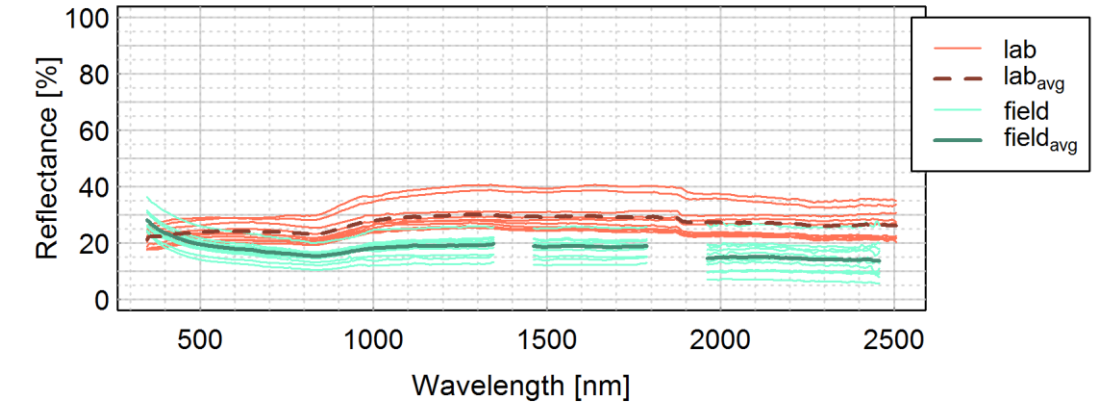

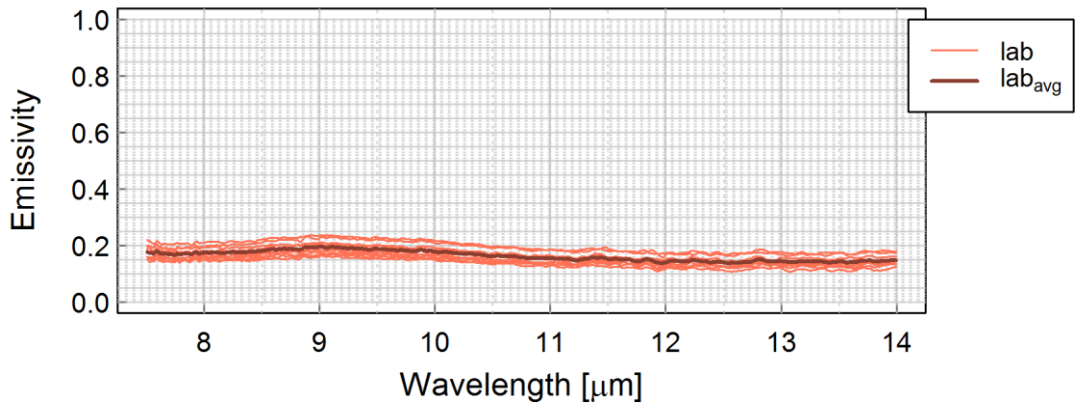

METAL$_{Z003}$

Class	Metal
Material	Metal with paint
Colour	Dark green
Status	New
Dimension [mm]	102 x 1 x 150

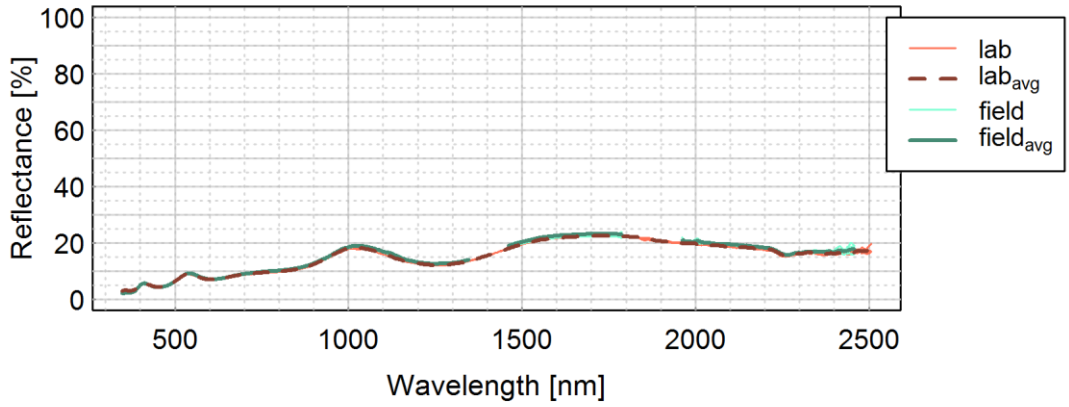

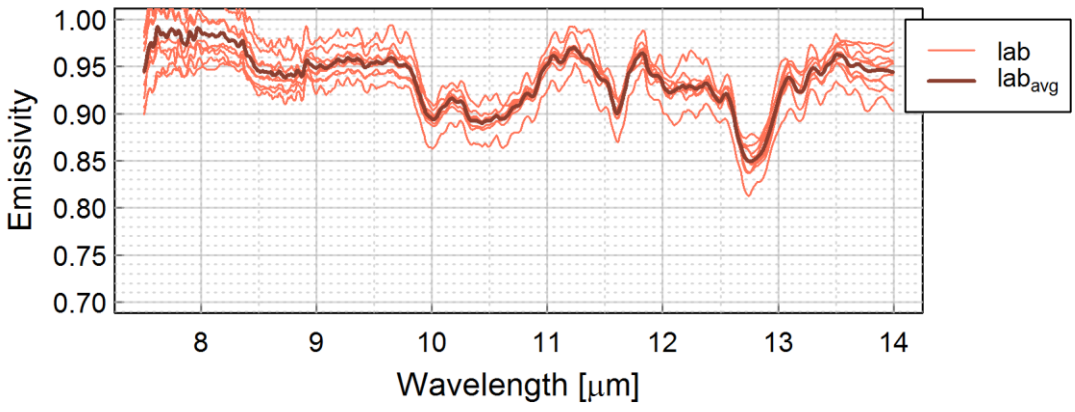

METAL$_{Z004}$

Class	Metal
Material	Metal with paint
Colour	Copper patina
Status	Weathered
Dimension [mm]	192 x 1 x 150

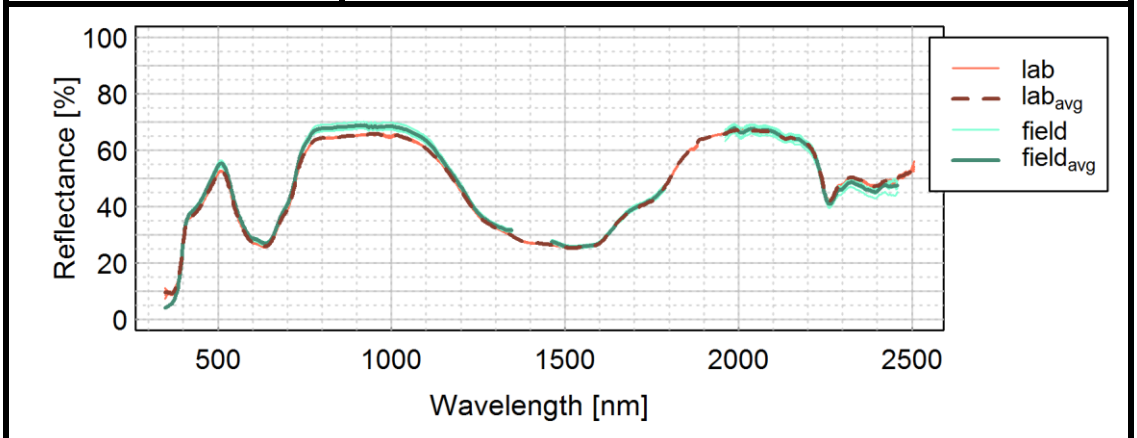

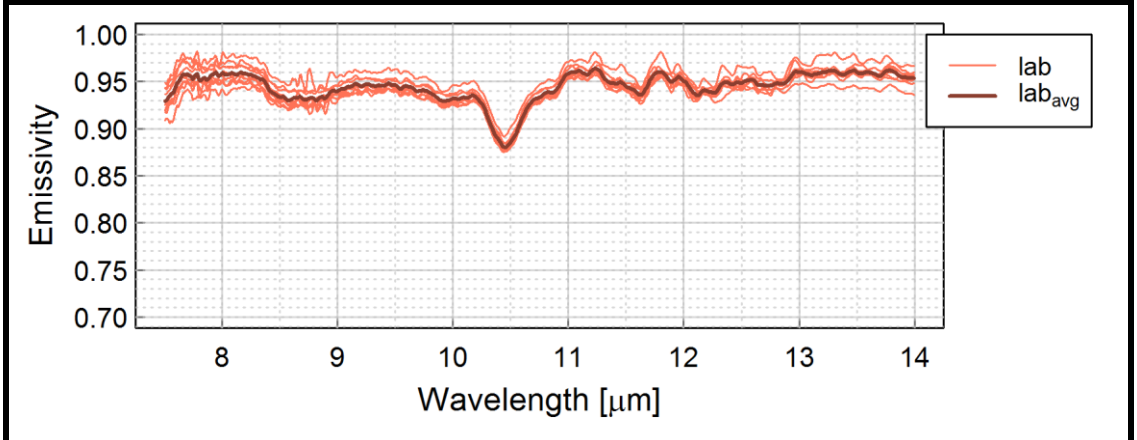

METAL$_{Z005}$

Class	Metal
Material	Metal with paint
Colour	Slate grey
Status	New
Dimension [mm]	152 x 1 x 205

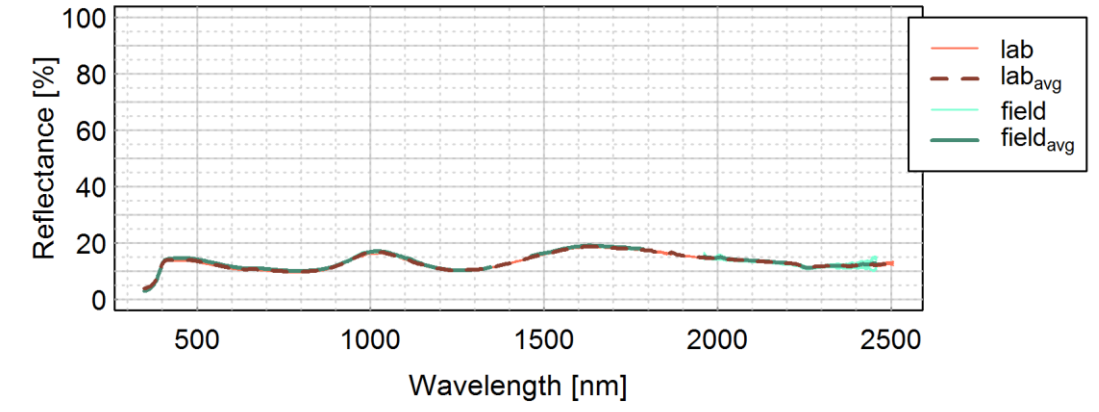

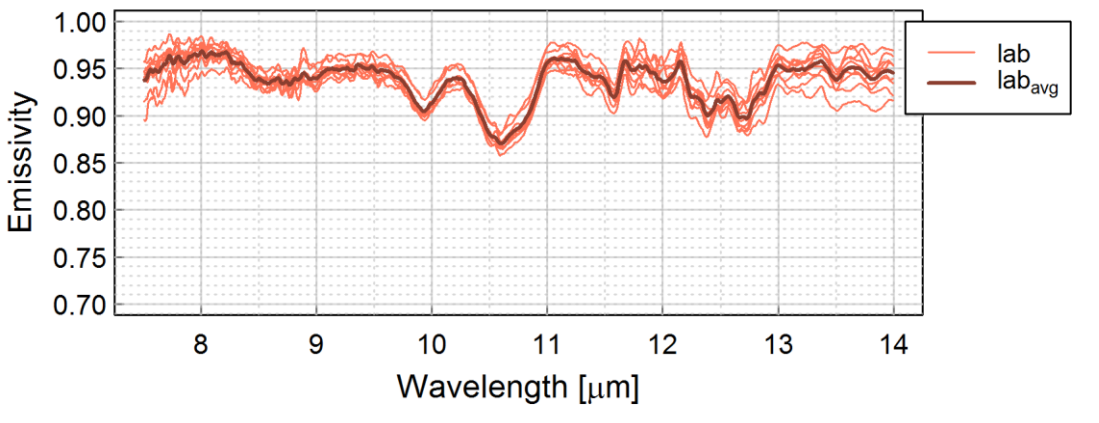

METAL$_{Z006}$

Class	Metal
Material	Aluminium
Colour	Grey
Status	Weathered
Dimension [mm]	220 x 1 x 230

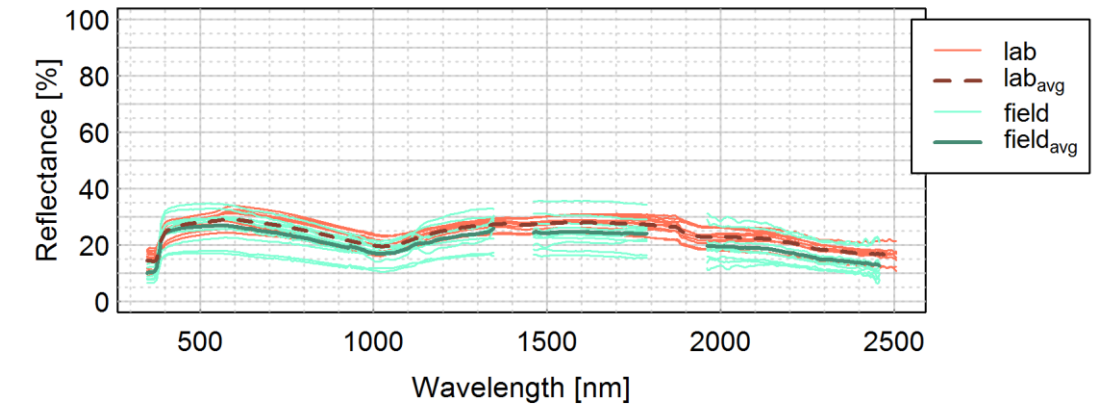

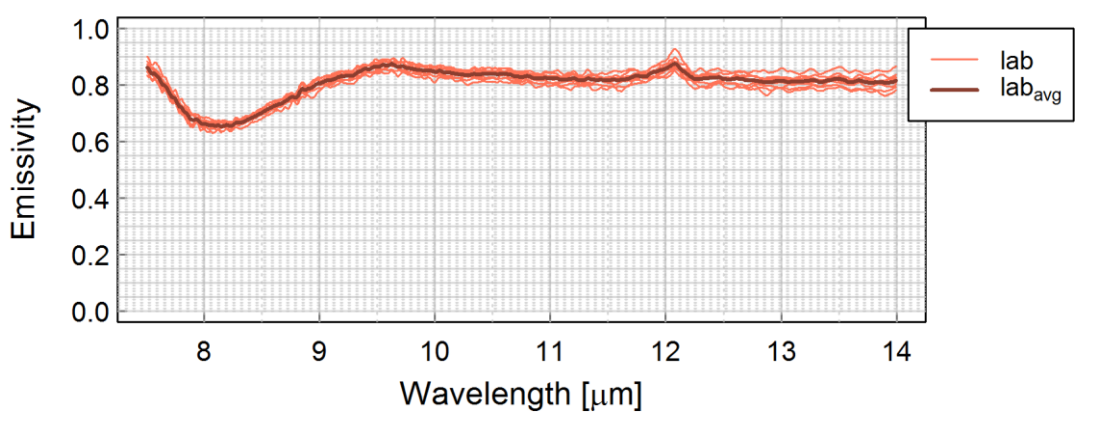

METAL$_{Z007}$

Class	Metal
Material	Lead
Colour	Grey
Status	Weathered
Dimension [mm]	254 x 2 x 200

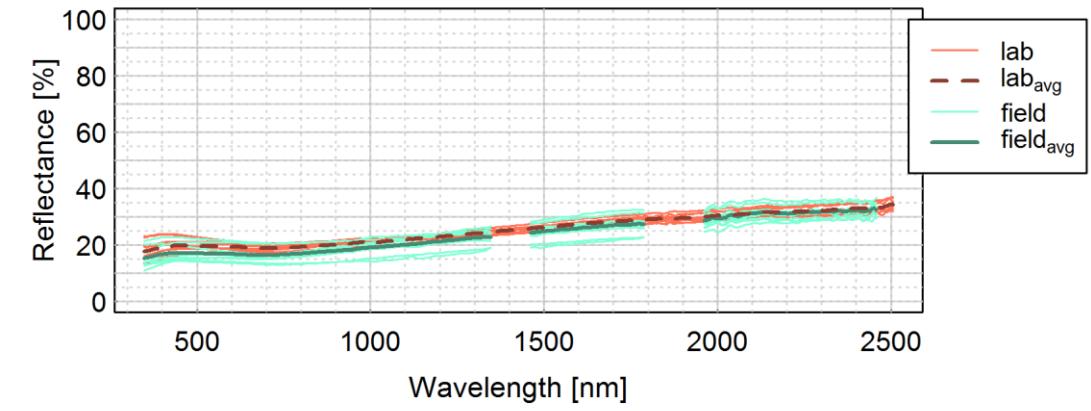

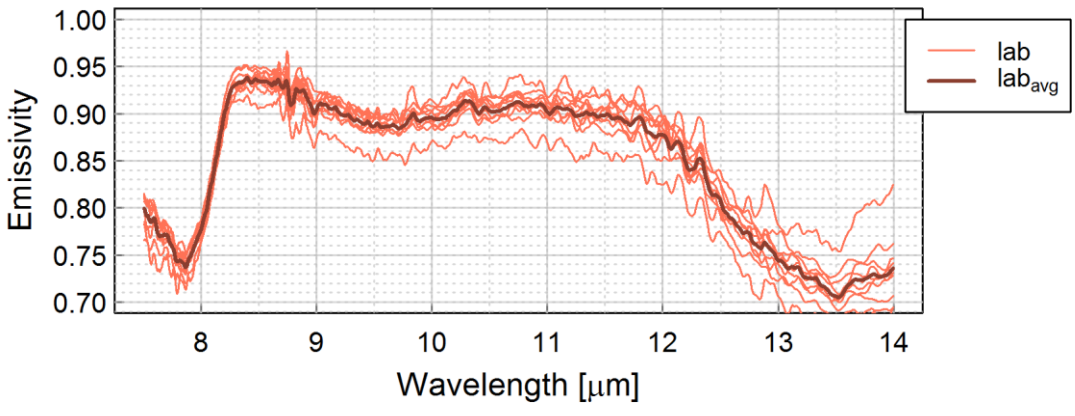

METAL$_{Z008}$

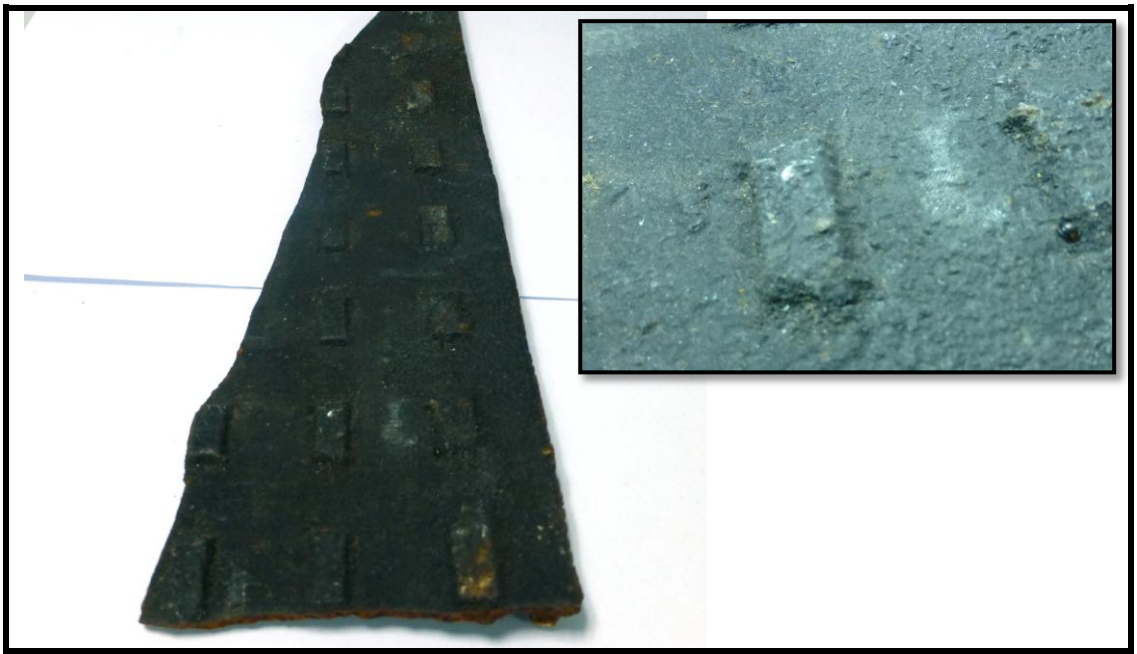

Class	Metal
Material	Iron
Colour	Black
Status	Weathered
Dimension [mm]	428 x 5 x 110

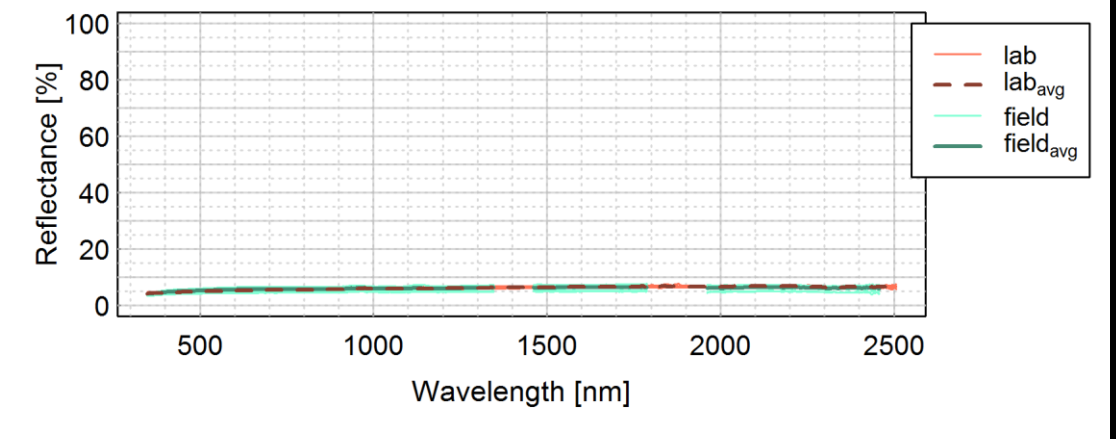

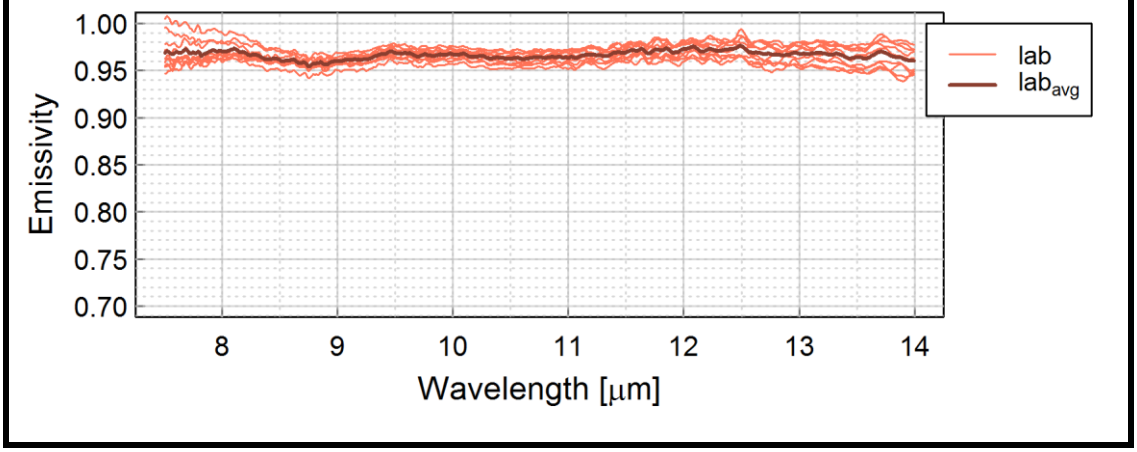

PVC$_{V001}$

Class	PVC roofing sheet
Material	PVC
Colour	Lead grey
Status	New
Dimension [mm]	146 x 1 x 204

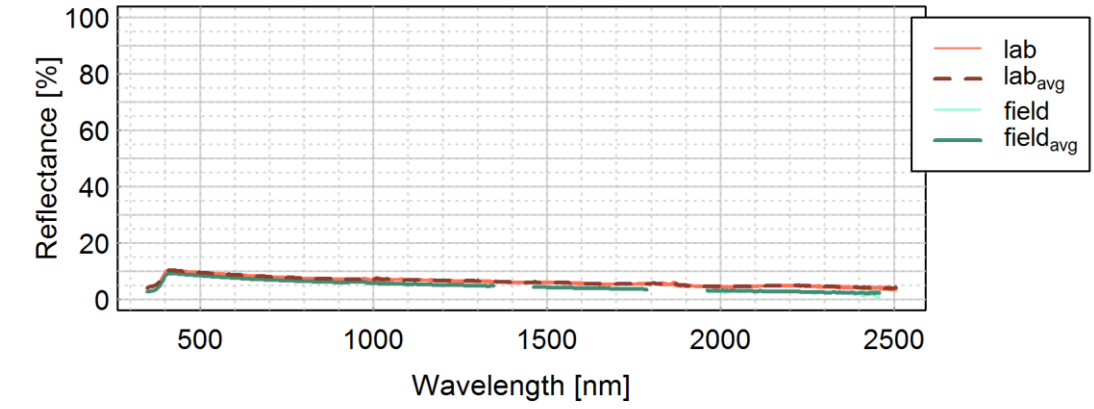

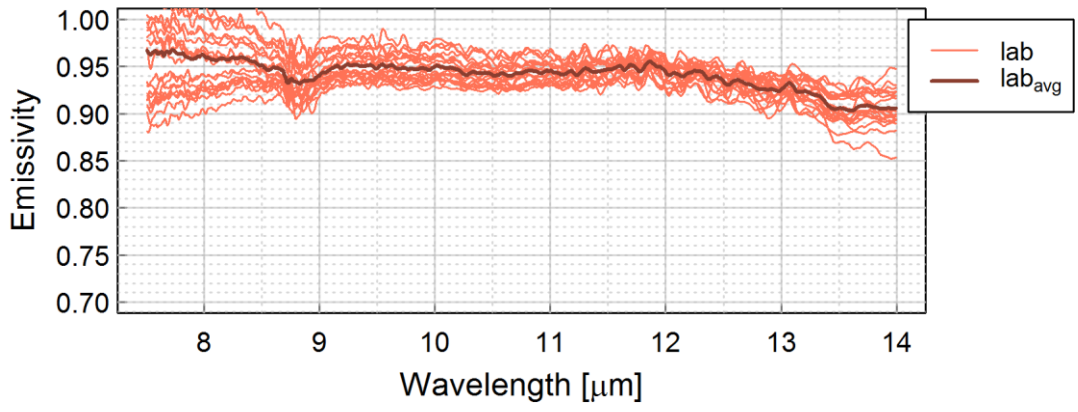

PVC$_{V002}$

Class	PVC roofing sheet
Material	PVC
Colour	Light grey
Status	New
Dimension [mm]	146 x 1 x 204

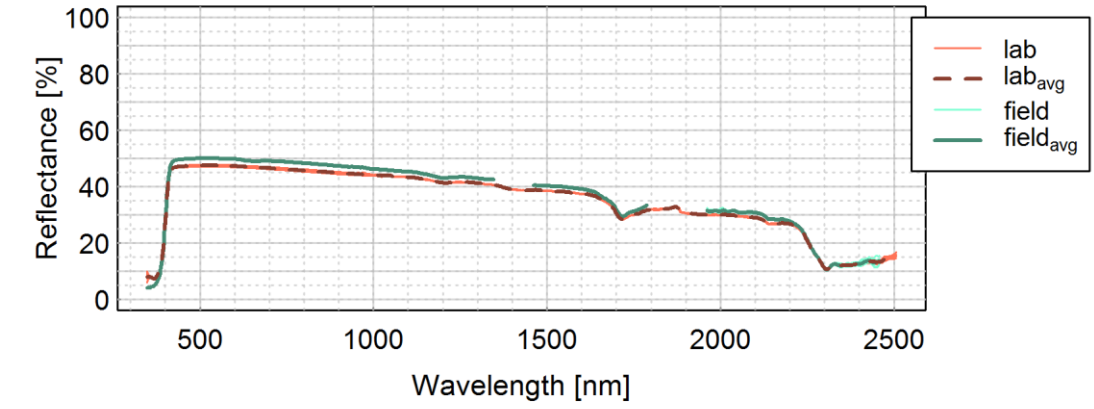

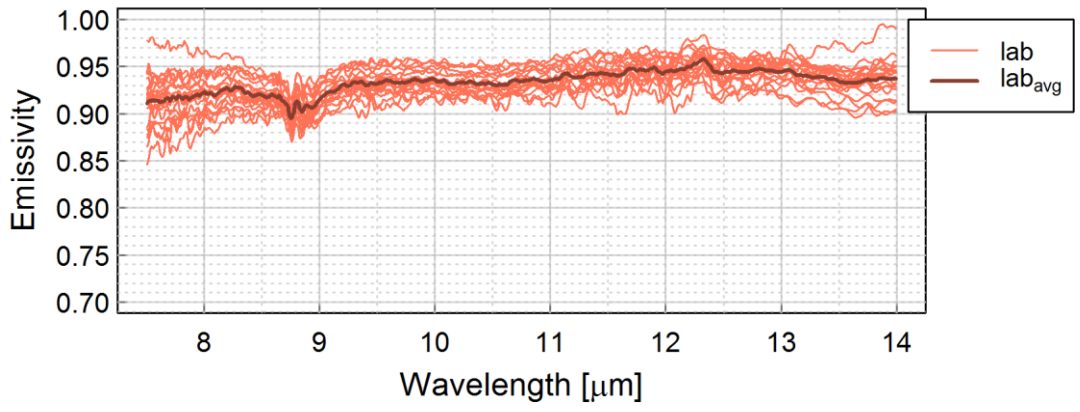

PVC$_{V003}$

Class	PVC roofing sheet
Material	PVC
Colour	Copper
Status	New/structured
Dimension [mm]	146 x 1 x 204

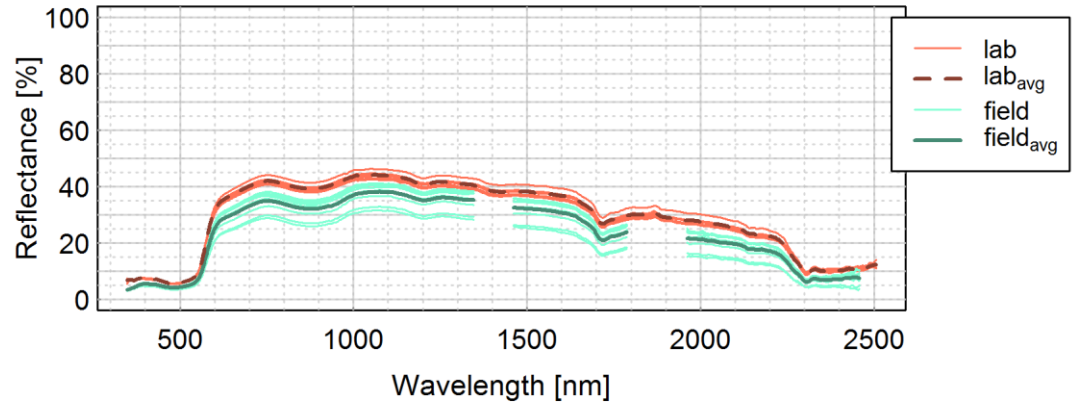

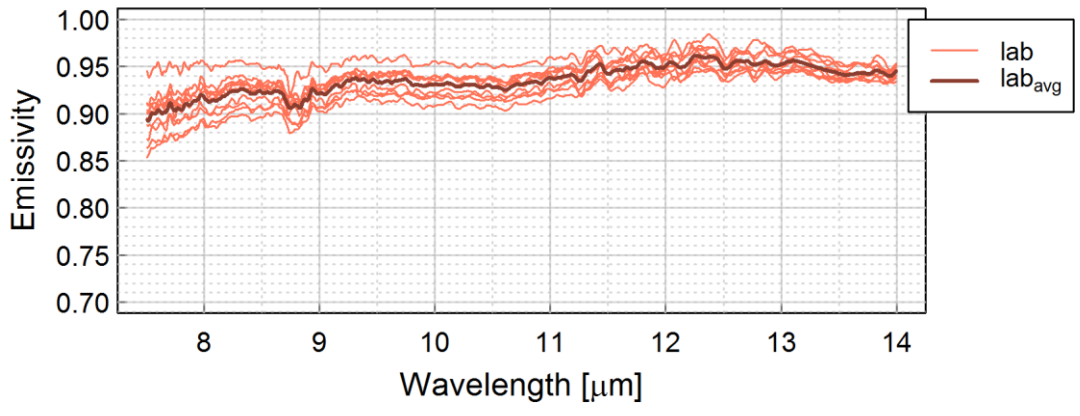

PVC$_{V004}$

Class	PVC roofing sheet
Material	PVC
Colour	Azure blue
Status	New
Dimension [mm]	146 x 1 x 204

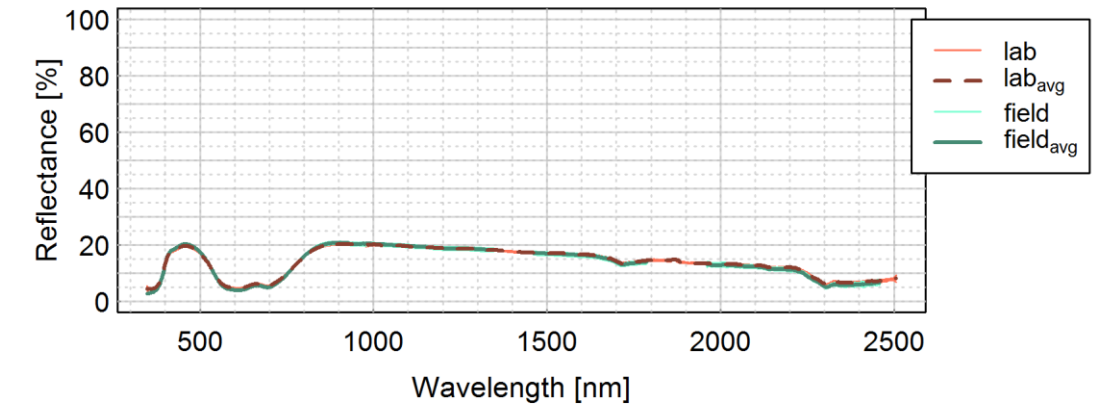

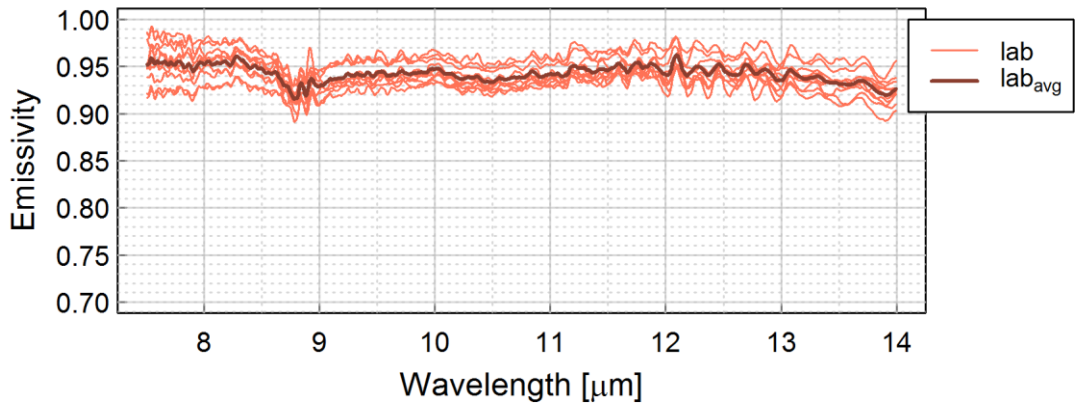

PVC$_{V005}$

Class	PVC roofing sheet
Material	PVC
Colour	Copper brown
Status	New
Dimension [mm]	146 x 1 x 204

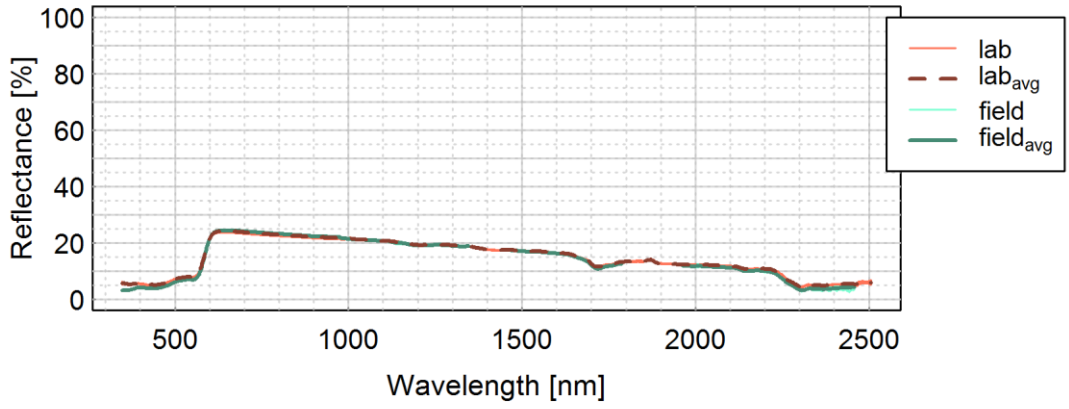

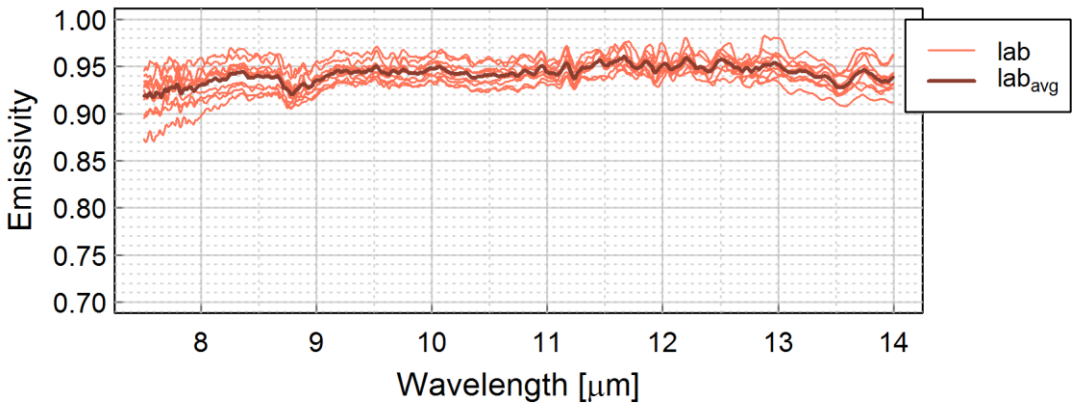

PVC$_{V006}$

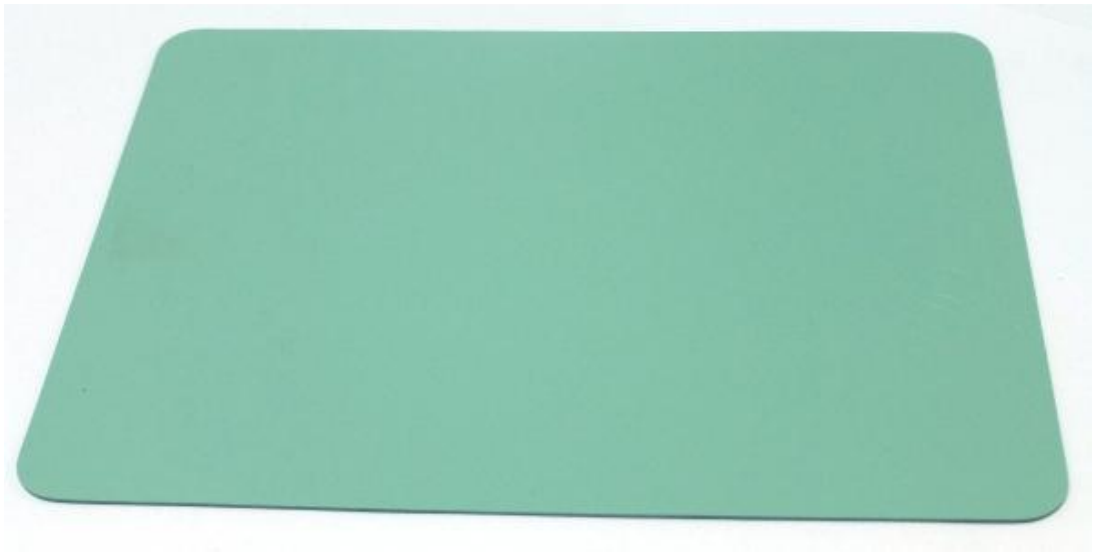

Class	PVC roofing sheet
Material	PVC
Colour	Copper patina
Status	New
Dimension [mm]	146 x 1 x 204

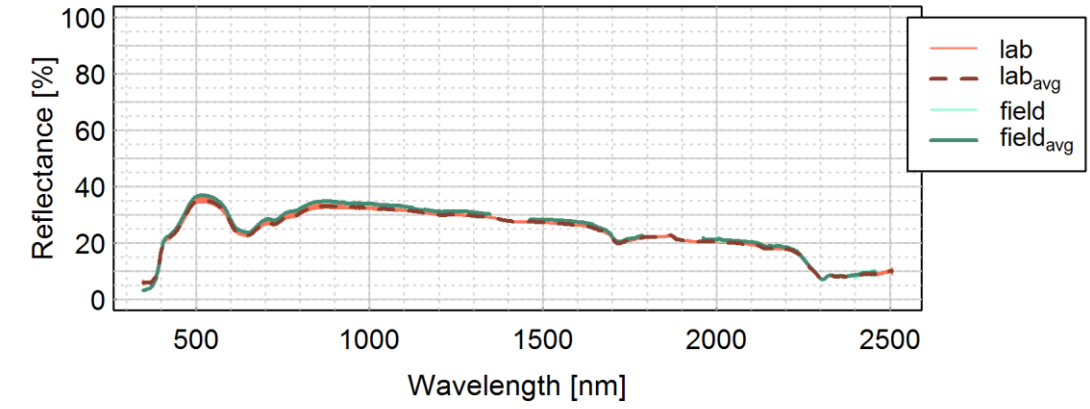

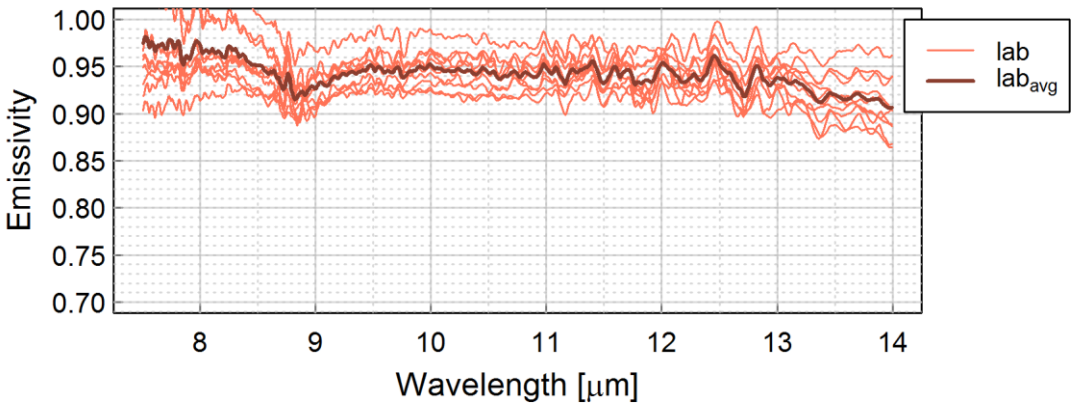

Appendix B Spectral emissivity measurements – outdoors

B.1 Introduction

Spectroscopy measurements of long-wave infrared (LWIR) emissivity have been conducted in this study (Chapter II) to characterise the radiative response of impervious urban materials. Observations were performed with a Fourier Transform InfraRed spectrometer (FTIR) under laboratory conditions and the emissivity retrieval was based on the *blackbody-fit* (BB-fit) method (Chapter II, Section II.3.2.2.3). Prior to these measurements presented, a series of observations was collected with a slightly different setup. During their analysis, however, instrument related problems have been revealed. Given this initially chosen setup has been used by other researchers (with the same instruments), the issues are briefly summarised (Section B.2). These measurements were performed outside, under clear sky conditions, allowing a different, presumably advantageous (compared to the BB-fit) approach, to be applied for the separation of temperature and emissivity. Given some information about the magnitude of the emissivity spectra (used for the compilation of the emissivity maxima database, Chapter II, Table II.2) is derived from these observations, this emissivity retrieval approach is introduced (Section B.3).

B.2 Issues with the initial instrument setup

The measurements were initially set up using a different instrument, the *MIDAC* FTIR loaned by NERC FSF; of the same model as the FTIR used in this study (Chapter II). A fixture, designed by NERC FSF, was mounted to the front of the spectrometer, holding the blackbody (BB) sources in a stable position (Figure B.1). In the centre of this fixture, a rotatable, gold-coated mirror is installed with an angle of 45°. Depending on its alignment, thermal radiation emitted by the target or gold plate (down-facing mirror), or one of the two BB sources (side-facing mirror) is reflected into the aperture of the FTIR spectrometer. A rotary knob at the front of the fixture allows for manual positioning of the mirror.

This setup was used both in the laboratory and in the field (i.e. outdoors). Given the target is required to be considerably warmer than the surroundings, in order to improve the signal to noise ratio (Chapter II), and the down-welling radiance from the sky is much lower than that emitted by the laboratory's ceiling and walls, laboratory measurements need to be performed at higher temperatures. The targets are heated to temperatures around 50–60°C and the BB sources required for radiometric calibration (Chapter II, Section II.3.2.2.1) are set to 40 and 70°C, respectively. Outdoors, the target temperatures were around 20–30°C so that the BB sources were set to 15 and 40°C, respectively.

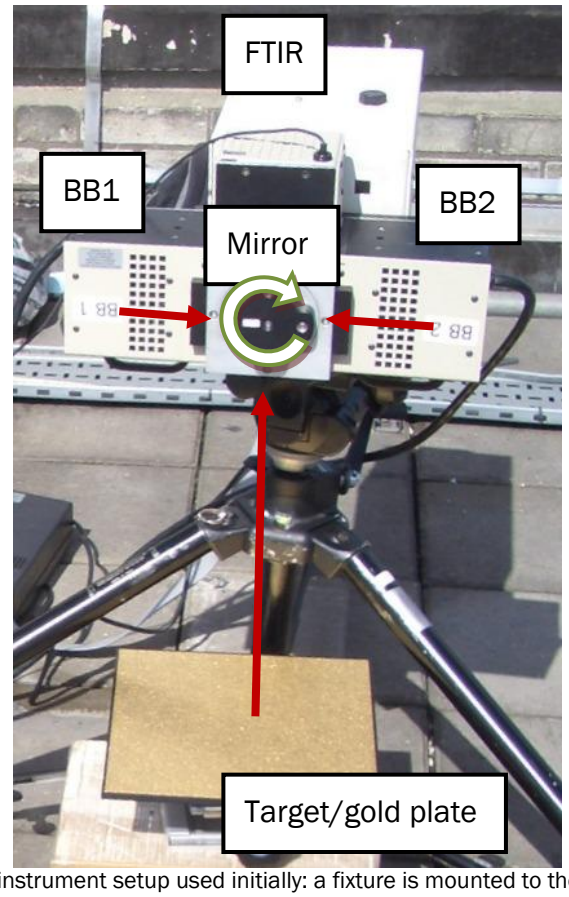

Figure B.1: Picture of the instrument setup used initially: a fixture is mounted to the front of the FTIR spectrometer holding a rotatable mirror that can be set to select radiation (indicated by red arrows) emitted from the target / gold plate, or one of the blackbody sources (BB1; BB2), respectively.

Measurements conducted with the rotating mirror showed different results for observations in the laboratory and outdoors (Figure B.2). Absolute emissivity in the spectral region of 8–9 µm is considerably higher when measured with the *hot* setup in the laboratory compared to the *warm* setup used outdoors. All spectra collected with the hot settings have a distinct absorption peak at about 8.1 µm. This bias was found to be a systematic, i.e. independent of the material sample measured, the time of observation (measurements were repeated on several days, both with the warm and hot settings) and location (measurements were conducted in different laboratories). A series of test measurements was performed. The analysis of various recorded energy spectra in raw DN (digital number) and calibrated spectra suggested that some component(s) of the instrumental system were absorbing more energy when operating temperatures (i.e. those of the target and the BB sources) were higher. Every component of the system absorbs/emits LWIR radiation, however, a fundamental assumption for the 2BB method for radiometric calibration (Chapter II, Section II.3.2.2.1) is the linearity of radiance with temperature (Section II.4.1.2). This approximation was not sufficiently fulfilled for the initial measurement setup (Figure B.1), causing changes in emissivity estimates with operating temperature (Figure B.2).

Finally, lab measurements were performed with a setup similar to the one used in this study (Chapter II), where no fixture is mounted to the instrument and target and blackbody sources are positioned manually in front of the spectrometer's aperture. Recorded energy spectra in raw DN

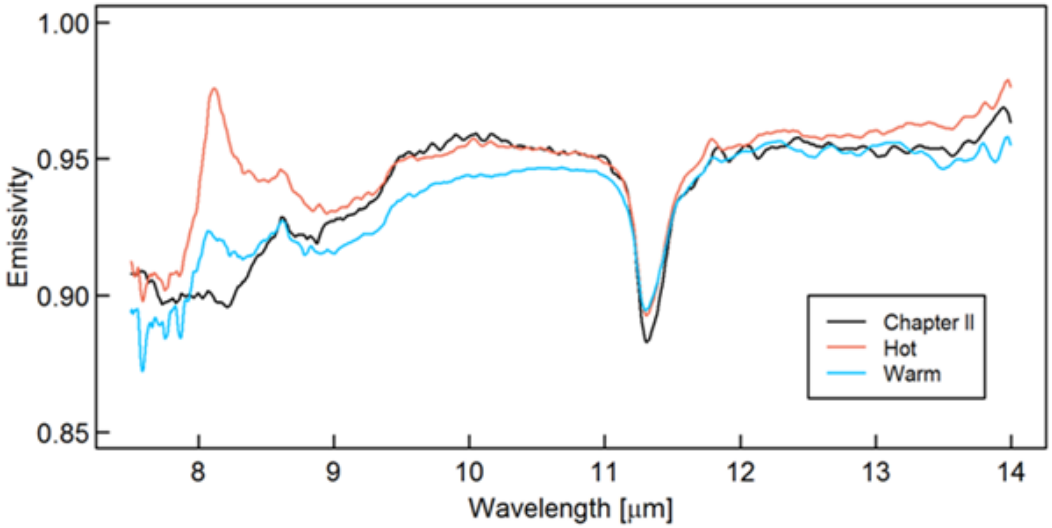

Figure B.2: Absolute LWIR emissivity of a concrete sample (C001, cf. Appendix A) measured with three different setups: the one used in this study (KCL FTIR, no mirror-fixture; Chapter II) and the initial setup (NERC FSF FTIR) with the mirror-fixture in the lab (hot) and outdoors (warm).

of laboratory measurements (i.e. using the hot settings) without the use of the rotatable mirror show clearly less absorption in the region between 8–9 µm (Figure B.3). Generally, some differences between the raw DN measurements with and without the mirror-fixture are explained by the difference in down-welling background radiation reflected by the target (and also the BB sources with a non-unitary emissivity of 0.96; Section II.3.1.2). However, this effect is not strong enough to explain the spectral variations and temperature dependencies detected in spectra that

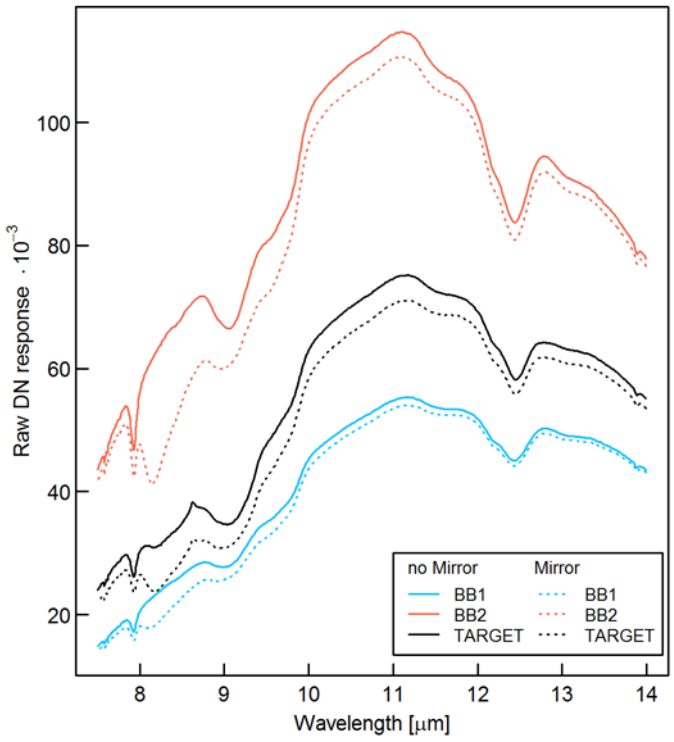

Figure B.3: Recorded energy spectra in raw DN observed with the FTIR (loaned by NERC FSF) in the lab from two BB sources (BB1=40 °C; BB2=90 °C) and a target (silica sand, 40 °C) by manually swapping the objects (solid lines) or using the rotatable mirror (dashed lines).

were measured using the mirror-setup. It is assumed that, given the two BB sources are constantly facing the mirror when attached to the fixture, the radiation emitted by those sources may heat up the latter. This again may have caused evaporation of some substance that potentially contaminated the mirror in the past.

B.3 Emissivity retrieval from outdoor spectrometer measurements

In order to derive emissivity from thermal infrared radiance observations, the surface temperature of the measured target is required as an input to the algorithm (Chapter II, Section II.3.2.2.3). The Iterative Spectrally Smooth Temperature / Emissivity Separation (ISSTES, Borel 1998) approach, was applied to analyse the FTIR spectrometer measurements collected outdoors. It is based on the fact that atmospheric absorption lines are superimposed on emissivity spectra if an incorrect temperature is assigned to the target in the retrieval process (Horton et al. 1998). Artefacts of atmospheric absorption (Figure B.4) cause underestimated (overestimated) emissivity if the target temperature is set too high (low). Using the ISSTES method, the most probable target temperature is detected by minimising this effect for a defined waveband (e.g. 8.9–9.4 µm, Figure B.4). This approach has the clear advantage of providing an inherent target temperature estimation. The only *a priori* knowledge required is a wavelength region with low spectral emissivity variations, defining the window for the smoothness optimisation.

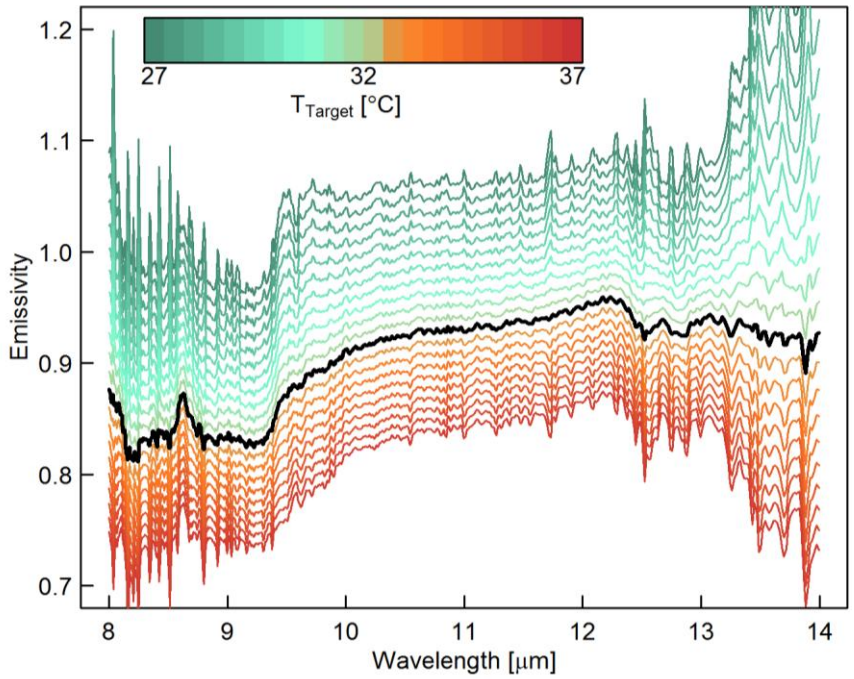

Figure B.4: Absolute emissivity of a sandstone sample (S001, cf. Appendix A) measured outdoors with the initial setup (rotating mirror, FTIR loaned by NERC FSF), for a range of potential target temperatures (T_{Target}). The final emissivity spectrum (thick line) is retrieved using the ISSTES method with an optimisation over the region 8.9–9.4 µm.

Appendix C The London Urban Micromet data Archive

C.1 Introduction

The London Urban Micromet data Archive (LUMA) was created in 2011 with the long-term objective of providing easy access to the data collected as part of this study in London, and also combining measured and modelled data from other cities (Figure C.1). Measurements from several sites across London, UK, form the initial database. Mechanisms for automatic data collection, processing and storage have been developed. To the extent possible, generic and standardised procedures are used to improve efficiency and transferability (e.g. between sites and cities). Common structures for data as well as meta information make LUMA user friendly to facilitate data sharing.

In LUMA, any details on instrument setup and changes of configurations in the measurement network are recorded in a central document, the *logbook* (Section C.2). A well-connected infrastructure (Section C.3) allows for remote system monitoring of the various measurement sites and enables automatic data collection (Section C.4). Raw measurement data are converted to common file formats, based on general conventions, and details on quality control and processing procedures are stored in LUMA (Section C.5). Data are made available for download

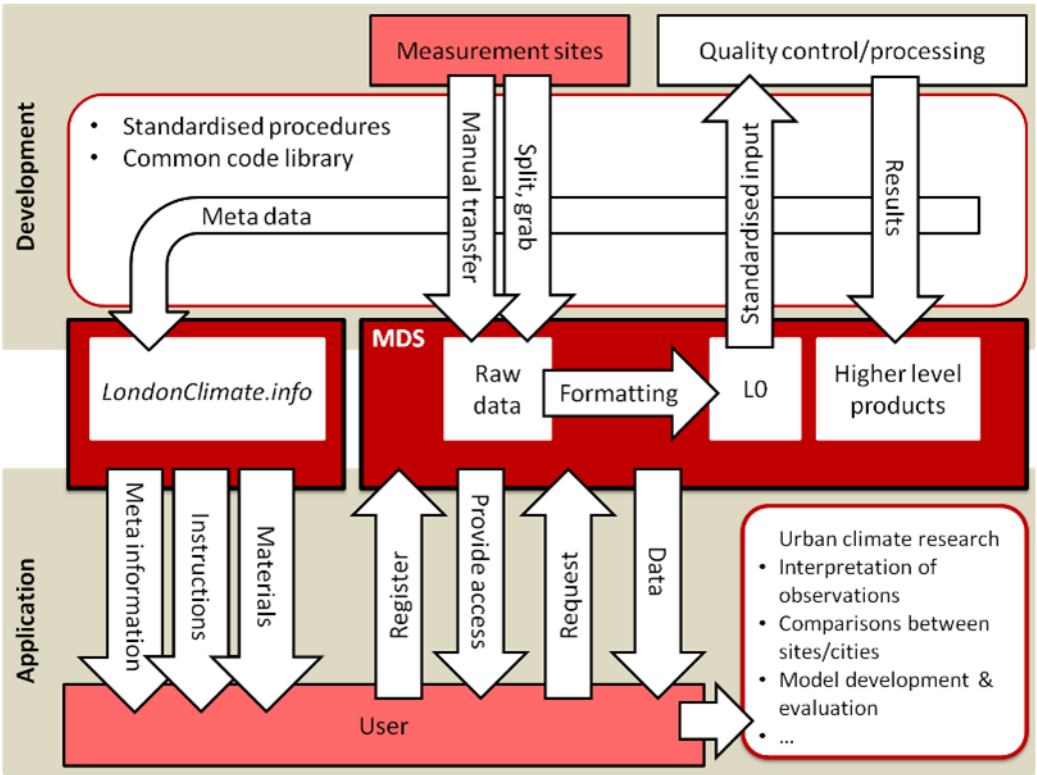

Figure C.1: Structure of the LUMA system. Data collection, processing and metadata management are closely linked via standardised automatic procedures and a common code library. This provides all necessary information to the LUMA user, constituting a comprehensive source of information for a variety of urban climate research applications. MDS: Main Data Server; see text for details.

to registered LUMA users on the web (*LondonClimate.info/LUMA/LUMA.html*; Section C.6).

C.2 Logbook

The logbook is the key document for the generation and maintenance of LUMA. It brings together information on sites, sensor configurations, raw file locations and auxiliary specifications (such as instrument calibration records) in one EXCEL (*MS Office*) workbook. Any changes made to the measurement sites, are manually recorded in this central document; both in terms of hardware (e.g. instrument location) and software (e.g. version of data logger programs) (Table C.1). A script (written in R, R Core Team 2005) is scheduled to automatically process the updated EXCEL file:

a) Sheets used by data processing programs (e.g. calibration details) are extracted from the workbook and stored as individual text files (*.csv format) on the data server.

b) The LUMA sheet and those of the individual sites (Table C.1) are extracted, converted to html and made available on the web (*LondonClimate.info/LUMA/LUMAsites.html*).

Thereby, the information gathered is easily and quickly accessible to: a) other processing scripts and b) LUMA users as well as the development team.

Table C.1: Structure of the LUMA logbook with various spreadsheet types. See text for details.

Spreadsheet	Description
DOWNLOAD	List of files in LUMA available for download
Contents	Summary of the logbook content
LUMA	List of sites included in LUMA, by city
Site details (e.g. *KSK*)	List of instruments operational at various sites; including time of operation, sensor location and orientation
Variables	List of variable names available in LUMA, by category
Titles	List of *titles*, i.e. the file name specifiers
Calibration	Calibration dates for relevant instruments
Meta tables (e.g. *MT1*)	Instrument and processing details, e.g. details on quality control
Settings (e.g. *EC_setting*)	Specific instrument settings, additional to those provided on the site details sheet
Raw file format (e.g. *KSN_TP_YYDOY.dat*)	Structure of raw files (mostly text file formats) including file location and name of data logger program (if applicable)

C.3 Infrastructure

Initially data are collected automatically at each instrument site and stored there. Eventually all data are centralised on one *main data server* (MDS; Linux, *Debian*), thus the infrastructure that connects the various sites and the MDS is a key element of the measurement network. There are two methods for the networks to operate:

- An internal network when instruments and computers have an IP address on the same sub-domain as the MDS. This is created by sharing PC drives and mounting them to the MDS file system which allows data to be pulled to the MDS.
- Alternatively, the instruments are on a different domain, in some cases behind a fire-wall, so the data need to be pushed to a virtual storage location (cloud memory, ftp sites) before being pushed or pulled to the MDS. The data are then pulled to the internal site (e.g. using secure file transfer protocol).

The bandwidths of the respective internet connection need to fulfil minimum requirements for the intended file transfer, which can become an issue for high frequency observations, i.e. large files. For remote (software) maintenance, computers at the measurement sites (mostly MS Windows) can be accessed using remote connection software (e.g. MS Windows Remote Desktop Connection, LogMeIn).

C.4 Data collection

In the LUMA measurement network, data are recorded in three different ways, depending on the type of instrument and application:

(a) Instruments collect and store data internally, using software from the manufacturer.

(b) Instruments are connected to data loggers and data logger programs (e.g. in *CRBasic*) perform sampling and initial calculations (such as calibration or averaging). Data logger support software (e.g. LoggerNet, *Campbell Scientific*) is then scheduled to transfer data from the logger to the on-site computer frequently.

(c) Instruments are directly connected to a computer (e.g. via USB), and software records the signal from the com-port (in LUMA, both ComCap*, Magenta Systems Ltd*, and *Python* scripts are used).

These setups produce different file formats. Some create separate files for specified time intervals (e.g. one file per day or hour), while data downloaded from external data loggers can be appended to existing files without renaming. In the latter case in LUMA, a script (written in C++ by Danilo Dragoni, when at Indiana University) is scheduled to split the files by time. This script can also be used to format the time stamp information and to define which data columns should be stored. This is controlled by a simple batch file and is applicable for a variety of file formats. Depending on the data type and sampling frequency (both determining the file size), raw data files are generated as hourly or daily files in LUMA.

Raw data files collected at remote sites (i.e. not in the local network) are transferred frequently (e.g. hourly, daily) to an ftp server (Section C.3). Individual raw files (or several combined in a zip archive) are transferred from the field computers or the ftp server to the MDS by one generic shell script. A simple text file (Table C.2) controls the *grab* script, indicating which files should be transferred.

Table C.2: Control file (*'FileLocations'*) for *grab* shell script.

Type	Source	Destination folder	Filename
1: hourly 2: daily 0: disabled	Complete file name including path	Path where file is moved to	Name of file at destination

The *grab* script runs hourly to collect the most recent files. It is scheduled to re-try collecting all data that have not been transferred within the preceding three days. The latter option has been implemented in order to automatically account for temporary loss of network connection (e.g. between a computer and the MDS) or other issues that might interrupt the continuous data stream (such as a temporary shutdown of the data logger support software). In case the

connection to a requested file cannot be established (e.g. because the file is missing or the respective computer is offline), an email is sent out automatically to the LUMA team. This 'alarm' email system prevents many types of problems going unnoticed for an extended period, so that issues can be resolved promptly to improve data capture rates.

C.5 Data base structure

A common file structure is used to organise LUMA. All **raw** data are aggregated, sorted hierarchically by year of measurement, city, site and measurement type. In the first processing step, all raw data are converted to daily files in netCDF (network Common Data Form, *Unidata*) format, using the CF-conventions (Eaton et al. 2011) as guidelines. *Global attributes* (applicable for all data in a file) and *variable attributes* (describing a specific variable) are inherently included in the netCDF files. The necessary auxiliary information is provided to the processing scripts (e.g. in R, MatLab, or IDL) either by the LUMA logbook (Section C.2) or separately created, file specific *meta* files. Variable names and units are chosen according to agreed standards and variables are grouped into categories ().

For R and MatLab, generic function libraries have been created which facilitate the retrieval of the respective information (e.g. programs can automatically check which instruments are operational extract the serial number of a specific sensor, depending on location and date). Especially when re-processing past data, this feature provides a convenient way of assigning meta information and is less prone to manual errors. The library also holds a generic function to conveniently read time series stored in netCDF format into R (*LonconClimte.info/LUMA/scripts.html*).

Similarly to the raw data, all **formatted** and **processed** data are stored according to a hierarchical folder structure, by year, city, level of processing, and site. The level of processing starts with the initial raw data (L0), i.e. those simply converted to NetCDF, and then increases for each set of quality control or processing steps (L1, L2, …). However, the level is specified as the same if only basic temporal averaging is performed (e.g. 15 min averages of 5 s raw data are also assigned to L0). Data from different sensors are stored in separate files unless the setup suggests a fundamental connection (e.g. data gathered by a series of thermocouples comprising a temperature profile). Data sets are specified by *Titles*, given by the instrument or processing procedure (Table C.3).

Table C.3: Variables specified in LUMA by category. The latest version of this list is provided online (*LonconClimate.info/LUMA/variables.html*). Specifications are listed in the same format used in the data files, i.e. using underscores '_' or dots '.' instead of spaces and no sub-/superscript.

Category	Name	Longname	Units
wind	WS	horizontal_wind_speed	m.s-1
	U	zonal_wind_component	m.s-1
	V	meridional_wind_component	m.s-1
	W	vertical_wind_component	m.s-1
	dir	wind_direction	degree
temperature	Tair	air_temperature	Celsius or K
	T_CNR	CNR_body_temperature	Celsius or K
	Tsfc	surface_temperature	Celsius
	Tsonic	sonic_temperature	Celsius or K
	Twater	River_Thames_Water_Temperature	Celsius
humidity	RH	relative_humidity	%
	C_H2O	water_vapour_concentration	mmol.m-3
	H2O_absorp	water_vapour_absorptance	dimensionless
	a	water_vapour_density	g.m-3
	q	specific_humidity	kg.kg-1
pressure	press	barometric_pressure	hPa
precipitation	RR	rain_rate	mm.h-1
	rain_acc	rain_accumulation	hits.cm-2
	rain_dur	rain_duration	s
	hail_acc	hail_accumulation	hits.cm-2
	hail_dur	hail_duration	s
radiation	Kdn	incoming_shortwave_radiation	W.m-2
	Kup	outgoing_shortwave_radiation	W.m-2
	Ldn	incoming_longwave_radiation	W.m-2
	Lup	outgoing_longwave_radiation	W.m-2
	Qstar	net_allwave_radiation	W.m-2
	Kdiff	diffuse_shortwave_radiation	W.m-2
	UVA_W	UVA_radiation	W.m-2
	UVB_W	UVB_radiation	W.m-2
	PAR_W	photosynthetically_active_radiation	W.m-2
	UVA_umol	UVA_radiation_umol	umol.m-2.s-1
	UVB_umol	UVB_radiation_umol	umol.m-2.s-1
	PAR_umol	PAR_radiation_umol	umol.m-2.s-1
	albedo	bulk_surface_albedo	dimensionless
	Sun	sunshine_status	%
surface_characteristics	albedo	bulk_surface_albedo	dimensionless
carbon_dioxide	C_CO2	carbon_dioxide_concentration	mmol.m-3 or kg.kg-1
	CO2_absorp	carbon_dioxide_absorptance	dimensionless
turbulence	ustar	friction_velocity	m.s-1
	Q_H	upward_turbulent_latent_heat_flux	W.m-2
	Q_E	upward_turbulent_latent_heat_flux	W.m-2
	F_CO2	upward_turbulent_carbon_dioxide_flux	umol.m-2.s-1
	zL	atmospheric_stability_parameter	dimensionless
atmosphere	BSC	height_normalised_backscatter	10-8.m-1.sr-1
	CLD_Height	Cloud_height	m
	CLD_Cover	Cloud_cover	%
	CLD_status	Cloud_detection_status	dimensionless
	vis_z	vertical visibility	m

Formatted and processed files are merged to annual files using cdo (Climate Data Operators; MPI 2013) implemented in a generic shell script which is run manually after data collation and daily

processing for a certain period and level is completed successfully. These annual files serve as the basis for most of the higher level processing and provide convenient input for data analysis.

Table C.4: Current LUMA content: data are specified by title, data level, and temporal resolution. Latest version of this list is provided online (http://*LonconClimte.info/LUMA/variables.html*).

Source	Title	Description	Data level	Description	Temporal resolution	Base resolution
Observations	WXT510	Automatic Weather Station, *Vaisala*	L0	Raw data	5 s & 1, 5, 15, 30 min	5 s
			L1	MT1 thresholds applied, align wind direction with BNG[1] north	1, 5, 15, 30 min	5 s
			L2	Gap fill by a) linear interpolation if gap <= 2h, b) data from alternative site (e.g. fill KSK with KSS), using correction for site specific differences, c) prediction based on day before and after if no data are available from alternative site	1, 5, 15, 30 min	5 s
	CNR1/CNR4	Net Radiometer, *Kipp & Zonen*	L0	Raw data	15 min	15 min
			L1	MT1 thresholds; night time Kdn & Kup set to 0	15 min	15 min
	Skye	UVA (SKU 420), UVB (SKU 430), and PAR (SKP215), *Skye*	L0	Raw data	15 min	15 min
			L1	MT1 thresholds	15 min	15 min
	PSP	Spectral Pyranometer, *Eppley*	L0	Raw data	15 min	15 min
			L1	MT1 thresholds, night time Kdn set to 0	15 min	15 min
	PIR	Spectral Pyrgeometer, *Eppley*	L0	Raw data	15 min	15 min
			L1	MT1 thresholds	15 min	15 min
	SPN1	Sunshine Pyranometer, *Delta-T*	L0	Raw data	15 min	15 min
			L1	MT1 thresholds	15 min	15 min
	rain gauge ARG100	Rain Gauge, *Campbell Scientific*	L0	Raw data	15 min	15 min
			L1	Gap filled	15 min	15 min
	Tinytag	Water temperature, *Tinytag*	L0	Raw data	1 min	1 min
	Li7500	Gas Analyser, *LI-COR Biosciences*	L0	Raw data	10 Hz	10 Hz
			L0	Averages of L0 raw data	30 min	10 Hz
			L1	Raw data, including quality control	10 Hz	10 Hz
			L1	Averages of L1 raw data	30 min	10 Hz
			L2	Raw data, including quality control and IMAS filter	10 Hz	10 Hz
			L2	Averages of L2 raw data	30 min	10 Hz

Li7500_ECpack	Eddy covariance data from Li7500 processed by Ecpack software (van Dijk et al. 2004) and QAQC (Kotthaus and Grimmond 2012, 2013a)	L0	Based on L0 raw data	30 min	10 Hz
		L1	Based on L1 raw data	30 min	10 Hz
		L2	Based on L2 raw data	30 min	10 Hz
CSAT3	Sonic anemometer, *Campbell Scientific*	L0	Raw data	10 Hz	10 Hz
		L0	Averages of L0 raw data	30 min	10 Hz
		L1	Raw data, including quality control	10 Hz	10 Hz
		L1	Averages of L1 raw data	30 min	10 Hz
		L2	Raw data, including quality control and IMAS filter	10 Hz	10 Hz
		L2	Averages of L2 raw data	30 min	10 Hz
CSAT3_Ecpack	Eddy covariance data from CSAT3 processed by ECpack software (van Dijk et al. 2004) and QAQC (Kotthaus and Grimmond 2012, 2013a)	L0	Based on L0 raw data	30 min	10 Hz
		L1	Based on L1 raw data	30 min	10 Hz
		L2	Based on L2 raw data	30 min	10 Hz
CL31_CLD	Ceilometer, *Vaisala;* Cloud information and diagnostics	L0	Raw data	15 s	15 s
		L0	Averages of L0 raw data	15 min	15 s
CL31_CLDW15; CL31_CLDW30; CL31_CLDW60	Processed CL31_CLD	L1	Smoothed raw data (windows of 15, 30, 60 min), cloud cover determined from cloud height	15 s	15 s
		L1	Averaged smoothed data, median cloud height and mean cloud cover	15 min	15 s
CL31_BSC	Ceilometer, Vaisala; Backscatter profile	L0	Raw data	15 s	15 s
		L0	Averages of L0 raw data	15 min	15 s
CL31_BSA	Aggregated backscatter profile from CL31_BSC	L1	Median backscatter over vertical atmospheric layer of 1000-6000 m	15 s	15 s
CL31_BSP	Processed backscatter profile from CL31_BSC	L1	Statistics of backscatter over vertical atmospheric layers	15 s	15 s

[1]BNG: British National Grid

C.6 External availability

LUMA is a powerful framework for the management of an extensive measurement network: it provides a tool to handle key meta data and facilitates data sharing. Plus the content of LUMA is available for external use. Registered users can request meteorological data from different cities, sites and time periods; raw data (L0), processed data (higher level products), as well as modelled data will eventually be provided. Once a dataset is ready for download, the details of the corresponding netCDF file are listed in the *DOWNLOAD* spread sheet of the LUMA logbook (Section C.2). This sheet is automatically converted to a table listing all available variables and the meta information required, the LUMA *CONTENT*. The latter is uploaded to the web (http*://LondonClimate.info/*LUMA*/CONTENT.csv*).

All relevant instructions, meta data and materials (Figure C.1) are provided online, e.g.:

- How to become a LUMA user (http*://LonconClimate.info/*LUMA/registration.html)
- How to place a data request (http*://LonconClimate.info/*LUMA/request.html)
- Which attributes are listed in the CONTENT (http*://LonconClimate.info/*LUMA/content.html).

Attributes that specify a dataset, i.e. those listed in the CONTENT list, can be summarised by categories (Table C.3). From the CONTENT list, required variables can be selected, reducing the file to become a new REQUEST list. The latter, a text file in csv-format, needs to be sent to LUMA as an email attachment from a registered email account. It comprises the following information: city, site, source, spatial info, temporal resolution, base resolution, title, name, units, category, data level, start time and end time.

A KCL developed Python based procedure, which automatically reads an incoming data request, checks for the availability of the data and also if the user is registered and permitted to download the requested variables. Then data are extracted from LUMA, again using cdo, and put on an ftp server from where the LUMA user can download a zip archive of NetCDF files after being notified via email.

Table C.5: Attributes listed in CONTENT.csv file, required for LUMA data request.

Type of information	Attribute	Column in CONTENT.csv	Description
Spatial	city	2	• City specifying the location of the measurement site or modelling domain. Datasets that cover more than one city are labelled under the country name or under "GLOBAL".
	site	4	• Datasets that include several sites or are spatial distributions in one city are labelled as "ALL". • If the data are provided as specific model input parameters, the attribute site can also be the model name.

	spatial info	11	• The spatial resolution if the file contains gridded data; units are given in "m", "km", “degree” or “arc_minute”. • The network if the data are related to a point measurement.
Source	source	5	Three general types of data sources are specified: • "model_output" can be a spatial dataset or a time series at one location, depending on the model and its settings. • "input_variable" describes data that match specific requirements and can therefore be used as input for certain models. • "observation" is the data type that specifies all datasets that originate from measurements. It includes raw data as well as processed data of higher levels. The same variable can be derived by different methods (e.g. model output or observation).
Variable	name	12	A commonly used abbreviation, e.g. ustar. • Might be extended by suffixes, such as: _mean (mean value), _sum (aggregated value), _max (maximum value) or _min (minimum value) • Some files include a variable in two different units. In order to differentiate, the name is extended by an abbreviation for the respective units. For example "_C" and "_K" is added to the name to distinguish between temperatures in Celsius and Kelvin. Given units are always provided, these extensions are self-explanatory.
	longname	14	A descriptive variable name, e.g. friction velocity.
	units	13	Mostly defined as SI-units, e.g. $m.s^{-1}$
	category	15	Category assigned to each variable, providing additional insight into the type of data. A variable can have more than one category (e.g. wind; turbulence).
	title	6	The title specifies name of the model, instrument or processing method.
	linked variables	16	Variables in LUMA are categorised into two types, the primary variables which are listed in the CONTENT file, and those which are considered auxiliary. These so-called linked variables are not listed individually but are rather provided automatically when the respective query is made. For example, if the variable "Tair" (i.e. air temperature) is requested, the associated linked variable "sd_Tair" (i.e. its standard deviation) is supplied as well.
Temporal	temporal resolution	9	Data for the various locations cover different time periods. The temporal resolution is listed in one of the following units: "Hz", "sec", "min", "hour", "month", or "year".
	base resolution	10	• For observations, this defines the temporal resolution of the former processing step (e.g. if samples of 1 s resolution are used for 10 min averages, the temporal resolution is 10 min and the base resolution is 1 s). • For model output, base resolution describes the temporal resolution of the forcing data.
Quality	data level	3	Observations as well as model data are available in various processing and quality levels (Table C.4).

Acknowledgements

The London Urban Micromet data Archive, LUMA, was developed with funding support from EUFP7 Grant agreement no. 211345 (BRIDGE) and NERC ClearfLo (NE/H003231/1), NERC ARSF (GB08/19), NERC FSF, EPSRC (EP/I00159X/1, EP/I00159X/2) Materials Innovation Hub and KCL. The LUMA archive system was developed and implemented by Simone Kotthaus, Dr Jiang-Ping He and Prof Sue Grimmond. All past and present members of the micrometeorological research group at KCL and University of Reading of Prof Sue Grimmond have contributed to the extensive micrometeorological measurement network across London, including site setup, software development, data quality control, and analysis. Namely, these are (in alphabetical order): Veronica Bellucco, Alex Björkegren, Matt Blackett, Cris Castillo, Jon Durrans, Oscar Finnemore, Mariana Lina Gouvea, Grace Healy, Leena Järvi, Mark de Jong, Jinda Sae-Jung, Simone Kotthaus, Fredrik Lindberg, Thomas Loridan, Lucía López Martínez, Will Morrison, John Mustchin, Lukas Pauscher, Pru Robinson, Alessandra Sala, Tom Smith, Marc Thomas, Helen Ward, and Duick Young; plus numerous students who have done checking of the daily plots. Technical support was provided by Alastair Reynolds, Paul Smith, Bruce Main, and Trevor Blackall. We thank KCL Directorate of Estates Facilities for giving us the opportunity to operate the various measurement sites at KCL Strand, Waterloo and Guys Campus. We thank Adrian Bowmann, Royal Borough of Kensington; Chelsea, for providing access to the sites NGT, NDT and NTT.